# Design and Fabrication of Single-Crystal Organic Photonic Circuit Modules Using Focused Ion Beam Lithography

A Thesis Submitted for the Degree of DOCTOR OF PHILOSOPHY



by Vuppu Vinay Pradeep

School of Chemistry
University of Hyderabad
(An Institution of Eminence)
Hyderabad-500046
INDIA

July-2023



# **CONTENTS**

Declaration		I
Certificate		U
Acknowledge	ements	Ш
List of Acrony	yms	V
Chapter-1	An Introduction to Photonic Components and their Fabrication Techniques	1-53
1.1.	Light confinement in optical waveguides	4
1.2.	Optical microresonators	6
	1.2.1. Fabry-Pérot (FP) optical resonators	7
	1.2.1.1. Free spectral range (FSR)	10
	1.2.1.2. Quality (Q) factor	10
	1.2.2. Whispering gallery mode (WGM) optical resonators	11
1.3.	Linear and non-linear optical properties	14
1.4.	Fabrication of nano/microstructures	16
	1.4.1. Bottom-up approaches	17
	1.4.1.1. Self-assembly	17
	1.4.1.2. Ambient pressure vapor deposition	17
	1.4.1.3. Microrod (Axial FP resonator)	18
	1.4.1.4. Microrod (Lateral FP resonator)	19
	1.4.1.5. Circular disk resonator	20
	1.4.1.6. Ring resonator	21
	1.4.1.7. Hexagonal disk resonator	22
	1.4.1.8. Square disk resonator	24
	1.4.2. Top-down approaches	25
	1.4.2.1. Atomic force microscopy (AFM) based lithography	25
	1.4.2.2. Focused ion beam (FIB) milling	26
	1.4.2.3. Flectron beam lithography (FBL)	26

	1.4.2.3.1. Fabrication of a silicon ring resonator	28
	coupled to a waveguide	
	1.4.2.3.2. Fabrication of a silicon disc resonator for sensing	29
	1.4.2.3.3. Fabrication of a silicon-based add-drop filter	30
1.5.		31
	1.5.1. Ion beam generation	33
	1.5.2. Directing and focusing the ion beam	33
	1.5.3. Beam-specimen interactions	34
	1.5.3.1. Electron and ion beams	35
	1.5.4. Factors influencing FIB milling	37
	1.5.4.1. Accelerating voltage	38
	1.5.4.2. Beam current	38
	1.5.4.3. Sputtering yield	39
	1.5.5. Nano/microscale effects in FIB milling	40
	1.5.5.1. Ion implantation	40
	1.5.5.2. Amorphization	40
	1.5.5.3. Redeposition	40
	1.5.6. Applications of FIB milling	41
	1.5.6.1. Fabrication of nanochannels of high-aspect-ratio	41
	1.5.6.2. Fabrication of plasmonic nanoparticles:  "sketch and peel" strategy	42
	1.5.6.3. Prototyping of 2D and 3D photonic structures	43
1.6.	Mechanophotonics for all-organic PIC fabrication	44
	1.6.1. Lifting of a single-crystal	44
	1.6.2. Breaking/cutting of a single-crystal	45
	1.6.3. Slicing and bending of a single-crystal	46
	1.6.4. Aligning/integrating of a single-crystal	47
	1.6.5. Extreme bending and transferring of a single-crystal	48
	1.6.6. Rolling of a twisted single-crystal	49
1.7.	Overview of the thesis	50

Chapter-2	<b>Ambient Pressure Sublimation Technique</b>	
	<b>Provides Polymorph-Selective Perylene</b>	54-67
	<b>Nonlinear Optical Microresonators</b>	
2.1.	Abstract	55
2.2.	Introduction	55
2.3.	Results and discussion	57
	2.3.1. Preparation of perylene microresonators via	57
	ambient pressure sublimation technique	37
	2.3.2. Growth of perylene microcrystals	59
	2.3.3. Photonic studies of $lpha$ - and $eta$ -form perylene crystals	60
	2.3.3.1. Excitation position dependency and crystal anisotropy on fluorescence (FL) intensity	61
	2.3.4. NLO studies and FDTD numerical calculations of $lpha$ - and $eta$ -form perylene crystal resonators	64
2.4.	Summary	67
Chapter-3	Focused Ion Beam Milling of Perylene Single-	
-	Crystals: Effects of Substrates, Etchants, and	
	Beam Parameters on Geometrically Precise	68-87
	Organic Photonic Modules	
3.1.	Abstract	69
3.2.	Introduction	69
3.3.	Results and discussion	70
	3.3.1. Preparation of perylene microcrystals	70
	3.3.2. Optimization of beam parameters to carve precise photonic architectures	71
	3.3.3. Effect of substrates and ion beam current	72
	3.3.3.1. Microcrystals on an ITO-PET substrate	73
	3.3.3.2. Microcrystals on a glass substrate	75
	3.3.4. Post-processing methods	77
	3.3.5. Effect of beam current on FL intensity and optical modes of resonators	78

		3.3.5.1. Fabrication of disk resonators using 0.4 nA beam current	79
		3.3.5.2. Fabrication of disk resonator using 0.1 nA beam current	82
	3.	3.6. Position-dependent FL studies on fabricated disk resonator	83
	3.	3.7. Pump-power-dependent studies on fabricated disk resonator	83
	3.	3.8. FL imaging and mapping of disk resonators	84
	3.	3.9. Fabrication of geometrically and dimensionally precise ring resonator	85
3.4	I. Co	onclusions	86
Chapter-4	4	Geometrical Shaping of Coumarin-153	
		Single-crystals into Next-Generation	88-97
		Optical Resonators	
•	4.1.	Abstract	89
4	4.2.	Introduction	89
4	4.3.	Result and discussion	90
		4.3.1. Preparation of coumarin-153 microcrystals	90
		4.3.2. Effect of gold coating on FL intensity of coumarin-153 microcrystals	91
		4.3.3. Fabrication of coumarin-153 disk resonators	92
		4.3.4. Photonic studies and FDTD numerical calculations of fabricated disk resonators	92
		4.3.5. Post-processing of fabricated disk resonators	96
4	4.4.	Conclusions	97
Chapter-!	5	A Tandem Approach to Fabricate a Hybrid,	
		Organic-Add-Drop Filter Using Single-	98-113
		<b>Crystal Disk-Resonators and Pseudo-Plastic</b>	30 113
		Crystal Waveguides	
Ę	5.1.	Abstract	99
į	5.2.	Introduction	99
	5.3.	Results and discussion	101

	5.3.1. Syntheses of BPyIN and BTD2CF <sub>3</sub>	101
	5.3.1.1. Synthesis of BPyIN	101
	5.3.1.2. Synthesis of BTD2CF <sub>3</sub>	101
	5.3.2. Steady-state optical properties	102
	5.3.3. Fabrication and photonic properties of perylene single-crystal disk resonators	103
	5.3.4. Photonic aspects of BPyIN and BTD2CF₃ microcrystals	106
	5.3.5. Fabrication of disk resonators-coupled optical waveguide	108
	5.3.6. Fabrication of hybrid organic add-drop filter (HOADF)	110
5.4	Conclusions	113
Chapter-6	Conclusions and Future Scope	114-118
6.1	Conclusions	114
6.2	Future scope of the work	117
	References	119
	Appendix A (Methods)	127
	Appendix B (Instrumentation)	128
	Research publications, patents, and presentations	134
	Curriculum vitae	137

**DECLARATION** 

I, Vuppu Vinay Pradeep, hereby declare that the matter embodied in this thesis entitled

"Design and Fabrication of Single-Crystal Organic Photonic Circuit Modules Using Focused

Ion Beam Lithography" is the result of my investigations carried out in the School of

Chemistry, University of Hyderabad, Hyderabad, India, from July 2017 to June 2023, under

the supervision of Prof. Rajadurai Chandrasekar.

In keeping with the general practice of reporting scientific observations, due

acknowledgments have been made wherever the work described is based on the findings

of other investigators. Any omission, which might have occurred by oversight or error, is

regretted. A report on plagiarism statistics from the library, University of Hyderabad, is

enclosed.

Vuppu Vinay Pradeep

Reg. No: 17CHPH35

I



#### **CERTIFICATE**

This is to certify that the thesis entitled "Design and Fabrication of Single-Crystal Organic Photonic Circuit Modules Using Focused Ion Beam Lithography" submitted by Vuppu Vinay Pradeep bearing registration number 17CHPH35 in partial fulfillment of the requirements for the award of Doctor of Philosophy in the School of Chemistry is a bonafide work carried out by him under my supervision and guidance. This thesis is free from plagiarism and has not been submitted previously in part or in full to this or any other University or Institution for the award of any degree or diploma.

Parts of this thesis have been published/communicated/filed for publication/patent as indicated below:

- 1. V. V. Pradeep et al. Adv. Opt. Mater. 2020, 8, 19013179. (Chapter-2)
- 2. V. V. Pradeep et al. Adv. Opt. Mater. 2022, 10, 2201150.
  - V. V. Pradeep et al. Cryst. Growth Des. 2023, DOI: 10.1021/acs.cgd.3c00653.
  - V. V. Pradeep et al. Indian Patent Application, E-2/1199/2023/CHE (filed).
  - V. V. Pradeep et al. Patent Corporation Treaty, IN2023/050278 (filed) (Chapter-3)
- 3. V. V. Pradeep et al. Nanoscale, 2023, DOI: 10.1039/D3NR02229C (Chapter-4)
- 4. V. V. Pradeep et al. Manuscript submitted (Chapter-5)

He has also presented oral/posters at the following conferences:

- 1. Best oral presentation prize in CHEMFEST-2022, SoC, UoH, Hyderabad, India.
- 2. Poster presentation in CHEMFEST-2020 and 2022, SoC, UoH, Hyderabad, India.
- 3. Poster presentation in ICFAST-2022, UoH, Hyderabad, India.
- 4. Poster presentation in Indo-Sweden, DST-VR conference, 2022, IIT Roorkee, Uttarakhand, India.

Further, the student has passed the following courses towards the fulfillment of the coursework requirement for Ph. D.:

	Course	Title	Credits	Grade
1.	CY-801	Research Proposal	4	Α
2.	CY-805	Instrumental Methods A	4	В
3.	CY-806	Instrumental Methods B	4	В

Prof. Rajadurai Chandrasekar

(Thesis Supervisor)

Dr. R. CHANDRASEKAR Professor School of Chemistry University of Hyderabad Hyderabad-500046, India School of Chemistry

Dean SCHOOL OF CHEMISTRY University of Hyderabad Hyderabad-500 046

#### **ACKNOWLEDGEMENTS**

I would like to express my deepest gratitude to acknowledge all those who helped and supported me during my research work.

I convey my profound gratitude and sincere thanks to my thesis supervisor Prof. Rajadurai Chandrasekar, for his invaluable guidance, constant encouragement, and support he gave me in carrying out my research work. His positive approach in every aspect was admirable and inspiring. He has always been approachable, helpful, and cooperative. I really appreciate his constant support and fruitful discussions from the bottom of my heart. Without him, I could not achieve so much today, and I also appreciate his patience and confidence in me. I will forever be grateful for giving me the opportunity to be a part of his research group.

I would also like to express my sincere thanks and immense pleasure to doctoral committee members Prof. Samar Kumar Das and Dr. Murali Banavoth and the present and former deans of School of Chemistry, University of Hyderabad.

I am sincerely thankful to all my colleagues in the School of Chemistry for fruitful scientific and social discussions and for making my research life productive. I wish to thank the financial sponsor CSIR, New Delhi, for providing a research fellowship. I would also like to thank UOH-IOE and DST-SERB for providing the required instrumental facilities.

My deepest gratitude is also to Prof. Tatiana Murzina, Moscow State University, Russia, for FDTD simulations, NLO microscopy studies, and fruitful collaboration. I would also like to thank Dr. Sai Rama Krishna Malladi for FIB experiments and collaboration. I also would like to extend my gratitude towards Mr. Manu Mathai at the advanced center for microscopy and microanalysis, IISc Bangalore, for assisting me during FIB experiments.

I would like to express my gratitude to all my seniors, Dr. Venkatakrishnarao, Dr. Venkata Ramudu, Dr. Radhika, Dr. Ravi, Ms. Jyoti, and Dr. Annadhasan, for their outstanding help and friendly atmosphere. I am grateful to have such wonderful lab mates and juniors, Mr. Vinod Kumar, Mr. Rohullah, Mr. Melchi, Mr. Ankur, Ms. Sindhuja, Ms. Vinaya Durga, and Mr. Anand, for their help.

I am thankful to University of Hyderabad for the excellent atmosphere and world-

class research facilities. It's my pleasure to acknowledge all the faculty, non-teaching staff,

and instrument operators of School of Chemistry for their help and assistance on various

occasions. I specially thank Mr. Durga Prasad, Mr. Sunil, Mr. Mahesh, Mr. Abraham, Smt.

Rani, Smt. Geeta, Mr. Mahender and Mr. Venkat anna.

At this time, I recall with deep respect to my teachers Rama Krishna sir, Keerthi sir,

Ganesh sir, Daniel Christy sir, Srinivasarao sir, Raviraju sir, and Mahapatra mam for their

perpetual inspiration, and it was their encouragement that paved me as a researcher. Also, I

like to pay my respectful regards to all my teachers at various stages of my academic life.

I am also lucky enough to have the support of many School of Chemistry seniors,

especially Dr. Ashok Pabbati, Dr. Vikranth, Dr. Anil Kumar, Dr. Suryanarayana, Dr. Ravinder,

Dr. Subham Dutta, Dr. Sateesh, Dr. Senthilnathan, and Dr. Rama Krishna for their help and

guidance at different stages of the journey. I thank my friends Shruti, Seema, Calvin, Sivaram,

Sasikanth, Hemanth, Vamshi, Noorul, Isha, and Navaneeta for their help and encouragement

during these years.

Looking back, finally, I thank my parents, Satyanarayana and Geeta, whom I adore

most, for their love, blessing, and confidence in me in building the platform of my life. Also,

I express my love to my brother, Srikanth, for his immeasurable affection and support.

Vuppu Vinay Pradeep

University of Hyderabad,

July 2023

IV

## **LIST OF ACRONYMS**

$\theta_i$	angle of incidence
$\theta_r$	angle of refraction
p	angular mode number
AFM	atomic force microscope
ф	azimuthal angle
m	azimuthal mode number
cm	centimeter
СТ	charge transfer
СОМ	confocal optical microscope
CW	continuous wave
τ	delay time
DR	disk resonator
$n_{eff}$	effective refractive index
Е	electric field
eV	electron volt
FP	Fabry-Pérot
FESEM	field emission scanning electron microscopy
FLIM	fluorescence lifetime imaging microscopy
FTO	fluorine-doped tin oxide
FDTD	finite-difference time-domain
FIB	focused ion beam
$\mathcal{E}_0$	free space permittivity
FSR	free spectral range
f	frequency
FWHM	full width at half maximum
Н	hardness
ITO	indium tin oxide

P(t)	time-dependent induced polarization
IR	infrared
L	length
$\chi^{(1)}$	linear electric susceptibility
$\chi^{(2)}$ , $\chi^{(3)}$	nonlinear electric susceptibilities
ε	materials permittivity
MHz	megahertz
μm	micrometer
mW	milliwatt
nA	nanoampere
nm	nanometer
ns	nanosecond
NIR	near-infrared
α'	optical loss
$ au_p$	photon life time
$\pi \cdots \pi$	pi-pi
<sup>1</sup> H	proton
Q-factor	quality factor
q	radial mode number
R	radius
n	refractive index
$\mathcal{E}_r$	relative permittivity
RR	ring resonator
RT	room temperature
$\Delta h$	stub height
$T_s$	sublimation temperature
t	sublimation time
T	temperature
TCSPC	time-correlated single photon counting

TEM	transmission electron microscope
TE	transverse electric
TM	transverse magnetic
TPA	two-photon absorption
TPL	two-photon luminescence
UV	ultra-violet
Vis	visible
$\lambda_{max}$	wavelength maximum or absorption maximum
WGM	whispering gallery mode

An Introduction to Photonic Components and their Fabrication Techniques

Photonics is a branch of science that deals with the study of the behavior and manipulation of light when it interacts with matter. It encompasses various fields such as optics, electronics, material science, quantum mechanics, and quantum electrodynamics and has numerous applications important for both fundamental research explorations and technological advancements. It is infiltrating all major industry sectors, from manufacturing and communication to medicine and environmental monitoring. The field of photonics is constantly evolving, with discoveries and technological developments being made each day, and it has revolutionized the way the data is communicated, processing information, diagnosing biological diseases, and producing renewable energy. As modern technology evolves, photonics will likely continue to play a vital role in advancing our world. Therefore, the development of efficient, compact, and cost-effective optical devices is in high demand for a variety of purposes, including high-speed data transfer, spectroscopy, material processing, and communication. [1-3] Photonic integrated circuits (PICs) are a critical element in the field of photonics, which is focused on the manipulation of light for various applications.



**Figure 1.1.** a) The world's first electronic integrated circuit, created on a small piece of germanium, consists of a transistor, resistors, and a capacitor, all integrated onto the same chip. Inset shows the photograph of the inventor, Jack Kilby. b) The first monolithic electronic integrated circuit in the hands of its inventor, Robert Noyce, fabricated by connecting all the components using copper wires on a single silicon chip. c) Optical image of the silicon-based photonic integrated circuit consisting of grating couplers, waveguides, splitters, and phase shifters. [Figure adapted from ref. 4-6].

The first rudimentary electronic integrated circuit (EIC) was constructed using germanium by Jack Kilby (Figure 1.1a). Later, in 1959, a monolithic EIC was fabricated by connecting all components using copper lines on a single silicon chip by Robert Noyce (Figure 1.1b). Similar to EICs, PICs consist of various photonic components such as waveguides, resonators, modulators, directional couplers, lasers, and detectors on a single chip, allowing for diverse functionality and efficient performance. Optical waveguides and

resonators (ring and disk geometries) are the main structural and functional building blocks of PICs. Optical waveguides act as signal transporters, whereas resonators confine the signal. The confined light can be amplified, routed (clockwise or anti-clockwise), and split in the desired directions. This tight confinement is responsible for the efficient transfer of photons between different components on the complex chip. The waveguide structures are typically comprised of silicon or complementary metal oxide semiconductor (CMOS) materials like gallium arsenide (GaAs) or indium phosphide (InP). These materials possess high refractive indices ( $n \approx 3.5$ -3.9) and low light propagation losses, enabling low-power consumption and high-speed data transmission. [7-11]

In recent years, optical circuits have been slowly poised to replace electronic circuits. Till-date, only silicon-based PICs have been created and deployed by leading international corporations like Smart Photonics, Luna, NeoPhotonics, Aifotec AG, CyOptics, Intel, Infinera, Enablance, etc., for commercial applications. High n, low-loss bending radius, and precise fabrication processes (electron beam lithography, EBL) are major benefits of silicon that prompted its sporadic use in photonic circuits. Scarcella et al. in 2016 reported a silicon-based PIC fabricated using the CMOS wafer-scale process (Figure 1.1c). [6] Even though Si-PICs have several advantages, there are a few drawbacks that pushed researchers to explore workable materials substitutes for Si-PICs. The main limitations of silicon are passive-only light transportation, expensive manufacturing and complex processing, small non-linear optical (NLO) coefficients, and structural non-reconfigurability due to its hardness (H =150 GPa). Si-based optical circuits employ optical modulators to produce various output signals for different logical functions. [11]

In this scenario, as an alternative to silicon, organic single-crystals provide fine adjustment of molecular optical absorption and emission regimes through the ease of molecular design and synthesis, high exciton binding energy, large NLO coefficients, chirality, light weight, mechanical flexibility (allows structural reconfigurability), and passive and active light transport, to emerge as a potential alternative. However, the micromanipulation of organic single-crystals for photonic application was an issue in employing them for PICs construction. Few research teams have excelled at creating various organic optical components in the last 15 years. In this regard, it is important to describe that Chandrasekar's research team at the University of Hyderabad has introduced a

research area called *mechanophotonics*, in which organic microcrystals were mechanically integrated using atomic force microscopy (AFM) cantilever tip to fabricate many prototype all-organic PICs (OPICs). Despite organic crystals' advantage over silicon, due to the lack of precise control over the crystal geometry of organic photonic modules, they are unable to enter the photonics market meant for real-time applications. Hence, it prompted an investigation of industrially viable techniques to build organic crystal photonic components for OPICs.

This thesis explores the potential of focused ion beam (FIB) milling of organic microcrystals to fabricate highly reproducible photonic components, viz. waveguides, disk resonators, ring resonators, bent waveguides, and directional couplers. This thesis provides a brief introduction to waveguides and resonators, followed by an overview of various microfabrication techniques like sublimation, self-assembly, and EBL. A significant focus on FIB milling, its fundamentals, and factors affecting milling are briefly given in the following sections. Finally, the *mechanophotonics* approach will be discussed, which is crucial for the integration of FIB-processed organic crystalline resonators with different emissive waveguides to achieve all-organic *hybrid* PICs.

#### 1.1. Light confinement in optical waveguides

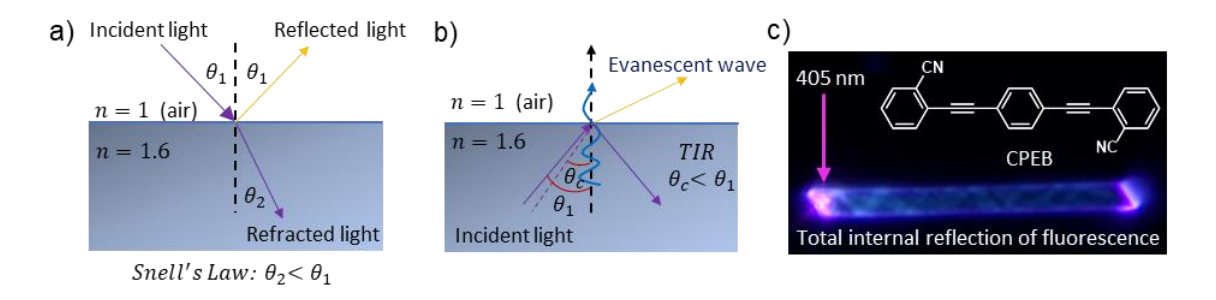
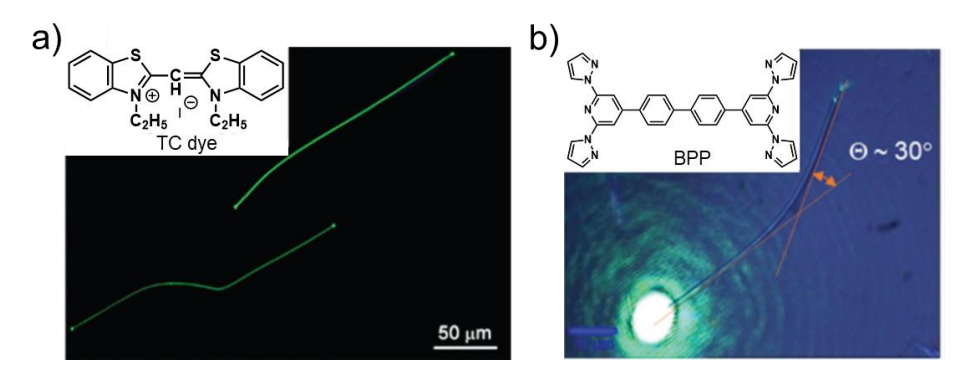


Figure 1.2. a) Refraction condition for light traveling from rarer to denser media according to Snell's law. The n values of crystal and air are 1.6 and 1, respectively. b) Condition for total internal reflection (TIR) and the origin of evanescent wave. c) TIR of the produced fluorescence in an organic CPEB microcrystal waveguide. Inset shows the molecular structure of CPEB [Figure adapted from ref. 15]

Optical waveguides are structures that can trap and transport light. This is achieved by designing an acicular waveguide that has high light reflectivity at its boundaries. The fundamental law of optics, known as Snell's law, describes how light bends when it crosses a barrier between two different media. It states that the angle at which light is refracted (or

bent) as it passes through the boundary is related to the ratio of n of two media. It can also be understood as when a light ray passes from a rarer (n =1; for air) to a denser (n =1.6; for organic material) medium, at the boundary, some of the light is reflected by the medium, and some of the light is refracted into the medium of high n (Figure 1.2a). In this case, the incident beam angle and reflected beam angle will be the same, i.e.,  $\theta_1$ , which is greater than the refracted beam angle ( $\theta_2$ ).

In another case, when the light traverses from a high n to low n media, if the incident angle exceeds the critical angle, the light undergoes total internal reflection (TIR) within the high n (=1.6) medium. In this process, a small portion of the beam leaks into the rarer medium (n =1) and decays exponentially with respect to distance from the surface and is known as the evanescent field or evanescent wave (Figure 1.2b). This evanescent wave opens the possibilities to attain optical coupling between two waveguides, optical splitters, fiber tapping, optical resonators, and wireless photonic devices. The fluorescence (FL) image of an organic microcrystal self-assembled from 1,4-bis(2-cyanophenylethynyl)benzene (CPEB), portraying the TIR and subsequent light propagation inside the waveguide (Figure 1.2c). [15]



**Figure 1.3.** a) The first flexible organic active optical waveguide from TC dye nanofibers. Inset shows the molecular structure of TC dye. b) The first flexible organic passive optical waveguide from BPP microcrystals. Inset shows the molecular structure of BPP. [Figure adapted from ref. 16 and 31].

In the last two decades, many organic crystal-based optical waveguides have been reported. One of the advantages is the active<sup>[15-29]</sup> and/or passive<sup>[30-34]</sup> nature of waveguides, depending on the light absorption range of waveguide material. Another important aspect is the mechanical flexibility of the organic crystalline optical waveguides, which can be used to guide the light at different angles. Further, the bent region (where the light leaks) can also be used effectively to couple other optical components. The first report

of a flexible active-type optical waveguide by Takazawa et al. in 2005<sup>[16]</sup> demonstrated the light-guiding ability of self-assembled nanofibers of 3-ethyl-2-[(3-ethyl-2(3H)-benzothiazolylidene)-methyl]benzothiazolium iodide (thiacyanine, TC) dye (Figure 1.3a). The self-assembled nanofibers show concentration and solvent-dependent emission. The first passive waveguide was reported by Chandrasekar et al. in 2013,<sup>[31]</sup> wherein they used flexible micron-sized tubular crystals of 4,4-bis(2,6-di(1H-pyrazol-1-yl)pyridin-4-yl)-biphenyl (BPP, Figure 1.3b).

#### 1.2. Optical microresonators

Optical microresonators have emerged as a critical component in the field of photonics due to their ability to trap light in a small volume. They are essential for numerous applications in sensing, spectroscopy, lasing, nonlinear optics, and quantum information processing. [35-52] Optical microresonators confine light in a microscale volume through TIR. The light is trapped within the resonator by the back-and-forth bouncing of light between two reflective surfaces, creating an interference pattern. The light-reflective surfaces can be mirrors or dielectric layers and can have various shapes, such as spheres, disks, squares, rectangles, hexagons, etc.

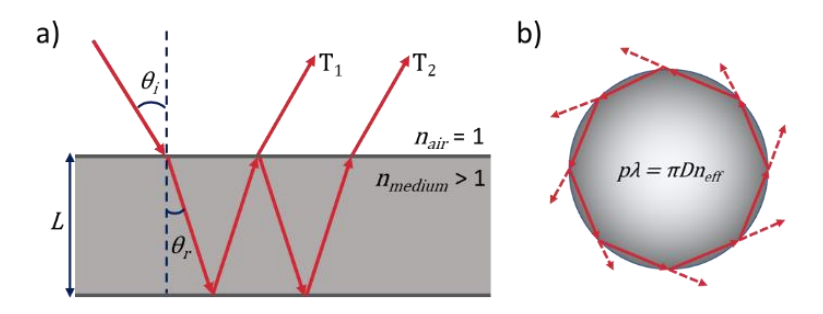


**Figure 1.4.** a) Fabry-Pérot and b) whispering gallery mode type microresonators and their resonance conditions. Symbols L,  $\theta_i$ ,  $\theta_r$ ,  $T_1$ ,  $T_2$ ,  $n_{air}$ ,  $n_{medium}$ , p,  $\lambda$ , D,  $n_{eff}$  denotes the length of the resonator, incident angle, refracted angle, transmitted waves, n of air and medium, mode number, wavelength of the light, diameter of the resonator, and effective n, respectively.

Significant progress has been made in the field of optical microresonators in the past few decades. Advances in nanofabrication techniques have allowed for the creation of resonators with increasingly complex shapes and designs, leading to improvements in their sensitivity and quality factor. Researchers are also exploring the use of new materials, such as 2D materials and plasmonic architectures, to create novel microresonators with unique

properties. There are several types of optical microresonators with various geometries. The most common types of optical microresonators include Fabry-Pérot (FP) and Whispering gallery mode (WGM) resonators (Figure 1.4).

#### 1.2.1. Fabry-Pérot (FP) optical resonators

Fabry-Pérot interferometers (FPIs) were created in the late 19th century and have been crucial in enhancing the resolution and applications of optical spectrometers.<sup>[53]</sup> These are microresonators that consist of two highly reflective parallel surfaces spaced apart by a distance that is an integral multiple of the light's wavelength. The light is trapped within the resonator by reflecting it between the two surfaces (Figure 1.4a and 1.5).

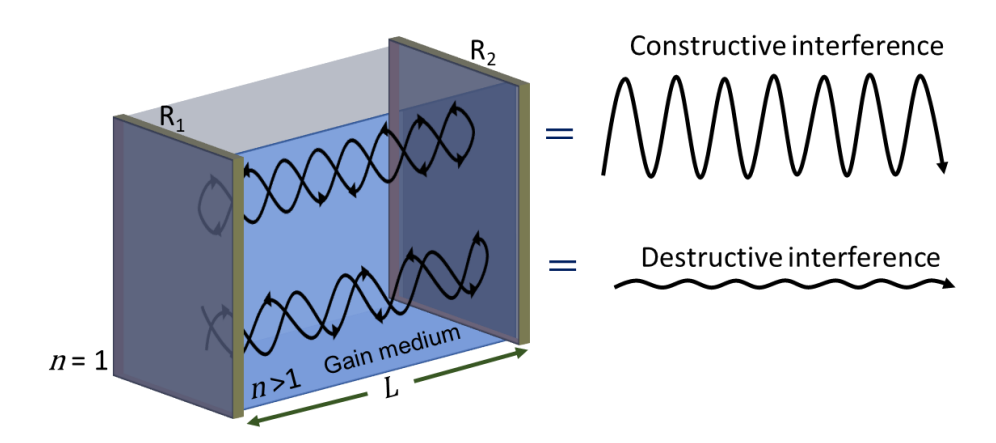


**Figure 1.5.** The graphical illustration of an FP resonator depicting the two scenarios of constructive and destructive interferences.

Two parallelly placed partially transmitting mirrors separated apart by a length L is a simple illustration of an FP resonator. While successively reflected beams with normal incidence have a path difference of 2L, interference results from multiple reflections of a light beam between its mirrors. As a result, constructive and destructive light interference occurs (Figure 1.5). For maximum constructive interference,

For maximum destructive interference,

FP resonators are a result of FPIs, where the emphasis is on the characteristics of the internally stored light rather than the transmitted or reflected intensity. An important phenomenon that occurs here is the formation of standing waves as a result of the superimposition of two oppositely traveling waves. Figure 1.6 shows the standing waves for

six frequencies. The solid red line represents a particular snap of a standing wave at a specific instant of time, and the dashed lines represent snaps at different times. The term "standing wave" refers to a wave that oscillates with an amplitude at each point along its length rather than propagating along it. Some points do not show any oscillation at all, and these are called "nodes" (N, Figure 1.6). Whereas specific points oscillate to maximum amplitudes; hence these are called "anti-nodes" (AN, Figure 1.6).

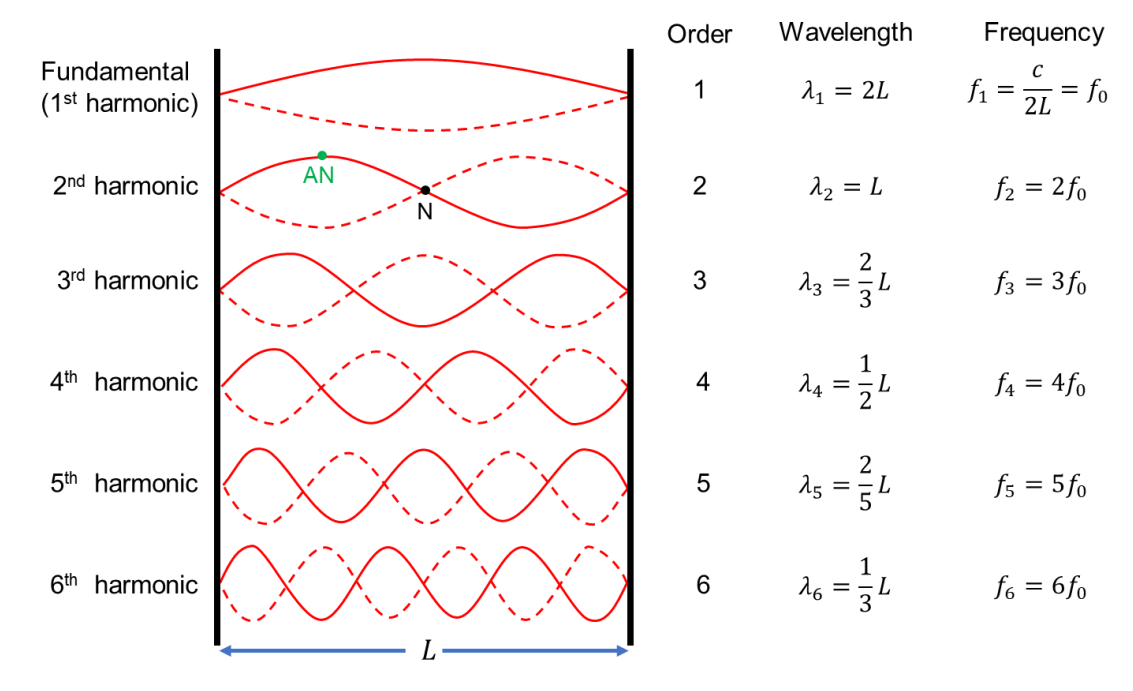


**Figure 1.6.** Standing waves of six different frequencies formed in an FP resonator. A representative AN and N are shown in the second harmonic.

Mathematically, the two traveling waves, which are propagating in opposite directions, can be written as:

$$D_R(x,t) = A\sin(kx - wt) \qquad ------ (3)$$

$$D_L(x,t) = A\sin(kx + wt) \qquad ------ (4)$$

The superimposition of these two waves, which is the sum of both the above equations, results in a standing wave and is given by,

$$= 2A \sin(kx)\cos(wt)$$
 ------ (6)

The amplitude (A) of a particular point at position x on the wave can be given as:

$$A(x) = 2A\sin(kx) \qquad ----- (7)$$

Hence, a standing wave having one anti-node is referred to as the first harmonic, two anti-nodes are called the 2<sup>nd</sup> harmonic, and so on. The order, wavelength, and corresponding frequencies of the six harmonics are shown in Figure 1.6. The nodes of the standing wave for the n<sup>th</sup> harmonic are at,

The anti-nodes are located at:

Generally, the frequency of the wave can be written as,

Let the sides of the resonator be a,b,L and the corresponding allowed resonant frequencies are given by,

where the speed of the light is denoted by c and the m, n, q are the integer values that correspond to the number of anti-nodes in a, b and L dimensions.

These anti-nodes and nodes are the resultant of the multiple reflections in the resonator. As mentioned earlier, superposition of two oppositely traveling waves (reflected light waves) results in constructive and destructive interferences, which in turn, causes the electromagnetic field inside the resonator to be enhanced. The constructive interference leads to the anti-nodes or resonant modes or peaks in the FL spectrum, which are also called optical modes. The destructive interference of the reflected waves results in nodes that lie in between the optical modes. The mode can also be understood as the electromagnetic field distribution that interprets the resonating light's course and frequency.

#### 1.2.1.1. Free spectral range (FSR):

The frequency separation between two adjacent resonant modes of an optical resonator is termed FSR. As the name implies, this is a spectra-free region. FSR is a fundamental property of an optical resonator and is determined by its length L,  $n_{eff}$  and mirror reflectivity of the resonator. Each resonant mode has a unique frequency and electric field distribution, and it is deterministic of a particular mode number. The FSR ( $\Delta\lambda$ ) can be understood as the separation between two successive resonant modes (m, m+1) and can be represented as, [55]

$$\Delta \lambda = \lambda_m - \lambda_{m+1} \qquad ----- (12)$$

The following equation describes how the FSR has an inverse relationship with the length,  $\boldsymbol{L}$  of a microresonator.

$$FSR (\Delta \lambda) = \frac{\lambda_m^2}{2L \, n_{eff}} \qquad ----- (13)$$

where  $\lambda_m$  is the maximum wavelength of that resonant mode. The essence of this equation is that, it gives the idea about the number of possible resonant modes in the resonator and can be tuned by varying the resonator size.

#### 1.2.1.2. Quality (Q) factor:

The Q-factor of an optical microresonator is a measure of its ability to store light. The higher the Q-factor, the longer the light can be trapped within the resonator, allowing for more efficient photon-matter interactions. Q-factors of optical microresonators can reach values as high as  $10^8$ , making them some of the most efficient light-trapping devices.

$$Q = \frac{\text{energy stored}}{\text{energy loss}} \longrightarrow (14)$$

The Q-factor can also be understood as the number of light oscillations that the resonator can sustain before losing a significant fraction of its energy. Q-factor can be calculated using the formula:

$$Q = \frac{f_0}{2\Delta f} \qquad ------ (15)$$

Where  $f_0$  and  $\Delta f$  is the resonant frequency of the resonator and the full width at half maxima (FWHM) linewidth of the resonance peak. The FWHM linewidth is a measure of the

broadness of the resonance peak and indicates the amount of energy lost by the resonator per cycle.

In the case of a microresonator, the Q-value is an inverse of overall losses associated with the optical resonator. It is the result of several intrinsic losses (like scattering, material absorption, and radiation loss via curvature defects) and extrinsic losses (including coupling loss). [56] The external loss arises due to the coupling between any two resonators, which can be used effectively to couple and route the light. The equation associated with all these losses can be written as,

$$\frac{1}{Q} = \frac{1}{Q_{material}} + \frac{1}{Q_{scattering}} + \frac{1}{Q_{radiation}} + \frac{1}{Q_{coupling}} \longrightarrow (16)$$

By optimizing the fabrication/assembly process, the resonator surface roughness and scattering  $loss^{[57]}$  can be reduced. The size of the resonator directly affects radiation loss, which can be decreased by controlling the dimension. Typically, a Q-value of  $10^3$ - $10^7$  is considered as high, and values above  $10^7$  are considered ultra-high. The microresonator which are with high Q-values are used as microlasers. As of now, the maximum Q-value reported for an F-P resonator is  $10^5$ , whereas  $10^{11}$  for WGM resonators, providing high energy density and a long photon lifetime for light-matter interaction processes. The development of high-Q optical microresonators has opened up new possibilities for research and innovation, and researchers continue to explore the potential of these devices for future applications.

#### 1.2.2. Whispering gallery mode (WGM) optical resonators

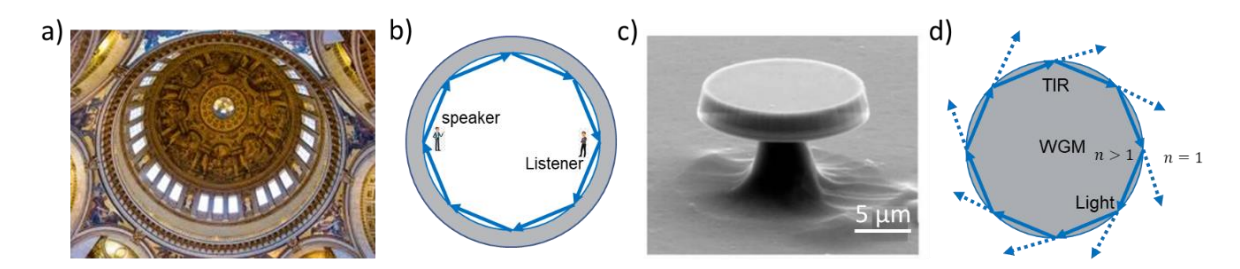


**Figure 1.7.** a) The interior doom view of St. Paul Cathedral, London. b) Schematics of acoustic WGMs. c) SEM image of gallium nitride microdisk fabricated via EBL. d) Schematic of light confinement in WGM microresonator. [Figure adapted from ref. 62 and 76].

WGM optical resonator is a type of optical resonator in which light is trapped and repeatedly reflected along the circumference of a curved surface. [61] This type of resonator owes its name to the acoustic whispering gallery effect observed in St. Paul's Cathedral in London, where sound waves propagate along the curved walls of the gallery due to total internal reflection (Figure 1.7a,b). [62,63] The WGM resonator can be made from a variety of materials such as glass, quartz, sapphire, inorganic molecules, organic molecules, or polymers and can have various shapes such as spheres, hemispheres, disks, toroids, cylinders, etc. [64-75] Figure 1.7c,d shows the gallium nitride WGM disk resonator fabricated using EBL [76] and the schematic of the light confinement, respectively.

The confinement of light in the WGM resonator is based on the phenomenon of TIR, where light traversing through a media with a higher n encounters an interface with a media of lower n, then the light is reflected back into the higher index medium. These WGM resonators can support a large number of resonant modes, where the light is confined and travels around the circumference of the resonator with minimal loss. The resonance frequencies of the WGM resonator are determined by the size and shape of the resonator, as well as the n of the resonator and the surrounding medium. Light can self-reinforce when it meets the resonance criteria as per eq. (17) after traveling one round around the resonator, light that does not meet the resonance criteria is eliminated.

$$p\lambda = \pi D n_{eff} \qquad ------ (17)$$

In this case, p is an integer that corresponds to the angular momentum of a photon that is circling inside a spherical resonator. Additionally, the polar, azimuthal, and radial mode numbers are used to describe these WGMs in resonators. The electromagnetic field's azimuthal and radial directions are represented by the letters m and q, respectively. A series of field oscillations in the  $\theta$ -direction are produced by the angular mode number p = l - m = 0, 1, 2,... Figure 1.8a shows the spatial structure of WGMs. The FSR, like with all resonators, is the typical mode spacing for a single-mode family. Figure 1.8b shows two mode families (blue and green lines), whose respective FSRs (FSR $_{\ell,1} \neq \text{FSR}_{\ell',2}$ ) are determined by geometric dispersion. Each mode family includes non-equatorial WGMs (q = 1, p = 0) at an offset frequency, along with equatorial WGMs (q = 1, p = 0) (Figure 1.8b). The frequency variations

of the WGMs from various mode families within a given spectral measurement frame enable unambiguous identification of p.<sup>[77]</sup>

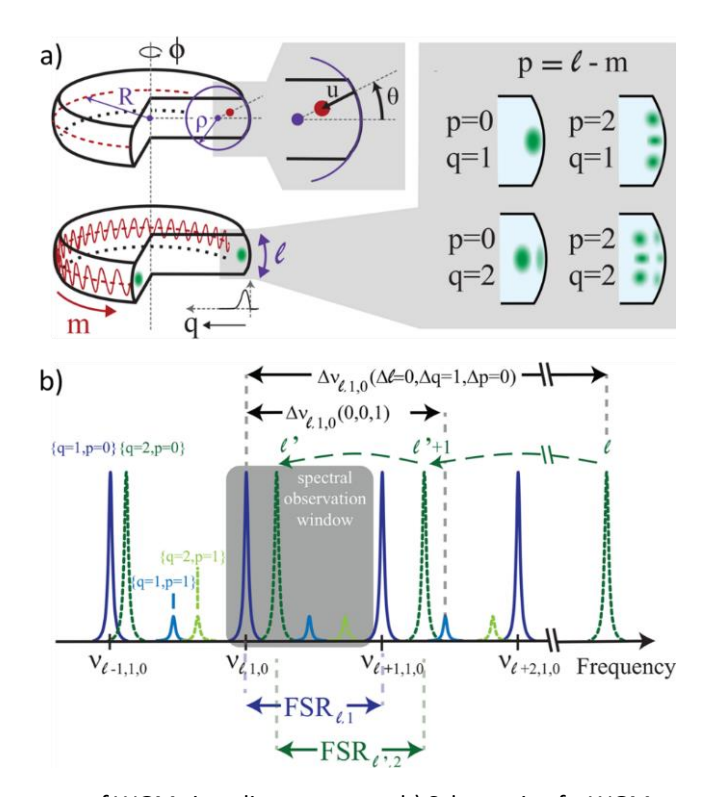


**Figure 1.8.** a) Spatial structure of WGMs in a disc resonator. b) Schematic of a WGM resonator mode spectrum to calculate FSR for two families (blue and green lines) of modes. [Figure adapted from ref. 77].

Polarization of the radiation is one of the characteristic attributes of WGM resonance. Each mode is distinguished by its polarization as transverse magnetic (TM) or transverse electric (TE), depending on whether the electric field is parallel or perpendicular to the fiber-length axis. Both TE and TM modes can be sustained in WGM resonators.<sup>[78]</sup> Here are the approximate equations with a correction term that have been implemented to determine the resonant wavelengths observed in the WGM resonator surrounded by an envelope of air.<sup>[55]</sup>

$$\lambda_{TM} \approx \frac{2\pi R n_1}{p + 1.856 p^{\frac{1}{3}} + \left(\frac{1}{2} - \frac{1}{n\sqrt{n^2 - 1}}\right)}$$
 (19)

For light to be confined inside the resonator using TIR, a WGM microresonator must have n>1. Therefore, given the same p,  $\lambda_{\rm TE}$  modes resonate at a longer frequency than  $\lambda_{\rm TM}$  modes.

#### 1.3. Linear and non-linear optical properties

In general, the non-linear light-matter interactions are too weak. These interactions can be understood by comparing the electric field strength of light waves  $(E_i)$  to that of the field in atoms  $(E_a)$ . $^{[79,80]}$  The typical field from sun is around  $E_1 \sim 600$  V/m, and the fields in atoms are about  $E_a \approx 10^{11}$  V/m (in optical intensity,  $I_a \approx 10^{20}$  W/m²). As  $E_i \ll E_a$ , deviation of electrons from the mean location by the light is minimal, suggesting the weak interactions of light with the matter. Therefore, high optical intensities are essential to observe nonlinear interactions. For instance, an  $I > 10^8$  W/m² is attained by a 50 mW laser that is directed to produce spots with sizes of a few tens of microns in order to expect nonlinear properties in organic materials. $^{[80]}$ 

In conventional linear optics, the polarization P(t) varies linearly with the electric field E(t). The corresponding equation can be written as,

$$P(t) = \varepsilon_0 \chi^{(1)} E(t) \qquad ------- (20)$$

Where  $\varepsilon_0$ ,  $\chi^{(1)}$  are the free space permittivity and the linear electric susceptibility. In contrast to linear optics, the polarization P(t) in non-linear optics (NLO) can be expanded using the power series in terms of E(t) and is represented as,

Where  $\chi^{(2)}$  and  $\chi^{(3)}$  are 2<sup>nd</sup>- and 3<sup>rd</sup>-order non-linear electric susceptibilities, respectively. Ideally, frequencies of the applied electric field determine these susceptibilities. However, it is assumed that the NLO medium reacts instantly (lossless and dispersionless medium), so these susceptibilities are taken as constants. Hence, for simplicity, in the above equations, P(t) and E(t) are taken as scalar quantities. The relationship between the material response and the applied electric field amplitude can be described by various processes. In non-resonant excitation conditions,  $\chi^{(2)}$  will be the order of  $\chi^{(1)}/E_a$ . As  $\chi^{(1)}$  is unity,  $\chi^{(2)} = 1/E_a \cong 1.94 \times 10^{-12} \,\mathrm{m/V}$ . In the same way, it is anticipated that  $\chi^{(3)}$  to be the order of  $\chi^{(1)}/(E_a)^2 \cong 3.78 \times 10^{-24} \,\mathrm{m^2/V^2}$ .

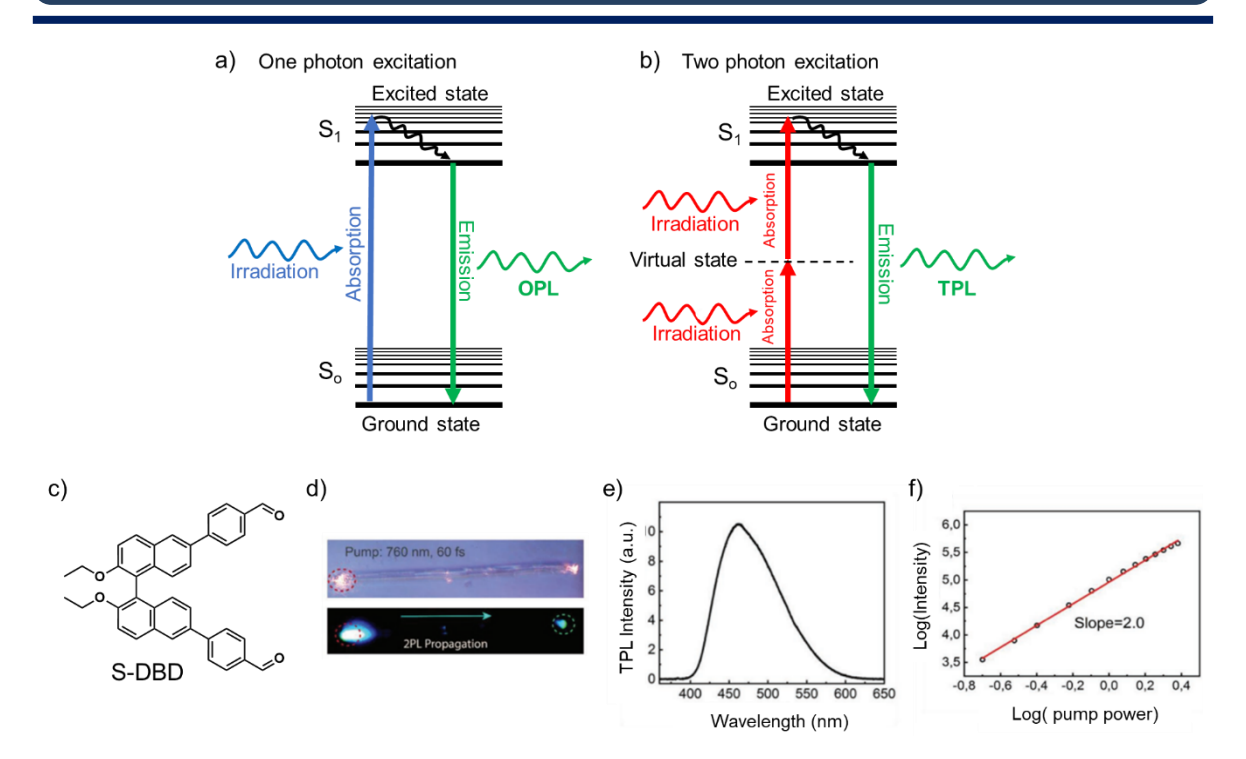


**Figure 1.9.** a,b) Jablonski diagrams represent the one-photon and two-photon optical processes, respectively. c) Molecular structure of S-DBD. d) Confocal optical microscope and TPL images of S-DBD microcrystal upon pulsed laser excitation. e) Single-crystal TPL spectrum of S-DBD microcrystal. f) Logarithmic-plot of TPL intensity vs. incident pump-power displaying slope value of 2. [Figure adapted from ref. 81]

Typically, in linear processes, the samples are irradiated by light sources of visible wavelengths. Figure 1.9a shows the one-photon excitation process, wherein the electron goes from the ground state to the excited state by absorbing the energy from an incident photon. FL is produced when an electron returns to the ground state from the excited state after non-radiative relaxation and releases a photon with a lower energy (longer wavelength) than the absorbed one. However, when a molecule absorbs the energy of two photons, it will decay by generating a photon that has higher energy (shorter wavelength) compared to the excitation photons (Figure 1.9b). Therefore, one-photon absorption (OPA) and two-photon absorption (TPA) are fundamentally different, which involve one-photon and simultaneous absorption of two photons by a molecule, respectively. Hence, OPA depends linearly on intensity, whereas TPA increases with the square of laser light intensity (Figure 1.9c). TPA is a NLO,  $\chi^{(3)}$  process, and it was experimentally demonstrated by Göppert-Mayer (GM).<sup>[82]</sup>

Ultrashort-pulsed lasers operating in the near-infrared wavelength region are often used to exploit multi-photon absorption events. Because high spatial and temporal

densities of low-energy photons are necessary for NLO processes. In this case, the infrared photon has less energy than the visible lasers, but pulsed lasers can still produce extremely high intensities. For example, N. Mitetelo et al. reported two-photon luminescence (TPL) from an organic microcrystal composed of self-assembled S-4,4'-(2,2'-diethoxy-1,1'-binaphthyl-6,6'-diyl)-dibenzaldehyde (S-DBD, see Figure 1.9c for molecular structure). [81] The NLO characteristics of the S-DBD microcrystal were studied by exciting it with a femtosecond (760 nm, repetition rate 80 MHz, pulse width 60 fs) near-infrared pulsed laser. Excitation at the left terminal of the S-DBD microrod (L=110  $\mu$ m and W=5  $\mu$ m) produced a bright TPL signal at the excitation position (red circle in Figure 1.9d) and propagated to the right terminal (Figure 1.9d). The recorded TPL spectrum at the right terminal has a  $\lambda_{max}$  of 460 nm (Figure 1.9e). Later, the pump power was increased gradually, and the recorded TPL intensity exhibited quadratic dependence (slope value of 2) of the pump power, which confirmed the two-photon excitation process (Figure 1.9f).

#### 1.4. Fabrication of nano/microstructures

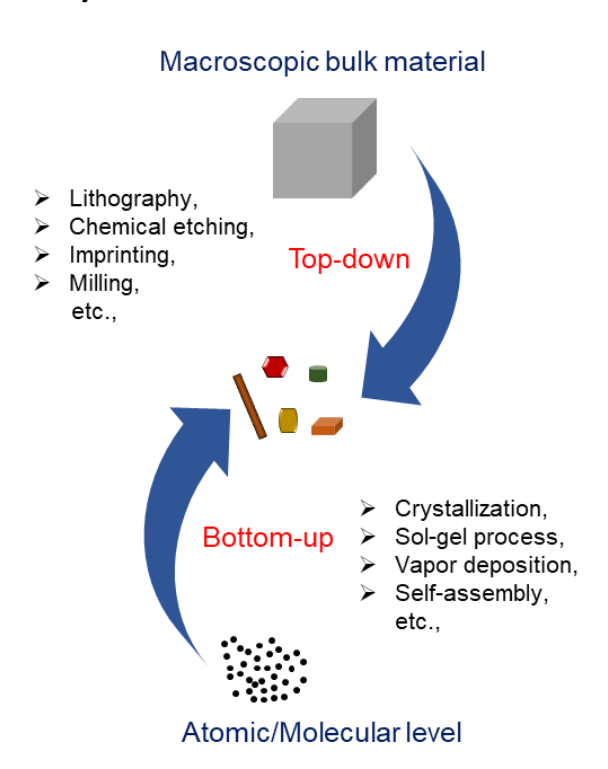


**Figure 1.10.** Nano/microfabrication methods: Top-down and bottom-up approaches.

Broadly, there are two conventional techniques for the fabrication of microstructures, namely, the top-down approach and the bottom-up approach (Figure 1.10). The processes are briefly explained in the following sections.

#### 1.4.1. Bottom-up approaches

In the "bottom-up" approach, the atoms and molecules assemble or aggregate together to form nano/microcrystals. [83] The arrangement of these molecules is assisted by one or more intra or intermolecular interactions like hydrogen bonding, halogen bonding,  $\pi \cdots \pi$  stacking, etc., and the weak forces of attractions like van der Waals forces (0.02-0.1 eV), and electrostatic forces (0.05-2.5 eV). [84-86] These weak interactions and minute forces are responsible for bringing the molecules or atoms together to get the nano/microcrystals. Self-assembly of small organic molecules or polymer molecules or nanoparticles produces microcrystals of a variety of shapes; Sublimation (pressure and vacuum assisted or ambient pressure) method, especially chemical vapor deposition, is mainly used in semiconductor industries for ultrapure thin film depositions of materials. The major bottom-up approaches are described in the following sections.

#### 1.4.1.1. Self-assembly:

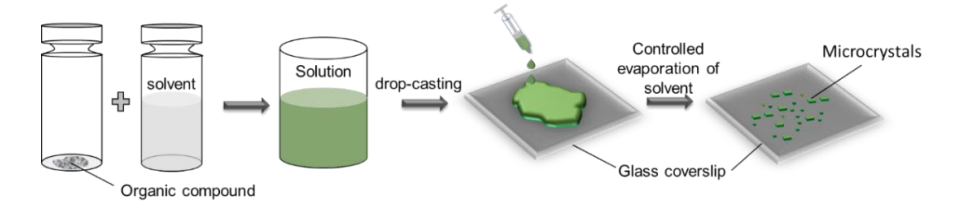
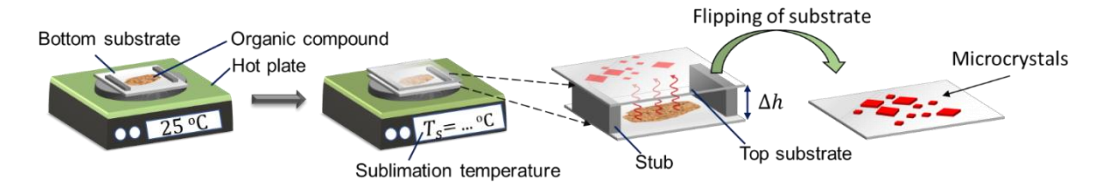


Figure 1.11. Graphics depicting the self-assembly of an organic compound into microcrystals on a substrate.

This is the process in which the solute is dissolved (or dispersed) in a solvent (or partially soluble or insoluble solvent), and the resulting solution is drop casted on a substrate (glass/ITO/FTO or any other material). The controlled evaporation of solvent results in nano/microcrystals. The shape and size of the microcrystals depend mainly on internal (concentration, solvent) and external (temperature, humidity, pressure) conditions (Figure 1.11).

#### 1.4.1.2. Ambient pressure vapor deposition:



**Figure 1.12.** Graphics depicting the ambient-pressure vapor deposition of an organic compound into microcrystals on a substrate.

This is a solvent-free technique that comes under the sublimation category. Unlike pure sublimation (where reduced pressure is used), this technique is carried out at ambient pressure. [87,88] Herein, the compound may be directly placed on a substrate (glass coverslip) and sublimed on to another substrate (glass coverslip or ITO/FTO coverslip) placed at variable heights ( $\Delta h$ ). Further, the temperature can be slowly increased to sublimation temperature ( $T_s$ ), and the compound is allowed to sublime for a particular time (t). Finally, the sublimation system is allowed to reach room temperature. The nano/microcrystals appear on the bottom of the top substrate. The shape, size, and concentration of the nano/microcrystals depend on  $T_s$ ,  $t_s$  and  $\Delta h$  (Figure 1.12).

Following are examples of molecular crystal resonators prepared via the bottom-up technique.

#### 1.4.1.3. Microrod (axial FP resonator):

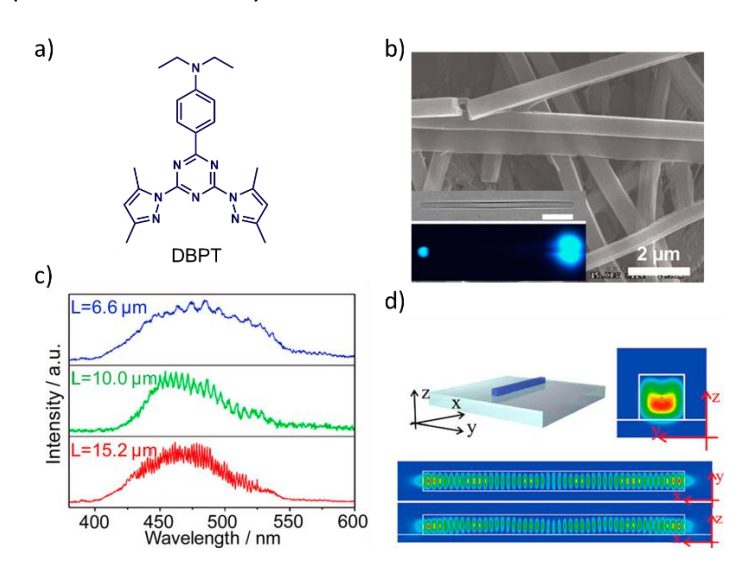


**Figure 1.13.** a) Molecular structure and b) SEM image of self-assembled microcrystals of DBPT. The inset shows the FL image of a single DBPT microcrystal. c) FL spectra of three representative DBPT microrods of varying lengths. d) Calculated electric field distribution of a DBPT microcrystal using FDTD numerical calculations. [Figure adapted from ref. 89].

Yao et al. in 2011 reported microcrystals of a FL dye, 2-(N,N-diethylanilin-4-yl)-4,6-bis(3,5-dimethylpyrazol-1-yl)-1,3,5-triazine (DBPT) using the intermolecular-interaction-induced solution self-assembly (Figure 1.13a).<sup>[89]</sup> The Scanning electron microscopy (SEM) images of the self-assembled 1D microcrystals show the smooth surface of the facets, which efficiently reflect and trap guided FL to form superior-quality microresonators (Figure 1.13b). As a result of the excitation of the microrods with a femtosecond pulsed laser, the

produced bright blue FL outcoupled at the tips of the microcrystals. The length-dependent FP modes (also known as axial FP-type resonator) were revealed by the FL spectra outcoupled at the ends of DPBT microcrystals with varying dimensions (L =6.6, 10.0, and 15.2  $\mu$ m, Figure 1.13c). They attributed this to the high reflectivity of the two flat-end facets. Figure 1.13d depicts the electric field distribution of 475 nm in a microcrystal (length = 6.6  $\mu$ m, width = 500 nm, height = 500 nm, and n = 1.767) placed on a substrate (silica, n = 1.45). The cross-sectional view shows the confinement of the electric field in the microcrystal. The efficient light guiding is evident in the mode profiles along the microcrystal, as well as the reflection and outcoupling at the end facets, which correspond to a typical axial FP-type resonator.

#### 1.4.1.4. Microrod (Lateral FP resonator):

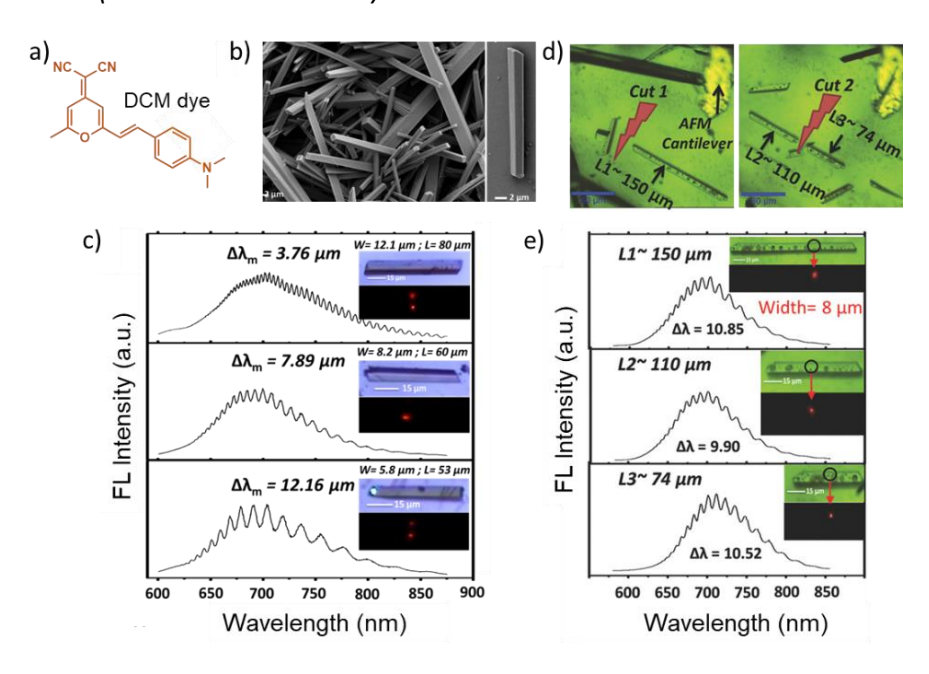


**Figure 1.14.** a) Molecular structure of DCM dye. b) FESEM image of the self-assembled rod-shaped microcrystals of DCM dye. Inset shows a close-up view of a single-crystal. c) FL spectra of three rod-shaped microcrystals of varying aspect ratios. The insets show their corresponding confocal optical microscopy and FL images upon excitation with a continuous wave laser. d) Confocal optical images of various-sized fragments cut from a long microcrystal. e) FL spectra of individual cut microcrystals. The insets show their corresponding confocal optical microscopy and FL images upon laser excitation. [Figure adapted from ref. 90].

Venkatakrishnarao et al. in 2015 reported rod-shaped microcrystals of 4-(Dicyanomethylene)-2-methyl-6-(p-dimethylaminostyryl)-4H-pyran (DCM dye), which are grown via self-assembly of the molecules in acetonitrile (Figure 1.14a,b).<sup>[90]</sup> The optically

excited rod-shaped microcrystal generated red FL and propagated to crystal termini. Interestingly, the FL spectrum revealed optical resonances extended to the NIR region, representing the microcrystal's light-trapping characteristic. The SEM images showed the smooth surface of the self-assembled rod-shaped microcrystals (Figure 1.14b). The authors took three representative microcrystals of varying aspect ratio W:L =12.1: 80; 8.2:60 and 5.8:53 and found that the number of peaks (FP modes) in the FL spectra reduced in the order of  $\approx$ 44,  $\approx$ 25, and  $\approx$ 17 (Figure 1.14c). To confirm the axial or lateral FP resonator nature, a long rod-shaped microcrystal (width =8  $\mu$ m) was cut into three fragments of different lengths ( $L_1$ ,  $L_2$ ,  $L_3$   $\approx$ 150, 110, 74  $\mu$ m respectively) (Figure 1.14d). Single-particle micro-spectroscopic studies of the cut microcrystals revealed similar mode spacing ( $\Delta\lambda$   $\approx$ 10 nm) despite their variable lengths (Figure 1.14e). Based on these experiments, the authors concluded that these microcrystals exhibited lateral FP-type resonances.

#### 1.4.1.5. Circular disk resonator:

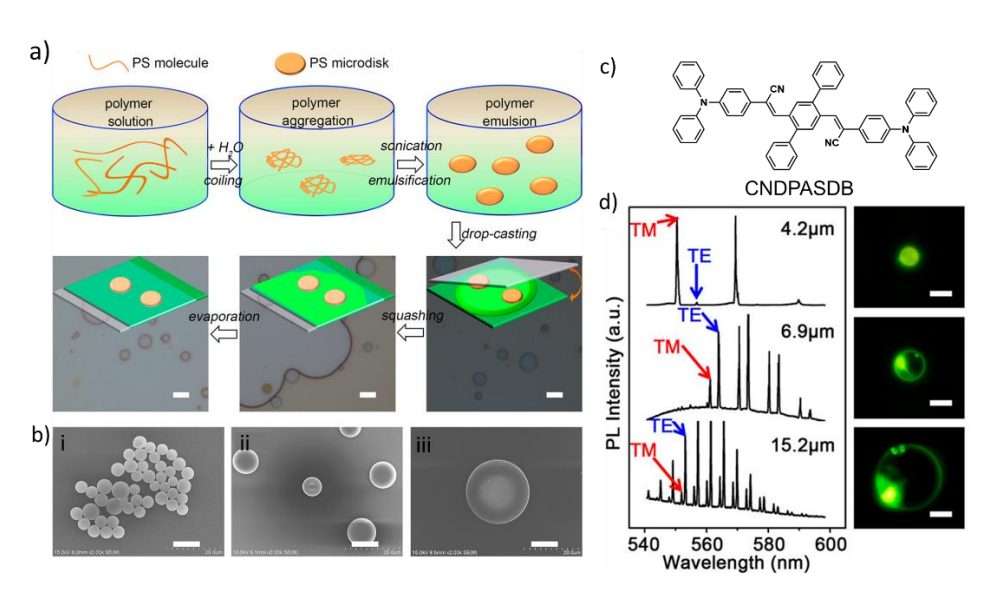


**Figure 1.15.** a) Graphic depicts polystyrene microdisks' fabrication process and corresponding optical images. b) FESEM images of polystyrene microdisks obtained by varying the amount of water (i:10, ii:20, and iii:30  $\mu$ L) in 1 mL polystyrene solution. Scale bar 10  $\mu$ m. c) Molecular structure of CNDPASDB. d) FL spectra (left) and FL images (right) of three different-sized CNDPASDB doped polystyrene microdisks. Scale bar 5  $\mu$ m. [Figure adapted from ref. 91].

Zhao et al. in 2015 reported flexible circular disc resonators obtained using the emulsion-solvent-evaporation method (Figure 1.15a).<sup>[91]</sup> Initially, N,N-dimethylformamide (DMF) solution of polystyrene was prepared. Later, the addition of water to the polystyrene solution induced gradual precipitation.<sup>[92]</sup> Due to the interfacial tension, low crystallinity

polymers tend to aggregate into spherical micelles (SMs).[93] As a result, a polystyrene micro-emulsion was created after ultrasonic treatment, which was verified by the polymer solution's increased light scattering intensity. They employed a minute gap between two glass slides as a platform during the drying of the PS micelles to generate the disk-shaped (resonator) structures. These SMs were compressed into disk-shaped geometries by the capillary force in the tiny gap (Figure 1.15b). Later, FL dye (1,4-Bis(α-cyano-4diphenylaminostyryl)-2,5-diphenylbenzene, CNDPASDB) was doped into the microdisks to attain WGM lasers (see Figure 1.15c for molecular structure). [91] By adjusting the volume of water injected (10 to 30  $\mu$ L), the diameter of the microdisks was tuned from 4 to 20  $\mu$ m. The dye-doped microdisks of varying diameters were excited with a femtosecond pulsed laser (wavelength 400 nm, pulse width 200 fs). This led to the appearance of a bright ringshaped FL pattern at the microdisk's outer periphery (Figure 1.15d, right), which indicates the TIR along the periphery of the disk resonator. The FL spectra collected at the periphery of the resonators revealed a series of sharp TE and TM polarized peaks due to WGM resonance (Figure 1.15d). The FSR values of the resonators decreased with the increasing diameter of the disk resonator.

#### 1.4.1.6. Ring resonator:

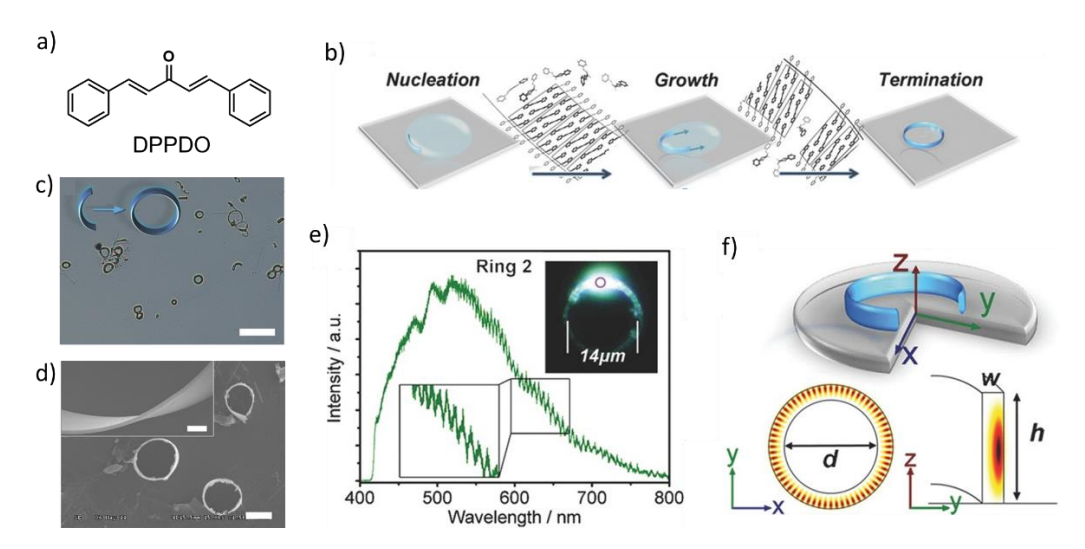


**Figure 1.16.** a) Molecular structure of DPPDO. b) The proposed mechanism for ring formation. c) Optical microscopy and d) SEM images of self-assembled DPPDO microrings. Scale bars 50 and 10  $\mu$ m, respectively. Inset shows the SEM image at the bent portion of the ring. Scale bar 2  $\mu$ m. e) FL spectrum of a DPPDO microring resonator with a diameter of 14  $\mu$ m. Inset shows the FL image. f) Calculated 3D electric field distribution of 550 nm mode in a ring resonator (d=4  $\mu$ m, w=500 nm, h=3  $\mu$ m, n=1.60). [Figure adapted from ref. 94].

In 2013, the microring resonators of 1,5-diphenyl-1,4-pentadien-3-one (DPPDO) were reported by Zhao et al. (Figure 1.16a). [94] A Self-assembly approach was adopted to fabricate these microrings by drop-casting on a glass slide (Figure 1.16b). This was accomplished by rapidly injecting a DPPDO stock solution in ethanol into ultrapure water under an ice-water bath setup. The resultant solution was drop casted and resulted in selfassembled microrings after solvent evaporation. The authors reported 4 mmol L<sup>-1</sup> is the critical concentration that permits ring formation (Figure 1.16c,d) and proposed a ring generation model enforced by interfacial tension. DPPDO should preferentially nucleate at the contact line of a micro-sized droplet on a glass substrate, indicating the rapid evaporation of solvent than its middle area. Therefore, the solution droplet was contained within the inner surface and provided an assembly pattern for a circle. The direction of molecular packing was then bent by the force of the liquid tension at the contact line, causing the aggregation of molecular units near the outer surface. The assemblies might develop into a curved belt that encircles the microdroplet with further solvent evaporation. Additionally, the weak intermolecular contact between the molecules in the solution droplet could allow them to fill the defects between the curved blocks and eventually resulting in microrings (Figure 1.16b).

Further, the excitation of a microring (diameter: 14  $\mu$ m) with a focused UV laser resulted in blue FL, which was guided around the ring. These propagated FL photons were trapped and subsequently outcoupled light signals showed WGM spectral modulation (Figure 1.16e). The confined light undergoes interference, which was determined as a typical WGM resonance in a numerical calculation of the local electric field distribution around microring using the finite element method (Figure 1.16f). [94]

#### 1.4.1.7. Hexagonal disk resonator:

Lead iodide crystals can be prepared by dissolving them in hot water, followed by cooling, resulting in bright yellow flake-like crystals. Lead iodide crystallizes in a hexagonal close-packed crystal structure in a layered fashion (Figure 1.17a). <sup>[95]</sup> Liu et al. reported WGM lasing from layered lead iodide crystals of hexagonal shape and studied the field distribution in the resonator. <sup>[96]</sup>

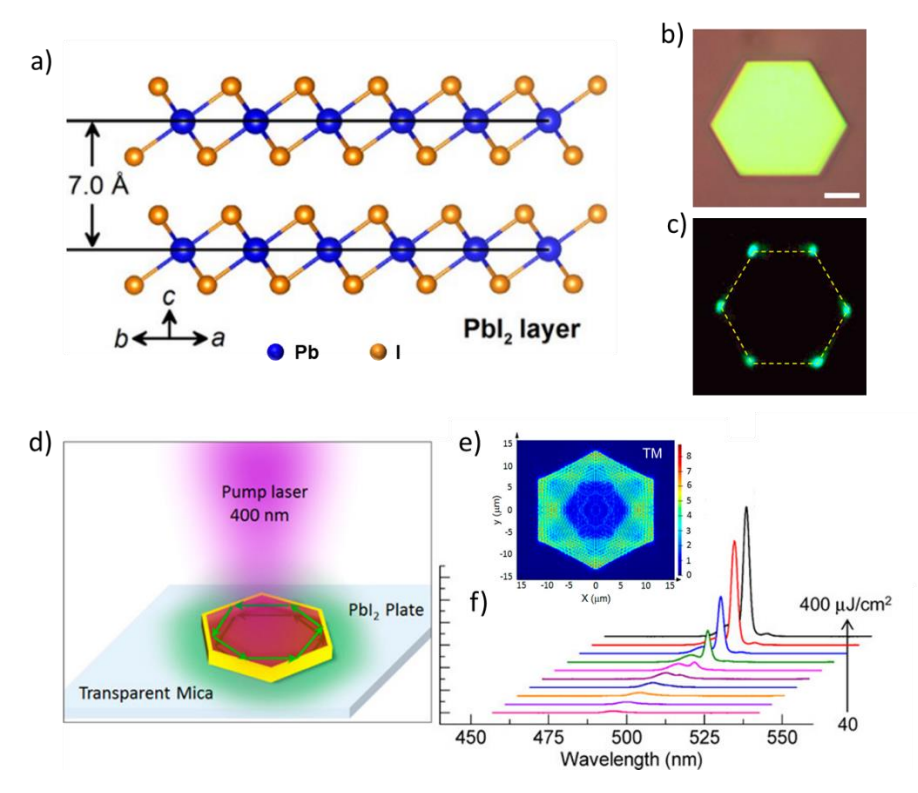


**Figure 1.17.** a) Layered structure of Pbl<sub>2</sub>. The arrows represent the directions of the crystallographic a-c axes. b) The optical and c) FL image of a Pbl<sub>2</sub> hexagonal disk resonator. Scale bar 5  $\mu$ m. d) Schematic depiction of a Pbl<sub>2</sub> single-crystal when excited with a pulsed laser. e) FDTD calculations of a representative Pbl<sub>2</sub> hexagonal disk resonator emitting TE mode. f) The gradual emergence of lasing from spontaneous emission in a hexagonal disk resonator of Pbl<sub>2</sub> demonstrated with the increase of the pump fluence from 40 to 400  $\mu$ J/cm<sup>2</sup>. [Figure adapted from ref. 95 and 96].

The single-crystalline hexagonal microdisks showed an FL around  $\approx$ 500 nm at 77 K upon excitation with a 400 nm femtosecond pulsed laser (Figure 1.17b,c). The schematic illustration of a single-crystal Pbl<sub>2</sub> hexagonal disk stimulated by a pulsed femtosecond laser is shown in Figure 1.17d. The calculated electric field distribution exhibited TE modes for the hexagonal disk resonator (edge length  $\approx$ 3  $\mu$ m; thickness  $\approx$ 150 nm, Figure 1.17e). The optical fields are tightly contained within the hexagonal microdisk resonator, and the WGMs are formed as a result of reflections occurring between the crystal's edges. At low pump fluence (< 100  $\mu$ J/cm<sup>2</sup>), the emission peak centered at 500 nm with a FWHM of  $\approx$ 6 nm was detected. Upon increase in pump fluence to  $\approx$ 200  $\mu$ J/cm<sup>2</sup>, a relatively sharp peak centered at around 502 nm with an FWHM of  $\approx$ 3.5 nm appeared. Further increase in the pump fluence (> 200  $\mu$ J/cm<sup>2</sup>), increased the emission peak intensity sharply, and the FWHM of the emission peak reduced to  $\approx$ 1.4 nm, which confirms the lasing action (Figure 1.17f). [96]

#### 1.4.1.8. Square disk resonator:

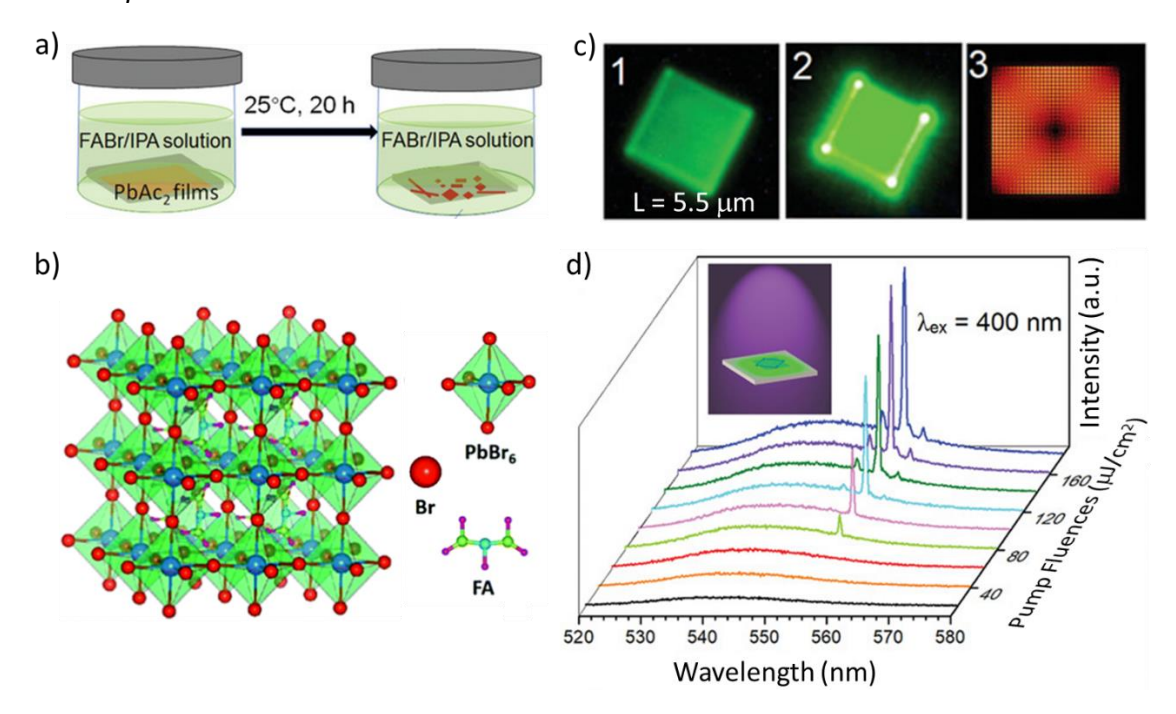


**Figure 1.18.** a) Schematic representation of the synthesis of FAPbBr<sub>3</sub> square-shaped perovskite microcrystals via surface-initiated solution growth method (IPA= isopropanol). b) Crystal structure of FAPbBr<sub>3</sub>. c) FL images captured below (1) and above (2) the lasing threshold. Calculated electric field distribution of square-shaped microcrystal (3). d) Pump fluence-dependent PL spectra of single FAPbBr<sub>3</sub> microcrystal. The inset image shows a graphic of a FAPbBr<sub>3</sub> microcrystal on a substrate pumped by a femtosecond pulsed laser. [Figure adapted from ref. 97 and 98].

Tang et al. reported WGM lasing from solution-processed formamidinium lead bromide perovskite (FAPbBr<sub>3</sub>) microdisks. The square-shaped perovskite crystals were synthesized using the surface-initiated solution growth (Figure 1.18a), [98] and the crystal structure is shown in Figure 1.8b. [97] The single FAPbBr<sub>3</sub> microcrystal of dimension (edge length:  $5.5 \, \mu m$ ) was excited with a pulsed laser (400 nm), resulting in an FL centered around 542 nm (Figure 1.18c). As the pump fluence increases, a prominent emission peak at 553 nm is observed, which is a sign of the presence of single-mode lasing action (Figure 1.8d). The inset of 1.18d shows the schematic of a square-shaped microdisk under laser excitation. The FL images showed the bright emissive edges and corners when excited above the threshold, indicating the effective light outcoupling at those positions of the square-shaped disk resonator (Figure 1.18c2). The calculated 2D TE mode distribution confirms the WGM-type resonator effect in the square-shaped microdisks (Figure 1.18c3).

#### 1.4.2. Top-down approaches

R. Feynman suggested this top-down approach in one of his famous lectures entitled "There is plenty of room at the bottom". [99] As the name indicates, it is the breakdown of bulk material into numerous nano/micrometer-sized particles. This is a subtractive process, and, in this approach, there are several methods or techniques available to obtain nano/microstructures. For example, EBL<sup>[100]</sup> and photolithography were used to make printed circuit boards or integrated circuits, reactive ion etching is used in the semiconductor industry, FIB milling for the preparation of transmission electron microscopy (TEM) lamella and atom probe tomographic samples, ball milling, AFM lithography, plasma FIB milling, PDMS micro-molding<sup>[101]</sup> to name a few. Some of the subtractive fabrication methods are briefed in the following sections.

#### 1.4.2.1. Atomic force microscopy-based lithography:

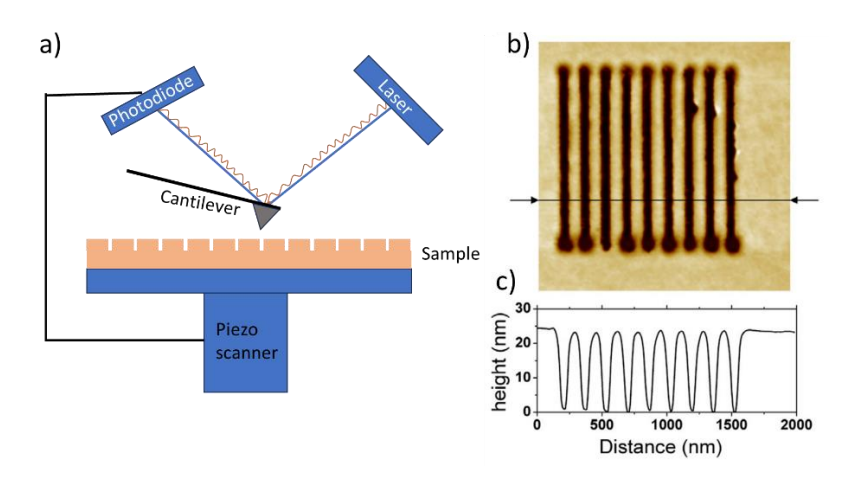


**Figure 1.19.** a) Schematic representing the AFM setup. b) AFM topography image showing the nanopatterned lines on a 25 nm thick PMMA layer deposited on silicon. c) The height and length profile corresponds to the black line shown in the topography image. [Figure adapted from ref. 102]

In addition to surface topography, using a subtractive method like etching or scratching, the AFM cantilever/probe is capable of writing on the surface. The cantilever/probe, which is typically operated in static mode, can etch patterns or structures onto surfaces through a forceful interaction between the tip and sample. The material is completely etched when the same spot is scratched repeatedly, and this serves as a tool to cut desired shapes out of microscale samples. For example, Martin et al. reported AFM nanolithography on a PMMA layer deposited on the silicon substrate. [102] For this, a thin layer of PMMA was deposited on a silicon substrate using the spin coater with a spin rate

of 400 rpm for about 30 s. Later, the lithography was performed using the non-contact mode cantilever (spring constant, 25 N/m) in a dynamic mode with a scan rate of 0.5  $\mu$ m/s (Figure 1.19a,b). The line profile in Figure 1.19c shows the depth of the patterned lines on the PMMA layer and is found to be 25 nm.<sup>[102]</sup>

#### 1.4.2.2. Focused ion beam (FIB) milling:

FIB milling is the technique used to create or pattern multiple nano/microsized objects from the bulk material. In this, the highly accelerated gallium/helium/neon/xenon/argon ion beam is focused onto a single point (of diameter 5-20 nm) and is raster scanned on the pattern to get desired material/structure by etching the material. This FIB milling is the central part of this thesis and is further elaborated in detail in section 1.5.

## 1.4.2.3. Electron beam lithography (EBL):

EBL is a valuable technique in industries like microelectronics, photonics, and nanotechnology because it can accomplish high-resolution detailing with nanometre precision (10 nm). [103] Because of its capacity for high-resolution linewidth drawing, and flexibility, it is extensively employed in the fabrication of semiconductor devices. Contrary to other lithography methods, the procedure is relatively slow and costly and necessitates specialized tools and expertise. The physical interaction of the electron beam with the substrate is central to the EBL concepts. Energy is transferred to the substrate material when the electron beam comes into contact with it. Depending on the type of material being used, this energy causes the material to go through a variety of chemical and physical changes. In some circumstances, the energy might make the substance more or less soluble in a specific solvent, which can be used to deposit or remove a substance with preference. In other instances, the energy might change the conductivity of the substance, making it easier or harder to form electrical connections. The size of the beam spot, which may go as minute as a few nanometres, affects the resolution of EBL. Deflection coils and magnetic lenses can be used to control the beam, allowing for precise beam location on the substrate.

A focused electron beam is utilized in the EBL nanofabrication method for printing a pattern on the substrate. An electron gun produces the electron beam, which is then

focussed via electro-magnetic lenses onto the surface of the substrate. An electron-sensitive film resist layer on the substrate reacts with the electrons, either by exposing it or removing it. For further material deposition or etching processes, this patterned resist can be employed as a mask (Figure 1.20a,b).

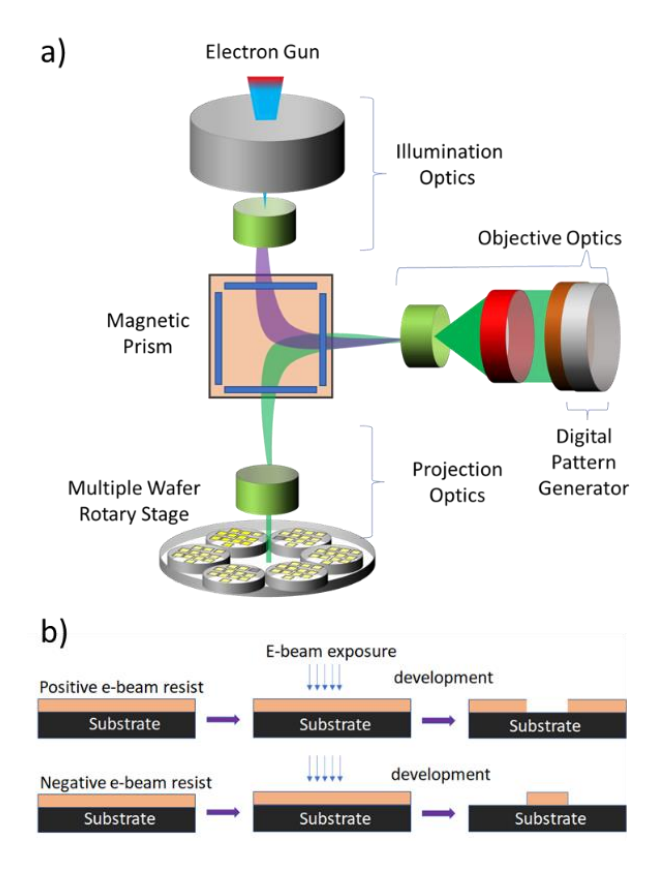


Figure 1.20. Schematic representation of a) EBL setup and b) process using a positive and negative resist.

Low-resolution microscopy uses thermionic sources made of lanthanum hexaboride (LaB<sub>6</sub>). However, for smaller energy spread and improved brightness, systems with greater resolution requirements must employ field electron emission sources (known as the cold cathode). Despite having a greater beam size, thermal field emission gun sources are favored because they provide better stability over the standard writing times of many hours. EBL can make use of magnetic and electrostatic lenses. However, magnetic lenses are preferred because electrostatic lenses have higher achromatic aberrations and cannot focus sharply.

The following equation provides the minimum amount of time to expose a given area for a given dose d. a = t. i, where d, a, t, i are the applied dose, area of exposure, exposure time, and beam current, respectively. [103]

By altering the exposing part's solubility, an electron beam can remove either exposed or unexposed material, which is referred to as positive and negative resist depending on the electron-beam resist and developer used, respectively. Polymethyl methacrylate (PMMA) is often used as an e-beam resist material. Higher doses of PMMA function as a negative resist, while lower levels of PMMA function as a positive resist. PMMA films with a thickness of 30 nm could be harmed by electrons with a 50 eV energy. <sup>[104]</sup> Using PMMA resist and a 100 KeV electron beam, a 20 nm pitch precision (10 nm lines and gaps) was obtained. <sup>[105]</sup> Highly complicated structures of very short length scales can be created and manufactured by repeating multiple steps of this kind.

EBL is employed in a variety of processes, such as the manufacture of nano- and micro-fluidic devices. Additionally, it is utilized in research to build tiny structures for examining the nanoscale characteristics of materials. EBL is a tool used in the semiconductor industry to etch patterns onto silicon wafers and to produce integrated circuits. Polymers, metals, and ceramics can be decorated with nanoscale designs using EBL. These patterns can be utilized to design filters, sensors, devices, etc.

The basic components of photonic integrated circuits include waveguides and resonators. Wherein circular-shaped resonators that confine, amplify, and route optical signals are the fundamental building blocks for the fabrication of PICs. [106-112] Depending upon their geometry, circularly shaped resonators are classified into ring resonators and disk resonators. These resonators are further discussed with an example in the following sections.

#### 1.4.2.3.1. Fabrication of a silicon ring resonator coupled to a waveguide:

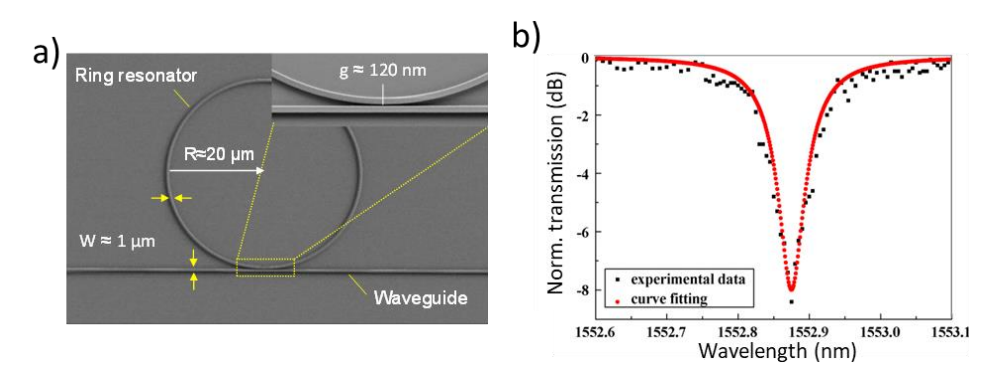


**Figure 1.21.** a) SEM image of silicon microring resonator coupled to a waveguide patterned via EBL technique. The inset shows a close view of the ring and waveguide junction. b) The corresponding spectral response from the fabricated ring resonator. [Figure adapted from ref. 113].

The ring resonators are used to direct the optical signal in the clockwise or anticlockwise direction. Li et al. reported a silicon microring in 2008 [113] wherein a ring-shape was etched onto a single-crystalline silicon-on-insulator wafer with a silicon slab (thickness  $\approx$ 250 nm) on top of silicon buffer film (thickness  $\approx$ 3 µm; to ensure no optical mode seepage into bottom wafer). The pattern is made using EBL followed by reactive ion plasma etching, resulting in a ring resonator of radius 20 µm. The SEM image of a linear waveguide coupled to one convex side of the ring shows a 120 nm air gap (Figure 1.21a). The spectral response from the ring resonator shows resonance at 1552.875 nm, and the obtained Q-factors related to intrinsic cavity loss ( $Q_l$ ), and the external coupling loss ( $Q_E$ ) are  $7\times10^4$  and  $3\times10^4$ , respectively (Figure 1.21b). Further, the optical loss is estimated and found to be 10 dB/cm.

#### 1.4.2.3.2. Fabrication of silicon disk resonator for sensing:

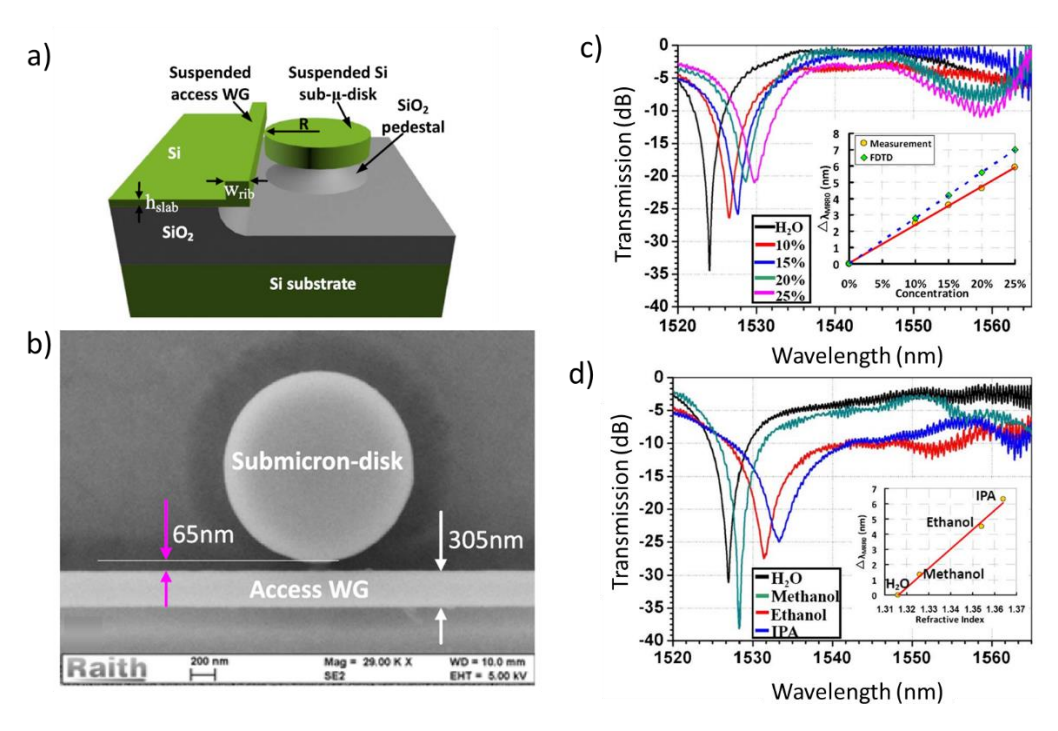


Figure 1.22. a) Schematic of the suspended silicon sub-micron disk with a suspended access waveguide. b) SEM image (top view) of the suspended submicron disk ( $R = 0.8 \,\mu\text{m}$ ). c) The optical response of the sub-micron disk resonator covered by NaCl solution with different concentrations (0-25%). The inset shows the shift in resonant wavelength with varying concentrations. d) The optical response of the submicron-disk resonator covered with different organic solvents. The inset shows the shift in resonant wavelength as the n of the organic solvent varies. [Figure adapted from ref. 114].

Since there is an optical field amplification in the microresonator whenever operated at the resonance wavelength, optical sensors based on optical microresonators have garnered a lot of interest. Wang et al. fabricated a silicon-based submicron disk along

with the access waveguide using a double-etching process (positive E-beam lithography-resist ZEP-520A followed by dry etching). They attained an ultra-small optical sensor with better sensitivity due to the enhanced evanescent field interaction with the analyte using the access waveguide, which is connected to a suspended submicron disk. Figure 1.22a depicts the graphical representation of the disk along with the access waveguide. The fabricated submicron disk (radius  $\approx$ 0.8  $\mu$ m) with a coupling gap of  $\approx$ 65 nm is seen in the SEM image (Figure 1.22b).

Further, they used this sub-micron disk as an optical sensor to measure the n of the gas or liquid. To characterize this, a tunable laser was used as a light source and coupled to the input port (one terminal of the waveguide), and the response at the output port (another terminal of the waveguide) was detected using the power meter. The optical response of the sub-micron disk resonator when covered with NaCl solution of varying concentrations (0-25%) and subsequent calculations revealed the changes in refractive index from 1.316 to 1.361 (Figure 1.22c). Similarly, refractive indices of organic solvents, namely, methanol, ethanol, isopropanol, and distilled water, were measured from optical responses from the sub-micron disk sensor (Figure 1.22d).

#### 1.4.2.3.3. Fabrication of a silicon-based add-drop filter:

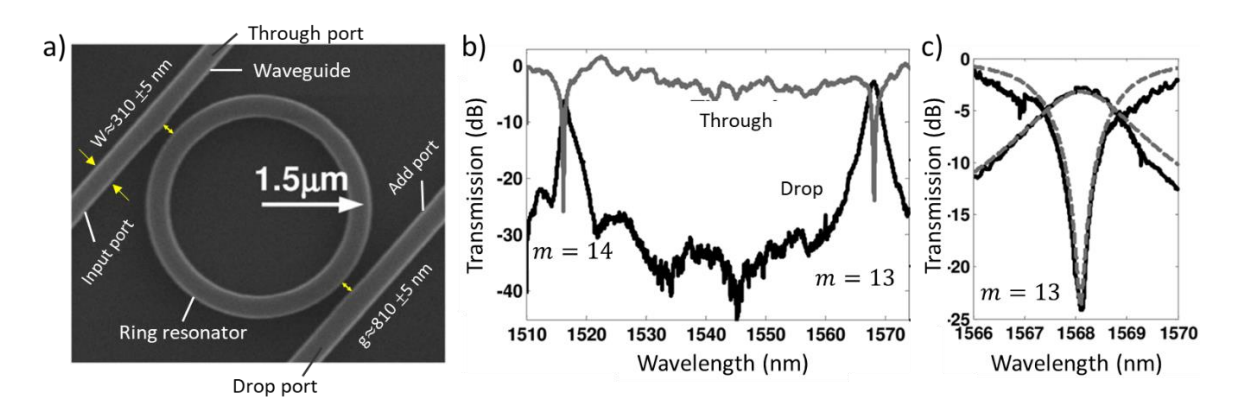


**Figure 1.23.** a) SEM image of silicon-on-insulator micro-ring add/drop filter. b,c) The spectral response of the device at through- and drop-ports. [Figure adapted from ref. 115].

The EBL fabricated micro-ring add/drop filter with a radius of 1.5  $\mu$ m on an SOI wafer comprising a 1  $\mu$ m buried oxide layer (n =1.45) and a 0.34  $\mu$ m Si layer (n =3.5) is shown in Figure 1.23a. The waveguide width and coupling space among the linear waveguide and the micro-ring are 310  $\pm$  5 and 180  $\pm$  5 nm, respectively.

The spectral results of the device's through and drop ports are displayed in Figure 1.23b. The FSR value of the resonance mode numbers at m =13 and 14 of the transmission spectra was 52 nm. The dashed lines shown in Figure 1.23c are calculated responses of the device for 1568 nm resonance, almost matching the obtained results. The micro-ring's intrinsic Q-factor is 3100. This value is lower than the theoretical Q-factor 9300 obtained from bending loss alone. These outcomes reveal the waveguide sidewall roughness and scattering from coupling junctions are responsible for the loss. However, the surface roughness was minimized by refining the etching process, whereas the crystal geometry was improved to reduce the coupling loss at the junction. [115]

Even though EBL selectively mills the substrate/material by utilizing patterned illumination to attain desired shapes, this technique implements harsh conditions like high temperatures or chemical etchants like strong acids (HF, CF<sub>3</sub>COOH, HCl, etc.) and hence, cannot be applied to organic materials.

## 1.5. FIB milling technology

FIB technology came into the picture in the early 1980s and became popular in the semiconductor industries. [116-120] In the area of material science and technology, it became an unprecedented machining tool for TEM sample preparation. [121-124] This technique provides in-situ advantages like maskless processing, precise control over the shape and size, high reproducibility, configurational flexibility, site-specific sample preparation, and ease of nano-fabrication on any surface of the solid materials. Further, these FIB systems continue to dominate in respective fields for direct writing (lithography) and surface modifications through gas-assisted etching in nanomachining and nano-prototyping. The conventional ion beams use a broader beam of ions through a mask to irradiate the specimen, whereas an intensely concentrated ion beam is used by FIB systems forming a scanning ion probe, thereby attaining nanoscale spatial resolution.

Mostly, these FIB systems are equipped with the SEM setup and are called dual-beam platforms (also known as multi-beam and two-beam platforms, Figure 1.24a). It consists of an electron beam column aligned vertically, an ion beam column equipped at a certain angle  $(52^{\circ} - 55^{\circ})$  to the electron beam column, micromanipulators, and detectors

(Figure 1.24b). The major components in the ion beam column are the ion source and the optics column (condenser lens, objective lens, apertures, deflectors, and scanning electrodes).

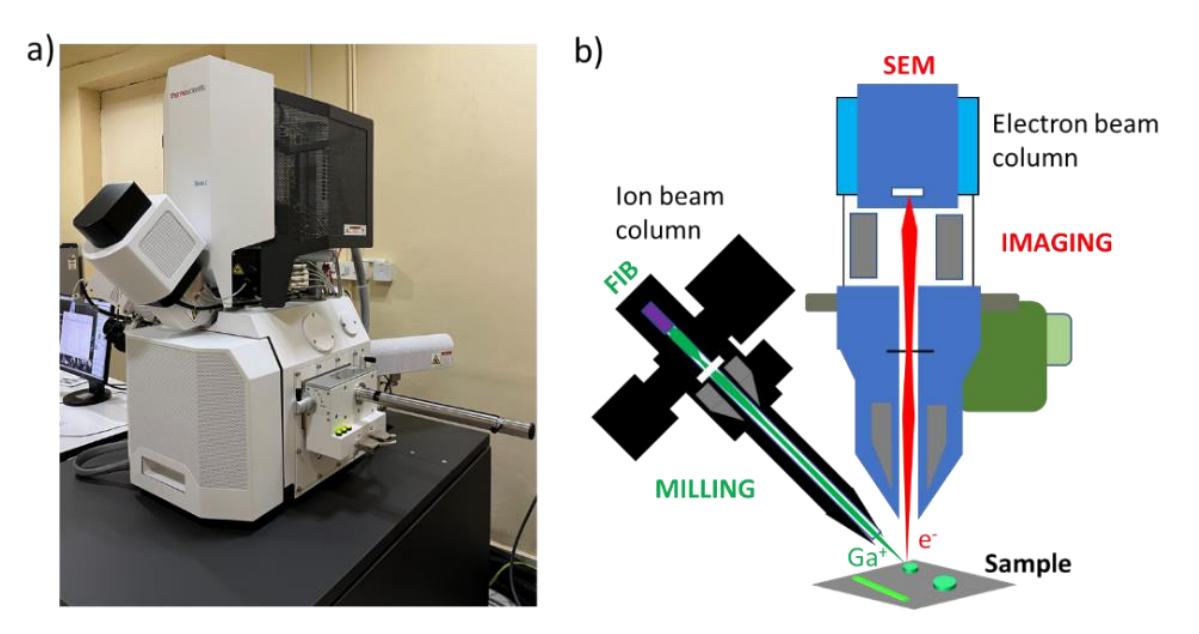


**Figure 1.24.** a) Photograph of a typical FIB-SEM instrument. b) Schematic showing the cross-sectional view of the FIB-SEM instrument.

FIB systems can use liquid metal ion sources (LMIS), such as Ga, Au, Si, Al, As, Cu, Ge, Fe, In, Pt, and Pd, with a beam spot generation capability of 10 nm. Out of all these sources, Ga is a highly preferred metal as it has many advantages over the others. The gaseous ion beams include helium, which provides excellent spatial resolution than the Ga ion source, but the milling times are high as it has a low mass. Recently, Bischoff et al. studied the usage of liquid metal alloy ion sources (PdAs, PdAsB, AuSi, AuSiB, NiB, and NiAs) having lower melting points in FIB systems.<sup>[125,126]</sup> Further, plasma sources are also incorporated into the FIB systems to attain higher milling rates than the conventional Ga-FIBs.<sup>[127,128]</sup>

The fundamental principle of FIB is the generation of a highly energetic beam of ions, directing and focusing them to the specimen using several sets of lenses, which serve the purpose of milling and imaging the targeted position on the sample. As this thesis is mainly focused on the FIB milling of organic crystals into photonic components, a detailed introduction will be given on FIB milling technology in the following sub-sections.

## 1.5.1. Ion beam generation

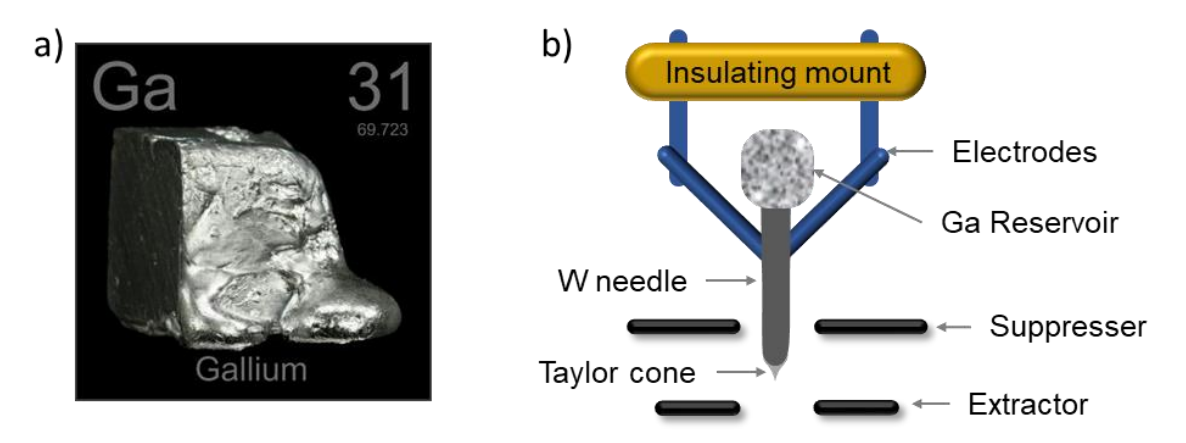


**Figure 1.25.** a) The photographic image of a piece of gallium metal. b) Schematic representation of gallium ion beam generation from liquid metal ion source (LMIS) chamber. [Figure adapted from ref. 129].

Gallium is extensively used as a source of ion beam as it possesses a low melting point (29.8 °C), low vapor pressure, low surface free energy, and importantly, it does not form any alloys with tungsten (Figure 1.25a). The gallium reservoir is attached to the heating coils and the tungsten needle. By applying the current, the coils heat up and melt the gallium. The liquid gallium drips down to the tungsten needle forming a Taylor cone. Due to the high potential near the tip of the tungsten needle, the electron from the gallium tunnels through the tungsten and thereby generating an ionized field (Figure 1.25b). The diverged or diffused ionized field passes through several lenses and, finally, forms a focused ion beam onto the specimen. Gaseous ion sources based on He and Ne ions are also in use.

## 1.5.2. Directing and focusing the ion beam

The optics section consists of apertures, condenser lens, deflectors, scanning electrodes, and the objective lens, which directs and accelerates the extracted Ga ions onto the specimen. The lens used in this ion column is an electrostatic lens instead of a magnetic lens (as we see in SEM and TEM). This is because the magnetic lenses are less effective on ions than they would be on electrons at the same

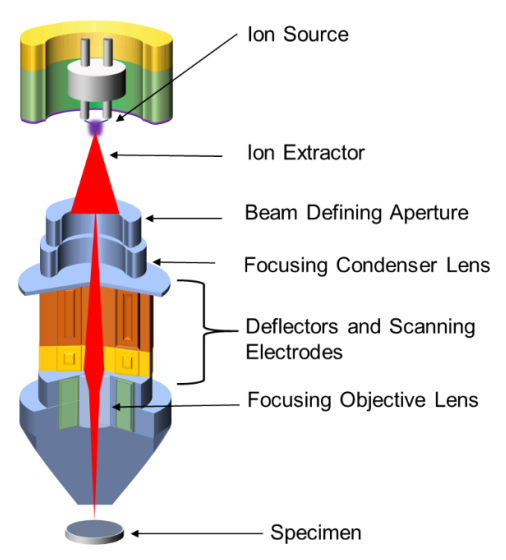


**Figure 1.26.** Graphic depicting the cross-sectional view of FIB column.

acceleration voltages because ions are heavier and move at slower speeds, have a weaker Lorentz force, and are more massive than electrons. The ion beam is focused onto the specimen's surface using the objective lens, while the condenser lens serves as a probeforming lens. The apertures are used to optimize the ion probe size, and the octupole lens is for beam deflection, alignment, and stigmatism correction (Figure 1.26).<sup>[130]</sup>

The probe is primarily defined by four interrelated parameters, namely, accelerating voltage  $(V_o)$ , probe current  $(i_p)$ , probe convergence angle  $(A_p)$ , and probe diameter  $(d_p)$ . The probe diameter can be written as,

$$d_n = (d_L^2 + d_d^2 + d_s^2 + d_c^2)^{1/2} \qquad ------ (23)$$

Where, 
$$d_I=\sqrt{\frac{4i_p}{b\pi^2A_p^2}}$$
;  $d_d=\frac{0.6\lambda_{DE}}{A}$ ;  $d_s=0.18C_{s1}A^3$ ;  $d_c=0.34C_{s2}A^3\left(\frac{\Delta E}{E_o}\right)$ ;

 $i_p$  = probe current.

 $V_o$  = accelerating voltage.

 $E_o$  = average energy of each ion (e.g., if  $V_o$  is 30 kV, then  $E_o$  is 30 keV).

 $\Delta E$  = energy spread of ions from the source.

 $\lambda_{DE}$ = average DE Broglie wavelength of each ion.

 $A_p$  = probe convergence angle.

A = beam convergence angle ( $\approx \alpha_p$  for objective lens).

b = brightness.

 $d_p$  = diameter of a probe containing 50% of probe current.

 $d_I$  = de-magnified, aberration-free source size at specimen plane.

 $d_d$  = diffraction aberration contribution to probe size.

 $d_s$  = spherical aberration contribution to probe size.

 $d_c$  = chromatic aberration contribution to probe size.

 $C_{\rm s1}$ = spherical aberration constant to probe size.

 $C_{s2}$  = chromatic aberration constant to probe size.

#### 1.5.3. Beam-specimen interactions

Understanding the beam-specimen interactions is crucial to utilize them for various nanofabrication processes. When an ion beam hits the specimen, several phenomena take

place due to a combination of elastic and inelastic collisions. The backscattered ions are generated when an elastic collision takes place between the atoms of the specimen and the focused beam of ions.

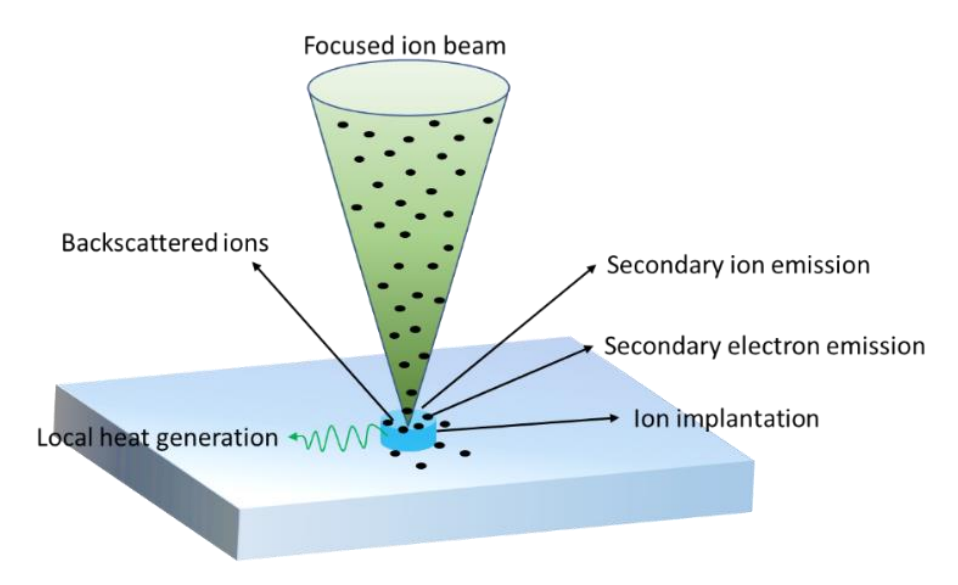


**Figure 1.27.** Schematic representation of various phenomena arising due to the interaction of focused ion beam with the sample.

Whereas, in an inelastic collision, when some amount of the primary ion beam's energy is transmitted to atoms on the specimen, secondary ions, secondary electrons, etc., are generated (Figure 1.27). These phenomena can attain imaging of the surface of the sample. [132,133] The target atoms will be sputtered off if the kinetic energy of the primary ion beam is higher than the surface binding energy. This method of material removal is physical sputtering, whose effectiveness is measured in terms of sputtering yield. [134,135] Depending on the energy of the ions, the beam-specimen interaction results in sputtering, amorphization, deposition, and implantation. Moreover, these interactions can co-occur and cannot be separated completely. Further, when the specimen is subjected to an ion beam, degradation can also happen, and the dominant mechanism among the above is not very well understood.

#### 1.5.3.1. Electron and ion beams:

Ion beam interaction with solid material function similarly to electron beam interactions from the viewpoint of charged particles. As the ions are heavier than the electrons, the nanofabrication tool for each beam is visibly different.

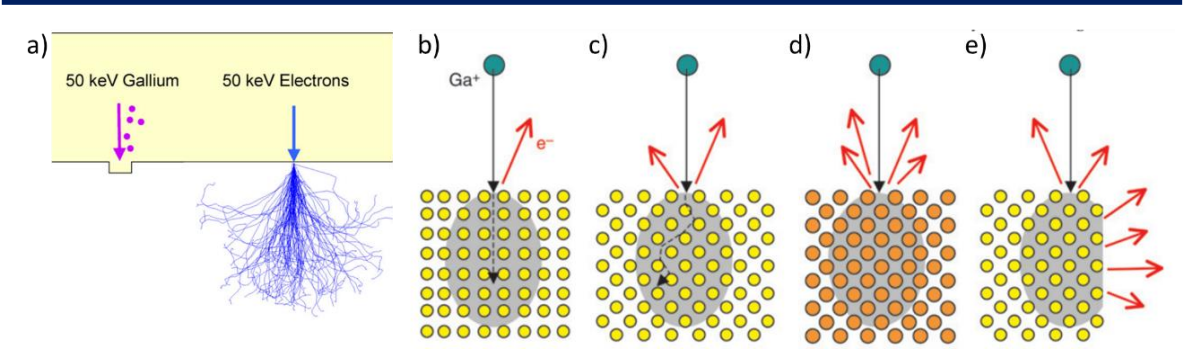


**Figure 1.28.** a) Simulated ion and electron beam penetration strength comparison in solid materials. Schematics depicting the impact of b,c) orientation of the crystal, d) atomic mass, and e) surface geometry as a 30 keV Ga ion beam collides with the sample. [Figure adapted from ref. 136 and 137].

Firstly, the ions penetrate into solids to a shallower depth than electrons leading to a series of physical and chemical actions because high-energy ions are sufficient to generate a chain of collisions of atoms near the solid surfaces, realizing the goal of FIB nanofabrication (Figure 1.28).<sup>[136,137]</sup> FIB nanofabrication can carry out tasks like irradiation, etching, and implantation without the need for a precursor gas. The electrons and ions have such an immense mass difference; electron beam-induced processing hardly ever produces secondary atoms, ions, or molecules. On the other hand, ion beam-induced fabrications can both create these particles and increase secondary electron emission. As a result, microscopic image from the electron beam and ion beam has significant differences.<sup>[138,139]</sup>

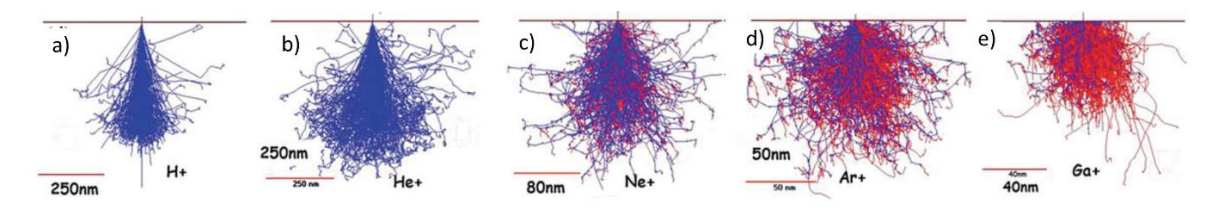


**Figure 1.29.** a) Simulations showing the interaction volumes of a) H, b) He, c) Ne, d) Ar, and e) Ga ions in a molybdenum substrate using 40 keV energy. [Figure adapted from ref. 140]

Figure 1.29 summarises the simulation results, which displays a contrast of the size and the contour of the interaction volumes for five distinct ions (H<sup>+</sup>, He<sup>+</sup>, Ne<sup>+</sup>, Ar<sup>+</sup>, and Ga<sup>+</sup>) hitting a molybdenum target at an incident beam energy of 40 kV. Among these, the lightest ion (H<sup>+</sup>) has more penetration and is approximately 500 nm. In the case of He<sup>+</sup>, the interaction volume is more and extends up to 250 nm. Whereas the heaviest ion (Ga<sup>+</sup>) has minimum primary interaction on the downward side and has a maximum penetration of 80 nm, hence exhibiting significant backscattering.<sup>[140]</sup> Therefore, He<sup>+</sup> offers a higher resolution and potentially miniaturized milling feature sizes, while Ga<sup>+</sup> is better suited for bulk milling

with greater efficiency at the expense of lower resolution. The helium, neon, and gallium ions have different masses; when it comes to milling, Ga is a heavy one, Ne is intermediate, and He is a fine one. Table 1.1 shows the various parameters associated with different ion beams.<sup>[135,141-143]</sup>

**Table 1.1:** Comparison of various beam parameters of He<sup>+</sup>, Ne<sup>+</sup>, Ga<sup>+</sup>, and Xe<sup>+</sup>.

Parameters	He⁺	Ne⁺	Ga⁺	Xe⁺
Minimum probe diameter	0.35 nm	1.9 nm	5 nm	10 nm
Range of acceleration voltage	5.0-40 kV	5.0-35 kV	1.0-30 kV	0.5-30 KV
Range of probe current	0.1-100 pA	0.1-100 pA	1.0 pA-100 nA	1.5 pA-2.5 μA
Sputter ratio/ion	1x	≈30x	≈60x	≈95x
Interaction volume at 30 kV on a silicon substrate	≈500 nm	≈150 nm	≈60 nm	≈20 nm

## 1.5.4. Factors influencing FIB milling

FIB milling is the standard material removal technique. The sputtering yield and material topography are determined by the ion beam's current and voltage. The acceleration voltage is measured in kV and typically reaches up to 30 kV in specific FIB systems. The beam current can attain a maximum of 100 nA and is dependent on the spot size, i.e., beam diameter (nm) and the current density (A cm<sup>-2</sup>). Ion beam milling can be used to carve lines, squares, rectangles, circles, and even complex structures in the specimen. A series of patterning can be obtained on the sample using the inbuilt / imported bitmaps to the user interface of FIB.

The significant advantage of this FIB milling is the ability to precisely regulate the size and shape of the milled pattern, and mainly, it does not require any mask. Therefore, desired geometries with tens of nanometre precision can be attained. It also ensures control over the local depth of the milled pattern along with the lateral position.

In order to understand the mechanism of FIB nanofabrication, researchers have investigated the effects of ion beam, scanning, and processing parameters on various materials (except organic crystals).<sup>[144]</sup> The scan area, scan speed, scan strategy, number of scans, scan width, aperture and pixel size, and bitmap design are the scanning parameters.

The ion beam's parameters are the ion energy, composition, and current. Dwell time, angle of incidence, mill depth, working distance, astigmatism, and defocus are the processing parameters. The conclusions of investigations into these parameters indicate a variety of nanoscale effects, including material redeposition, ion implantation damage, and amorphization. Some of the significant parameters are discussed below.

#### 1.5.4.1. Accelerating voltage:

The accelerating voltage increases the momentum of the ion species. The gallium ion source is maintained at a positive potential in relation to the ground by the acceleration voltage (Figure 1.25b).<sup>[145]</sup> The range of acceleration voltage is from 0.5 to 30 kV and is dependent on the manufacturer. The ions escape the column at a faster rate and impart higher energy to the specimen when the acceleration voltage is elevated. Since it has no effect on the probe current, raising the acceleration voltage is favorable. The probe size of 1 nm can be attained for ion energies of more than 30 keV, but the milling duration rises to get a proper structural feature<sup>[146]</sup>.

#### 1.5.4.2. Beam current:

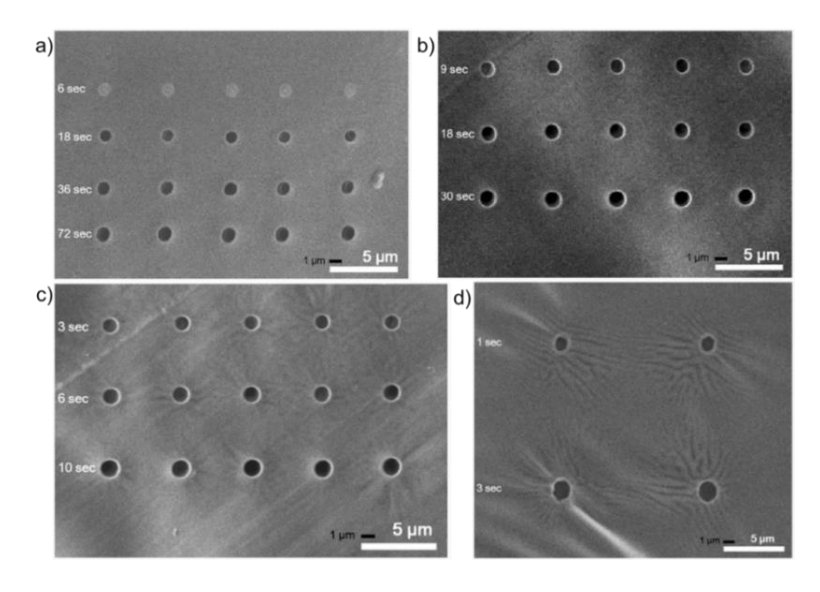


**Figure 1.30.** SEM images of PS-*b*-PMMA polymer sheet when subjected to a) 10 pA, b) 100 pA, c) 300 pA, and d) 1000 pA beam currents to attain circular holes. [Figure adapted from ref. 147].

The aspect ratio of material under fabrication can also be tuned by varying beam currents. Beam spot sizes are determined by the magnitude of distinct beam currents. The beam current becomes a crucial process parameter to illustrate how the spot size influences the operation, and it can reach up to 100 nA.<sup>[148]</sup> For instance, at a 30 kV acceleration

voltage, a 3 nm probe diameter can be attained by using a 1 pA beam current.<sup>[149]</sup> Generally, a larger primary beam current will cause the material to sputter from the surface more quickly. Therefore, a lower beam current must be employed if high-resolution imaging is essential. By modulating the current of the ion beam or deploying smaller spot sizes, the sputtering frequency can be rapidly and precisely regulated.<sup>[149]</sup> With the use of low current ion beams, high-quality channels can be attained at the expense of huge milling duration, hence severely affects the production rate and cost.<sup>[150]</sup>

For example, the effect of beam current on polymer thin films was studied by Kim et al. in 2011. [147] They reported the systematic study of FIB damage on thin polymer films by varying the beam current and the exposure time by keeping the constant voltage. The SEM images of fabricated holes in the PS-b-PMMA polymer sheet are shown in Figure 1.30. With a beam current of 10 and 100 pA, the morphology of the polymer was retained. Whereas, with a beam current of 300 and 1000 pA, the SEM images clearly showed the distorted morphology and resulted in wrinkles in the polymer sheet (Figure 1.30a-d). The authors attributed this damage to the ion beam heating.

#### 1.5.4.3. Sputtering yield:

The material removal is characterized in terms of sputtering yield, described as "the number of atoms ejected from the specimen surface per incident ion" at given ion beam parameters. The yield typically varies from 1 to 50 atoms per ion and is influenced by a number of variables, such as the mass of the specimen atoms and ions, their energies, the direction in which they impinge on the specimen, the temperature of the specimen, and their flux. As ion energy increases, the sputter yield initially increases, but when energy increases past the point at which ions may penetrate deeply into the substrate, the yield begins to drop. This is because the ions are trapped in the substrate, which results in implantation or doping 154.

**Table 1.2:** The sputtering yield of various materials for 30 keV Ga<sup>+</sup> ions.

Material	Range (nm)	Sputtering yield (atom/ion)
Silicon	27	2.6
Copper	10	11.0
Aluminum	24	4.4
Silver	11	14.0

The typical sputter yield varies with the incidence angle, energy, and materials.<sup>[155]</sup> Table 1.2 shows the sputtering yields of a few different materials obtained using 30 keV Ga<sup>+</sup> ions.<sup>[156]</sup>. Because there are various aspects (like beam shape and the redeposition) associated with it, the sputter yield cannot be utilized directly to calculate the material removal rate during milling<sup>[157]</sup>.

## 1.5.5. Nano/microscale effects in FIB milling

## 1.5.5.1. Ion implantation:[157]

The capture of Ga ions in the material results in ion implantation. The sputtering activity can insert gallium ions into the specimen. As a result, the local composition of the sample inside the interaction volume might change. Gallium implantation may result in skeletal structure modifications along with alternating the mechanical, thermal, electrical, and optical characteristics of the milled sample.

## 1.5.5.2. Amorphization:[134]

The crystalline substrate that is subjected to a focused beam of ions may experience material amorphization, which can possibly cause the substrate to swell. This mechanism, which causes the loss of crystallographic orientation, can be explained by a significant movement of atoms inside the impact window. Amorphization is frequently encountered during the creation of TEM specimens and could pose a considerable challenge to the crystalline structures. Therefore, using low ion beam energies can greatly help limit the effects of amorphization during the polishing stage during the preparation of TEM or APT samples.

#### 1.5.5.3. Redeposition:[153]

Due to a lack of thermodynamic equilibrium, sputtered particles that leave the surface of the material in the gaseous form are very likely to condense back into the solid phase upon hitting the nearby specimen surfaces. As a result, some of the ejected atoms tend to stick to the sputtered surfaces and result in unwanted debris. Redeposition can be lessened by employing low ion doses (such as currents), depositing protective layers with low ion energy, and by tailoring the geometries of ion milling.

## 1.5.6. Applications of FIB milling

#### 1.5.6.1. Fabrication of nanochannels of high-aspect-ratios:

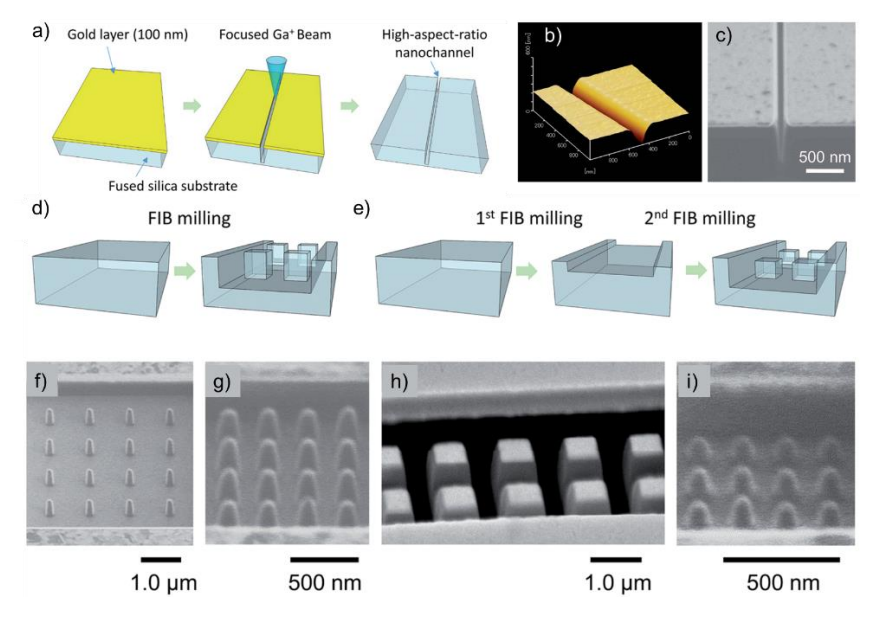


**Figure 1.31.** a) Schematic depicting the process of FIB milling for the fabrication of high-aspect-ratio nanochannels. b) AFM and c) SIM images of fabricated nanochannel of 100 nm deep on fused silica. Schematic representation showing d) one-step and e) two-step FIB milling strategies. f) Low-density and g) high-density nanopillar arrays obtained using a one-step strategy on fused silica. h) Low-density and i) high-density nanopillar arrays obtained using a two-step strategy on fused silica. [Figure adapted from ref. 158].

Xu et al. demonstrated the flexible and in-situ fabrication of nanochannels with high aspect ratio and nanopillar arrays on fused silica using FIB. [158] These nanochannels are very important in nanofluidic devices to understand the behavior of liquids in the nanospace. To fabricate this, they coated the fused silica with a 100 nm thick Au layer to protect it from charging, as the fused silica is an insulator. Upon optimizing the conditions like beam voltage and beam current, they successfully milled the silica into a higher aspect ratio channel of width 100 nm and depth 500 nm. The schematic representation of FIB milling, AFM image, and secondary ion image (SIM) image of nanochannel are presented in Figure 1.31a-c.

Two different methods were followed to fabricate nanopillars; wherein the first step (flexible one-step FIB milling), they directly milled the nanopillars on the substrate, and in the second step, in-situ two-step FIB milling (top layer milling and fabrication of pillars) was adopted. In both scenarios, they achieved good nanopillars with different gaps. In the case of the former procedure, both nanochannels and nanopillars were simultaneously fabricated, resulting in equal height (depth) of nanochannel and nanopillars (Figure

1.31d,f,g). The latter method follows the in-situ sequential milling, which results in lesser heights of nanopillars than the nanochannel (Figure 1.31e,h,i). Variable aspect ratios (0.9 to 2.5) of nanopillars were fabricated with different widths/diameters. The density (ratio of sizes of nanopillar to that of free space) of nanopillars was adjusted in FIB milling. Both methods (flexible and in-situ) provided resolution when the gap between the pillars is more. Finally, they claim that the technique is helpful in fabricating nanofluidic devices with high throughput. [158]

## 1.5.6.2. Fabrication of plasmonic nanoparticles: "sketch and peel" strategy

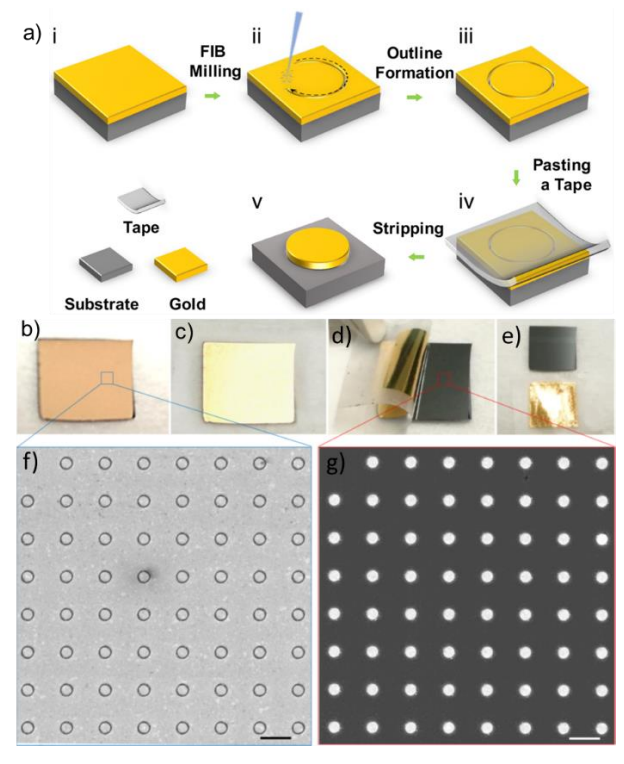


**Figure 1.32.** a) Schematic representation of sketch and peel strategy for fabrication of plasmonic nanostructures using FIB milling. Pictures depicting the sample fabrication process: b) after drawing the outline on 30 nm thick gold film with FIB milling. c) after pasting transparent scotch tape, d) while removing the tape, e) and after peeling off. f) Pre- and g) post-peeling SEM images of fabricated structures. The periodic gold disks were fabricated on a  $1\times1$  cm<sup>2</sup> silicon substrate with a pitch of  $2.5~\mu m$  and a diameter of 800 nm. Scale bar  $2~\mu m$ . [Figure adapted from ref. 159].

Creating inverse plasmonic structures (like nanoslits and nanoholes) using FIB is common. However, designing and fabrication of isolated and/or array of assemblies of plasmonic nanostructures are impractical with FIB in real-life applications, as milling is a subtractive process. Chen et al. in 2016 came up with an approach called sketch and peel

(Figure 1.32a).<sup>[159]</sup> They milled trenches around the targeted shape and removed the excess material using adhesive tape.

For this, a 30 nm Au layer was deposited on a silicon substrate, and the outlines were milled using a Ga<sup>+</sup> beam to attain a periodic array of nanodisks of 800 nm diameter (Figure 1.32b,c,f). Later, a scotch tape was pasted and carefully pealed to acquire an array of plasmonic nanostructures (Figure 1.32d,e,g). In order to attain complete isolation of preferred shapes from the Au film, the authors milled the outlines a little deeper into the silicon substrate, i.e., the depth of contours was more significant than the Au film.<sup>[159]</sup>

#### 1.5.6.3. Prototyping of 2D and 3D photonic structures:

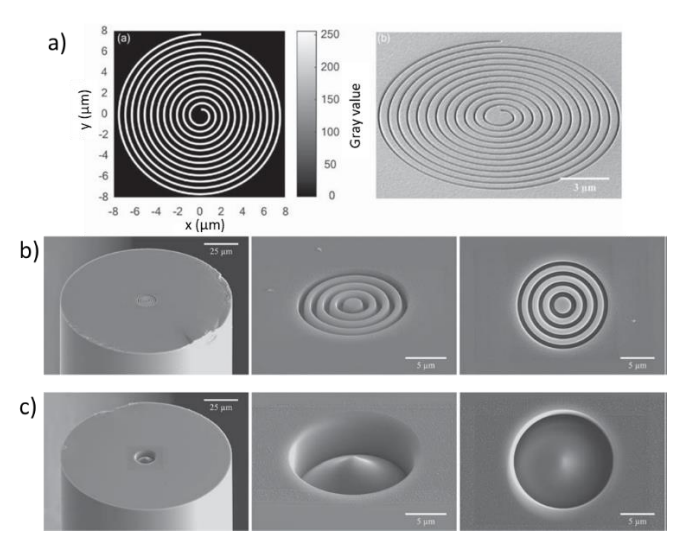


**Figure 1.33.** a) Bitmap and SEM image of fabricated Archimedean spiral of twelve turns on an optical fiber tip. b,c) SEM images of Fresnel phase plate (2D prototype) and axicon (3D prototype) on a fiber tip in different viewing angles, respectively. [Figure adapted from ref. 160].

A review on FIB applications in optical fibers was published by Sloyan et al. in 2021. [160] Wherein one of the reports was on the FIB milling technique for fabricating 2D and 3D photonic structures. To date, optical fibers are an effective medium of telecommunication. The authors demonstrated the novel prototypes of photonic structures on the optical fiber tip for enhancing the fiber-to-chip coupling. A twelve-turn Archimedean spiral (2D asymmetric design) of 205 nm slit width, 594 nm period with a first-turn inner radius of 0.5  $\mu$ m was fabricated (Figure 1.33a). This was achieved after 56 min of focused Ga<sup>+</sup> beam exposure with 30 kV and 24 pA beam parameters. Similarly, a Fresnel phase plate (FPP) was also designed on the tip of the optical fiber. Figure 1.33b shows the FPP on a fiber tip in different view angles; 30 kV and 80 pA were used to attain this 2D structure. Finally,

by using the technology of generating bitmaps of different gradients, they achieved 3D designs as well (Figure 1.33c). A 6  $\mu$ m high axicon was fabricated using the ion beam parameters of 30 kV and 0.43 nA. Finally, the authors proposed that these fabricated structures can enhance fiber-to-chip coupling.

## 1.6. Mechanophotonics for all-organic PIC fabrication

Fabrication of all-organic PICs involves integrating multiple organic photonic modules, like optical waveguides (straight and bent), resonators, modulators, and lasers, on a photonic platform. A flexible manufacturing method is required for the systematic arranging of numerous optical components on a substrate. Mechanical micromanipulation became the foremost tool for constructing all organic PICs. This novel micromanipulation technique was first demonstrated by Chandrasekar and his group at the University of Hyderabad, termed *Mechanophotonics* technique. [12-14] It is an emerging field in organic nanophotonics that focuses on employing the cantilever tip of AFM to mechanically manipulate organic optical microcrystals toward fabricating bent waveguides, resonators, interferometers, add-drop filters, and circuits. The lifting, breaking/cutting, slicing, bending, aligning, integrating, transferring, and rolling of microcrystals are the critical steps in the fabrication of OPICs. A brief overview of reported micromechanical operations is discussed below.

## 1.6.1. Lifting of a single-crystal

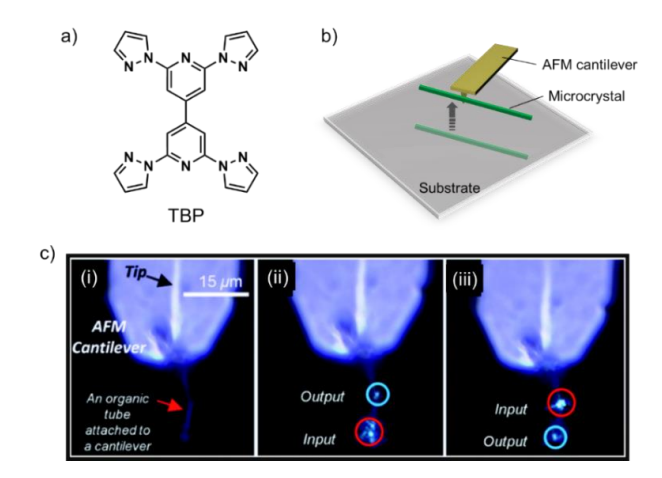


**Figure 1.34.** a) Molecular structure of TBP. b) Schematic depicting the lifting of TBP single-crystal from the glass substrate using the AFM cantilever tip. c) Confocal optical microscopy images of TBP microcrystal attached to an inverted AFM cantilever under (i) ambient light and (ii and iii) 488 nm laser excitation. The red and blue circles denote the laser input and output. [Figure adapted from ref. 161].

In 2014, Basak et al. used an AFM cantilever tip to lift the microcrystal of 2,2',6,6'-tetra(1H-pyrazol-1-yl)-4,4'-bipyridine (TBP) from the glass substrate (Figure 1.34a). [161] Figure 1.34b shows the schematic of the lifting operation using an AFM cantilever tip. Further, they lifted the microcrystal with an AFM cantilever tip and inverted the cantilever to study the optical waveguiding property without the influence of the substrate. For this, one end of the microcrystal was excited with a 488 nm laser, and the passively guided light propagated to the other terminal (Figure 1.34c). [161]

#### 1.6.2. Breaking/cutting of a single-crystal

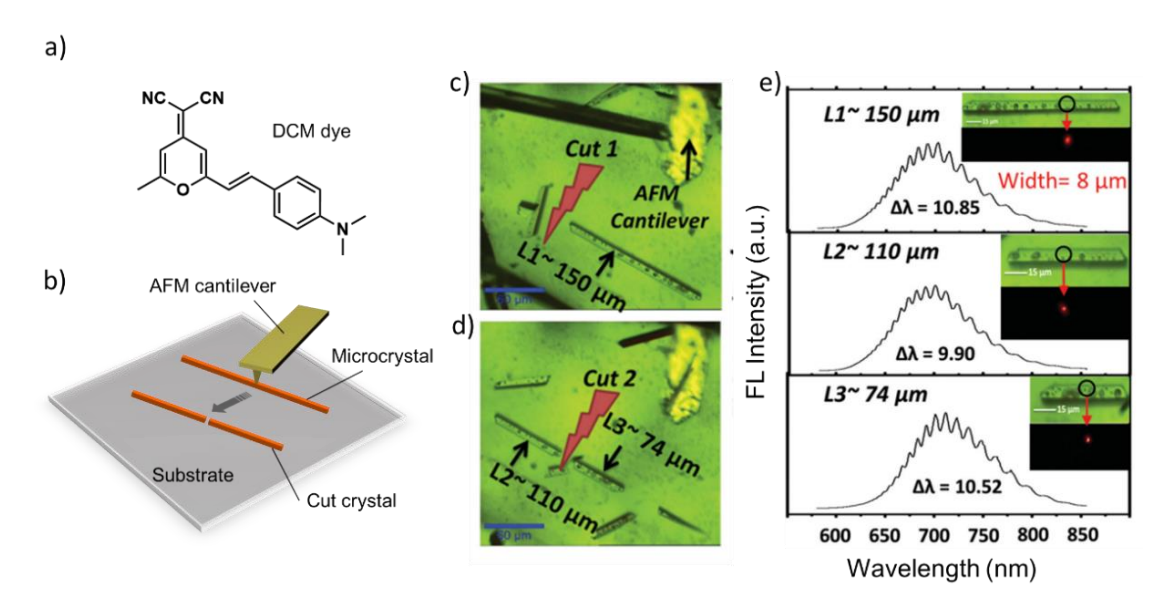


**Figure 1.35.** a) Molecular structure of DCM dye. b) Schematic depicting the breaking of microcrystal using the AFM cantilever tip. c,d) Confocal optical microscopy images of microcrystal after cutting into three fragments. e) Single-crystal FL spectra of cut microcrystals of three different lengths. Insets show the corresponding bright and dark field images of cut microcrystals upon laser excitation. [Figure adapted from ref. 90].

To prove the lateral F-P resonator nature of the DCM dye (Figure 1.35a) microcrystal, Venkatakrishnarao et al. in 2016 used the AFM cantilever tip to manipulate a selected crystal resonator and cut it into three fragments of different lengths (L1= 150 µm; L2= 110 µm; and L3= 74 µm) so that the lateral dimensions (W= 8 µm) were identical (Figure 1.35b-d). Later, the individual microcrystals were excited with a 488 nm laser; despite their varying lengths, the collected FL spectra revealed almost the same mode spacing ( $\Delta\lambda \approx$ 10 nm), thereby confirming the lateral FP resonator type (Figure 1.35e). [90]

## 1.6.3. Slicing and bending of a single-crystal

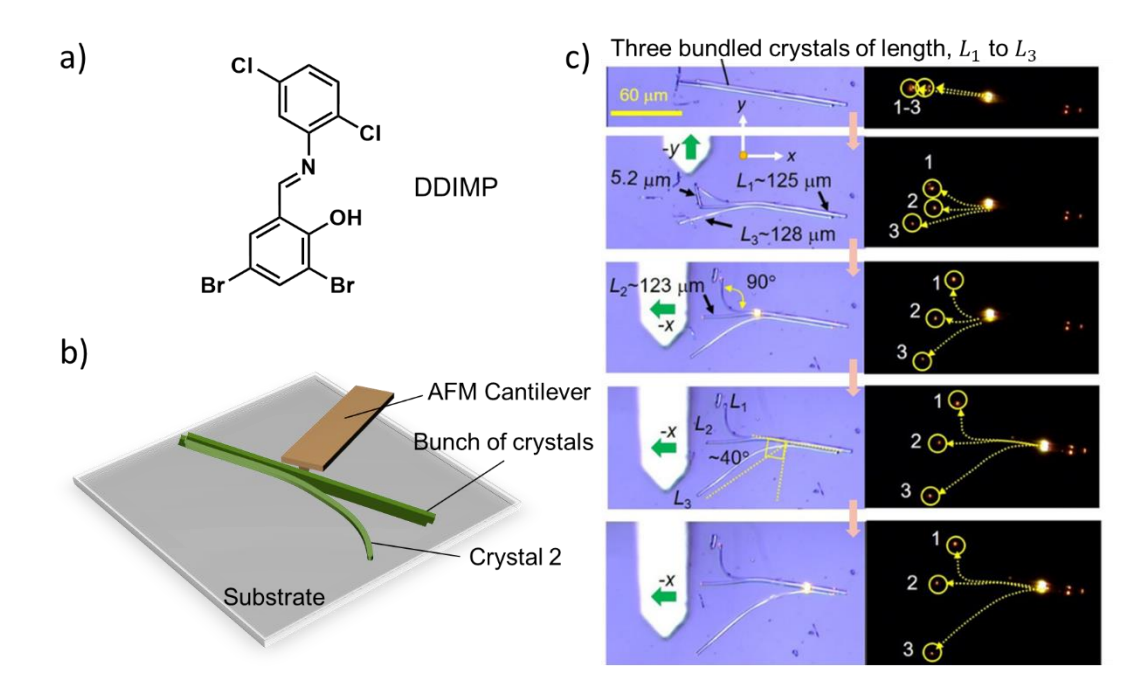


**Figure 1.36.** a) Molecular structure of DDIMP. b) Schematic depicting the slicing and bending of microcrystals from a bunch of crystals using the AFM cantilever tip. c) A series of confocal optical microscopy images (left) and FL images (right) showing the slicing and bending of the microcrystals using the AFM cantilever tip. [Figure adapted from ref. 24].

Generally, most of the organic crystals are brittle. However, some peculiar crystals show flexibility under mechanical force. These flexible crystals are classified into two types, namely, elastic and plastic crystals. Elastic crystals regain their shape after removing the external stress, whereas plastic crystals show permanent deformation upon releasing the external stress. In 2020, Annadhasan et al. micromanipulated the flexible microcrystals of (E)-2,4-dibromo-6-(((2,5-dichlorophenyl)imino)methyl)phenol (DDIMP) with the aid of an AFM cantilever tip (Figure 1.36a).<sup>[24]</sup> They found that upon releasing the external force (retraction of AFM cantilever tip from the microcrystal), the microcrystal did not regain its original shape, showing the *pseudo-plasticity* of flexible crystals on a glass substrate. This arises due to the larger adhesion between the crystal and its substrate compared to the crystal shape regaining force.<sup>[24]</sup>

By taking advantage of the pseudo-plasticity, the authors showed the slicing and bending of microcrystals from a bunch of crystals (Figure 1.36b,c). The control over the AFM cantilever tip's position and force-inducing direction is vital to attain the desired shape.

Therefore, careful manipulation of crystals using micromechanical tools like bending and slicing with an AFM cantilever tip allowed meticulous positioning of crystals into desired geometries (Figure 1.36c, left). The corresponding FL images upon optical excitation showed the waveguiding nature of the DDIMP bent single-crystals (Figure 1.36c, right).<sup>[24]</sup> This pseudo-plastic behavior opened new possibilities to create various curved crystal optical modules necessary for the fabrication of OPIC.

## 1.6.4. Aligning/integrating of a single-crystal

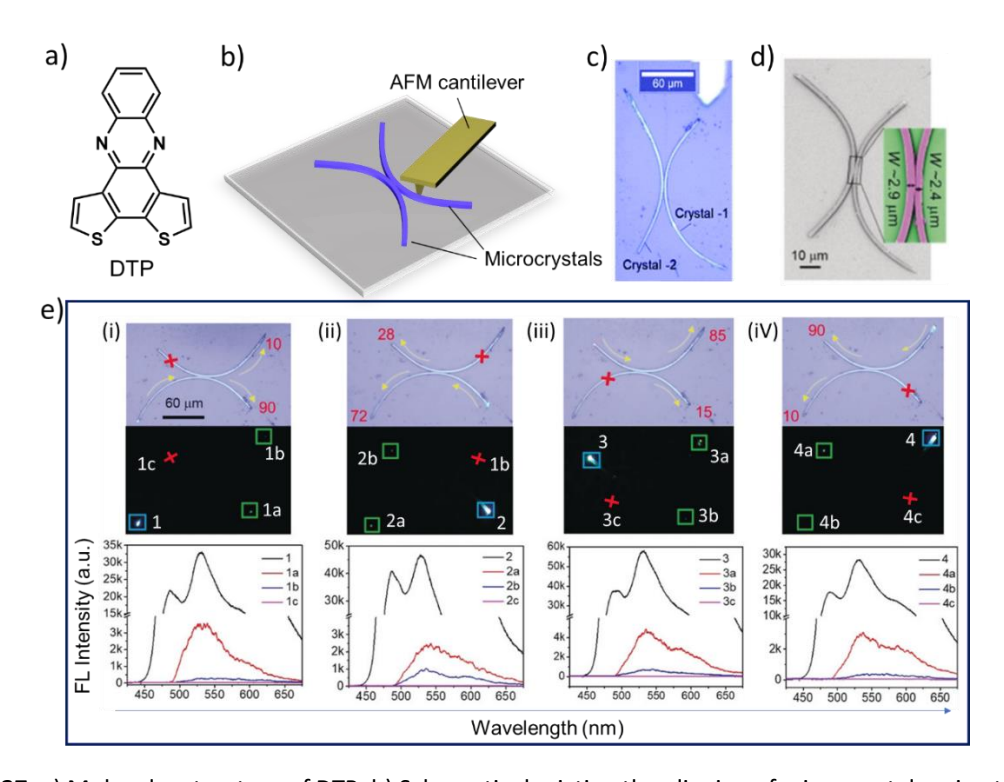


**Figure 1.37.** a) Molecular structure of DTP. b) Schematic depicting the aligning of microcrystals using the AFM cantilever tip. c) Confocal optical microscopy and d) FESEM image of fabricated monolithic 2×2 directional coupler (DC). Inset shows the close view of the junction of DC along with its widths. e) Confocal optical microscopy image (top), FL image (middle) and the corresponding FL spectra (bottom) of fabricated DC upon laser excitation at each terminal. The red crosses represent no signal at the corresponding output terminal. The dotted yellow lines show the light propagation directions. The numbers in red color show the optical-splitting ratio of the DC. Blue and green boxes represent input and output terminals, respectively. [Figure adapted from ref. 162].

In the same year, Annadhasan et al. reported dithieno[3,2-a:2',3'-c]phenazine (DTP) crystals based 2×2 directional coupler (DC) (Figure 1.37a). They made a monolithic DC out of the self-assembled DTP microcrystals to split the light beam into two (Figure 1.37c). For this, initially, a bent arc-shaped crystal-1 with an end-to-end spacing of  $\approx$ 156  $\mu$ m was

fabricated by bending the top and bottom endings of the crystal with an AFM tip (Figure 1b). Further, one more crystal, which has an end-to-end distance of  $\approx$ 173 µm, was made and placed next to arc-shaped crystal-1. Due to this positioning, two arcs' mid-convex points can touch together to form a DC (Figure 1.37b). The FESEM image of the DC shows a width of  $\approx$ 2.9 and  $\approx$ 2.4 µm for crystal-1 and crystal-2, respectively, at the coupling junction without any noticeable gap (Figure 1.37d). Later, photonic studies were performed to prove the directional splitting behavior of light in the fabricated monolithic circuit (Figure 1.37e). [162]

## 1.6.5. Extreme bending and transferring of a single-crystal

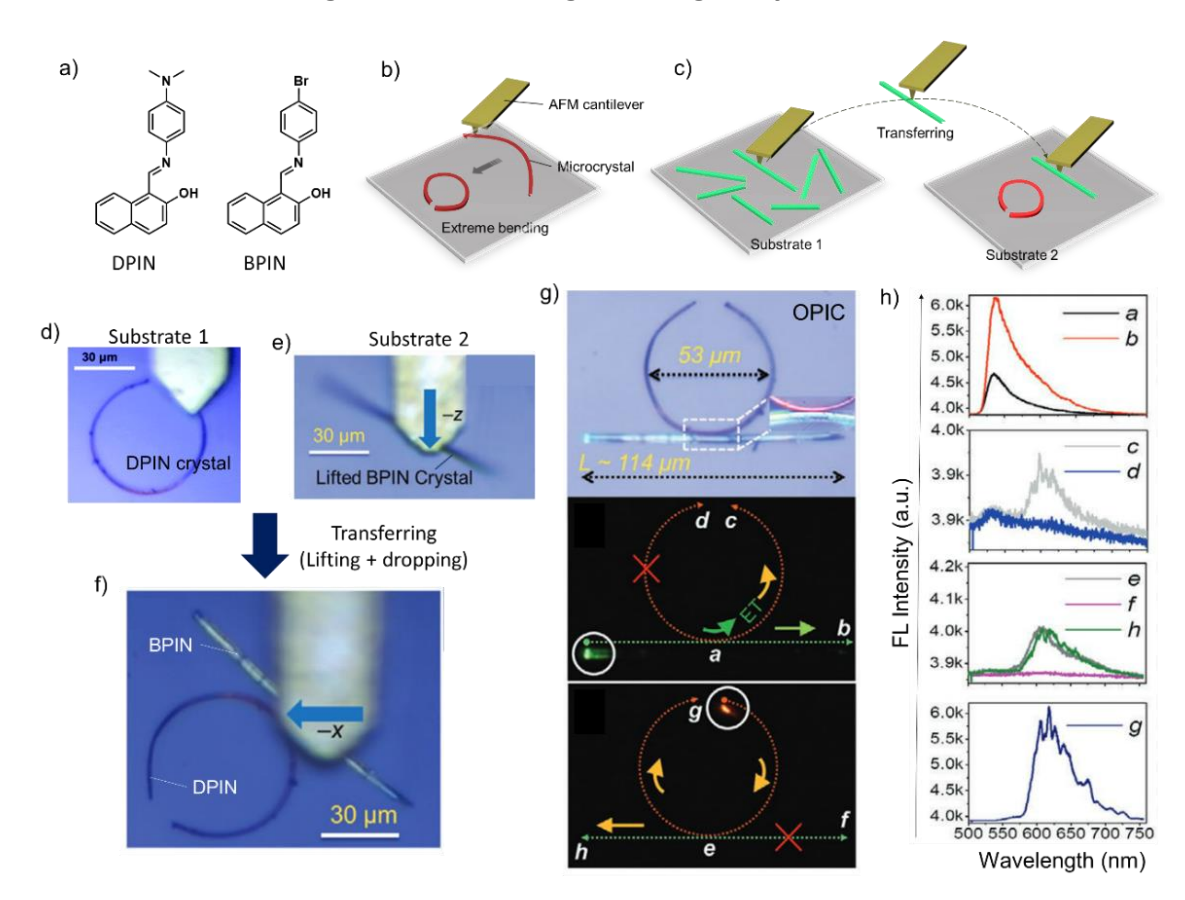


**Figure 1.38.** a) Molecular structures of DPIN and BPIN. b,c) Schematic depicting the extreme bending and transferring of microcrystals from one substrate to another using the AFM cantilever tip. d) Confocal optical microscopy image of DPIN microcrystal while extreme bending. Confocal optical microscopy images of e) lifting of a BPIN microcrystal from substrate 2 and f) dropping it on substrate 1 to fabricate an OPIC. g) Confocal and FL images of fabricated OPIC. Inset shows the color-coded FESEM image of the junction. h) The FL spectra show the optical response of the fabricated OPIC. [Figure adapted from ref. 110]

In 2021, Ravi et al. demonstrated the extreme *bending* of (E)-1-(4-(dimethylamino)-phenyl)imino-methyl-2-hydroxyl-naphthalene (DPIN) microcrystals and *transferring* of (E)-

1-(4-bromo)iminomethyl-2-hydroxyl-naphthalene (BPIN) crystal from one substrate to another (1.38a).<sup>[110]</sup> The graphics in Figure 1.38b,c show the micromechanical operations utilized in this work, i.e., extreme *bending* and *transferring* of microcrystals, respectively. Wherein the transfer operation includes *lifting*, followed by the *dropping* of microcrystals at the desired locations (Figure 1.38d-f). Using these micromechanical operations, the authors fabricated a hybrid OPIC and studied the photonic properties by exciting at one terminal and analyzing the outputs at the rest of the terminals. The confocal and FL images of the fabricated OPIC upon laser excitation at different terminals are presented in Figure 1.38g. The corresponding FL spectra showed mechanism-selective (active/ passive) and direction-specific optical signals from the fabricated OPIC (Figure 1.38h).<sup>[110]</sup>

#### 1.6.6. Rolling of a twisted single-crystal

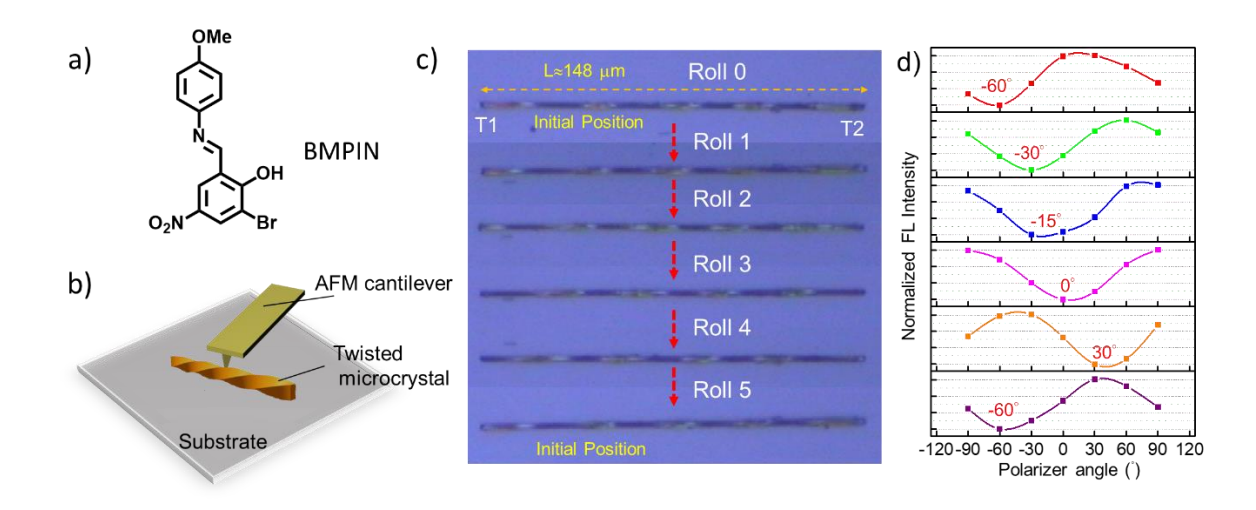


**Figure 1.39.** a) Molecular structure of BMPIN. b) Schematic representation of the rolling of twisted microcrystal using the AFM cantilever tip on a silica substrate. c) Series of confocal optical microscopy images of a 148 μm long BMPIN twisted crystal showing the translational motion of the microcrystal. d) FL intensity versus the polarizer angle plot for each roll. The excitation and collection positions are at T2 and T1, respectively. [Figure adapted from ref. 163].

Rohullah et al. in 2022, reported the naturally twisted crystals of (E)-2-bromo-6-(((4-methoxyphenyl)imino)methyl)-4-nitrophenol (BMPIN, Figure 1.39a). [163] They found that these self-assembled twisted microcrystals were rollable upon mechanical force, and Figure 1.39b shows the corresponding diagram. The AFM cantilever tip was used to exert a mechanical force perpendicular to the twisted microcrystal's long axis. In addition to

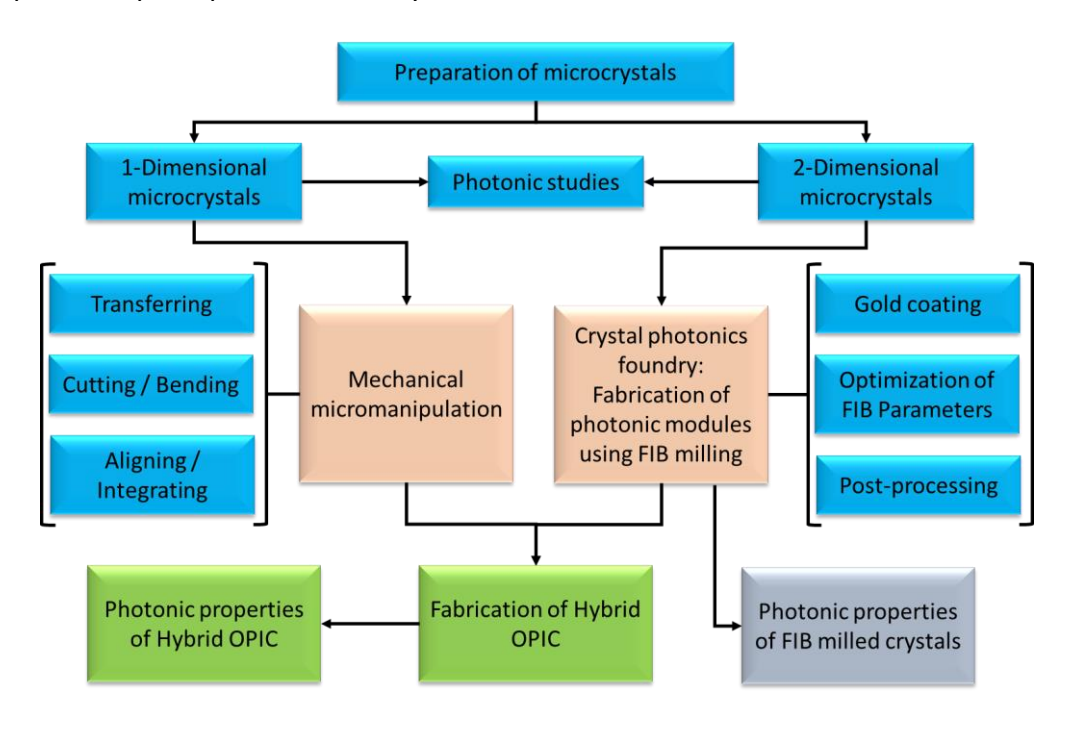
mechanical rolling movement, the twisted crystalline organic waveguide acts as a polarization rotator by changing the output signal polarization (Figure 1.39c,d). By combining mechanical locomotion and photonic properties, the twisted-crystal resonator presents a new dimension in mechanophotonics.<sup>[163]</sup>

## 1.7. Overview of the thesis

This thesis attempts to develop a technique capable of constructing highly reproducible, dimensionally precise organic crystalline optical modules using focused ion beam milling technology. The current-day photonics technologies heavily bank on inorganic compounds like silicon or silicon-based semiconductor materials compatible with complementary metal oxide semiconductor technologies (CMOS). [2,164,165] The rapid consumption of silica sand by the construction industry, glass and ceramic industries, and the exorbitant cost of producing ultra-pure silicon required for electronic grade silicon chips (EG-Si) in combination with harsh fabrication processes for Si-based photonic integrated circuits (PICs) possess enormous environmental challenges. Apart from financial and environmental concerns, the Si-PICs suffer from inherent disadvantages like passive-only signal transmission, difficulty in producing hybrid circuits, and non-reconfigurability because of high stiffness ( $H \approx 150$  GPa). [165] Recently, researchers from the University of Hyderabad attempted to address these issues by constructing PICs using alternative materials like flexible organic optical crystals. The unique ability of flexible crystals to be deformed into various optical geometries (bent waveguides, ring resonators, [107-109,166] directional couplers, [162,167] etc.) shows their potential for photonic applications. The ease of fabricating hybrid photonic circuits with the help AFM based mechanophotonics technique warrants their utility for optical device applications. However, the inability to achieve precise control over the geometrical size and shape and the mechanical anisotropic nature of flexible crystals are major setbacks and question the large-scale scalability of the organic photonic circuits.

Therefore, the main objective of the thesis is to construct various photonic components like resonators (ring, circular, rectangular, square, hexagonal, and octagonal disks), waveguides, directional couplers, and related components with high geometrical reproducibility, apt for the bulk-scale construction of hybrid PICs needed for the photonics

industry. The accomplishment of desired goals necessitates a novel crystal shape-altering technique that enables the cutting of organic single-crystals into pre-defined geometries. Therefore, a critical understanding of the interaction of focused ion beams with organic single-crystals is mandatory. Hence a multidisciplinary approach combining important areas of physics, chemistry, and materials engineering alongside following the customary nanophotonic principles is necessary.



**Scheme 1.1.** The multidisciplinary approach of the thesis.

The main obstacles in achieving the desired goals are i) choosing the appropriate organic material with optical attributes, ii) selecting a suitable crystal growth method, iii) optimizing the milling conditions, and iv) carefully selecting the crystal's absorption and emission properties to construct the required photonic circuit. The general approach followed in this thesis is presented in Scheme 1.1. Perylene is a semiconductor material and a potential material for photonic investigations. Firstly, the perylene microcrystal's growth conditions should be optimized to achieve single polymorphs (square-shaped  $\alpha$  and rhombus-shaped  $\beta$ ) exclusively using a cost-effective sublimation technique at ambient pressure. The as-grown microcrystals act as WGM resonators (linear and NLO regimes) due to their mirror-like light-reflecting facets. The finite-difference-time-domain (FDTD) numerical calculations disclose the electric field distribution of the trapped light in the microcrystals, which supports the experimentally observed WGM resonances. This

technique provides a typical range of sizes of resonators at a particular sublimation temperature and duration. However, the truth is, in nature, the geometrical shape of the microcrystal cannot be precisely controlled. Nanophotonic circuit industries are keen on designing, fabricating, and testing optical components made from new materials. Organic materials are budding as a potential alternative to silicon and its derivatives. Nonetheless, these organic photonic modules' access to the market is stuck due to difficulty in maintaining high geometrical and dimension precision. Hence, FIB milling technology is a potential technique that can be incorporated to achieve predefined geometries of perylene microresonators with high geometrical and size precision.

The FIB milling of organic microcrystals to attain photonic modules is not known previously. Therefore, a detailed study of substrates (conductive and non-conductive), protective layer etchants, and beam parameters provides the expected insights to fabricate desired optical components. Indium-tin-oxide-coated polyethylene terephthalate (ITO-PET) can serve as the conductive substrate, whereas borosilicate glass coverslip serves as a non-conductive substrate. The effects of known gold etchants (like Lugol's iodine solution and the exposure to HCN vapors) on perylene single-crystals to remove gold coating after electron-imaging uncovers the effect of gold layer on the optical component's performance. Later, the beam currents are amended to attain geometrically and dimensionally precise perylene single-crystal photonic microresonators viz. circular, rectangular, square, hexagonal, and octagonal disk and ring resonators. The perylene microresonators effectively induce light confinement inside the optical cavity.

Further, the milling conditions become valid to carve various disk resonators (circular and rectangular) from a different organic molecular single-crystal, namely 2,3,6,7-Tetrahydro-9-(trifluoromethyl)-1H,5H,11H-[1]benzopyrano(6,7,8-ij)quinolizin-11-one (coumarin 153). The high quantum yield nature of coumarin-153 allows FL retainment after milling; thereby, post-processing is not mandatory. The photonic studies and the FDTD calculations in coumarin-153 microresonators reveal the light confinement pattern inside the crystal.

The tandem use of FIB milling and mechanical micromanipulation to attain hybrid OPIC is a novel strategy for achieving hybrid photonic circuits. The fabrication of hybrid

organic-add-drop filter (HOADF) requires FIB milled perylene disk resonators and pseudo-plastic crystal waveguides, namely, (*E*)-1-(((5-bromopyridin-2-yl)imino)methyl)naphthalen-2-ol (BPyIN) and (*Z*)-2-(3,5-bis(trifluoromethyl)phenyl)-3-(7-methoxybenzo[c][1,2,5]thiadiazol-4-yl)acrylonitrile (BTD2CF<sub>3</sub>). Even though the FIB milling technique allows automation, scalability, and reproducibility anticipated by industrial manufacturers, the translocation of milled optical components from one substrate to another is a challenge for the construction of hybrid OPICs. The mechanophotonics approach becomes crucial for integrating two or more photonic components at the OPICs construction site. The perylene disk resonators can route the light clockwise and anticlockwise, depending on the input light. Integration of these disk resonators with BTD2CF<sub>3</sub> and BPyIN with the help of AFM cantilever tip provides the first-of-its-kind HOADF. The HOADF functions as a typical add-drop filter by allowing directed-light propagation in a controlled pathway.



Ambient Pressure Sublimation Technique
Provides Polymorph-Selective Perylene
Nonlinear Optical Microresonators

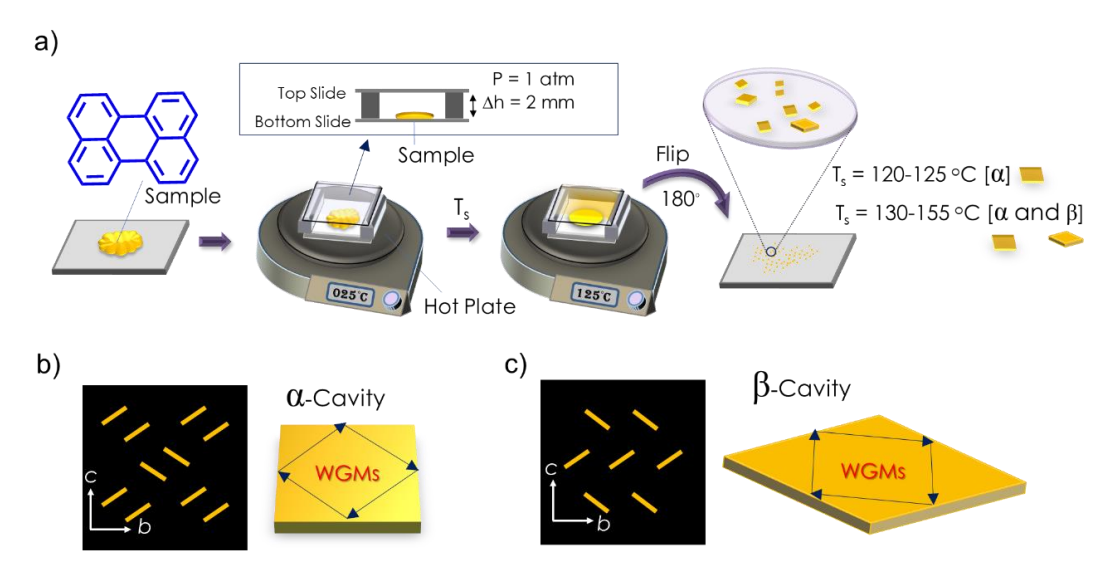
## 2.1. Abstract

This chapter demonstrates the cost-effective, straightforward, and reliable sublimation technique to obtain microscale polymorphic perylene crystals in a phase-selective manner at ambient pressure. The primary focus of the experiment involves the precise monitoring of sublimation temperature and duration to obtain distinct polymorphic forms (referred to as square-shaped  $\alpha$  and rhombus-shaped  $\beta$ ). These forms exhibit smooth surfaces and sharply defined reflective edges, which are crucial characteristics for a microcrystal to function as an optical resonator. Additionally, the  $\alpha$  microcrystals exhibit a vibrant yellow fluorescence, while the  $\beta$  microcrystals display a distinct green fluorescence. Notably, both these polymorphic perylene microcrystals demonstrate properties of whispering gallery mode (WGM) resonators operating in both linear and nonlinear optical regimes. Our experimental findings are supported by numerical calculations using the finite difference time domain method, confirming the WGM-resonator behavior and revealing the intricate localization of the electric field. Moreover, the quadratic relationship between emission intensity and laser power proved the two-photon absorption characteristics of these photonic resonators when stimulated by infrared lasers.

## 2.2. Introduction

Perylene and its derivatives are widely utilized as semiconducting organic materials in optoelectronics and light-emitting devices industries. [168-171] It exits in two polymorphic forms, namely  $\alpha$  and  $\beta$ . [172] While some research papers have explored the self-optical waveguiding properties of square-shaped  $\alpha$  perylene crystals under one-photon excitation in the linear optical regime, [173,174] their potential as nanophotonic resonators in both the linear and nonlinear optical regimes remains unexplored. However, the realization of organic NLO crystalline resonators is quite rare due to their intrinsic nature, and only a limited number of reports exist in the literature. Intrinsic NLO resonators necessitate strong NLO activity, such as two-photon absorption, and high-quality microcrystals with high refractive indices and smooth, mirror-like facets to achieve effective feedback. The growth of high-quality organic crystals is crucial for optimizing the light storage efficiency of microcrystal-based nanophotonic devices.

Unfortunately, the irreversible phase transition of the  $\beta$  polymorph to the more stable  $\alpha$ -form has posed a significant challenge in the development of comparative optoelectronic and photonic devices based on these two forms. Although the existence of two polymorphic forms of perylene has been known for a long time, there is currently no viable technique available for the clean and selective growth of ultra-pure single-crystals in specific forms. Existing methods, such as solvent-assisted self-assembly techniques, often require surfactants resulting in thin-film deposition along with microcrystals. [175] In a recent study, air-sublimation of perylene only yielded the  $\alpha$ -form without systematic temperature optimization.<sup>[87]</sup> Another report demonstrated the fabrication of both polymorphs by organic molecular beam deposition of perylene onto silicone-oil-covered substrates. [176] On the other hand, physical vapor transport (PVT) is an effective technique for growing large, ultra-pure organic crystals, but it typically involves the use of inert gas and, at times, requires very low pressure. [177] Therefore, this chapter focuses on elucidating a simple and efficient sublimation growth method for perylene directly on glass substrates (without silicone oil coating) at selected temperatures, under ambient pressure, and without the need for inert gas flow, to obtain access to its polymorphic forms, particularly the  $\beta$ -form.



**Scheme 2.1.** a) Schematic diagram of the phase-selective growth of perylene microcrystals as a function of sublimation temperature  $(T_s)$ . b,c) Graphical representation of  $\alpha$ - and  $\beta$ -form microscale NLO resonators which support WGMs along with their corresponding solid-state packing diagrams, respectively.

In this study, a sublimation technique at ambient pressure is introduced, aiming to grow single-crystals of perylene's  $\alpha$  and  $\alpha/\beta$  polymorphic forms. The growth process involves maintaining specific temperature ranges, approximately 120-130 °C for the  $\alpha$ -form

and 131-155 °C for the  $\alpha/\beta$ -form. Importantly, these temperature ranges enable control over the microdimension range of the desired crystalline phases (see Scheme 2.1a and Figure 2.1a). Significantly, these polymorphic forms exhibit WGMs when subjected to both linear and nonlinear optical excitations. By employing FDTD calculations, the localization patterns of the electromagnetic field within these  $\alpha$  and  $\beta$  microresonators are revealed at different wavelengths.

#### 2.3. Results and discussion

# 2.3.1. Preparation of perylene microresonators via ambient pressure sublimation technique

Perylene, a rigid polycyclic molecule (Scheme 2.1a), exhibits crystallization in a monoclinic symmetry with a P2<sub>1</sub>/c space group, displaying centrosymmetric characteristics. It exists in two distinct polymorphic forms:  $\alpha$  and  $\beta$ , distinguished by their square and rhombus shapes, respectively. In the ordered crystalline state, the  $\alpha$ -form adopts a dimeric arrangement with a sandwich-herringbone motif, while the  $\beta$ -form exists as a monomer with a  $\gamma$ -type herringbone structure (Scheme 2.1b,c). The molecular packing modes of these polymorphic forms indicate H- and J-aggregation types for the  $\alpha$  and  $\beta$ -forms, respectively. Notably, optical excitation of the  $\alpha$  form results in vivid yellow fluorescence, while the  $\beta$ -form emits green fluorescence.

The growth process of  $\alpha$ -form microcrystals was initiated as follows: A perylene sample (<1 mg) was transferred to the heating apparatus by depositing the sample on the clean borosilicate glass coverslip at ambient conditions. Later, two stubs of approximate thickness of 2 mm were positioned on either side of the bottom substrate containing the sample. A clean coverslip, acting as the substrate, was carefully placed on top of the glass stubs (Scheme 2.1a). The gap ( $\Delta h$  =2 mm) between both substrates was optimized to maintain the lower temperature on the top substrate than the bottom substrate. This arrangement facilitated the condensation of perylene melt droplets on the top substrate, leading to nucleation and successive growth of microcrystals. The temperature of the bottom substrate containing the perylene was gradually increased, with stepwise increments of 5 °C at a time. The emergence of  $\alpha$ -form microcrystals (of dimensions 6-8  $\mu$ m) on the top substrate was observed when the temperature of the heating apparatus reached

around 120-125 °C (sublimation temperature,  $T_s$ , Figure 2.1b). These crystals exhibited lower energy facets (100) aligned parallel to the glass substrate, and a few standing crystals with lower energy facets oriented orthogonal to the glass substrate were also observed.

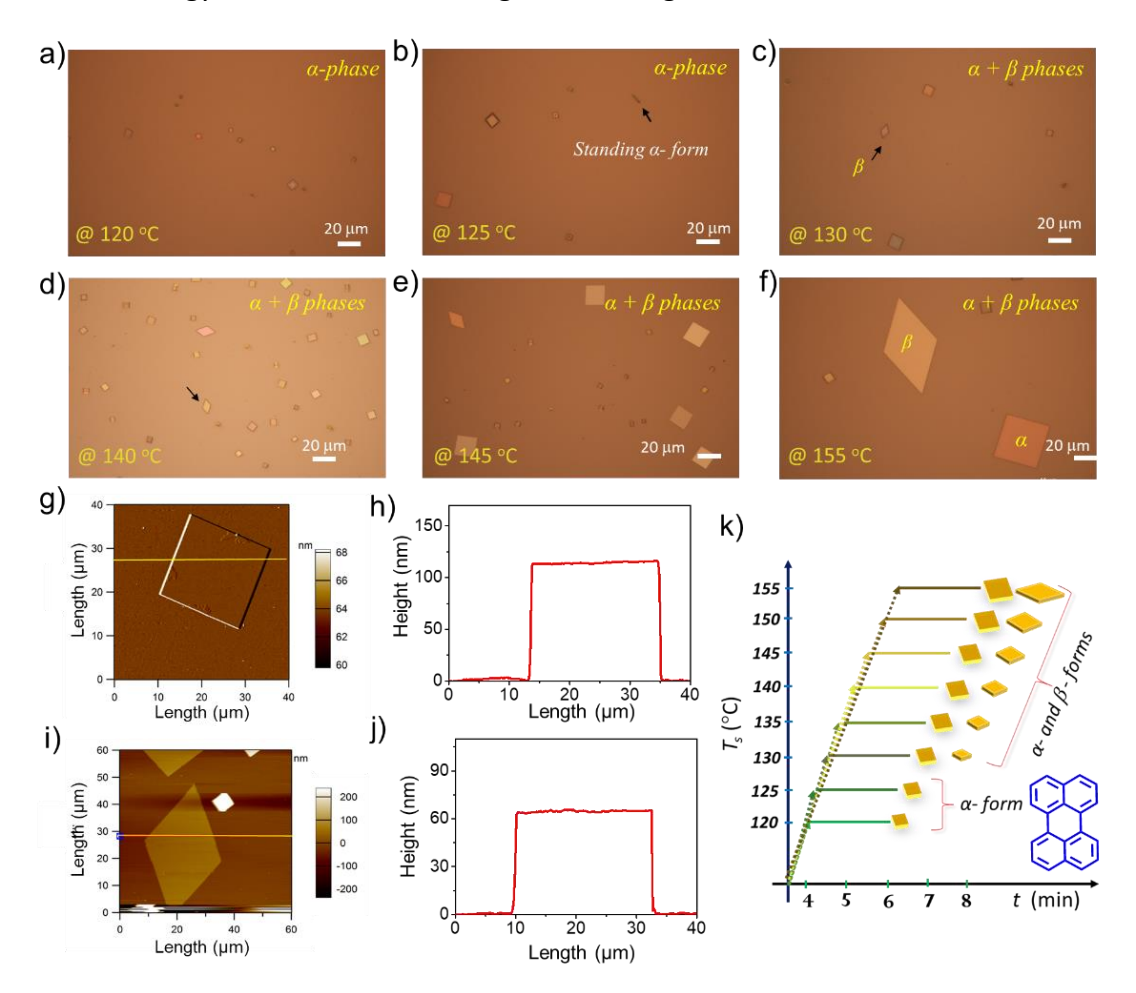


**Figure 2.1.** a-f) Optical microscope images showing the formation of  $\alpha$ -and  $\beta$ -forms at selected  $T_s$  values. g,i) AFM topography images of  $\alpha$  and  $\beta$ -form crystals and h,j) their height and length profiles correspond to the yellow lines in the topography images. k) Plot showing the size and phase selection using sublimation temperature  $(T_s)$  and sublimation time (t).

The initiation of visible  $\beta$ -form crystals is observed at a temperature of  $\approx$ 130 °C, and the microcrystal growth continues until  $\approx$ 155 °C in conjunction with the  $\alpha$ -form (Figure 2.1c-f). AFM investigations of square-shaped  $\alpha$  and rhombus-shaped  $\beta$ -forms at specific regions revealed the thickness of the  $\alpha$ -form ( $\approx$ 110 nm) is akin to that of the  $\beta$ -form ( $\approx$ 70 nm) (Figure 2.1g-j). Mostly, the  $\beta$ -form microcrystals grow parallelly to the substrate in comparison to its  $\alpha$ -form. Remarkably, the  $\beta$ -form crystals obtained through this technique exhibit stability at ambient conditions without transforming to the  $\alpha$ -form. By optimizing

the  $T_s$  and t, the controlled growth of polymorphic perylene microcrystals within the desired size range on the coverslip was achieved (Figure 2.1k).

### 2.3.2. Growth of perylene microcrystals

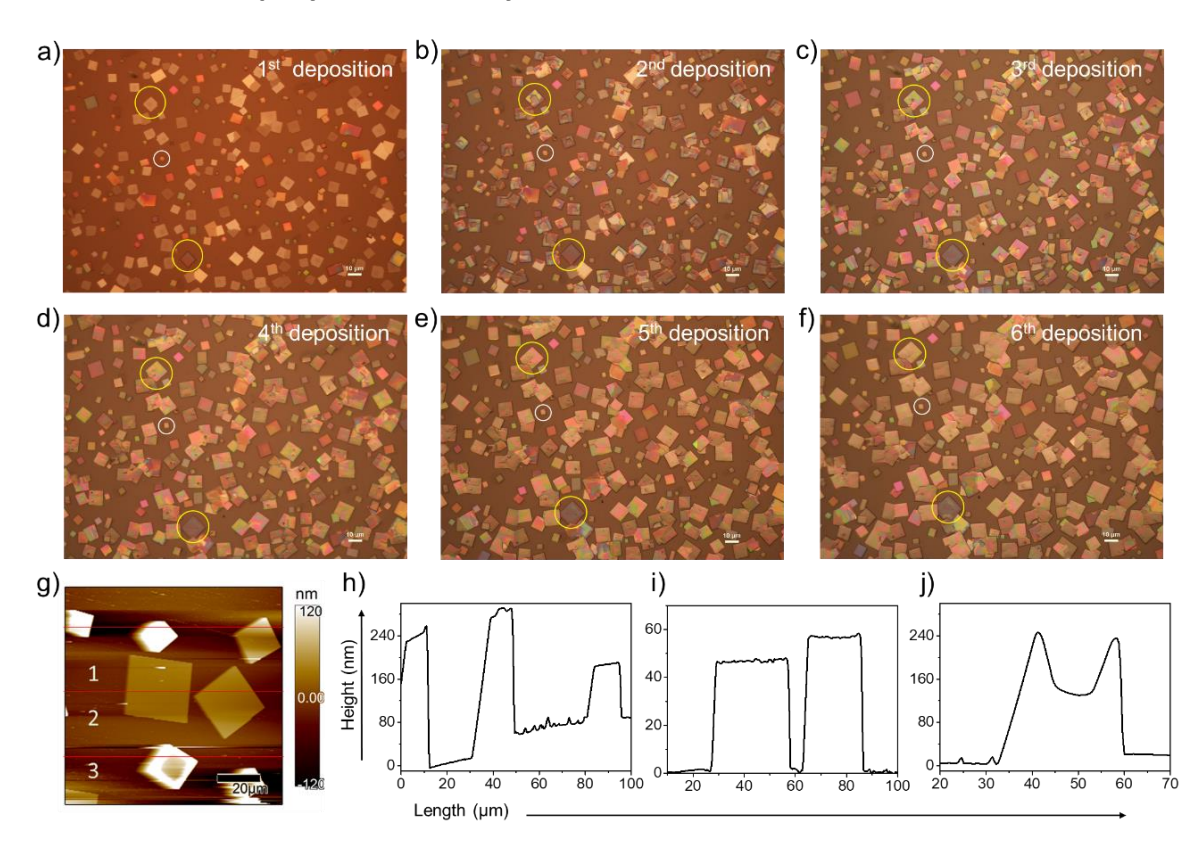


**Figure 2.2.** a-f) Optical microscopy images of  $\alpha$  polymorphs at 125 °C by repeated sublimation. g) AFM topography image of  $\alpha$  polymorphic microcrystals. h-j) AFM height and length profile of microcrystals at three lines 1-3 shown in the topography image, respectively. Scale bar 10  $\mu$ m.

To investigate the growth dynamics of microcrystals, a designated area of 240  $\mu$ m² was selected. The growth rate of the microcrystals was monitored over time using a systematic study at each minute over the six-minute duration (Figure 2.2a-f). The polarized microscopy and AFM topography images obtained at different sublimation times reveal the following findings: (i) Majority of microcrystals exhibited their growth with (100) facet aligned parallelly to the glass substrate, characterized by a height of approximately 70 nm at 125 °C. However, the growth rates varied among the crystals with increasing t. (ii) The AFM investigations reveal that the tiny microcrystals seem to grow predominantly in the vertical direction (height  $\approx$ 250 - 275 nm at 125 °C), whose growth appeared to be stagnant in the polarized microscopy images collected at various intervals. (iii) No new microcrystal nucleation points were observed in empty areas on the substrate, even at extended

sublimation times. (iv) Prolonged *t* promoted the evolution of new nucleation points exclusively towards the pre-existing microcrystals' edges. The selectivity in nucleation sites suggests preferential molecular transport toward existing microcrystals from the empty regions (Figure 2.2).

### 2.3.3. Photonic studies of $\alpha$ - and $\beta$ -form perylene microcrystals

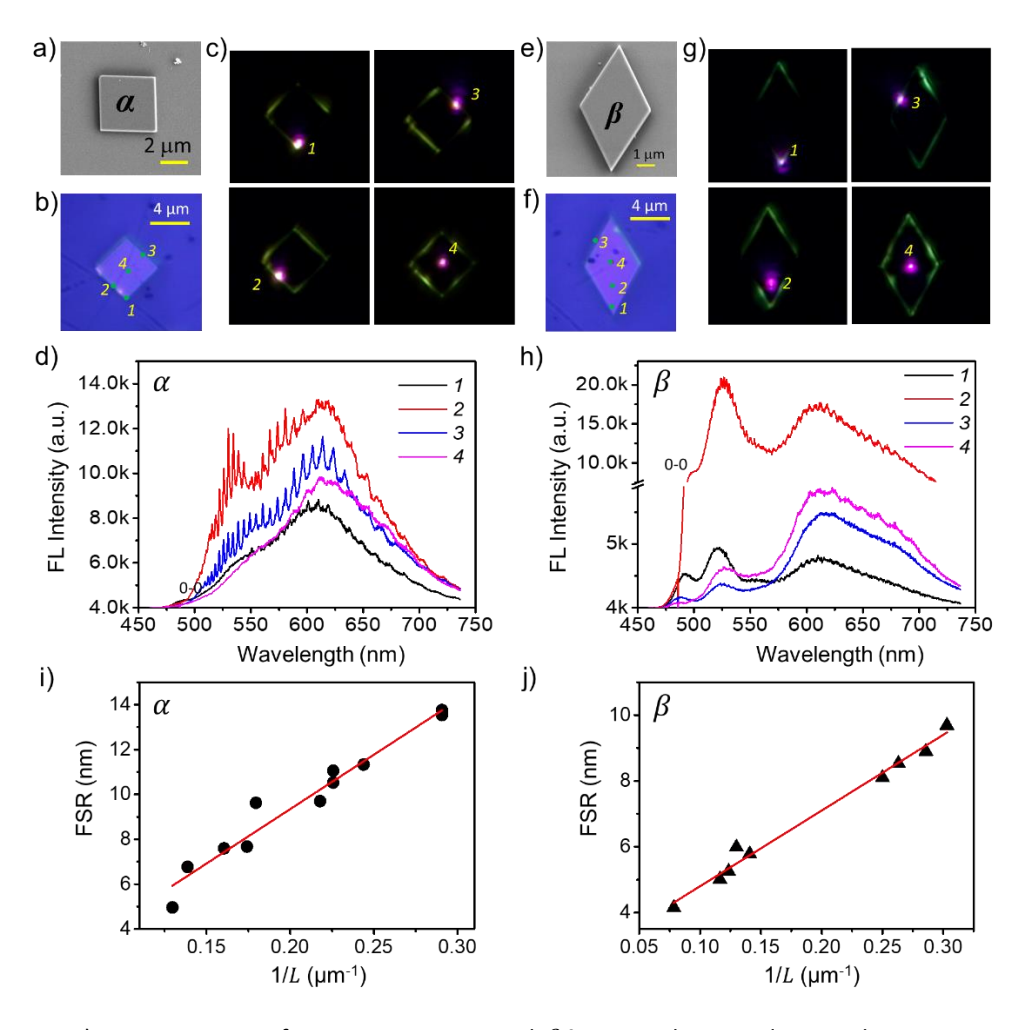


**Figure 2.3.** a,e) FESEM images of representative  $\alpha$ - and  $\beta$ -form perylene single-crystal microresonators. b,f) Confocal optical microscopy images of  $\alpha$  and  $\beta$ -forms of perylene microresonators before electronic excitation with 405 nm CW laser. Labels 1-4 show the optical excitation positions. c,g) FL images of  $\alpha$  and  $\beta$  resonators excited at positions labeled as 1-4. d,h) Reflection mode WGM spectra of  $\alpha$  and  $\beta$  perylene resonators collected at positions 1-4. i,j) FSR versus 1/L of perylene  $\alpha$ - and  $\beta$ -form microresonators.

Representative images acquired using FESEM exhibit the mirror-like facets of the  $\alpha$  and  $\beta$  polymorphs (Figure 2.3a,e). In order to investigate the presence of optical-resonator characteristics, photonic studies were performed on microcrystals. The square-shaped

microcrystal ( $\alpha$ -form) was excited with a continuous-wave laser (wavelength: 405 nm, objective: 150×; spot size:  $\approx$ 0.8  $\mu$ m), resulting in the yellowish FL with distinct optical resonances observed in the range of 470-750 nm. These resonances in the FL spectrum arise from constructive interferences of specific wavelengths (Figure 2.3d). Furthermore, photonic investigations on rhombus-shaped microcrystals ( $\beta$ -form) demonstrated FL spectra with significant peak intensities observed at  $\approx$ 485, 520 nm, 555 nm (very weak), and 610 nm (Figure 2.3h). The emission band at  $\approx$ 487 nm (0-0 emission band) was found to be weaker in the  $\alpha$ -form microcrystals, whereas it exhibited stronger intensity in the  $\beta$ -form microcrystals. This confirms the  $\theta$ -type (0-0; forbidden transitions) and  $\theta$ -type (0-0; allowed transitions) molecular aggregation present in the  $\alpha$  and  $\theta$ -form resonators, respectively.

Moreover, the FL spectra displayed periodic sharp peaks, which arise due to the confinement of FL photons within the microresonator through repeated back-forth circulation at the mirror-like facets. These sharp peaks suggest the occurrence of WGM resonances, as dictated by the microcrystal shape. The verification of the resonance mode type was further accomplished by plotting the FSR of different-sized microcrystals as a function of resonator edge length (L) (Figure 2.3i,j). The FSR value, calculated for microcrystals of varying sizes in both  $\alpha$  and  $\beta$  forms, exhibited a linear relationship with 1/L, confirming the presence of WGM-type resonances in the polymorphic crystals.

### 2.3.3.1. Excitation position dependency and crystal anisotropy on FL intensity:

Interestingly, the intensity of the FL bands exhibits variations depending on the excitation positions. A systematic experiment was conducted to thoroughly investigate the intensity dependence, wherein the  $\alpha$ -form microcrystal was excited at 4 distinct positions (1-4, Figure 2.3b,c). When the crystal was excited at the corner position (1) and the center position (4), the obtained signals exhibited relatively weak intensity and poorly resolved WGMs. This observation suggests that the excitation at these specific locations does not efficiently couple with the resonator, resulting in a diminished signal response. On the other hand, excitation at the crystal edges (positions 2 and 3) yielded pronounced WGMs with enhanced resolution and higher intensity. The strong interaction between the incident photons and the crystal edges resulted in well-defined WGMs in the FL spectra (Figure 2.3d). In a similar vein, the  $\beta$ -form crystal also displayed excitation position-dependent spectral

intensity and WGM characteristics. By exciting the  $\beta$  crystal at positions 1 to 4, a clear dependence of the spectral intensity and the quality of resolved WGMs on the excitation position was observed (Figure 2.3f-h). These findings further emphasize the significance of excitation position and its impact on the FL bands and WGMs in the FL spectra of both  $\alpha$  and  $\beta$  crystal resonators.

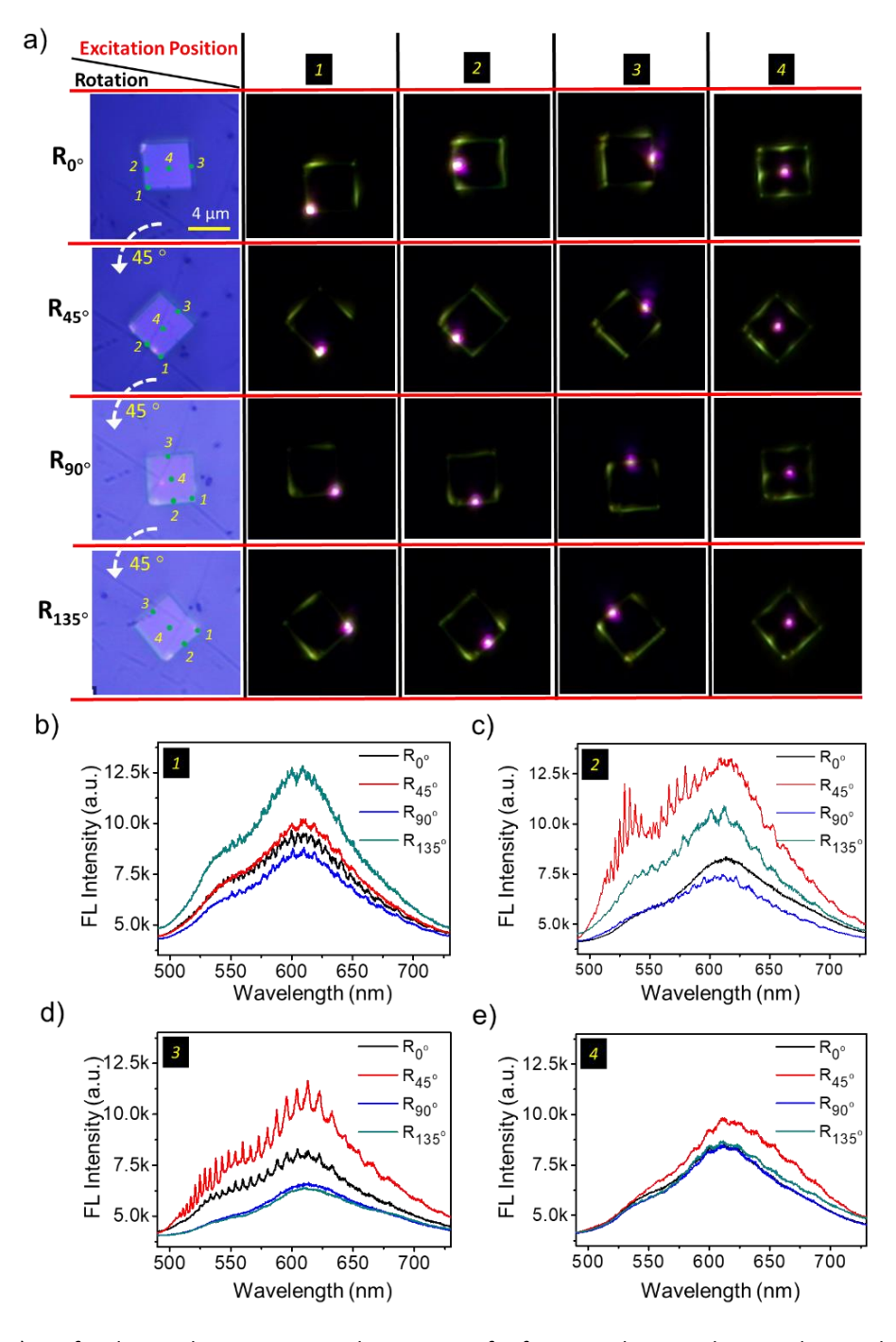


**Figure 2.4.** a) Confocal optical microscopy and FL images of  $\alpha$ -form perylene single-crystal excited at positions 1-4 by rotating 45° each time. b-e) WGM spectra collected at positions 1-4 for each 45° rotation, respectively.

To investigate the influence of anisotropic behavior in perylene microcrystals on the FL spectra, each polymorphic single-crystal was excited at 4 different points for every 45° rotation. The resultant FL intensity obtained at 1 to 4 points was sensitive to the orientation of microcrystal, confirming the crystal anisotropy (Figure 2.5 and 2.6).

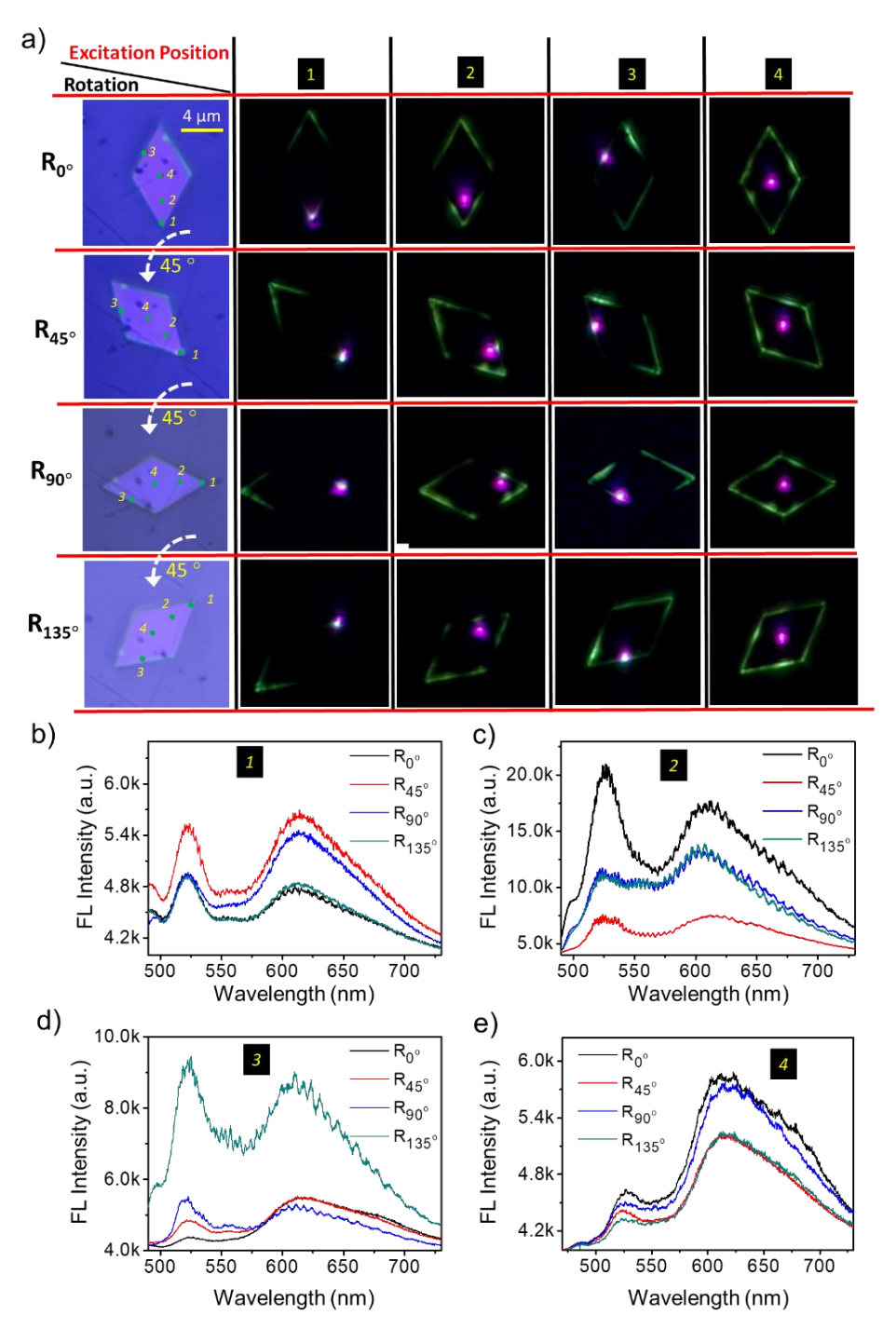


**Figure 2.5.** a) Confocal optical microscopy and FL images of a  $\beta$  -form perylene single-crystal excited at positions 1-4 by rotating 45° each time. b-e) WGM spectra collected at positions 1-4 for each 45° rotation, respectively.

To corroborate the anisotropic nature and domain orientation within the microcrystals, a polarized light microscope equipped with a variable polarizer (P), an analyzer (A), and a rotating stage were employed. The polarizer and analyzer were maintained orthogonal to each other while the stage was rotated from 0° to 90°. Notably, at 0° and 90°, the images appeared bright with maximum intensity (output signal 1, Table 2.1), indicative of aligned domains. In contrast, at 45°, the images exhibited near-darkness (output signal 0, Table 2.1), implying that the domains within the crystals were predominantly oriented in either the direction of the polarizer or the analyzer (Table 2.1). These images distinctly revealed the presence of optical anisotropy, wherein the  $\alpha$  resonators exhibited diagonal optical axes (any of the two directions), while the  $\beta$  resonators have optical axes along the long axis of the crystal (Table 2.1). These optical axes signify the inherent anisotropic properties of the polymorphic crystals, providing valuable insights into their optical characteristics and orientation-dependent responses.

**Table 2.1:** Anisotropic nature of polymorphic microcrystals.

	Angle between polarizer and analyzer	Crystal orientation $\alpha$ or $\beta$		Output	
1	90	Without crystal		0	
2	90	0		1	
3	90	45	$\Diamond$	0	$\Diamond$
4	90	90		1	

# 2.3.4. NLO studies and FDTD numerical calculations of lpha- and eta-form perylene crystal resonators

To investigate the NLO properties of the  $\alpha$  and  $\beta$ -forms of perylene, a thorough examination of the microcrystals was carried out using a custom-built NLO microscopy setup. In this experimental setup, a single microcrystal was excited using a femtosecond pulsed laser (wavelength: 780 nm, repetition rate: 80 MHz, pulse width: 60 fs), employing a high numerical aperture  $100\times$  objective to achieve a focused spot size of 1  $\mu$ m (Figure 2.6a,e). Significantly, several experiments unveiled a strong TPL originating from  $\alpha$  and  $\beta$  microcrystals, with emission occurring within the range of approximately 460-650 nm. It is noteworthy that this TPL closely matches the one-photon pumped FL (Figure 2.6b,f), albeit with a slightly narrower bandwidth.

Furthermore, WGMs were observed in the TPL spectra of  $\alpha$  and  $\beta$ -forms of perylene microcrystals. To assess the size-dependency of these WGMs, the FSR values were estimated from the TPL spectra of crystals with varying sizes. The FSR values were obtained by extracting the WGM spectra from the raw TPL spectra after subtracting the non-resonant TPL background (Figure 2.6b,f, blue and red lines). As expected for WGM resonators, the FSR values for both polymorphic resonators exhibited a relationship of FSR with 1/L. Additionally, these resonators demonstrated Q-factors of about 500 (Figure 2.6i,j). These findings establish that the  $\alpha$  and  $\beta$ -forms of perylene crystals possess the NLO properties and can serve as effective WGM resonators when operated with infrared lasers.

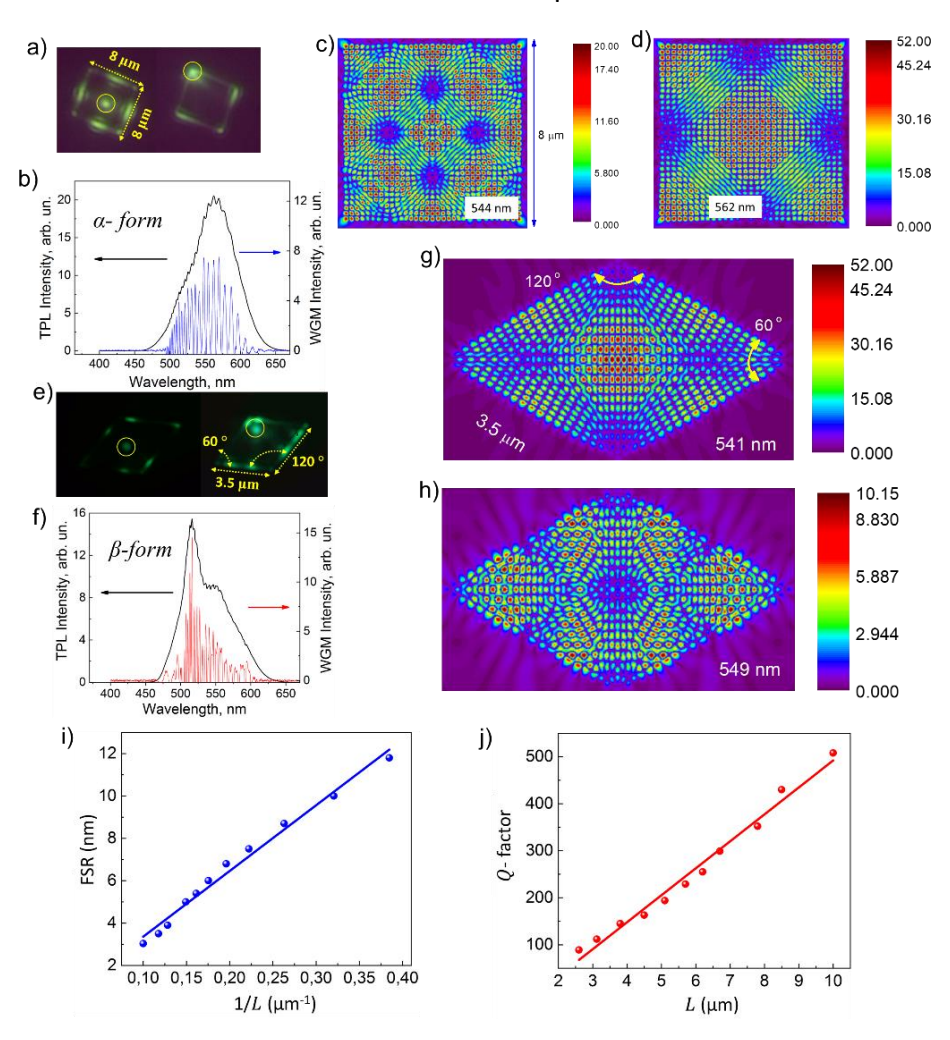


**Figure 2.6.** a,e) Optical microscopy images of TPL in  $\alpha$  and  $\beta$ -forms of perylene single-crystals excited at two different positions (shown as yellow circles). b,f) Experimental TPL spectra with WGMs from  $\alpha$  and  $\beta$ -forms of perylene resonators. The blue and red lines show the pure WGM spectra with subtracted nonresonant background TPL. FDTD calculations:  $|E_z|$  distribution for the wavelengths (see the inset label) that correspond to the WGMs of c,d)  $\alpha$ -form with 8 μm edge length and g,h)  $\beta$ -form with 3.5 μm edge distance and angles 120 and 60 degrees. Plots of i) FSR vs. 1/L and j) Q-factor vs. L for the WGMs observed in the TPL.

To validate the resonator type and to investigate the electric field distribution within the microresonators, FDTD numerical calculations were conducted using Lumerical FDTD Solutions software for both polymorphic crystals (Figure 2.6c,d,g,h). The calculations employed the geometrical parameters of real polymorphic microcrystals, specifically an  $\alpha$ -form crystal with a L of 8  $\mu$ m and a  $\beta$ -form crystal with a L of 3.5  $\mu$ m along with edge angles of 120° and 60°, respectively. The n of the crystals was set to 1.7, and the calculations results revealed the distribution of  $|E_z|$  for wavelengths corresponding to the prominent WGM peaks in the  $\alpha$ - and  $\beta$ -form resonators, specifically  $\lambda$  =544,562 nm and 541,549 nm, respectively (Figure 2.6c,d,g,h).

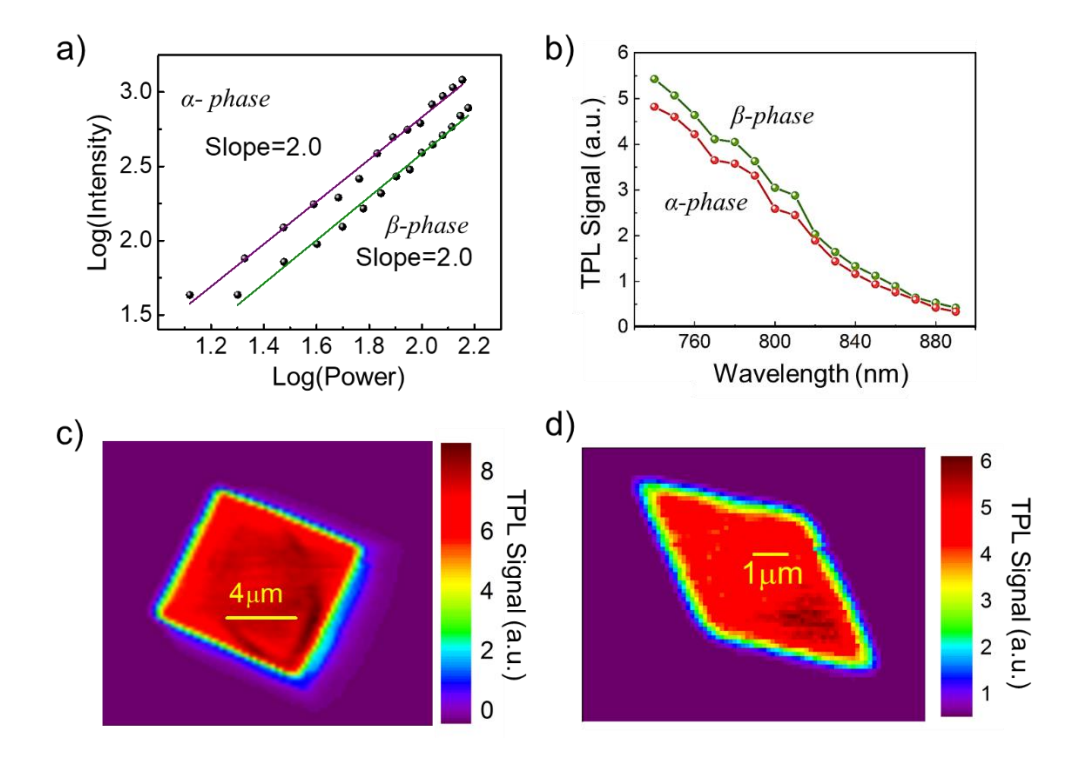


**Figure 2.7.** a) Logarithmic plot of TPL intensity versus pump-power for  $\alpha$ - and  $\beta$ -forms of perylene single-crystal resonators. b) TPL intensity as a function of pump wavelength for both forms, respectively. c,d) NLO microscopy two-dimensional maps of  $\alpha$ - and  $\beta$ -forms of perylene single-crystal resonators displaying the distribution of TPL signals, respectively.

Furthermore, the TPL signal intensity was measured at various pump powers, and the resulting plot on a logarithmic scale demonstrated a slope value of 2, confirming the two-photon nature of the absorption process in both polymorphic forms (Figure 2.7a). Two-dimensional maps of the scattered TPL intensity from the  $\alpha$  and  $\beta$  microcrystals (Figure 2.7c,d) supported the uniform distribution of the NLO signal from these optical resonators. Additionally, the dependence of TPL signal intensity on the pump wavelength was analyzed

to gain insights into the TPA cross-section of these polymorphic resonators. Each resonator was excited using a tunable femtosecond laser within the range of 740-890 nm while maintaining constant power. The resulting plot (Figure 2.7b) for both  $\alpha$  and  $\beta$  polymorphic crystals clearly demonstrated a significant increase in TPL intensity as the pump wavelength decreased, signifying the maximum TPA occurring at higher frequencies.

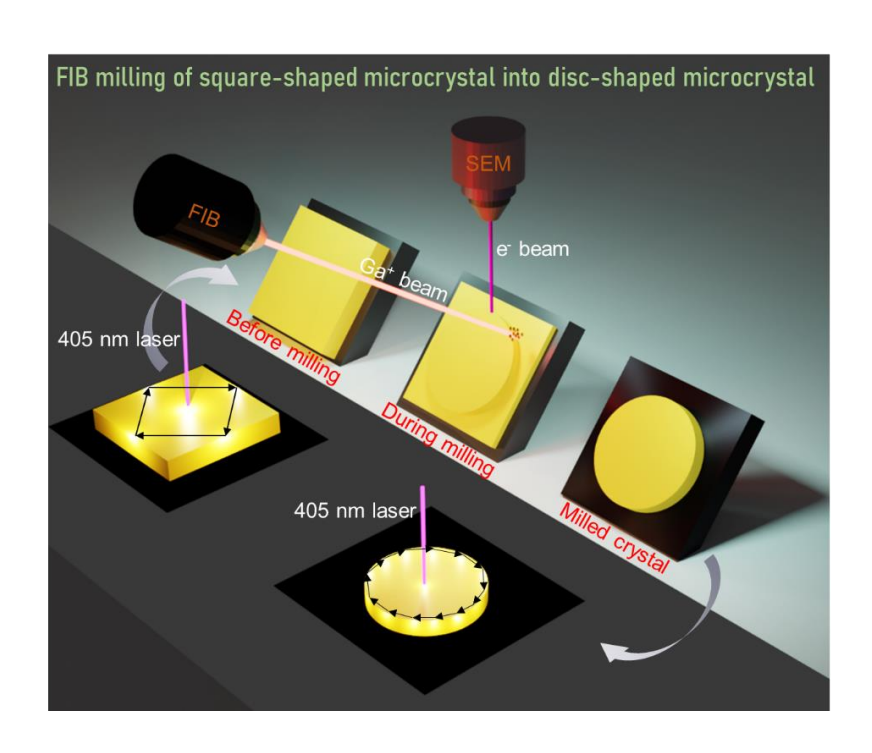
### 2.4. Summary

This chapter demonstrates the preparation of both square-shaped ( $\alpha$ ) and rhombus-shaped ( $\beta$ ) perylene polymorphic optical microresonators via the ambient pressure vapor deposition technique. The single-crystalline  $\alpha$  and  $\beta$  polymorphic microresonators exhibit remarkable nanophotonic capabilities as WGM resonators, which can be activated through both one- and two-photon pumping mechanisms. The FDTD numerical calculations gave insights into the electric field distribution within these microresonators for a particular wavelength. The calculations result strongly support the experimental observations of WGM resonances, confirming their existence. Notably, a fascinating characteristic of the  $\alpha$  and  $\beta$  polymorphic microresonators is the detection of WGMs within the TPL signal, a rarely observed phenomenon in similar systems.

These findings demonstrate the promising potential of these semiconductor-based NLO resonators, which can be efficiently activated by infrared lasers, for the advancement of organic nanophotonic devices. The distinctive properties exhibited by perylene-based microresonators offer new prospects for creating various geometrically different photonic modules using FIB milling suitable for the PICs industry.



Focused Ion Beam Milling of Perylene Singlecrystals: Effects of Substrates, Etchants, and Beam Parameters on Geometrically Precise Organic Photonic Modules



\*This chapter is adapted from:

V. V. Pradeep, R. Chandrasekar\*, <a href="mailto:arXiv:2203.14218v1">arXiv:2203.14218v1</a> [physics.optics], <a href="mailto:Adv. Opt. Mater.">Adv. Opt. Mater.</a> 2022, 10, 2201150, <a href="mailto:doi.org/10.1002/adom.202201150">doi.org/10.1002/adom.202201150</a>. <a href="mailto:V. V. Pradeep, R. Chandrasekar">V. V. Pradeep, R. Chandrasekar</a>, <a href="mailto:Indian Patent Application, E-2/1199/2023/CHE">Indian Patent Application, E-2/1199/2023/CHE</a> (filed) <a href="mailto:Patent Application, E-2/1199/2023/CHE">Patent Corporation Treaty, IN2023/050278</a> (filed).

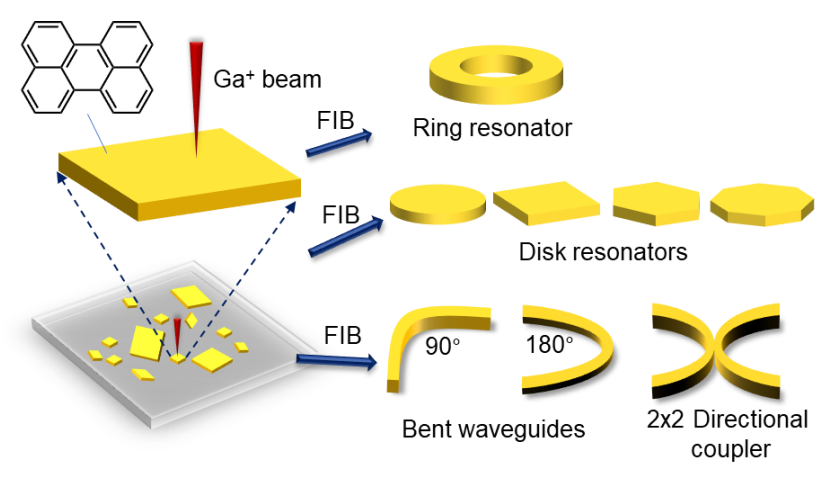
V. V. Pradeep, G. Ummethala, S. R. K. Malladi, \* R. Chandrasekar\* *Cryst. Growth Des.* **2023**, doi.org/10.1021/acs.cgd.3c00653.

### 3.1. Abstract

To create commercially viable all-organic microelectronic and nanophotonic components, highly repeatable manufacture of organic optical crystals with well-defined geometry and dimension is essential. This chapter presents the optimization of focused-ion beam milling parameters, post-processing methods, and the effect of various substrates on the FL intensity of the organic microresonators. This technique can modify the size and shape of square-shaped perylene single-crystal resonators into multiple photonic architectures. The usage of optimized conditions resulted in precisely crafted crystal resonators that exhibit shape- and size-dependent optical modes. This processing method can be used for different organic crystals due to its universality and excellent repeatability to produce optical components suited for commercial nanophotonic device applications.

### 3.2. Introduction

In PICs, the shape and size of microcomponents are the two critical factors that determine photonic device characteristics. Till now, the controllability of microscale shape and size suitable for PICs has been successfully achieved to industrial perfection in silicon and silicon-derivates and group III-V semiconductors using electron-beam-lithography and associated etching processes. [2,164,165] Further, cutting-edge PICs require innovative materials platforms. As a result, the desire to employ molecular organic crystals as optical elements to create all-organic PICs with commercially viable precision manufacturing techniques grows day by day.



**Scheme 3.1.** Fabrication of various micro-optical modules from self-assembled perylene single-crystals using FIB milling.

Herein, this chapter demonstrates the focused Ga ion-assisted milling of perylene microcrystals grown on different substrates (indium tin oxide coated polyethylene terephthalate film, ITO-PET, and borosilicate glass) into various photonic modules. Firstly, the two substrates serve as a medium to explore the effect of conductive and non-conductive layers on microcrystal growth morphology. Secondly, the microcrystals on the substrates were milled using different beam currents to optimize perfect milling parameters for organic crystals. Thirdly, the post-processing methods allowed the retention of FL intensity and resonator activity. Finally, the perylene single-crystal microresonators were micromachined into the desired disk-, ring- and rectangular-shaped optical resonators using FIB milling (Scheme 3.1).

### 3.3. Results and discussion

### 3.3.1. Preparation of perylene microcrystals

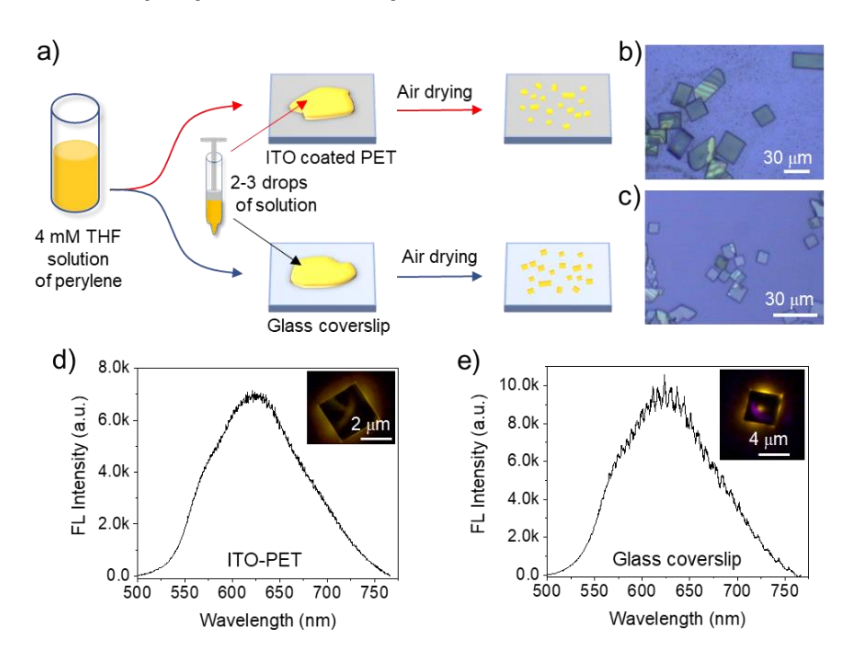


**Figure 3.1.** a) Schematic representation of crystal growth via self-assembly approach on ITO-PET and glass substrate. b,c) Confocal optical microscopy images of perylene microcrystals grown on ITO-PET and glass substrate. d,e) FL spectra of perylene single-crystal grown on ITO-PET and glass substrate, respectively. Insets show the corresponding FL images.

Self-assembly is a bottom-up technique incorporated to attain  $\alpha$ -form perylene microcrystals naturally on a clean coverslip. For this, HPLC grade tetrahydrofuran solution of commercially available perylene (1 mg/1 mL, 4 mM) was prepared, sonicated for 30 s, and kept for 5 min without disturbance. Later, 2-3 drops ( $\approx$ 20  $\mu$ L) of perylene solution were

drop-casted on two different clean substrates, namely, ITO-PET and a borosilicate glass coverslip (Figure 3.1a). As a result of solvent evaporation, square- and rectangular-shaped  $\alpha$ -form microcrystals grow in various sizes. The confocal optical microscope images of microcrystals grown on ITO-PET and glass substrate revealed the square- and rectangular shapes without any significant effect of substrate on growth morphology (Figure 3.1b,c). Optical excitation at the center of the microcrystals with a 405 nm CW laser resulted in a yellow FL (insets of Figure 3.1d,e), and the corresponding FL spectra revealed the resonator activity of these single-crystals (Figure 3.1d,e).

### 3.3.2. Optimization of beam parameters to carve precise photonic architectures

The perylene microcrystals grown on ITO-PET were directly subjected to FIB milling, whereas perylene microcrystals on glass coverslip were coated with a thin layer of gold using the sputter coater before FIB milling. The JEOL JIB 4700F FIB-SEM was used to mill the specified perylene microcrystals into various geometries. The FIB column was 52° inclined from the SEM column.

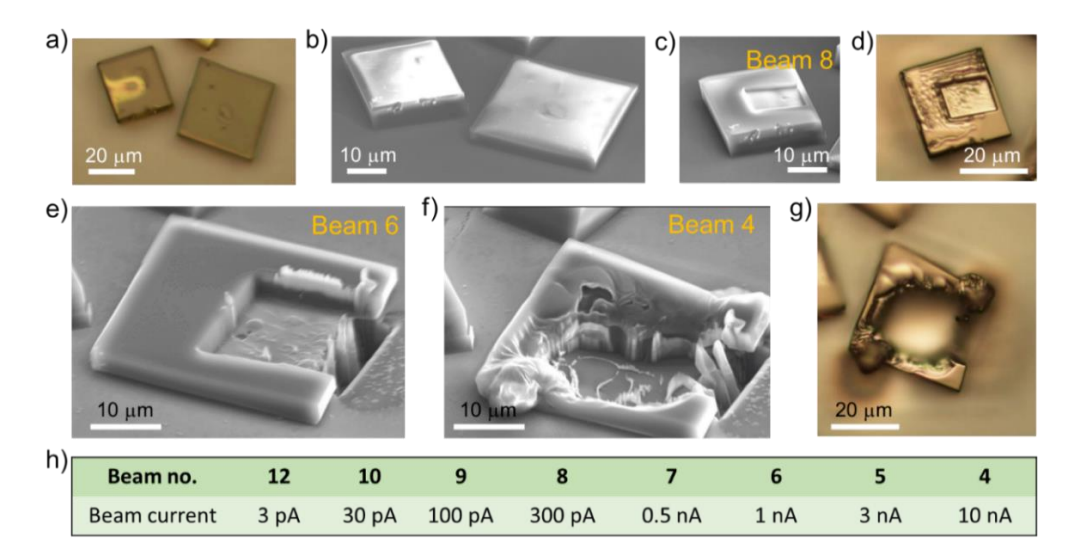


**Figure 3.2.** a) Optical microscope and b) SEM images (tilt view) of selected perylene single-crystals on ITO-PET substrate before FIB milling. SEM images after FIB milling with c) beam 8, e) beam 6, and f) beam 4 corresponding to 300 pA, 1 nA, and 10 nA, respectively. d,g) Optical images of the FIB milled crystals. h) Table representing the beam number and the corresponding beam current.

Initially, using an arbitrary/reference crystal, the field of view alignment for SEM and FIB was carried out, followed by the beam's alignment for various Ga ion beam currents (in this case, beam 12, 8, 6, 5, and 3). Each beam number corresponds to a certain ion beam current (Figure 3.2). To understand the effect of various ion beam currents, two perylene

single-crystals were selected and subjected to three different beam currents: beam 8, 6, and 4 (0.3, 1.0, and 10 nA) (Figure 3.2a,b). The selected crystals were tracked down in SEM and imaged using 5 kV accelerating voltage. Later, the sample substrate was aligned orthogonal to the FIB column, and the imaging was carried out with a beam current of 3 pA (beam 12). Using a focused ion beam (30 kV and beam 8) on one of the crystals for about 15 min, a rectangular trench was made with smooth edges (Figure 3.2c). Further, 2 μm depth rectangular trench milling was performed on another crystal using beam 6, which consumed around 17 min (Figure 3.2e). The crystal edges were smooth, with a minute redeposition near the trench edges. Later, the same crystal was subjected to beam 4 for a rectangular trench for about 5 min, which resulted in an irregular shape with heavy redeposition (Figure 3.2f). The above experiment suggested that lower beam currents produce precise shapes at the expense of higher milling time. Further, the use of higher beam currents caused more damage to the crystals compared to lower beam currents. After FIB-SEM studies, the optical images of milled crystals were taken (Figure 3.2d,g). Hence, beam 6 (1 nA) with 30 kV was chosen as an ideal condition for FIB milling after compromising between the milling time and the desired shape smoothness.

### 3.3.3. Effect of substrates and ion beam current

Imaging a non-conductive sample in the electron or ion microscopes results in static charge accumulation on and around the sample. To avoid the charging of crystals under FIB-SEM conditions, two different substrates were used for microcrystals' self-assembly: (i) on a conductive substrate (ITO-PET) and (ii) on a glass coverslip and then coating with a conductive gold layer. Optical microscopy images of crystals grown on the two substrates exhibited several square- and rectangular-shaped microcrystals of various dimensions (Figure 3.1b,c). Depending on the solvent evaporation rate, the size of the microcrystals varied from  $\approx 5$  to 40  $\mu$ m in length and  $\approx 0.2$  to 6  $\mu$ m in thickness.

The commercially available ITO-PET (Sigma Aldrich, Product no. 639281) was used in these experiments, which has a 72 nm thick ITO coating on a PET (127  $\mu$ m thick) substrate. The refractive index of ITO and borosilicate glass coverslips at 632.8 nm is 1.85844 and 1.51446, respectively. The PET film has a refractive index of about 1.57-1.64, and for organic crystals, it ranges from 1.6 to 1.8.

### 3.3.3.1. Microcrystals on an ITO-PET substrate:

The ITO-PET substrate containing perylene microcrystals was kept in the FIB-SEM setup and scanned using the electron beam (accelerating voltage: 5 kV). Six representative crystals (crystal-I to crystal-VI) on the ITO-PET substrate were selected to fabricate various resonators and waveguides (1st panels, Figure 3.3a-f).

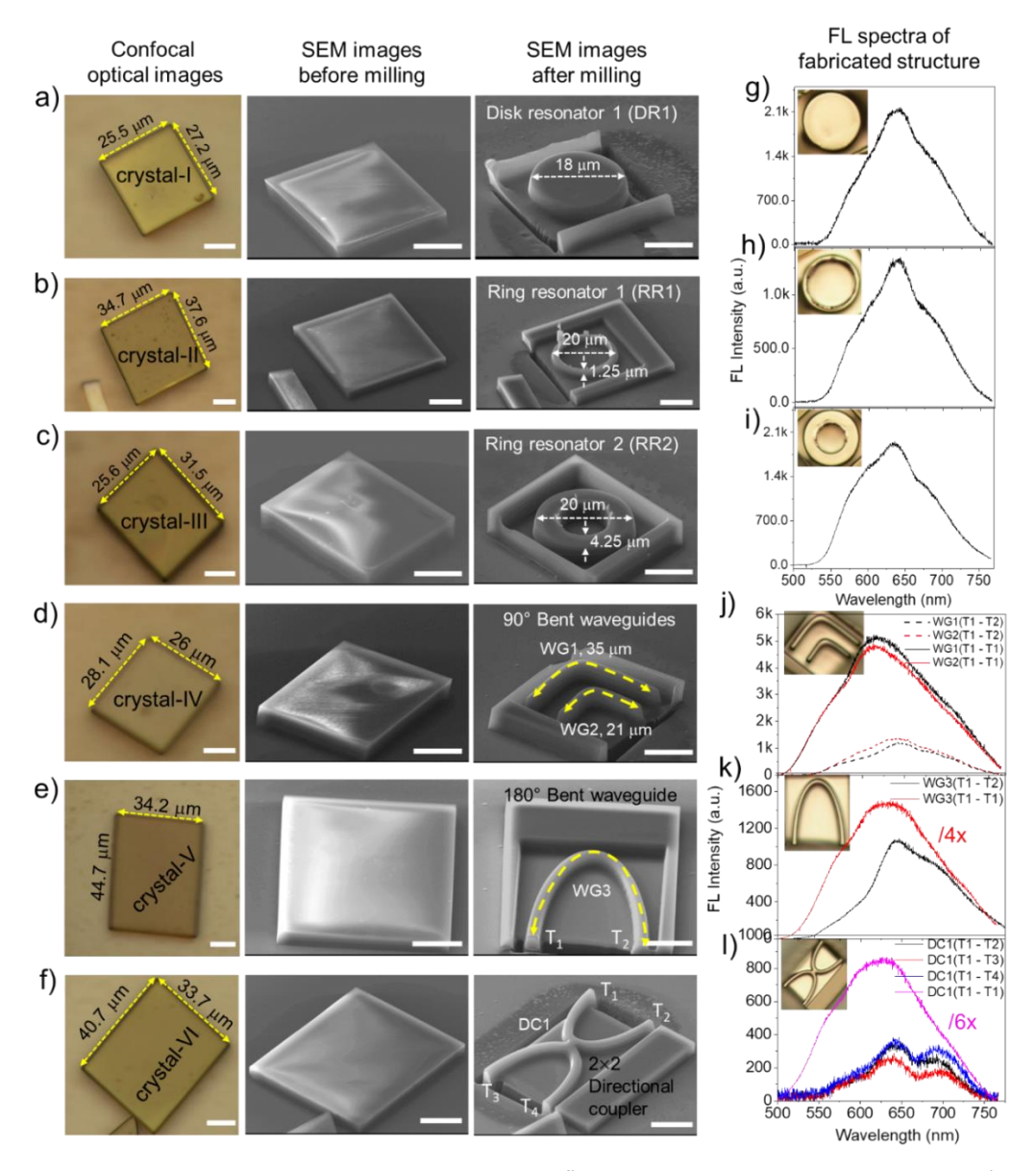


**Figure 3.3.** Perylene crystals on an ITO-PET substrate. a-f) Optical microscope and SEM images (tilt view; before and after milling) of selected perylene microcrystals (namely, crystals-I to -VI). Scale bar 10  $\mu$ m. g-l) The corresponding FL spectra of fabricated microstructures. Here, T1-T2 represents the excitation-detection positions of respective structures. Insets show the corresponding optical images.

To fabricate a circular disk, a 25.5×27.2  $\mu m^2$  perylene single-crystal-I was identified in SEM (2<sup>nd</sup> panel, Figure 3.3a). Using the pre-defined circular shape function (Figure 3.4a)

and the optimized beam parameters (1 nA and 30 kV), the crystal-I was milled into a disk with a diameter of 18  $\mu$ m (3<sup>rd</sup> panel in Figure 3.3a). Similarly, crystal-II (34.7×37.6  $\mu$ m²) and crystal-III (25.6×31.5  $\mu$ m²) were milled into rings having outer and inner diameters of 20, 17.5  $\mu$ m, respectively for ring1 and, 20, 11.5  $\mu$ m, respectively for ring2 (Figure 3.3b,c and Figure 3.4b,c). The confocal micro-spectroscopy studies were performed on the fabricated crystal resonators in a transmission mode geometry. Optical excitation with a 405 nm continuous wave laser (4 mW power, 0.5 s integration time, and ten accumulations) generated a yellowish FL at the excited position and outcoupled at the circular periphery. The FL spectrum collected at the periphery revealed a bandwidth of ≈525-775 nm (Figure 3.3g-i).

To fabricate the waveguides, perylene single-crystal-IV to crystal-VI were identified (1st panels, Figure 3.3d-f). The crystal-IV was milled (beam 6 and 30 kV) to fabricate two 90° bent waveguides (WG1 and WG2) of lengths 35 and 21  $\mu$ m, respectively (3rd panel, Figure 3.3d and Figure 3.4d). Similarly, crystals-V and -VI were milled to achieve a 180° bent waveguide (WG3) of length 65.8  $\mu$ m and a 2×2 directional coupler (DC1) (3rd panels in Figure 3.3e,f and Figure 3.4e,f). The optical waveguiding nature of the milled waveguides was established from the controlled excitation of a portion of milled waveguides with a 405 nm continuous wave diode laser.

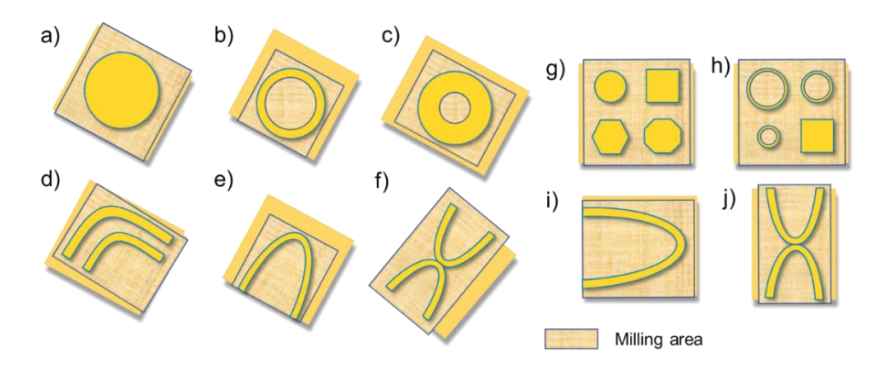


**Figure 3.4.** Bitmap images used for fabricating disk resonators, ring resonators, bent waveguides, and directional coupler of perylene single-crystals on a-f) ITO-PET and g-j) glass substrates.

Initially, excitation of the left terminal of WG1 resulted in the generation of yellowish FL ( $\approx$ 500-775 nm collected using a 150× objective), and the same light propagated towards the other end of the waveguide as a reabsorbed signal due to overlap of perylene's FL with its absorption spectrum ( $\approx$ 540-775 nm, Figure 3.3j). The WG2 also exhibited similar waveguiding properties. However, the outcoupled FL intensity was higher in WG2

compared to that in WG1 due to the smaller optical propagation path in the earlier. Similarly, excitation of the left end of WG3 and the subsequent detection at the right end exhibited an FL band covering from 550 to 775 nm region (Figure 3.3k). To study the optical signal propagation in DC1, one of the termini (T1) of DC1 was optically excited; it resulted in an FL ranging from 525-775 nm (Figure 3.3l). As expected from the DC's geometry, the FL signal was detected at T2 and T4. Usually, in traditional DCs, no signal is observed at T3 due to circuit geometry; however, an optical signal at T3 was detected, possibly due to a wider cross-section at the junction or back reflection of the light from T4 (3<sup>rd</sup> panel, Figure 3.3f). The different line shapes in the spectra at T1 to T4 can be attributed to molecular anisotropy exhibited by perylene crystals.<sup>[88]</sup>

### 3.3.3.2. Microcrystals on a glass substrate:

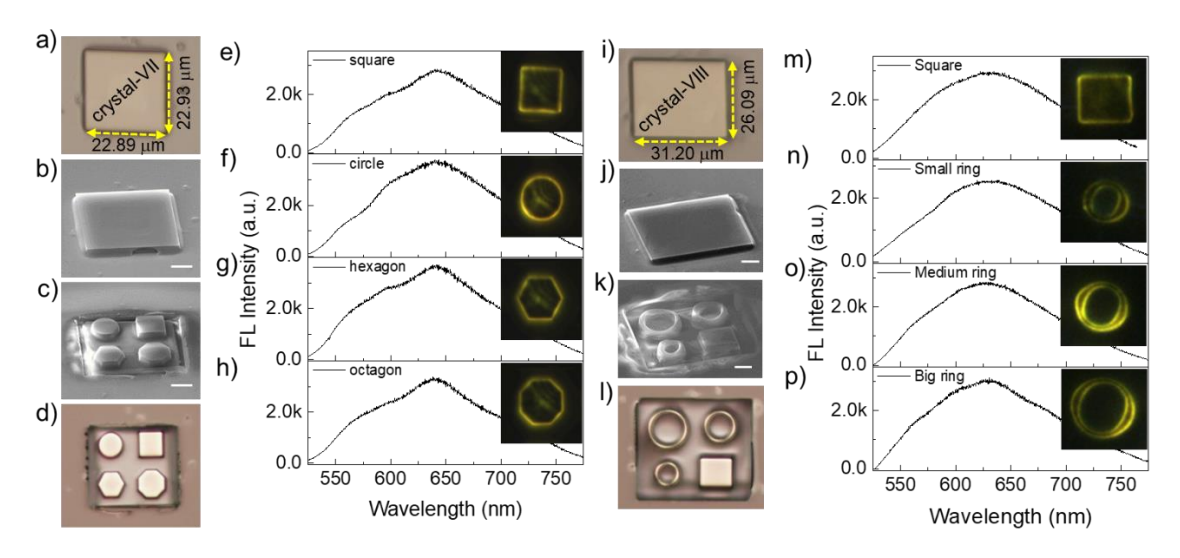


**Figure 3.5.** Perylene crystals on a glass substrate. a,i) Optical microscope and b,j) SEM images (tilt view) of selected perylene single-crystals (crystal-VII and -VIII). c,k) SEM (tilt view) and d,l) optical microscope images of FIB milled selected perylene single-crystals (crystal-VII, and -VIII) into various shaped resonators. e-h,m-p) The corresponding FL spectra of fabricated resonators. Insets show the FL images. Scale bar 5 μm.

The glass substrate containing gold-coated microcrystals was examined through SEM, and four representative crystals were selected, namely crystal-VII, -VIII, -IX, and -X. To fabricate four microdisks of different geometries (circular, square, hexagonal, and octagonal), all on a gold-coated *single* perylene crystal, crystal-VII with a large surface area (22.89×22.93  $\mu$ m²) was selected (Figure 3.5a,b). Importantly, as the crystals were gold coated, direct Ga<sup>+</sup> exposure to the crystal was minimal while imaging and adjusting the imported bitmap (of four resonators, Figure 3.4g) in the FIB window.

The milling duration was around 47 min to achieve four resonator geometries of dimensions 6.9  $\mu$ m (diameter, circle), 6.9  $\mu$ m (edge length, square), 4.1  $\mu$ m (edge length, hexagon), and 3.3  $\mu$ m (edge length, octagon) when optimized beam parameters (30 kV; beam current of 1 nA) were employed (Figure 3.5c,d). Similarly, the crystal-VIII of surface area 31.20×26.09  $\mu$ m² (Figure 3.5i,j) was milled into three ring-shaped and a square-shaped resonator (Figure 3.5k,l). The outer/inner diameters of the obtained ring resonators were 10.8/9.2  $\mu$ m (big ring), 8.65/7.2  $\mu$ m (medium ring), and 6.3/5.4  $\mu$ m (small ring). The fabricated resonator geometries were washed with Lugol's iodine solution to remove the gold layer after successful FIB milling (discussed in detail in section 3.3.4). The confocal micro-spectroscopic studies were performed on these milled polygonal and ring-shaped crystals by exciting their central region with 405 nm (power of 4 mW). As a result, the milled crystals revealed a yellow FL (525-775 nm, Figure 3.5e-h,m-p) at the excitation point and bright FL at the crystal's periphery indicating light confinement (insets of Figure 3.5e-h,m-p). In particular, the inner and outer circular periphery of the rings were clearly visible due to the production of high FL.

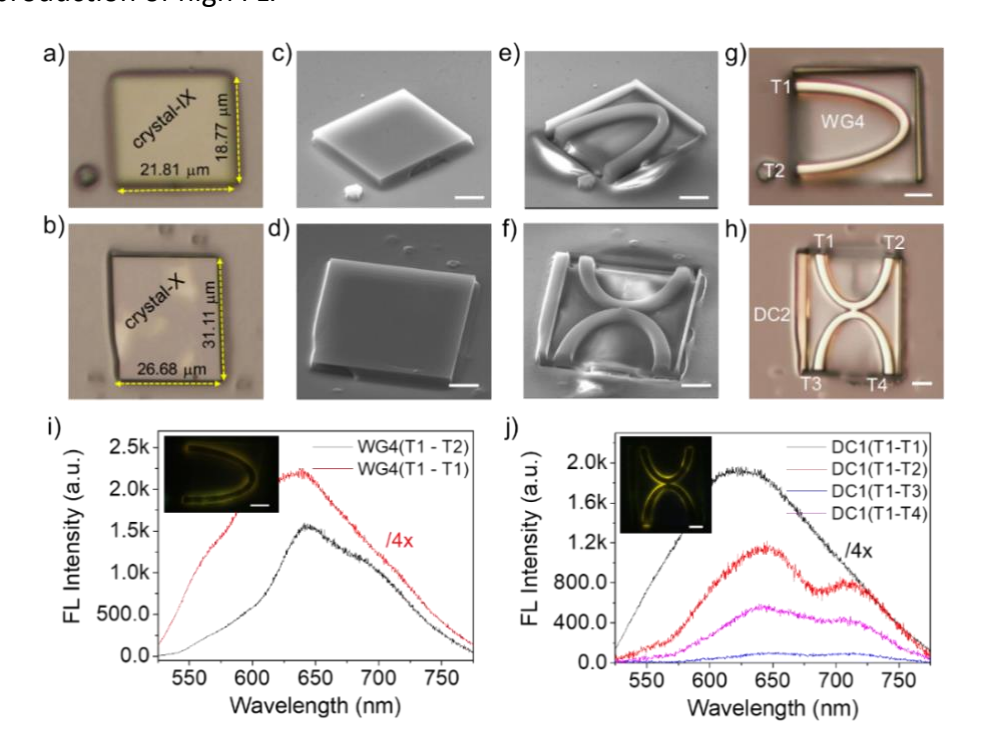


**Figure 3.6.** Perylene crystals on the glass substrate. a,b) Optical microscope and c,d) SEM images (tilt view) of selected perylene single-crystals (crystal-IX and crystal-X). e,f) SEM (tilt view) and g,h) optical microscope images of FIB milled selected perylene single-crystals (crystal-IX and crystal-X) into WG4 and DC2. i,j) The FL spectra of the fabricated WG4 and DC2. Here T1-T2 represents the excitation-detection positions of respective fabricated geometries. Insets show the corresponding FL images. Scale bar 5 μm.

To fabricate the bent waveguide and the DC from the self-assembled perylene single-crystals on a glass substrate, crystal-IX, and crystal-X were identified (Figure 3.6a-d). The crystal-IX of dimensions:  $21.81\times18.77~\mu m^2$  was milled into a U-shaped waveguide (WG4) with a  $180^{\circ}$  bent using beam 6 and 30 kV accelerating voltage (Figure 3.6e,g). Similarly, the crystal-X (dimensions:  $26.68\times31.11~\mu m^2$ ) was carved into a  $2\times2$  directional coupler (DC2) (Figure 3.6f,h). The photonic studies were performed on the fabricated WG4 and the DC2 using the same confocal optical microscope in the transmission mode setup. Optical excitation of terminal T1 of WG4 with a 405 nm laser generated a yellowish FL (475-775 nm, red line in Figure 3.6i) and was propagated towards terminal T2. The FL spectrum recorded at the terminal T2 of WG4 (150× objective with an integration time of 0.5 s and for ten accumulations) showed suppression of a part of the FL band due to the reabsorption (black line in Figure 3.6i).

Similarly, the excitation of terminal T1 of DC2 showed propagation of FL to the other three termini, T2, T3, and T4 (Figure 3.6j). Ideally, there should not be any output in terminal T3, but the joint of the DC is wide enough to allow the propagation of some light to T3. Compared to the DC on ITO-PET, the FL intensity on the coverslip was relatively high (more than double). This is because the crystals on ITO-PET were directly exposed to the Ga ion beam during milling, whereas the crystals on the coverslip were protected with a gold layer; hence the damage was minimal in the case of gold-coated crystals.

### 3.3.4. Post-processing methods

The protective layer (gold) from the microcrystals and the substrate can be removed by a gold etchant which does not react with organic crystals. This work followed two methods: viz. washing with Lugol's iodine solution (method-1) and exposure to HCN vapors (method-2).

Method-1: Lugol's Iodine solution was prepared using 10 g of potassium iodide, 5 g of iodine, and 100 ml of distilled water. The glass substrate containing FIB-milled microcrystals was placed in a petri dish, and the freshly prepared Lugol's iodine solution was added gently via the walls. The substrate was allowed to soak for about a minute, and then the solution was pipetted out using a dropper, followed by distilled water wash (Figure 3.7a-f).

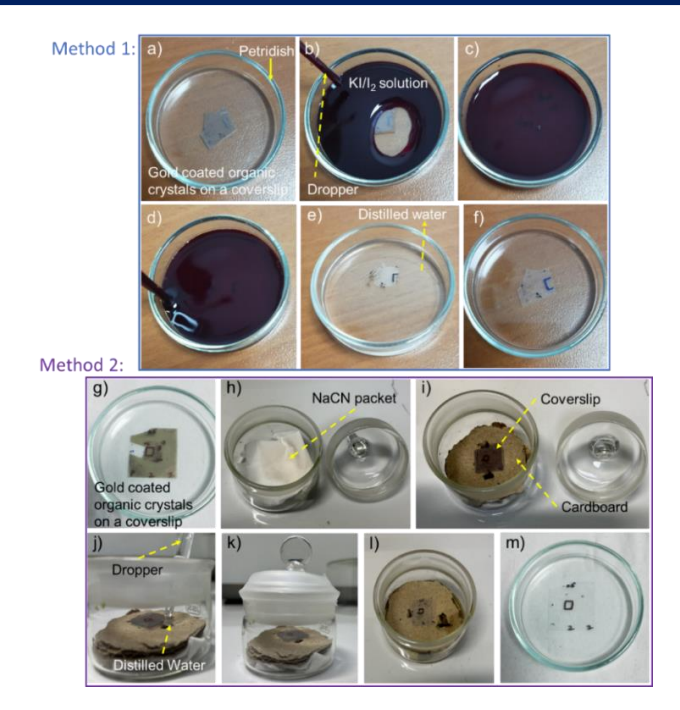


**Figure 3.7.** Photographs showing the gold removal using a-f) Lugol's iodine solution and g-m) HCN vapors, respectively.

Method-2: This procedure involves the generation of highly toxic vapors; hence the complete process was carried out in a fume hood. Initially, 1 g of NaCN was placed on the tissue paper and made into a packet. Later, the pack was placed in the glass container, and a cardboard having 2-3 holes was placed over it. The gold-coated substrate (FIB milled microcrystals containing coverslip) was gently placed on the cardboard. Finally, 3-4 drops of water were added through the holes of the cardboard, and the glass container was closed using the lid and tightly sealed using parafilm tape (Figure 3.7g-m). The added water droplets react with NaCN, resulting in the generation of HCN vapors. These vapors slowly react with the gold layer on the substrate. Within a day, the gold layer was completely reacted with NaCN, and the formed AuCN was settled on the coverslip. Finally, the gold-layer free microcrystals containing substrate was obtained after washing with distilled water.

### 3.3.5. Effect of beam current on FL intensity and optical modes of resonators

The FL intensity after milling into pre-defined architectures is relatively low, and most importantly, there is no signature of optical resonances (Figure 3.3g-i, Figure 3.5e-h,m-p). It is essential to mention that the crystal that was chosen for milling and the beam current need to be further optimized to retain the FL from the milled crystal. Though the

higher ion dose accelerates the milling process, it also causes undesirable amorphization of the crystal surface and deep ion implantation (turning the area black), instigating FL quenching and uneven n of the crystal. The milling resolution depends on the ion beam diameter, and the beam current control the latter. The smaller the current, the higher the milling resolution that can be attained to mill only the targeted areas. To perform this optimization, FIB milling was carried out on Thermo Scientific SCIOS 2 Dual Beam instrument, and pre-defined shapes in the software, like circles and rectangles, were used.

### 3.3.5.1. Fabrication of disk resonators using 0.4 nA beam current:

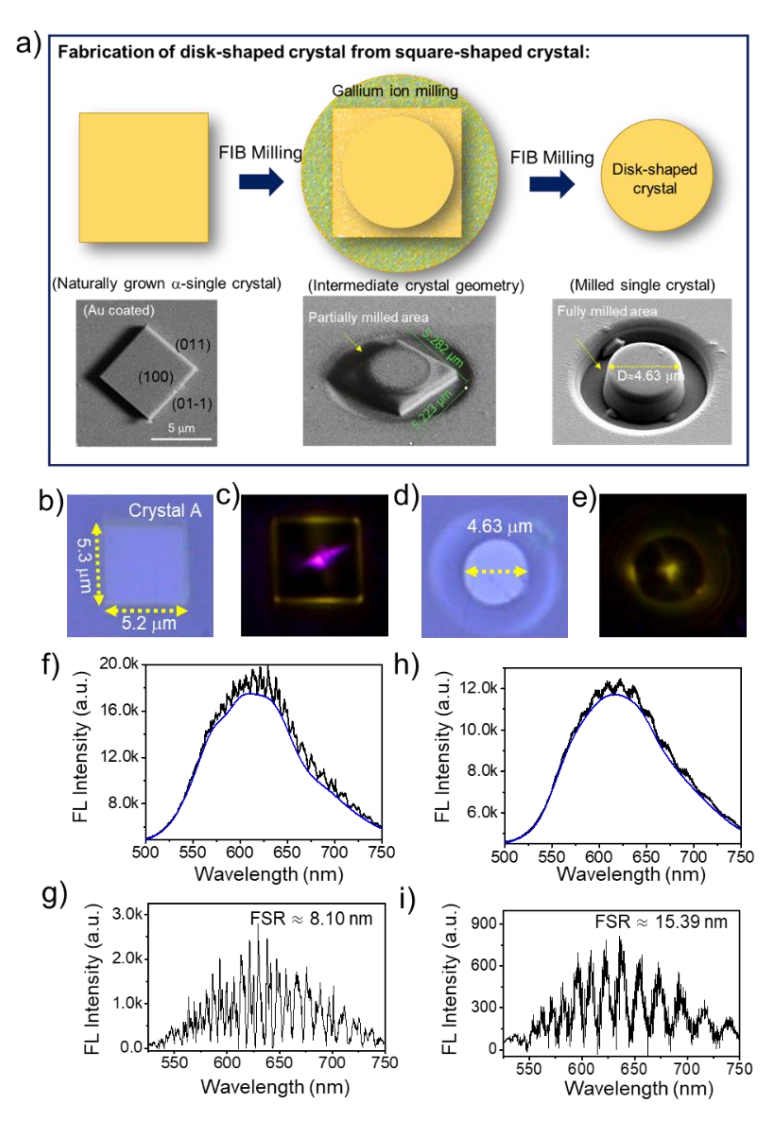


**Figure 3.8.** a) Schematic of FIB milling of naturally grown square-shaped perylene single-crystal A into a circular disk shape. The corresponding FESEM images of crystal before and after milling are shown below the graphics. b,d) Confocal optical microscopy and c,e) FL images of a square-shaped perylene single-crystal A and fabricated circular disk resonator, respectively. The corresponding f,h) FL spectra and g,i) the background-subtracted FL spectra displaying optical resonances in crystal A before and after FIB milling, respectively.

The acceleration voltage was maintained at 30 kV, whereas the beam current was reduced from 1 nA to 0.4 nA. Two perylene single-crystals, A and B, grown on glass coverslip were identified and subjected to FIB milling. The shape of the selected perylene single-crystals A and B was precisely converted to circular- and rectangular-shaped geometries, respectively, with size reduction (Figure 3.8a and 3.9a).

A nearly square-shaped ( $\approx$ 5.2×5.3 µm²) perylene single-crystal A was selected (Figure 3.8b). The major crystal facets were found to be (100), (011), and (01-1). Firstly, the single-particle micro-spectroscopy experiments were performed in a transmission mode geometry to determine the resonator characteristics of the selected single-crystals. When crystal A was excited on the (100) facet (Excitation: 0.05 mW; objective:  $60\times$ ), it displayed a bright yellow FL at its four (011), (01-1), (0-1-1) and (0-11) facets (Figure 3.8c). The recorded FL at one of the edges displayed a broad spectrum covering the bandwidth of  $\approx$ 525-775 nm region exhibited a series of pairs (transverse magnetic, TM; and transverse electric, TE) of sharp peaks indicating WGM resonances (Figure 3.8f).

The background-subtracted FL spectra displayed optical modes, and the FSR value was found to be  $\approx 8.10$  nm (Figure 3.8g). The resonator characteristics of the square-shaped perylene crystal shown in the FESEM image arise due to multiple circulations by the crystal's four-light-reflective facets. Later, the crystals containing substrate was gold coated, and milling was performed orthogonal to (100) facet using a gallium ion beam (30 kV and 0.4 nA) to attain a circular disk of diameter 4.63  $\mu$ m (Figure 3.8a,d). The down panel of Figure 3.8a shows the FESEM images of the crystal before, during, and after milling. The gold coating on the sample was removed by washing it with a gold etchant (Lugol's iodine solution). Photonic experiments on the circular disk resonator exhibited an intense FL spectrum supporting relatively broad optical modes with an FSR of 15.39 nm (Figure 3.8h,i). The number of optical modes depends on the geometry and size of the resonators. From the circular shape of the crystal, it is evident that these optical modes occur due to WGM resonances.

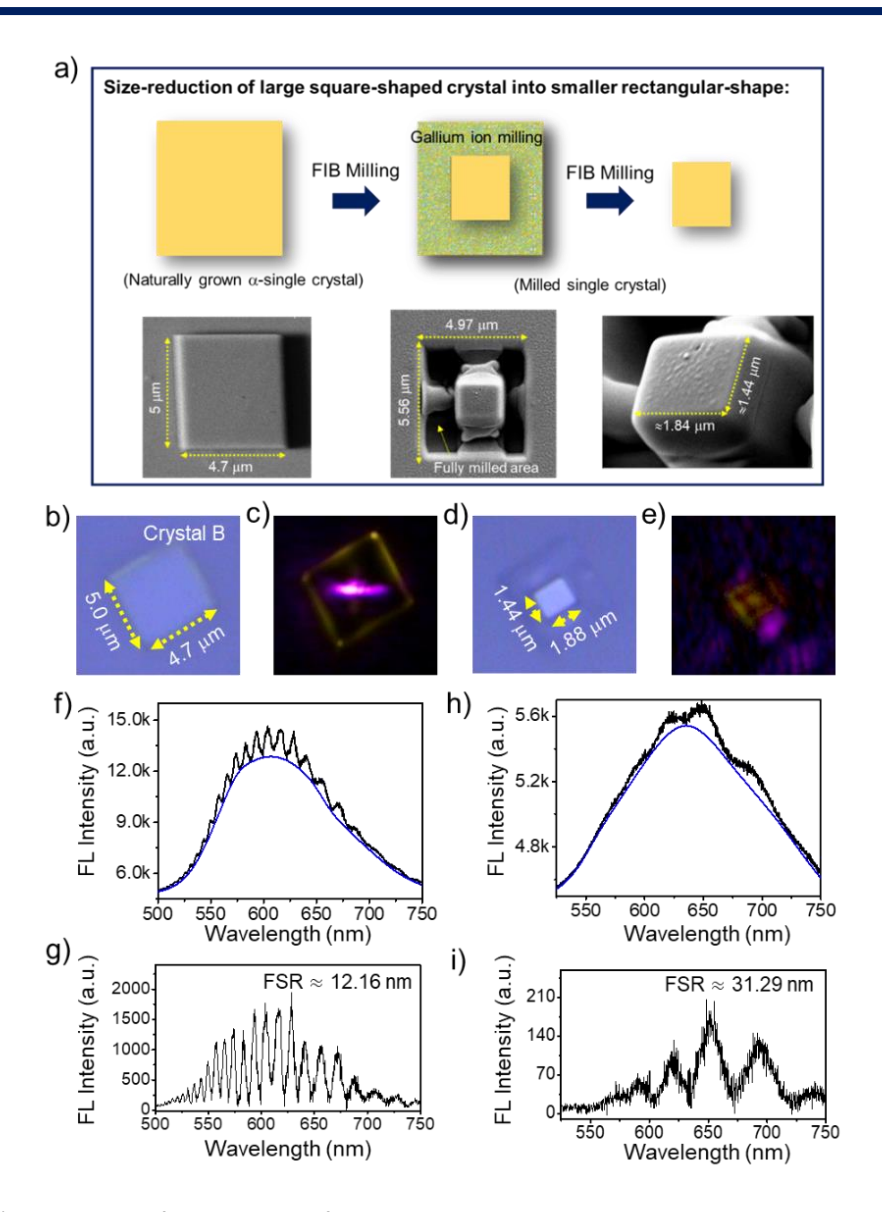


**Figure 3.9.** a) Schematic of FIB milling of naturally grown square-shaped perylene single-crystal into a rectangular disk shape. The corresponding FESEM images of crystal before and after milling are shown below the graphics. b,d) Confocal optical microscopy and c,e) FL images of a square-shaped perylene single-crystal and fabricated rectangular disk resonator, respectively. The corresponding f,h) FL spectra and g,i) the background-subtracted FL spectra displaying optical resonances in crystal B before and after FIB milling, respectively.

Similarly, crystal B of dimensions  $\approx 5 \times 4.7 \ \mu m^2$  displayed optical resonances in FL spectra when subjected to a 405 nm laser (power: 0.05 mW), and the FSR value was found to be 12.16 nm (Figure 3.9b,c,f,g). Milling the crystal into a smaller rectangular crystal of dimensions 1.84×1.44  $\mu m^2$  and subsequent optical experiments display relatively broader modes with an FSR of 31.29 nm (Figure 3.9d,e,h,i). The increase in the full-width-at-half-

maximum of FP modes and FSR values are in line with the inverse relationship of FSR with the resonator dimension.

### 3.3.5.2. Fabrication of disk resonator using 0.1 nA beam current:

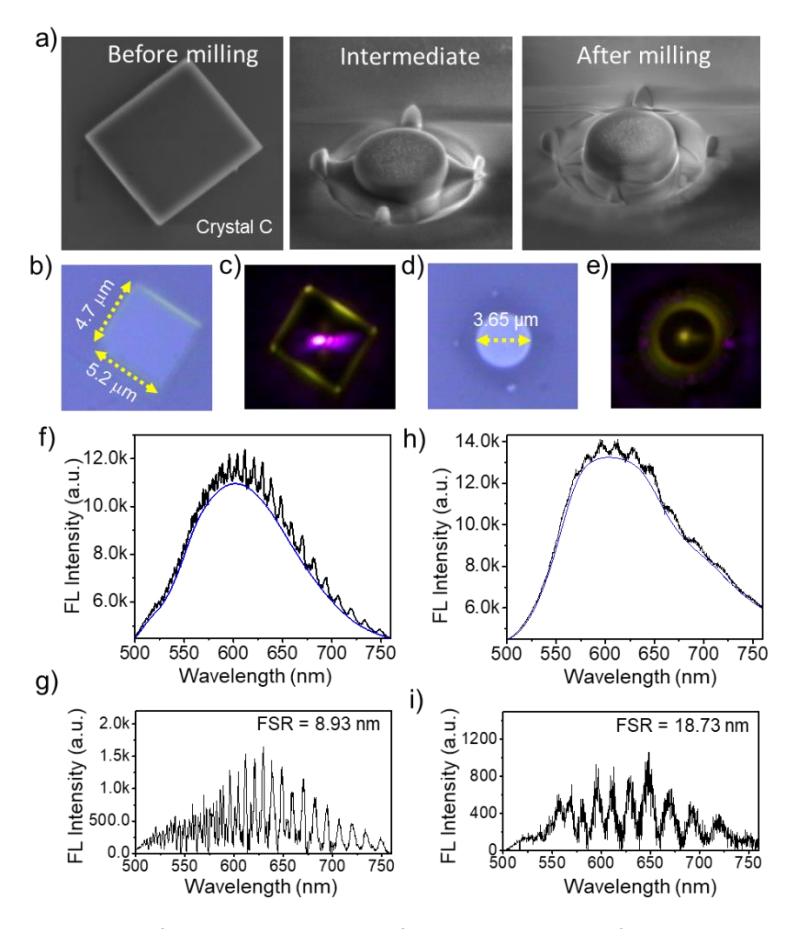


**Figure 3.10.** a) SEM images of the microcrystal before, during, and after milling. b,d) Confocal optical microscopy and c,e) FL images of a square-shaped perylene single-crystal C and fabricated circular disk resonator, respectively. The corresponding f,h) FL spectra and g,i) the background-subtracted FL spectra displaying optical resonances in crystal C before and after FIB milling.

The beam current was further reduced to 0.1 nA to fabricate another circular-shaped disk-resonator (Figure 3.10a). For this, crystal C of dimensions  $\approx 4.7 \times 5.2~\mu\text{m}^2$  was selected, and photonic experiments were carried out with 0.05 mW power (405 nm continuous-wave laser), resulting in optical modes with FSR 8.93 nm (Figure 3.10b,c,f,g). The selected crystal was subjected to FIB milling with a lower (0.1 nA) beam current for the same accelerating voltage (30 kV). These parameters increased the milling time; further, the resultant circular disk-shaped crystal of diameter 3.65  $\mu$ m showed brighter FL with low laser pump power (2 mW) (Figure 3.10 d,e). This observation is in line with the amorphization reduction as the Ga ion exposure on the unmilled crystal area is minimal. As expected, the

subsequent optical experiments on the fabricated disk resonator exhibited broader optical modes (FSR 18.73 nm) in the FL spectrum (Figure 3.10h,i).

### 3.3.6. Position-dependent FL studies on fabricated disk resonator

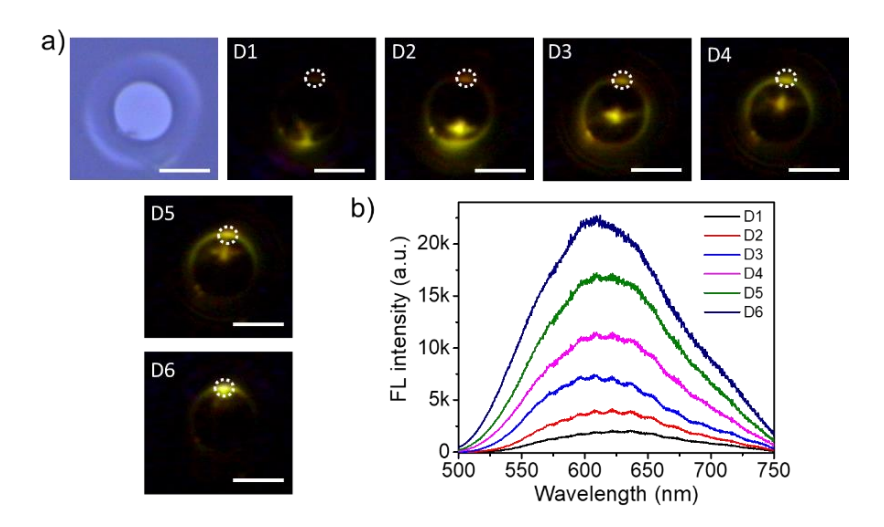


**Figure 3.11.** a) Bright and dark field confocal optical microscopy images of fabricated resonator when excited with a 405 nm continuous-wave laser at different positions. The white dotted lines represent the detection position. Scale bar 4  $\mu$ m. b) The corresponding FL spectra for an input power of 4 mW.

To study the excitation-position-dependency on the FL spectra, the fabricated circular disk resonator was excited at six different places (D1 to D6 in Figure 3.11a) using a 4 mW laser pump power. The FL spectra were collected at constant position (D6) for all excitation positions. As the distance between the excitation and collection position narrows down, the intensity of FL spectra increased (Figure 3.11b). This is in line with the fact that the optical loss increases with increased propagation distance.

### 3.3.7. Pump-power-dependent studies on fabricated disk resonator

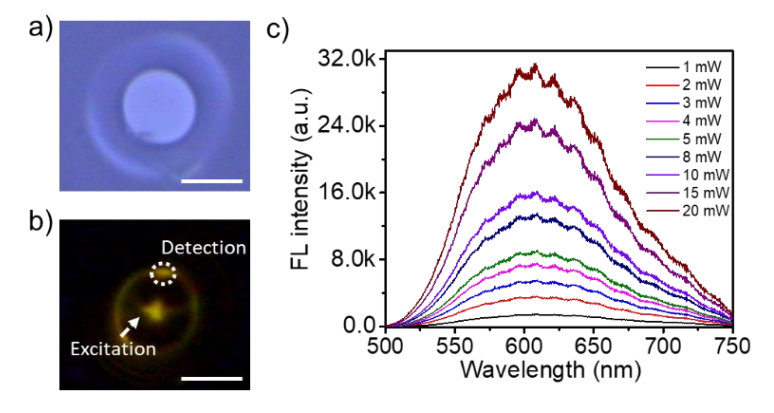


**Figure 3.12.** a) Confocal optical microscopy and b) FL images of fabricated circular disk resonator. Scale bar 4  $\mu$ m. c) The corresponding FL spectra with various pump powers.

The influence of pump power was studied to understand the stability of the fabricated circular disk resonator. Initially, it was excited at the center, and the spectrum was collected at the periphery using a power of 1 mW (Figure 3.12a,b). Further, the pump power was increased to 2, 3, 4, 5, 8, 10, and finally, 20 mW. As expected, the FL intensity increased by increasing the pump-power, and interestingly, the disk resonator was stable even at high pump-powers (Figure 3.12c).

### 3.3.8. FL imaging and mapping of disk resonators

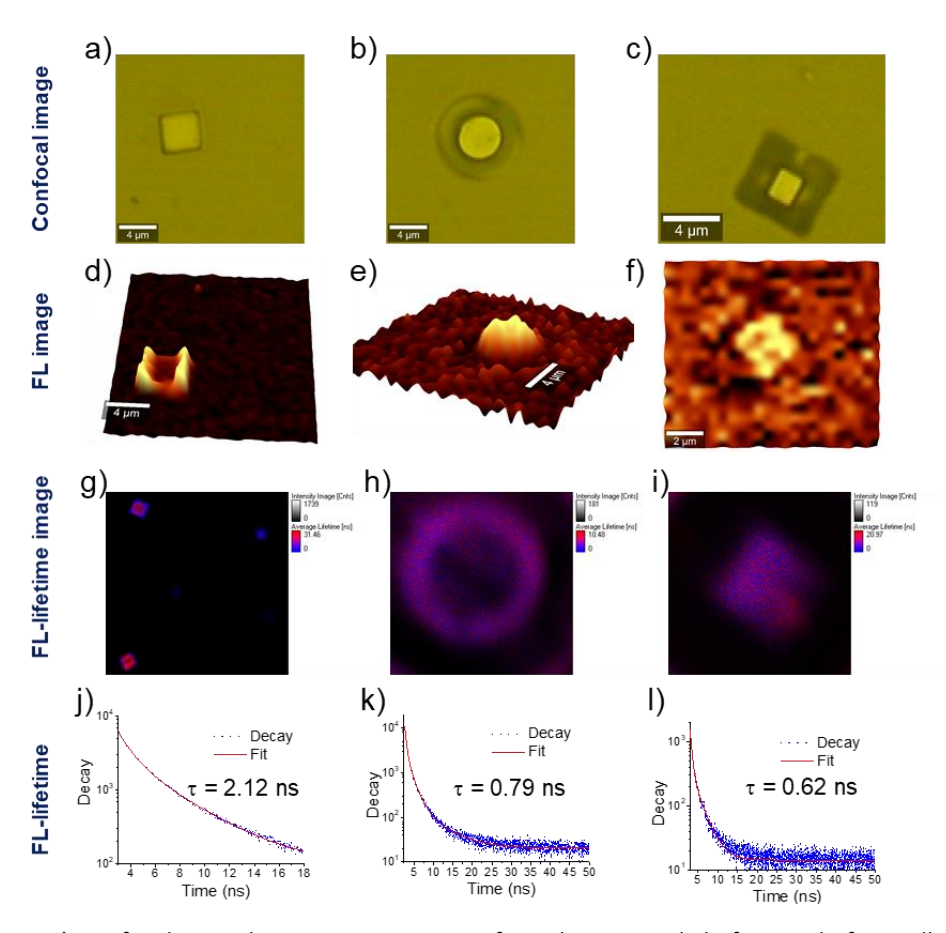


**Figure 3.13.** a-c) Confocal optical microscopy images of perylene crystals before and after milling. d-f) The corresponding FL images. g-i) FL lifetime images of perylene crystals before and after milling. j-l) The corresponding FL lifetime decay plot with estimated average lifetime values.

The images of FL and FL-lifetime of perylene crystals before and after gallium ion milling are shown in Figure 3.13. The FL images show that the milled crystals exhibited nearly uniform intensity distribution within the crystal (Figure 3.13d-f). The fabricated circular disk showed a well-resolved FL lifetime image with a high FL signal from the rim due to circumnavigating light at the crystal-air interface. On the other hand, a nearly equal

spread of FL was observed for the fabricated rectangular disk. Unlike ordinary crystals, the lifetime values of crystal resonators are different as the resonator's Q-factor determines the photon lifetime (trapped light) of the FL within the crystal by the relation,  $Q \approx \tau_p$ . The average lifetime decay values of milled crystals are slightly lowered compared to before milling (Figure 3.13 g-I).

### 3.3.9. Fabrication of geometrically and dimensionally precise ring resonator

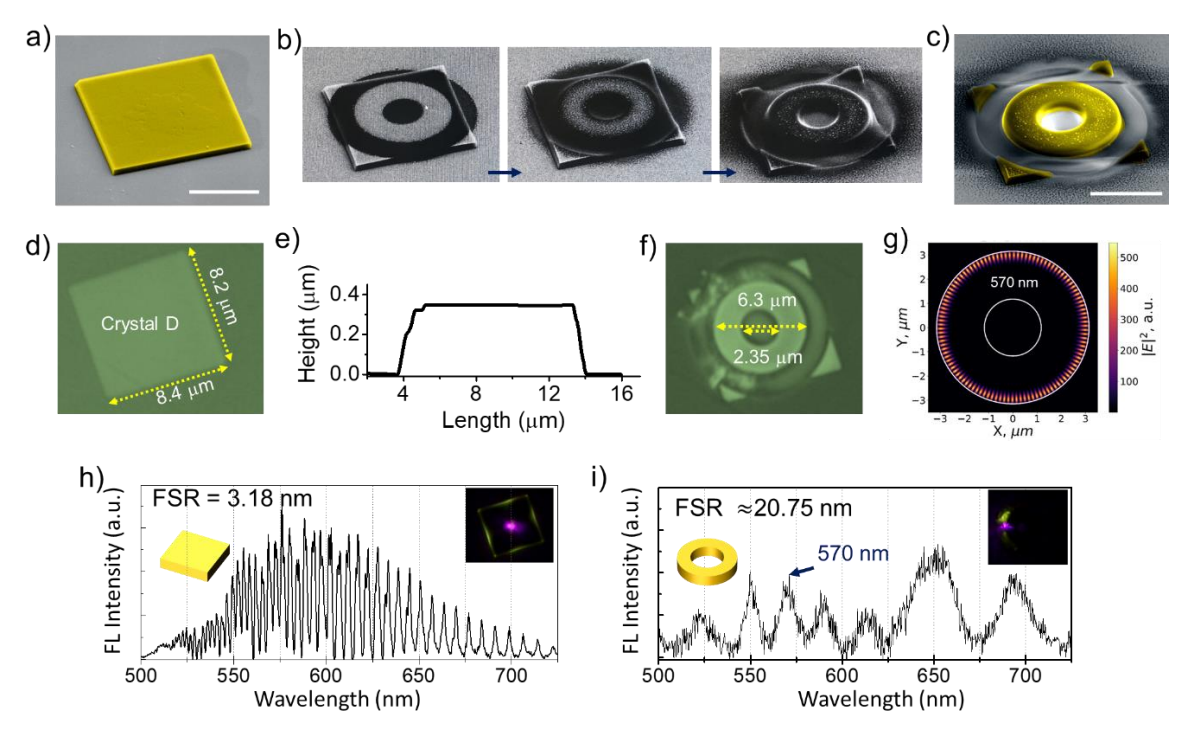


Figure 3.14. a,c) The color-coded FESEM images of perylene microcrystal before and after milling into a ring resonator. Scale bar 4  $\mu$ m. b) Series of screenshots taken during FIB milling. d,f) Confocal optical microscopy images of perylene microcrystal before and after milling into a ring resonator. e) Height profile of the selected microcrystal measured using AFM. FDTD calculations displayed g)  $|E_z|^2$  distribution for the 570 nm mode in the ring resonator. h,i) The FL background subtracted spectra of perylene microcrystal before and after milling. Insets show the graphical and FL images.

Attaining a ring-shaped microcrystal with specific dimensional requirements via crystal growth techniques like crystallization, self–assembly, sublimation, etc., is practically not possible. Hence, a naturally grown single perylene crystal D (dimensions  $8.4\times8.2~\mu\text{m}^2$ ) was selected to obtain a ring geometry of the desired size via FIB milling. The gold-coated crystal D was milled into a ring-shaped geometry with outer and inner diameters of 6.3  $\mu$ m and 2.35  $\mu$ m, respectively (Figure 3.14a,c). The sequential carving of perylene microcrystal into a ring resonator was performed using FIB milling (30 kV and 100 pA, Figure 3.13b). The

color-coded FESEM and the optical microscope images of the ring-shaped perylene crystal showed smooth crystal surface morphology (Figure 3.14c,f).

Before milling, the photonic studies on crystal D revealed the WGM-type resonator effect with an FSR of 3.18 nm (Figure 3.14h). Contact mode AFM exhibited the smooth surface of microcrystal, and the thickness is about 0.35  $\mu$ m (Figure 3.14e). After the removal of the gold coating, the ring resonator was excited with a 405 nm continuous wave laser, and the FL spectrum was recorded at the outer convex periphery. The FL spectrum revealed relatively broad optical modes having an FSR of 20.75 nm, signifying the resonator characteristics (Figure 3.14i). Later, FDTD numerical calculations revealed that the electric field distribution ( $|E_z|^2$ ) of the trapped light (for example, 570 nm optical mode) is predominantly confined at the outer periphery of the ring resonator (Figure 3.14g). The ring resonator modes look like modes of disk resonators with the same diameter, as the inner diameter of the ring resonator is too small to influence electric field distribution.

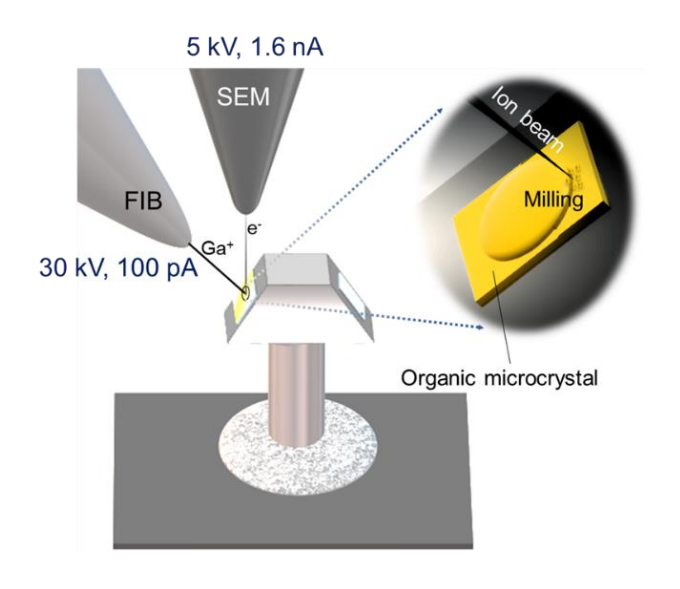
### 3.4. Conclusions

In summary, FIB milling has been employed to carve perylene single-crystal resonators into different geometries and sizes. The effects of various substrates, namely, ITO-PET and glass coverslip, and post-processing techniques (removal of the gold layer) were demonstrated. The fabrication of disk-, rectangular- and ring-shaped photonic resonators is a proof-of-principle experiment that can also be applied to other molecular crystals. The following points are pertinent for successfully milling FL organic crystals while retaining their optical emission intensities and n homogeneity. Milling parameters and crystal thickness need to be appropriate to minimize the amorphization of the exposed crystal surface. Thinner crystals take less milling time than thicker ones as the molecular mass to be removed around the crystal is less. This minimizes Ga ion exposure to the unmilled crystal area. Further, lowering the beam current reduces beam spot size, providing higher milling focus and minimizing ion exposure to unmilled crystal area. Thicker gold coating (30 – 40 nm) not only helps as a conductive layer for SEM imaging but also protects the crystal surface from the Ga ion beam. FIB-based secondary-ion imaging of crystals during milling should be avoided to lessen the ion implantation on the crystal surface. Such cases change the n within the crystal inconsistently.

The presented technique can be used directly to fabricate circular-, rectangular-, ring-, rod-shaped, and any other possible geometries required to create photonic modules such as resonators, waveguides, lasers, interferometers, gratings, couplers, modulators, photonic crystals, and circuits. As the geometry and dimension of the molecular crystals can be precisely controlled down to the microscale, this technique can also be applied to the industrial-scale production of organic crystal photonic modules for PICs.



# Geometrical Shaping of Coumarin-153 Single-crystals into Next-Generation Organic Optical Resonators



### 4.1. Abstract

This chapter unravels the generality of FIB milling and post-processing techniques on an organic molecular crystal, namely, 2,3,6,7-Tetrahydro-9-(trifluoromethyl)-1H,5H,11H-[1]benzopyrano(6,7,8-ij)quinolizin-11-one (coumarin-153). FIB micromachining of self-assembled/sublimed coumarin-153 single-crystals results in pre-defined circular and rectangular-shaped microcrystals with geometrical and dimensional precision. The employed ion beam parameters are 30 kV and 100 pA. The photonic studies on shaped microcrystals revealed optical traits without post-processing and can be attributed to the large photoluminescence quantum yield (17%) of coumarin-153 microcrystals. The FDTD numerical calculations support the electric field distribution in these optical resonators. The demonstrated FIB milling technique enables industrial-scale production of optical components, circuits, and devices.

### 4.2. Introduction

To meet the industrial PICs standard, there is an urge to generalize the FIB milling technique on organic-based materials that offers precise cutting and shaping of organic microcrystals into desired shapes and sizes without affecting the photonic traits. Most notably, the time to prototype is much shorter and far more precise in FIB milling than in other lithography methods. However, the details about universalizing this technique for chemically different organic microcrystals are not yet explored.

Therefore, this work presents the generality of the FIB milling and processing techniques for another molecular crystal, namely bright-green-FL *2,3,6,7-Tetrahydro-9-(trifluoromethyl)-1H,5H,11H-[1]benzopyrano(6,7,8-ij)quinolizin-11-one* (coumarin-153, Figure 4.1a). A bottom-up approach, such as sublimation at ambient pressure, is employed to attain microcrystals (Figure 4.1c). FIB micromachining of these single-crystals of random shape produces predetermined circular and rectangular disk-shaped photonic resonators with high geometrical and dimension precision (Figure 4.1f). The optimized beam parameters are crucial to minimizing ion deposition and retaining the crystal's FL. The extreme nanometer precision possible with FIB milling enables FDTD numerical calculations, allowing the prediction of the optical performance of milled photonic components.

However, generalizing this milling technique for chemically different molecular microcrystals (aromatic hydrocarbons and molecules with reactive functional groups) grown by different techniques, viz., self-assembly and sublimation, are important.

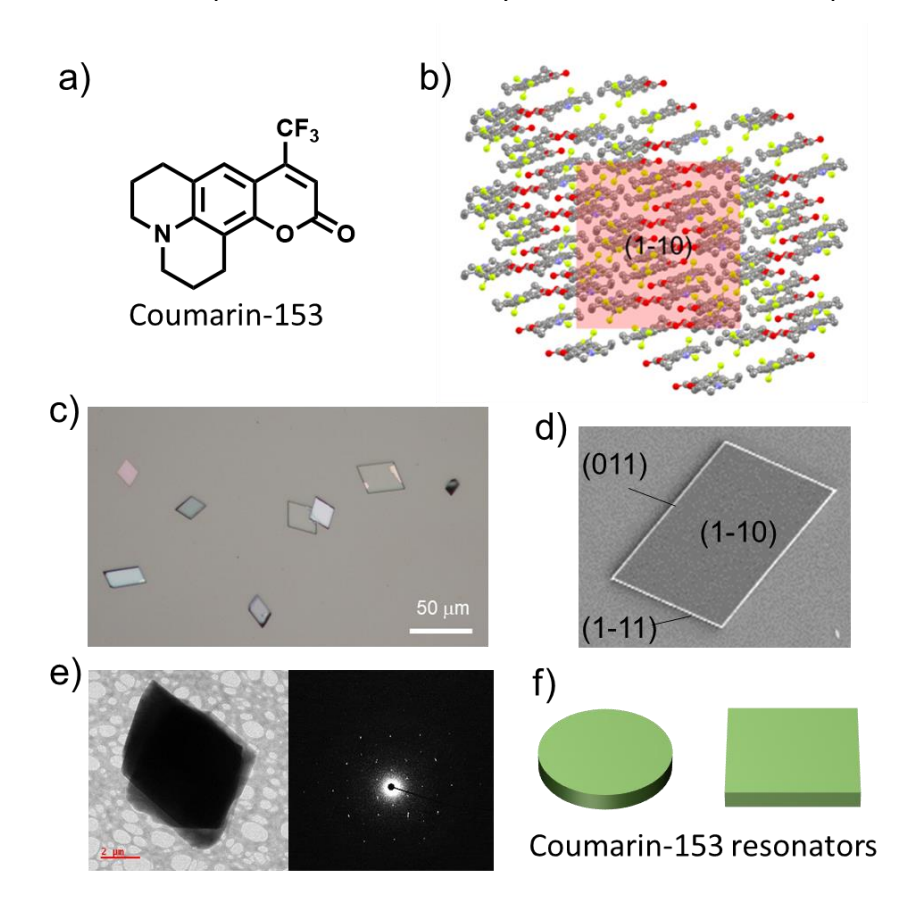
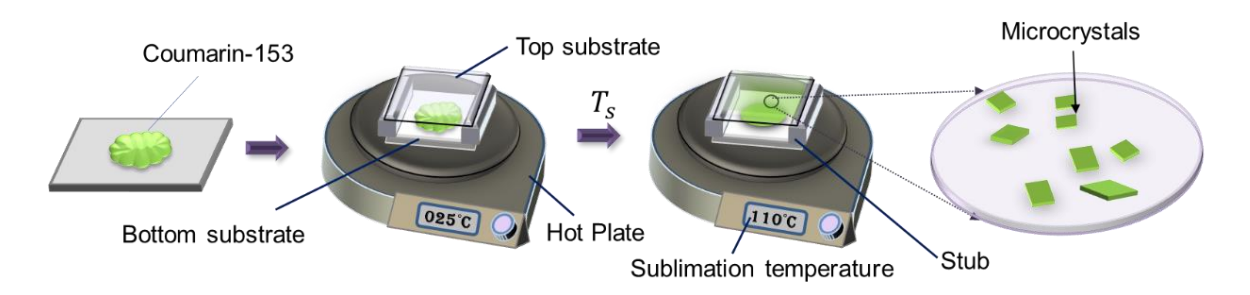


**Figure. 4.1.** a) Molecular structure of Coumarin-153. b) Molecular packing of coumarin-153 in (1-10) facet. c) Optical microscopic images of coumarin-153 microcrystals. d) FESEM image of a single coumarin-153 microcrystal along with its facets. e) TEM images and selected area electron diffraction data of coumarin-153 microcrystals. f) Graphical images of FIB milled microresonators of various shapes and dimensions.

### 4.3. Results and discussion

### 4.3.1. Preparation of coumarin-153 microcrystals



**Scheme 4.1.** Schematic diagram of ambient pressure vapor deposition technique for the preparation of coumarin-153 microcrystals.

Coumarin-153 exists in two polymorphs, namely, form I and form II. The ambient pressure vapor deposition technique was used to prepare selectively form II coumarin-153 microcrystals. For this, <1 mg of the compound on the coverslip was directly sublimed to another substrate and placed at a height ( $\Delta h$ ) of 1 mm using two glass stubs. The optimized sublimation temperature and time are 110 °C and 1 minute, respectively. Then, the sample was slowly cooled to room temperature to obtain numerous microcrystals on the top coverslip (Figure 4.1c and Scheme 4.1). The single crystal x-ray analysis of coumarin-153 crystals grown via sublimation technique reveal a triclinic system as reported previously, [179] and the major facets were found to be (1-10), (110), and (001) (Figure 4.1b,d). Optical microscope and FESEM of coumarin-153 microcrystals show smooth crystal facets (Figure 4.1c,d), and the TEM studies confirmed their single-crystalline nature (Figure 4.1e).

### 4.3.2. Effect of gold coating on FL intensity of coumarin-153 single-crystals

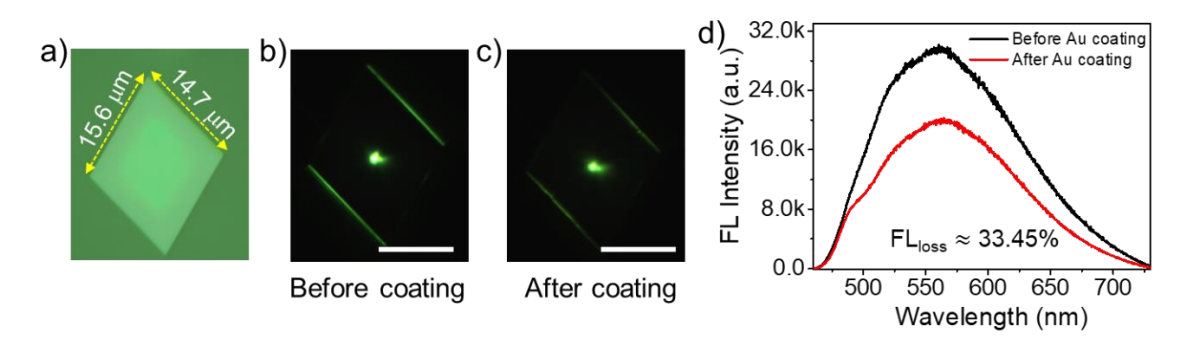


**Figure 4.2.** a) Confocal optical microscopy image of a selected coumarin-153 single-crystal. FL images of coumarin-153 single-crystal b) before and c) after gold-coating. d) The corresponding FL spectra of coumarin-153 single-crystal before and after gold coating. Scale bar 10  $\mu$ m.

The micro-spectroscopic studies on coumarin-153 single-crystal (dimensions:  $15.6\times14.7~\mu\text{m}^2$ ) were carried out in transmission mode under confocal microscopy setup (Figure 4.2a). Excitation (405 nm, diode laser) of the selected microcrystal generated a green FL, and the same was transduced to the crystal edges (Figure 4.2b). The spectrum collected at one of the edges revealed a broad FL spectrum ranging from 485 to 725 nm, corresponding to the polymorphic form-II<sup>[179]</sup> (Figure 4.2d, black line). Later, the same microcrystal was gold-coated, and the optical studies showed a similar broad band but with reduced FL intensity (Figure 4.2c,d). The calculated loss in FL intensity is about 33.45%, and the measured absolute quantum yield of coumarin-153 is around 17%.

### 4.3.3. Fabrication of coumarin-153 disk resonators

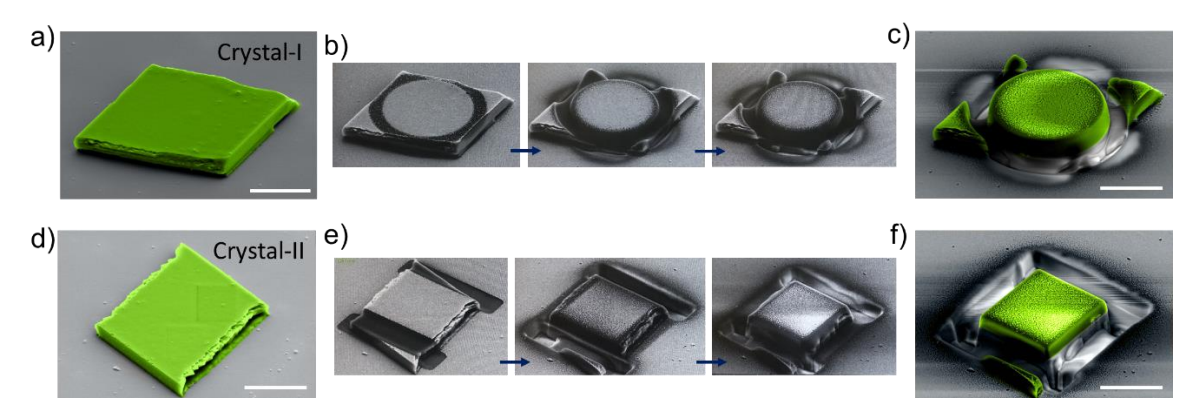


**Figure 4.3.** a,d) The color-coded FESEM images of selected coumarin-153 microcrystals (I and II). b,e) The series of photographs taken during the FIB milling process. c,f) The fabricated circular and rectangular disk resonators from crystal-I and -II, respectively. Scale bar 4  $\mu$ m. Note: The rough edges in a and d are due to the damage caused by AFM-tip during contact mode topography in AFM.

Two representative coumarin-153 microcrystals of dimensions (crystal-I:  $9.8\times9.4~\mu m^2$ ; crystal-II:  $9.9\times8.3~\mu m^2$ ) were selected (Figure 4.3a,d, 4.4a and 4.5a) and the thickness was measured using contact mode AFM and is found to be 1.18 and 0.91  $\mu m$ , respectively (Figure 4.4b and 4.5b). The color-coded FESEM images show the rough edges of the crystals during AFM measurements in contact mode (Figure 4.3a,d). The crystals were gold coated, and FIB milling (30 kV and 100 pA) was performed orthogonal to (1-10) facet of crystal-I to fabricate a circular disk of dimension 7.5  $\mu m$  (diameter) (Figure 4.3b and 4.4c). The color-coded FESEM reveals the geometrical perfection and smooth finishing of the fabricated microdisk (Figure 4.3c). Similarly, a rectangular disk of dimensions  $6.3\times5.5~\mu m^2$  (length×width) was fabricated using 30 kV and 100 pA (Figure 4.3e,f).

# 4.3.4. Photonic studies and FDTD numerical calculations of fabricated disk resonators

To check the optical characteristics, photonic studies were performed on crystal-I and -II before FIB milling (Figure 4.4a and 4.5a). The crystal-I generated a bright green FL when excited with a 405 nm CW laser at the center (Excitation: 0.05 mW; objective:  $60\times$ ). The generated FL circulated within the microcrystal and is out-coupled at the edges. The recorded broad FL (objective 150 $\times$ , NA: 0.95) spectrum covering the  $\approx$ 485-725 nm region

exhibited sharp peaks, confirming the crystal's microresonator activity (Figure 4.4e,g). The resonator characteristics of these crystals arise due to multiple reflections of FL by the light-reflective edges of the crystal. The FSR value of the crystal resonator was found to be  $\approx 3.81$  nm (Figure 4.4g). Interestingly, after FIB milling and without removal of the gold layer, the photonic experiments (Excitation: 0.3 mW) revealed the resonator activity of the fabricated circular disk-shaped crystal with an FSR of 6.25 nm (Figure 4.4f,h). This can be attributed to the high quantum yield of the coumarin-153. Further, FDTD numerical calculations confirm the distribution of light's electric field around the periphery of the fabricated circular disk for the representative 595 nm mode (Figure 4.4d).

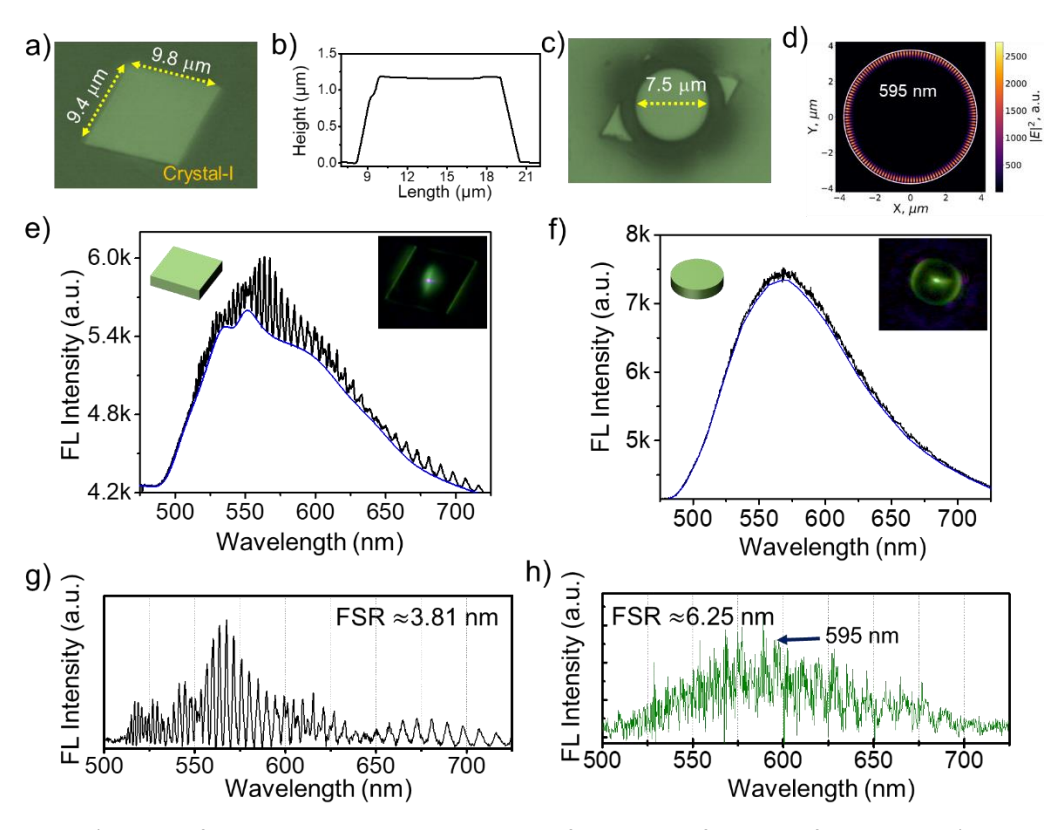


**Figure 4.4.** a,c) The confocal optical microscopy images of crystal-I before and after milling. b) Height profile of crystal-I measured using AFM before FIB milling. d) FDTD calculations displaying  $|E_z|^2$  distribution for the 595 nm mode in the circular disk resonator. FL spectra of crystal-I e) before and f) after FIB milling. Insets show the graphical and FL microscope images. g,h) The extracted optical resonances from FL spectra shown in e and f, corresponding to crystal-I before and after milling.

Similarly, crystal-II revealed the resonator activity upon continuous wave laser excitation (power:0.05 mW, Figure 4.5a,d) with an FSR of 4.07 nm (Figure 4.5f), and the corresponding FL image shows the bright edges (Inset, Figure 4.5d). Later, the fabricated

rectangular disk displayed intense FL along with significant optical resonances (excitation: 0.3 mW) without any post-processing treatment (Figure 4.5e). The corresponding FSR value is calculated and is found to be 8.15 nm (Figure 4.5g). This is in line with the literature that, as the size of the resonator decreases, the FSR value increases. The FDTD calculations on the rectangular disk resonator show the electric field for the wavelength 582 nm and 642 nm is concentrated at the middle of the edges (Figure 4.5h,i).

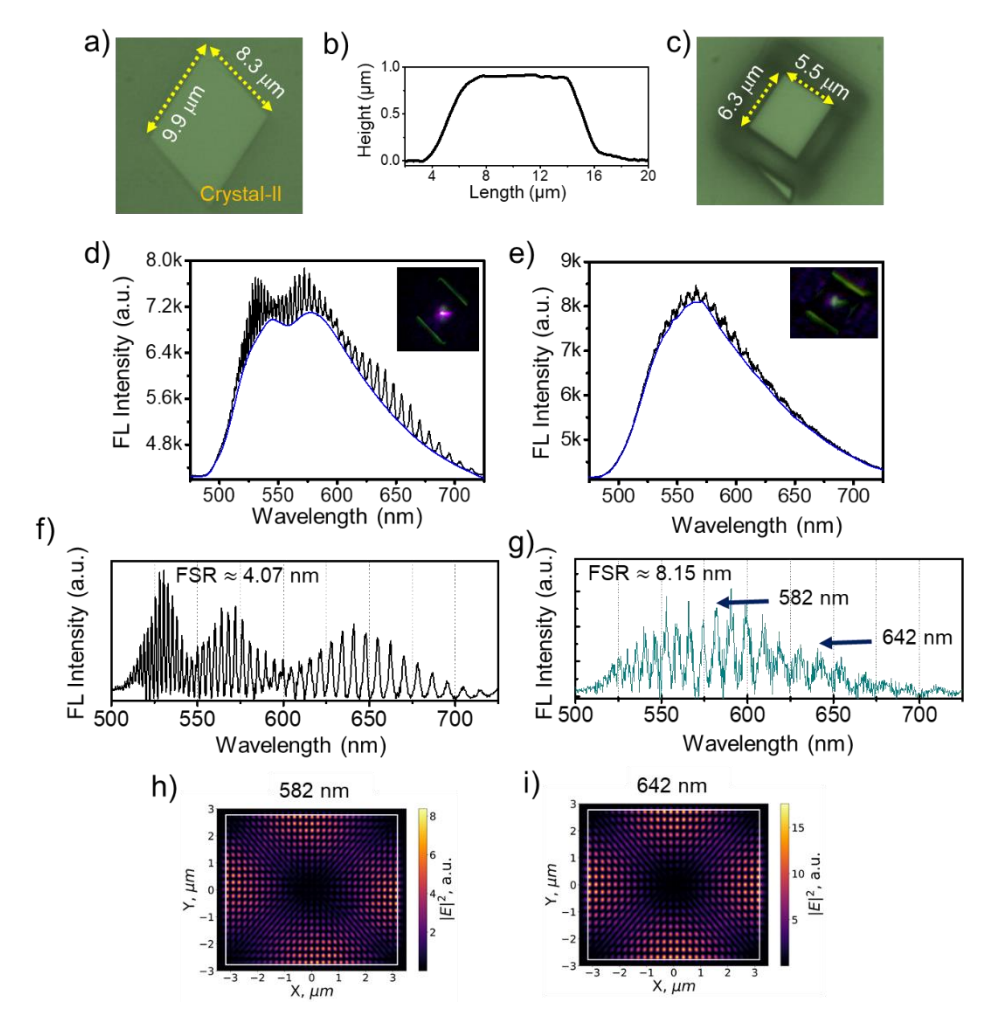


**Figure 4.5.** a,c) Confocal optical microscopy images of crystal-II before and after milling. b) Height profile of crystal-II measured using AFM. FL spectra of crystal-II d) before and e) after FIB milling. Insets show the FL image of crystals upon focused laser excitation. f,g) The extracted optical resonances from FL spectra shown in d and e for crystal-II before and after FIB milling. FDTD calculations display  $|E_Z|^2$  distribution for the h) 582 and i) 642 nm modes in the rectangular disk resonator.

To further understand the electric field distribution in 3D, a smaller circular disk resonator of diameter 2.5  $\mu$ m was fabricated using FIB milling from the parent coumarin-153 microcrystal of dimension 11×9  $\mu$ m<sup>2</sup> (Figure 4.6a,c). The thickness of the crystal was

measured using AFM in contact mode and was found to be 1.33  $\mu$ m (Figure 4.6b). Photonic studies exhibited the resonator activity before and after fabricating into a circular disk (Figure 4.6d,e). The calculated FSR values of the crystal before and after milling are found to be 4.8 and 23.14 nm, respectively. The FL images of crystal upon optical excitation were shown in the insets of Figure 4.6d,e. A power of 0.05 and 0.3 mW was used to collect the FL spectra before and after the fabrication of the circular disk, respectively.

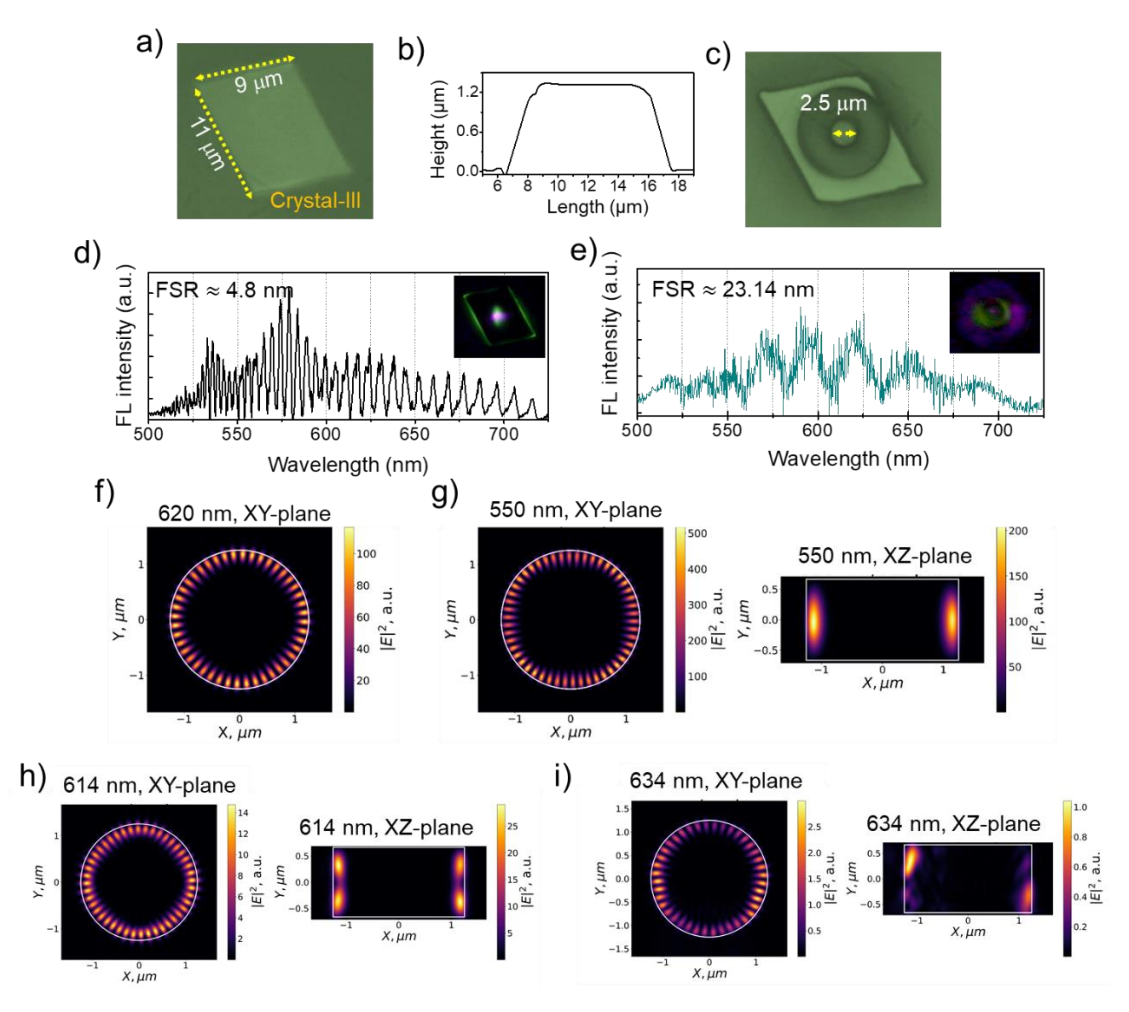
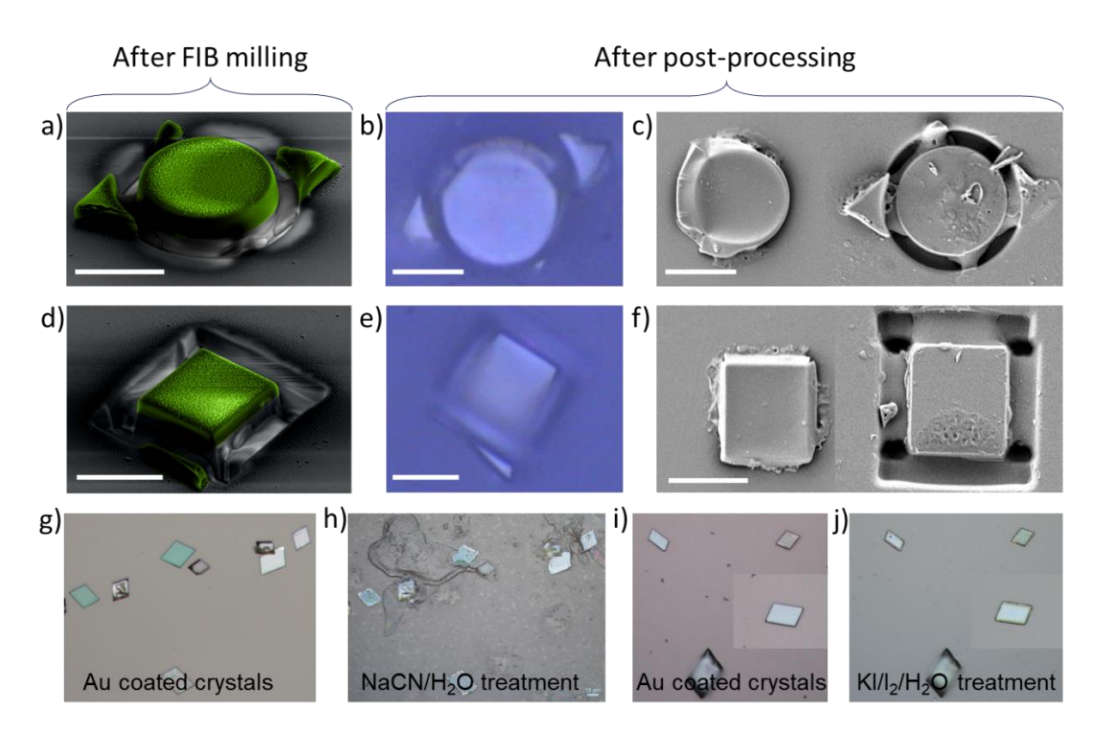


Figure 4.6. a,c) The confocal optical microscopy images of crystal-III before and after milling into a circular disk of diameter 2.5  $\mu$ m. b) Height profile of selected coumarin-153 microcrystal measured using AFM. d,e) The background-subtracted FL spectra displaying optical resonances from crystal-III before and after FIB milling into a circular disk resonator. The insets show the FL images of microcrystals upon focused optical excitation. FDTD calculations display  $|E_z|^2$  distribution for f) 620, g) 550, h) 614, and i) 634 nm in the circular disk resonator of diameter  $\approx$ 2.5  $\mu$ m.

The 2D and 3D FDTD calculations were performed for the fabricated single-crystal circular disk for 620, 550, 614, and 634 nm modes (Figure 4.6f-i). As expected from the geometry, the 2D FDTD shows the localization of an intense electric field around the circular

periphery. The calculated azimuthal mode numbers for 620 nm and 550 nm peaks are 22 and 25, which suggests that the resonator acts as a WGM type. Further, common WGMs were obtained for 550 nm (Figure 4.6g). WGMs with higher-order field distribution in a plane perpendicular to the mode circulation direction with a lower Q-factor were obtained for 614 nm (Figure 4.6h). Further, Figure 4.6i shows the mode circulating not in a plane parallel to the substrate. These modes have low *Q*-factor too, but perhaps they have different radiation patterns and can be detected easier than higher Q-factor modes. The left panels in Figure 4.6g-i exhibit field distribution cross-sections parallel to the substrate plane located at half of the resonator's height above the substrate, and the right panels are cross-sections perpendicular to the substrate. White lines denote resonator borders.

#### 4.3.5. Post-processing of fabricated disk resonators



**Figure 4.7.** a,d) The color-coded FESEM images of circular and rectangular disk resonators of coumarin-153 single-crystals after FIB milling, respectively. b,e) Confocal optical microscopy images of disk resonators after post-processing with Lugol's iodine reagent. c,f) FESEM images of disk resonators after post-processing and micromanipulation with AFM cantilever-tip. g,h) Optical microscope images of coumarin-153 microcrystals after gold coating and after treatment with NaCN/H<sub>2</sub>O, respectively. i,j) Optical microscope images of coumarin-153 microcrystals after gold coating followed by treatment with KI/I<sub>2</sub>/H<sub>2</sub>O, respectively.

The color-coded FESEM images of the fabricated circular and rectangular disk resonators (Figure 4.7a,d) were subjected to Lugol's iodine solution (KI/I<sub>2</sub>/H<sub>2</sub>0), followed by

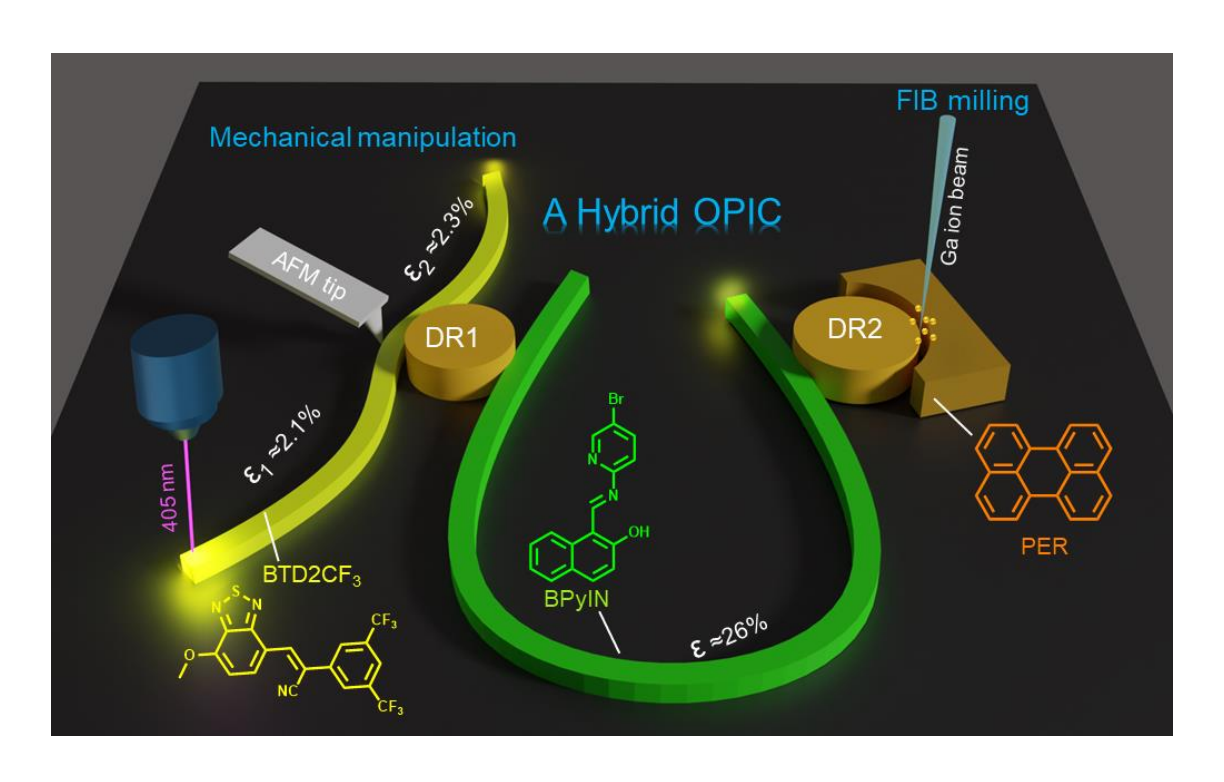
distilled water wash. After the post-processing, confocal microscope images of disk resonators revealed slight distortion in shape but are not clearly evident (Figure 4.7b,e). Later, the disk resonators were moved from the actual position using the AFM cantilever tip (micromanipulation), and the subsequent examination under FESEM revealed that the fabricated disks were damaged (Figure 4.7c,f). Further, optical microscopy studies were carried out on a selected area of coumarin-153 microcrystals to study the effect of both the gold etchants, i.e., exposure to HCN vapors (Figure 4.7g,h) and treatment with Lugol's iodine solution (Figure 4.7i,j), respectively. In both cases, the microcrystals were damaged, which is evident from optical microscope images (Figure 4.7g-j). Therefore, the coumarin-153 microcrystals were reactive towards both the gold etchants. Due to relatively high quantum yield, coumarin-153 disk resonators show high FL intensity and optical modes, even without gold removal. Hence, the coumarin-153 crystals did not require any of this post-processing treatment. One more option can be the usage of a conductive substrate (ITO-PET) to grow coumarin-153 microcrystals; thereby charging effect in the electron/ion microscopy can be nullified.

#### 4.4. Conclusions

In summary, FIB milling was performed to obtain organic photonic components, namely, circular and rectangular disk resonators from coumarin-153 single-crystals. The fabricated photonic components revealed optical traits after milling. During the chemical treatment, coumarin-153 crystals are reactive. Due to a relatively high quantum yield (17%), coumarin-153 crystal resonators show high FL intensities and optical modes, even without gold removal. Hence, the coumarin-153 crystals did not require any of this post-processing treatment. The FDTD numerical calculation revealed light's electric field inside the crystal microresonators was localized at the periphery of the circular disk resonator and middle of the edges for the rectangular resonator, respectively. These results validate the generality of the FIB milling technique to carve out optical components of precise shape and dimension from organic single-crystals. The field of crystal photonics foundry, i.e., FIB milling of organic crystals into photonic modules, has the potential to produce industrial-scale manufacturing of organic photonic circuitry and devices.



A Tandem Approach to Fabricate a Hybrid,
Organic-Add-Drop Filter Using Single-Crystal
Disk-Resonators and Pseudo-Plastic Crystal
Waveguides



#### 5.1. Abstract

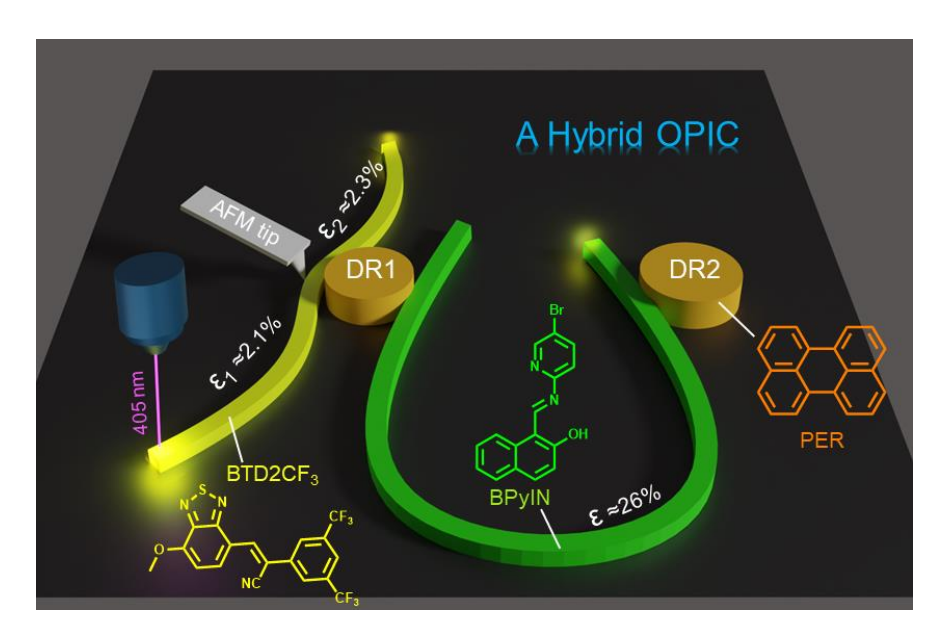
This chapter demonstrates a novel approach to construct a key optical component, namely a hybrid organic add-drop filter (HOADF), by tandem use of two different techniques, namely, mechanophotonics (micromechanical manipulation) and crystal photonics foundry (focused ion beam, FIB-assisted crystal milling). The successful mechanical integration of FIB-milled, yellow-emissive, perylene disk resonators to two chemically and optically different pseudo-plastic microcrystal waveguides, namely yellow-orange-emitting (Z)-2-(3,5-bis(trifluoromethyl)phenyl)-3-(7-methoxybenzo[c][1,2,5] thiadiazol-4-yl)acrylonitrile (BTD2CF<sub>3</sub>) and green-emitting (E)-1-(((5-bromopyridin-2-yl)imino)methyl)naphthalen-2-ol (BpyIN) provides a three-component HOADF. The fabricated HOADF can produce, split, and route light signals of different wavelengths in a controlled fashion as anticipated from the circuit geometry.

#### 5.2. Introduction

The ability to control and guide photons in desired directions is instrumental in devising an effective PIC. [7-14,180,181] In this regard, circularly shaped resonators that confine, amplify, and route optical signals are one of the fundamental building blocks for the construction of PICs. [12-14,106-109] Recently, the pseudo-plastic behavior of elastic crystals was exploited using the mechanophotonics approach (an AFM cantilever tip-driven crystal micromanipulation technique) to fabricate various organic crystal-based optical components and circuits.<sup>[24]</sup> However, these flexible crystals are mechanically deformable only in one direction and rarely in two directions, indicating the molecular anisotropic nature and limiting their universal use. Moreover, the dimensional accuracy and precise reproducibility of self-assembled microcrystals remain a concern. Therefore, to accept organic crystals as trustworthy materials for PICs, there is an ardent need to illustrate i) molecular orientation independent material's processing of crystals into various shapes, ii) geometrical and dimension precision, iii) reproducibility, iv) bulk scale manufacturability, and v) universality of the method to most organic crystals. Therefore, the FIB milling technique allows automation, scalability, and reproducibility anticipated by industrial manufacturers. Moreover, the translocation of milled optical components from one substrate to another impedes the construction of hybrid OPICs, where the

mechanophotonics approach becomes crucial for integrating two or more optically emissive materials at a place.

This chapter unravels a tandem approach for fabricating an innovative hybrid OPIC by utilizing both crystal photonics foundry and mechanophotonics processing strategies. Initially, single-crystalline organic disk resonators (DRs, with diameters DR1=3.88, DR2=4.83 μm, and DR3=4.83 μm) are fabricated using the FIB milling technique from yellow emissive perylene microcrystals. Later, two pseudo-plastic crystals namely, green-emitting (E)-1-(((5bromopyridin-2-yl)imino)methyl)naphthalen-2-ol (BPyIN)[110] and yellow-orange emitting, (Z)-2-(3,5-bis(trifluoromethyl)phenyl)-3-(7-methoxybenzo[c][1,2,5] thiadiazol-4yl)acrylonitrile (BTD2CF<sub>3</sub>)<sup>[182]</sup> were transferred to the circuit fabrication site on SiO<sub>2</sub> substrate using AFM cantilever-tip-assisted mechanical micromanipulation (Scheme 5.1, insets). Mechanical integration of two DRs with a U-shaped BPyIN waveguide allows efficient transport of optical signals from one DR to another. Finally, the tangential integration of a BTD2CF<sub>3</sub> waveguide to DR1 offers a hybrid organic add-drop filter (HOADF) and controls the light path as expected from the circuit design. The demonstration of such techniques and technologies improves the scalability of achieving industrially viable photonic devices and circuits.



**Scheme 5.1**. Graphics depicting the functioning of hybrid organic photonic integrated circuit achieved with the help of *mechanophotonics* (micromechanical manipulation) and *crystal photonics foundry* (FIB milling) techniques. Insets show the molecular structures of organic crystals.  $\varepsilon$  represents the strain caused on the crystal due to mechanical bending.

#### 5.3. Results and discussion

#### 5.3.1. Syntheses of BPyIN and BTD2CF<sub>3</sub>

#### 5.3.1.1. Synthesis of BPyIN:

Scheme 5.2. Synthesis of BPyIN.

2-Hydroxy-1-naphthaldehyde (5 mmol, 1eq) and 2-amino-5-bromo pyridine (5 mmol, 1eq) were taken in ethanol in a 100 mL round-bottomed (RB) flask. The reaction mixture's temperature was set to 70 °C for 4 hrs. The resultant green precipitate was cooled to rt and purified by recrystallization in chloroform to obtain green needles of BPyIN (Scheme 5.2). [110] Yield: 82%. ¹H NMR (400 MHz, CDCl<sub>3</sub>):  $\delta$  (ppm) 15.36 (s, 1H), 9.95 (d, 1H), 8.52 (d, 1H), 8.15 (d, 1H), 7.85 (dd, 1H), 7.78 (d, 1H), 7.64 (d, 1H), 7.52 (dt, 1H), 7.33 (dt, 1H), 7.09 (d, 1H), 6.94 (d, 1H); ¹³C NMR (100 MHz, CDCl<sub>3</sub>):  $\delta$  (ppm) 176.86, 152.25, 151.44, 149.96, 141.12, 139.25, 133.87, 129.40, 128.62, 128.14, 123.92, 119.47, 117.66, 116.92, 109.13; FT-IR ( $\bar{\nu}$  cm<sup>-1</sup>): 2035, 1966, 1616, 1536, 1466, 1320, 1289, 1127, 820, 741; HR-MS: m/z Calculated: 326.01, 328.01, Found: 327.01, 329.01; UV-Vis (Solid-state):  $\lambda_{abs-max}$  509 nm and  $\lambda_{FL-max} \approx 538$  nm (green emission); m.p  $\approx 234-236$  °C.

#### 5.3.1.2. Synthesis of BTD2CF<sub>3</sub>:

**Scheme 5.3.** Synthesis of  $BTD2CF_3$ .

Sodium methoxide (10 mmol, 2 eq) and bis(3,5-trifluoromethyl)phenyl acetonitrile (5 mmol, 1eq) were taken in 15 mL of methanol in 100 mL RB. 7-Bromobenzo[c][1,2,5]thiadiazole-4-carbaldehyde (5 mmol, 1eq) was slowly added to the RB drop-by-drop over 10 minutes. The reaction mixture's temperature was set to 60 °C for 4 hrs. The resultant yellow precipitate was cooled to rt and purified by recrystallization in methanol to obtain BTD2CF<sub>3</sub> crystals (Scheme 5.3).<sup>[182]</sup> Yield: 74%. <sup>1</sup>H NMR (400 MHz, CDCl<sub>3</sub>):  $\delta$  8.75 (d, 1H), 8.55 (s, 1H), 8.18 (s, 2H), 7.92 (s, 1H), 7.01 (d, 1H), 4.15 (s, 3H); FT-IR ( $\bar{\nu}$  cm<sup>-1</sup>): 2920, 2851, 2222, 1596, 1538, 1373, 1277, 1236, 1169, 1110, 1029, 969, 890; HR-MS: m/z Calculated: 429.04, Found: 432.24; UV-Vis (Solid-state):  $\lambda_{abs}$  bandwidth extends up to 590 nm and  $\lambda_{FL-max} \approx$ 586 nm (yellow-orange emission); m.p  $\approx$ 332-334 °C.

#### 5.3.2. Steady-state optical properties

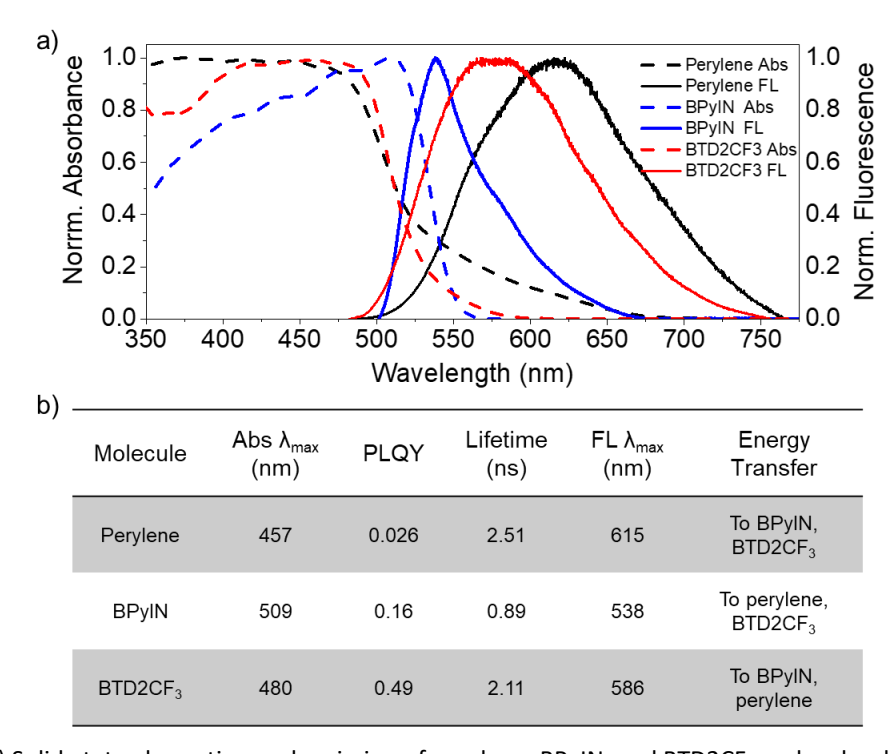


**Figure 5.1.** a) Solid-state absorption and emission of perylene, BPyIN, and BTD2CF<sub>3</sub> molecules. b) Table shows the summary of molecules' optical absorption maxima, PLQY, FL lifetime, FL maxima, and energy transfer.

The solid-state optical characteristics of perylene revealed its absorption spectrum consisted of  $\lambda_{max}$  at 457 nm with its tail extending to 675 nm, whereas its emission covers the range of 475–775 nm (Figure 5.1a). The absolute PLQY of the perylene was measured to be 0.026, with a typical FL lifetime of 2.51 ns (Figure 5.1b). Similarly, the BPyIN and BTD2CF<sub>3</sub> had an absorption maximum at 509 and 480 nm, respectively, while their emission

occurred in the green ( $\lambda_{max} \approx 538$  nm) and yellow-orange ( $\lambda_{max} \approx 586$  nm) region. The absolute PLQY of BPyIN and BTD2CF<sub>3</sub> molecules were measured to be 0.16 and 0.49, respectively (Figure 5.1).<sup>[110,182]</sup> Importantly, there is a possibility for energy transfer (*ET*) from BTD2CF<sub>3</sub> to perylene, BPyIN to perylene, perylene to BTD2CF<sub>3</sub>, and perylene to BPyIN due to the overlap of optical absorption of one crystal with the emission of other (Figure 5.2).

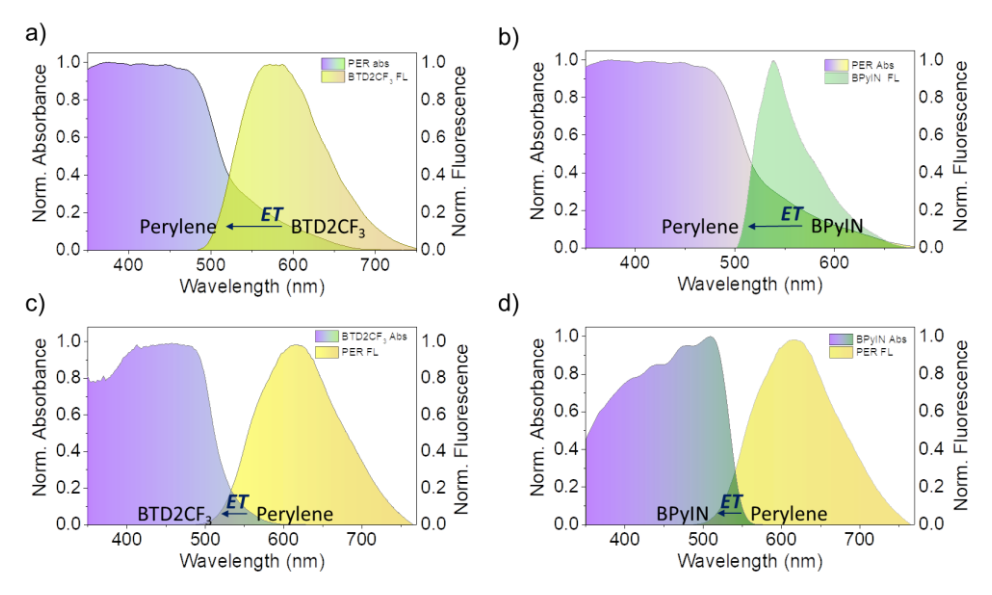


**Figure 5.2.** The possible energy transfers from a) BTD2CF<sub>3</sub> to perylene, b) BPyIN to perylene, c) perylene to BTD2CF<sub>3</sub>, and d) perylene to BPyIN.

# 5.3.3. Fabrication and photonic properties of perylene single-crystal disk resonators

The directional dependence of molecular orientation is necessary for pseudo-plastic crystals, whereas this FIB milling technique allows the construction of curved geometries like circular DRs, irrespective of the molecular orientational preference. For this purpose,  $\alpha$ -form yellow emissive perylene single-crystals were prepared. The detailed self-assembly procedure of perylene microcrystals is provided in chapters 2 and 3. To investigate the size-dependent optical resonator effect and subsequent utilization for hybrid PICs, an irregular-shaped perylene crystal (thickness  $\approx\!2.5~\mu m$  measured by AFM) was selected (Figure 5.3a). For this, intentionally, a single perylene crystal was broken into three pieces using an AFM cantilever tip force. The broken pieces are movable with an AFM cantilever tip. Therefore, after milling, the obtained resonators can also be moved and integrated with other optical modules to attain hybrid OPIC.

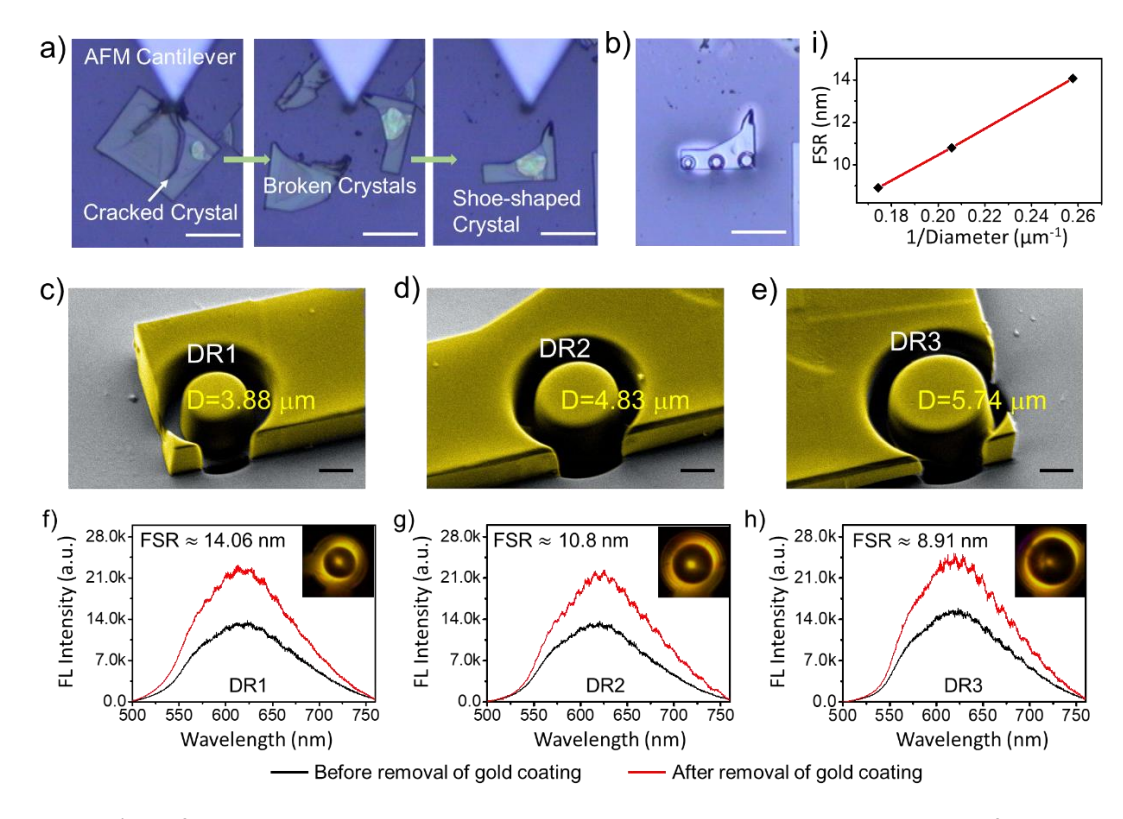


**Figure 5.3.** a) Confocal optical microscope images showing the micromechanical breaking of a rectangular-shaped perylene single crystal producing a shoe-shaped crystal. b) Confocal optical image of three different-sized circular DRs made by FIB milling on the shoe-shaped crystal. c-e) The color-coded FESEM images of fabricated circular DRs of varying diameters. f-h) The corresponding FL spectra before (black line) and after (red line) removal of gold coating using the gold etchant. Insets show the FL microscope images. i) The plot of FSR vs. 1/diameter shows the linear dependency of FSR on the diameter of the fabricated DRs. Scale bars 30 μm (white) and 2 μm (black).

As the perylene crystals are not electrically conductive, a thin layer of gold was coated to facilitate simultaneous FESEM studies during milling and to minimize ion implantation on the milled crystal facets. Notably, the FIB milling (beam parameters: 30 kV and 100 pA) of perylene crystals was performed on the widest (100) plane, which lacks ordered packing to absorb external stress (Figure 5.3b). In fact, the crystal can be milled along any direction by placing the corresponding crystal's face perpendicular to the ion beam. Therefore, the molecular orientational preference, as required for mechanical flexibility, can be successfully overcome using the FIB technique. Upon milling, three circular disks (namely, DR1, DR2, and DR3) of diameters 3.88, 4.83, and 5.74 µm were obtained on a shoe-shaped single perylene crystal (Figure 5.3b). The color-coded FESEM images show the fine finishing and smooth surface morphology of the fabricated DRs (Figure 5.3c-e).

After the fabrication of DRs, their optical properties were investigated on a confocal optical microscope setup in the transmission mode by irradiating them (at the center of the DR) with a 405 nm continuous wave diode laser (power 0.1 mW). At the point of excitation, yellow FL of perylene was observed without any sign of optical resonances (Insets of Figure 5.3f-h). The FL spectrum recorded at the DR's periphery (displaying ring-shaped bright emission) possessed periodic sharp peaks indicative of WGMs (Figure 5.3f-h). However, the optical modes observed in these three DRs were not well pronounced due to the gold coating present on the surface of the disks (Figure 5.3f-h, black lines). Therefore, the gold layer on the cover slip consisting of the fabricated DRs was removed by treating it with Lugol's iodine solution. The spectra collected at the periphery of the resultant DRs revealed enhanced FL spectral intensity with clearly observable optical modes (Figure 5.3f-h, red lines), and the FSRs were measured to be 14.06, 10.8, and 8.91 nm for DR1, DR2, and DR3 respectively. This result shows that the resonator effect is preserved in microdisks of varying diameters as supported by decreased FSR values with an increase in resonator diameter in accordance with the formula FSR ≈1/D (Figure 5.3i).

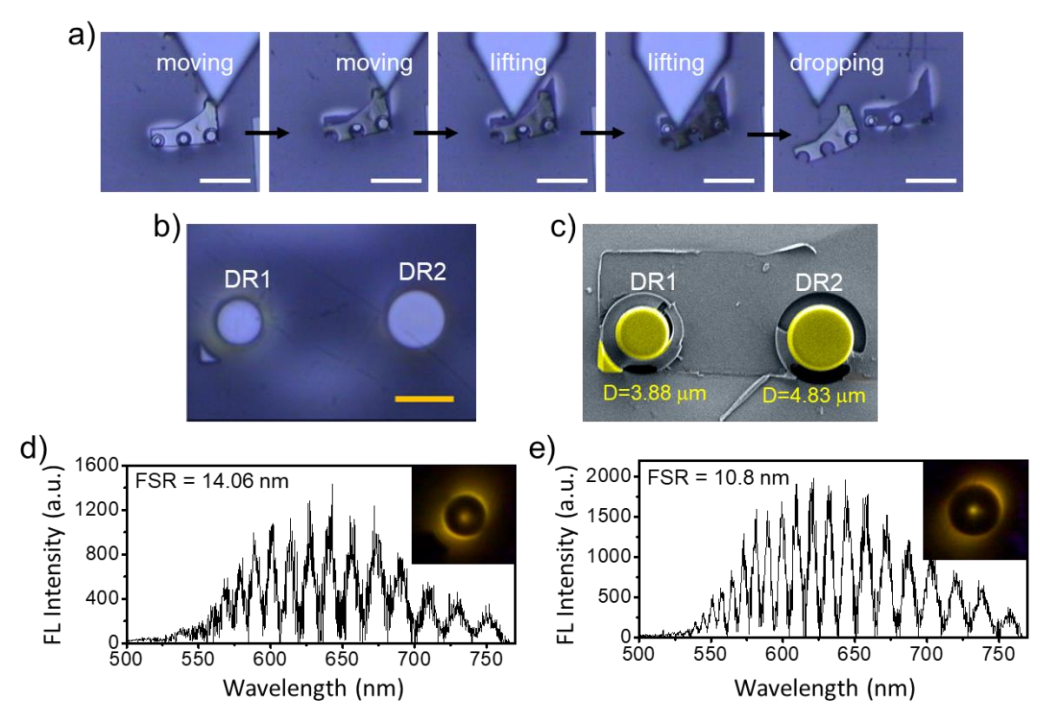


**Figure 5.4.** a) Confocal optical microscopy images showing the micromechanical separation of the parent crystal from perylene DRs. b,c) Confocal optical microscopy and color-coded FESEM images of isolated DRs, respectively. d,e) The background-subtracted FL spectra displaying optical resonances from DR1 and DR2, respectively. Note: The original FL spectra recorded for DR1 and DR2 are shown in Figure 5.3f,g. Insets show the FL images of the DRs when excited with a 405 nm laser. Scale bars 30  $\mu$ m (white) and 5  $\mu$ m (yellow).

Later, to create the envisioned hybrid OPIC, the milled DRs were subjected to post-mechanical processing using the AFM cantilever tip to isolate the DRs from the parent crystal physically. In this present geometry, moving the DRs with the AFM cantilever tip could cause mechanical fracture due to the absence of stress-absorbing channels in the crystal. Hence, the parental crystal was carefully moved, lifted, and dropped aside using the AFM cantilever tip (Figure 5.4a). One of the fabricated DRs (DR3) also came out along with the parent crystal while removing the latter. The confocal and color-coded FESEM image shows the defect-free, isolated DRs (Figure 5.4b,c), and their photonic studies showed the resonator activity with the same FSRs (14.06 nm for DR1 and 10.8 nm for DR2, Figure 5.4d,e).

#### 5.3.4. Photonic aspects of BPyIN and BTD2CF<sub>3</sub> microcrystals

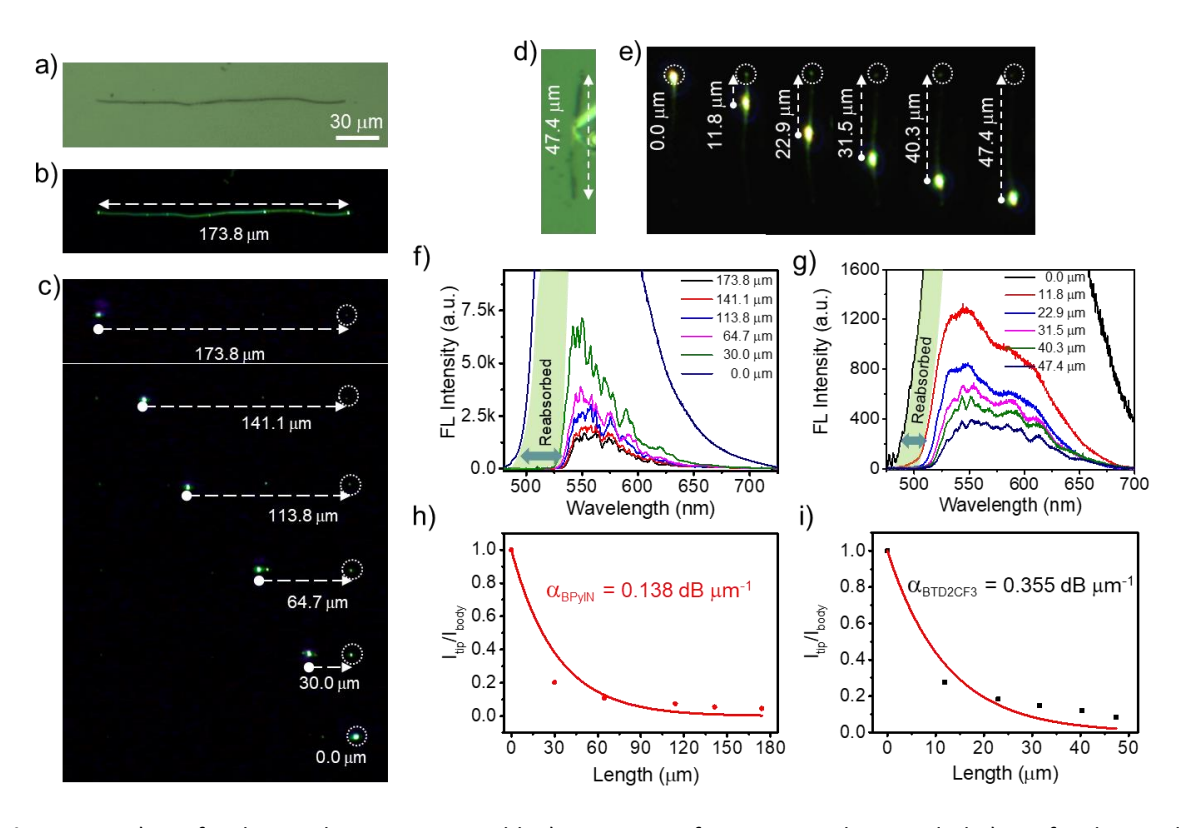


**Figure 5.5.** a) Confocal optical microscopy and b,c) FL images of a BPyIN single-crystal. d,e) Confocal optical microscopy and FL images of a BTD2CF<sub>3</sub> single-crystal. Excitation position-dependent FL spectra recorded at the f) right terminal of the BPyIN waveguide and g) top terminal of the BTD2CF<sub>3</sub> waveguide. h,i) Optical loss calculated from the plot of I<sub>tip</sub>/I<sub>body</sub> vs. distance for BTD2CF<sub>3</sub> and BPyIN waveguides, respectively.

The fabrication of hybrid OPICs mandates the integration of different emissive materials with diverse optical functionalities on a single chip. In this aspect

mechanophotonics approach becomes pivotal in transferring all the required materials onto a single chip. Therefore, the envisioned BPyIN and BTD2CF<sub>3</sub> microcrystals were prepared using a bottom-up, self-assembly technique using the reported literature. [110,182] The micromechanical properties of BPyIN and BTD2CF<sub>3</sub> were documented to illustrate the first crystal-based interferometer and wavelength division multiplexer, organic respectively.[110,182] The anisotropic nature of mechanical compliance exhibited by such organic crystals is well-documented, and the same was reiterated by the unidirectional mechanical flexibility along the (-101) plane for BPyIN and (110) plane for BTD2CF<sub>3</sub> crystals, respectively. [110,182] Thereby, it is customary to have a particular molecular orientation to achieve bent waveguides in flexible organic waveguides.

Initially, a BPyIN microcrystal of length  $L \approx 173.8 \ \mu m$  was chosen to explore the mechanophotonic aspects (Figure 5.5a). The bright FL at the tips of the BPyIN microcrystal in the confocal FL microscope image suggests its waveguiding property (Figure 5.5b). To confirm the same, the BPyIN microcrystal was excited with a 405 nm continuous wave laser using a confocal optical microscope in the transmission mode. The BPyIN microcrystal produced a bright green FL  $\lambda_2(A)$ , with a bandwidth of  $\approx$ 482-700 nm at the point of excitation (Figure 5.5c). The generated signal traveled towards the right tip to yield a reabsorbed signal  $-\lambda_2(A)$  with a bandwidth of  $\approx$ 525-700 nm (Figure 5.5f). The positiondependent waveguiding studies revealed a decrease in the FL intensity at the right tip as the separation between excitation and collection points increased. The optical loss ( $\alpha'$ ) of the BPyIN waveguide was calculated to be 0.138 dB  $\mu m^{-1}$  from the fit of  $I_{tip}/I_{body}$  vs. distance between excitation and collection points (Figure 5.5h). Similarly, a BTD2CF<sub>3</sub> microcrystal of  $L \approx$  47.4 µm was selected and subjected to 405 nm laser irradiation for optical waveguiding studies (Figure 5.5d). Upon excitation at one of the termini, it generated a bright yellow FL  $\lambda_3(A)$  with a bandwidth of  $\approx$ 480-755 nm and transduced the FL to the other terminal of the microrod, confirming the waveguiding nature (Figure 5.5e). The position-dependent waveguiding studies revealed  $\alpha'$  of  $\approx 0.355$  dB  $\mu m^{-1}$  for the BTD2CF<sub>3</sub> waveguide (Figure 5.5g,i).

#### 5.3.5. Fabrication of disk resonators-coupled optical waveguide

The BPyIN and BTD2CF<sub>3</sub> crystals display pseudo-plastic behavior in the microregime on the silica substrate. By taking advantage of this pseudo-plasticity, a novel HOADF was planned to fabricate by combining FIB milled DRs' with the BPyIN and BTD2CF<sub>3</sub> microcrystal waveguides. Firstly, a BPyIN microcrystal was lifted from the substrate consisting of only BPyIN microcrystals with the help of the AFM cantilever tip (Figure 5.6a,b). The lifted microcrystal was carefully dropped near the perylene DRs (Figure 5.6c). Later, this 173.8  $\mu$ m long bent BPyIN waveguide was cut into a shorter waveguide of  $L\approx65~\mu$ m to fit in the gap between DR1 and DR2, as shown in Figure 5.6d,e and 5.7a,b. Excitation of one of the termini (G1; here G stands for green FL) of the BPyIN microcrystal with 405 nm laser showed the guided green FL corresponding to  $-\lambda_2$ (A) at the opposite terminal (G2) (Figure 5.6f, black line). Additionally, optical resonances were observed in the FL spectra due to light confinement in the microcrystal waveguide (Figure 5.6f, black line). Similarly, G2 was excited, and the outcoupled FL at G1 exhibited a similar FL spectrum with optical modes (Figure 5.6f, red line).

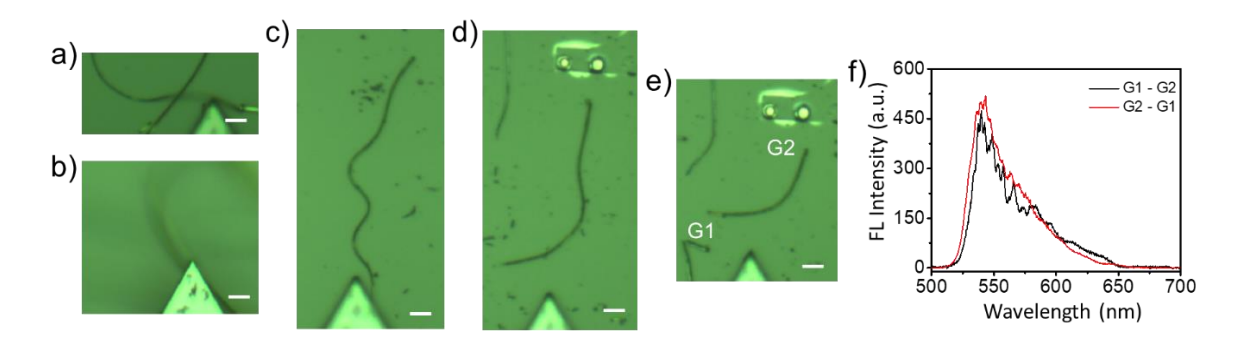
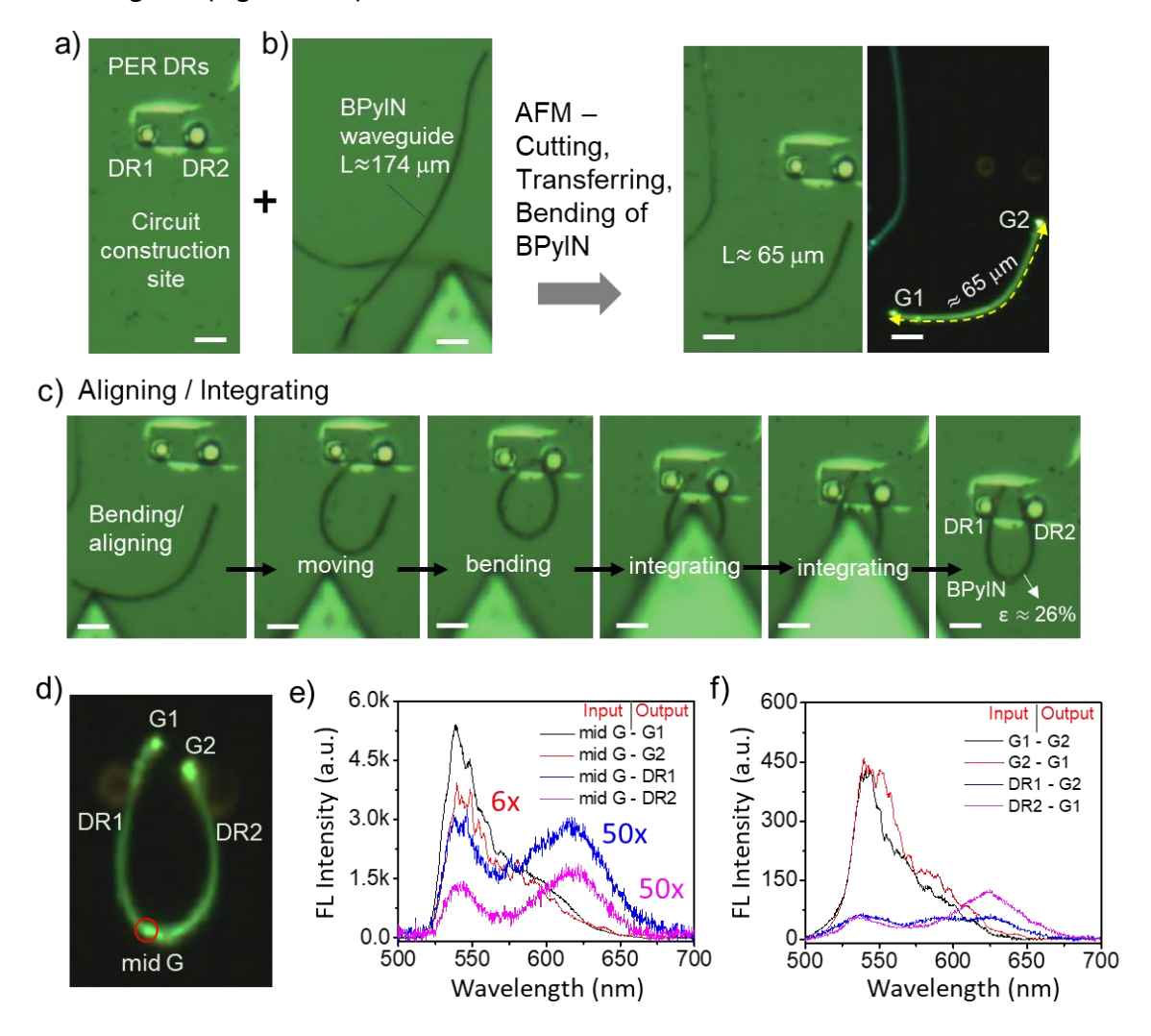


Figure 5.6. a-e) Confocal optical microscope images displaying transfer and cutting of a BPyIN microcrystal. f) The FL spectra collected at G2 and G1 of the BPyIN microcrystal shown in e, when excited at G1 and G2, respectively. Scale bar  $10 \, \mu m$ .

The integration of a BPyIN waveguide with the DRs was the most crucial step in the fabrication of hybrid OPIC. The main reasons are: i) the micromanipulation is a manually operated process, ii) the microcrystal with a 180° bent may develop extreme strain, iii) the operational area is smaller compared to the size of AFM cantilever (140×50  $\mu$ m) any turbulence of cantilever near the DRs may lead to resonator damage. The integration process involves micromanipulation steps like moving, bending, aligning, and integration (Figure 5.7c). After integration, the strain developed at the 180° bent region of the BPyIN

microcrystal was about 26% which is higher than the maximum reported strain values (usually in the range of 3-11%) for flexible organic crystals. The FL image of the BPyIN microcrystal waveguide coupled DRs circuit shows the physical contact between DRs and the waveguide (Figure 5.7d).



**Figure 5.7.** Confocal optical microscope images of a) the circuit construction site. b) AFM cantilever tip-based cutting and transferring of a BPyIN crystal waveguide closer to the circuit construction site. c) Micromechanical integration of BPyIN waveguide with DRs to construct DRs-coupled waveguide. d) The FL image of the DRs-coupled waveguide. FL spectra were recorded at various ports when excited at e) the centre of the BPyIN waveguide and f) tips of the BPyIN waveguide and perylene DRs. The terminology G1-G2 represents excitation at the G1 position and FL signal collection at the G2 position. Scale bar 10 μm.

To understand the optical communication between DRs and bent waveguide, the center of the BPyIN waveguide (labeled as 'mid G') was excited (405 nm). As expected, both the termini (G1 and G2) of the BPyIN waveguide exhibited outcoupling of a green FL (Figure 5.7e). The signal at G2 possesses explicit optical modes compared to the same observed at

G1 because of smooth rectangular crystal facets at G2 end. Interestingly, the FL spectra at G1 and G2 possessed an additional band centered at 620 nm, apart from BPyIN's green FL ( $\lambda_{max}$  538 nm), corresponding to the perylene emission maximum. This can be ascribed to partial radiative excitation of perylene DRs at the coupling region due to ET (from BPyIN to perylene, Figure 5.2b) and the simultaneous presence of two signals ( $\lambda_{max} \approx 538$  nm and  $\lambda_{max} \approx 620$  nm) in the DR-coupled waveguide.

This was further confirmed from the spectra collected at DRs (1 and 2), where both BPyIN and perylene FL bands were evident (Figure 5.7e, blue and pink lines). Therefore, there is a significant contribution arising from the optical communication between perylene and BPyIN waveguide in the functioning of DRs-coupled waveguide. Similarly, the optical characteristics of the DRs-coupled waveguide when light is provided at G1, G2, DR1, and DR2 are presented in Figure 5.7f. When perylene DRs are excited, the resultant spectrum at G1 or G2 consists of residual perylene signal (see blue and pink spectra in Figure 5.7f), indicating that only part of the evanescently coupled perylene FL is absorbed (via ET) to produce BPyIN FL, while the unabsorbed light passively outcouples at G1 or G2.

#### 5.3.6. Fabrication of hybrid organic add-drop filter (HOADF)

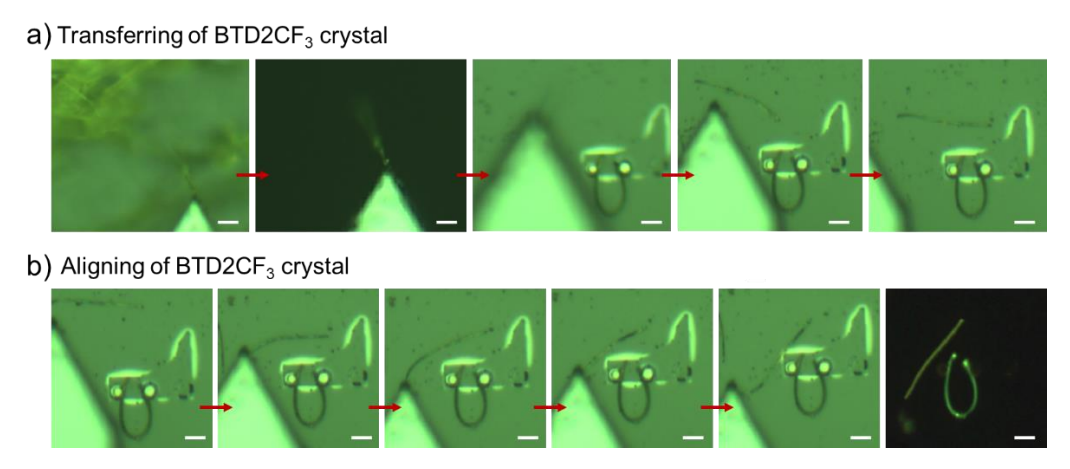
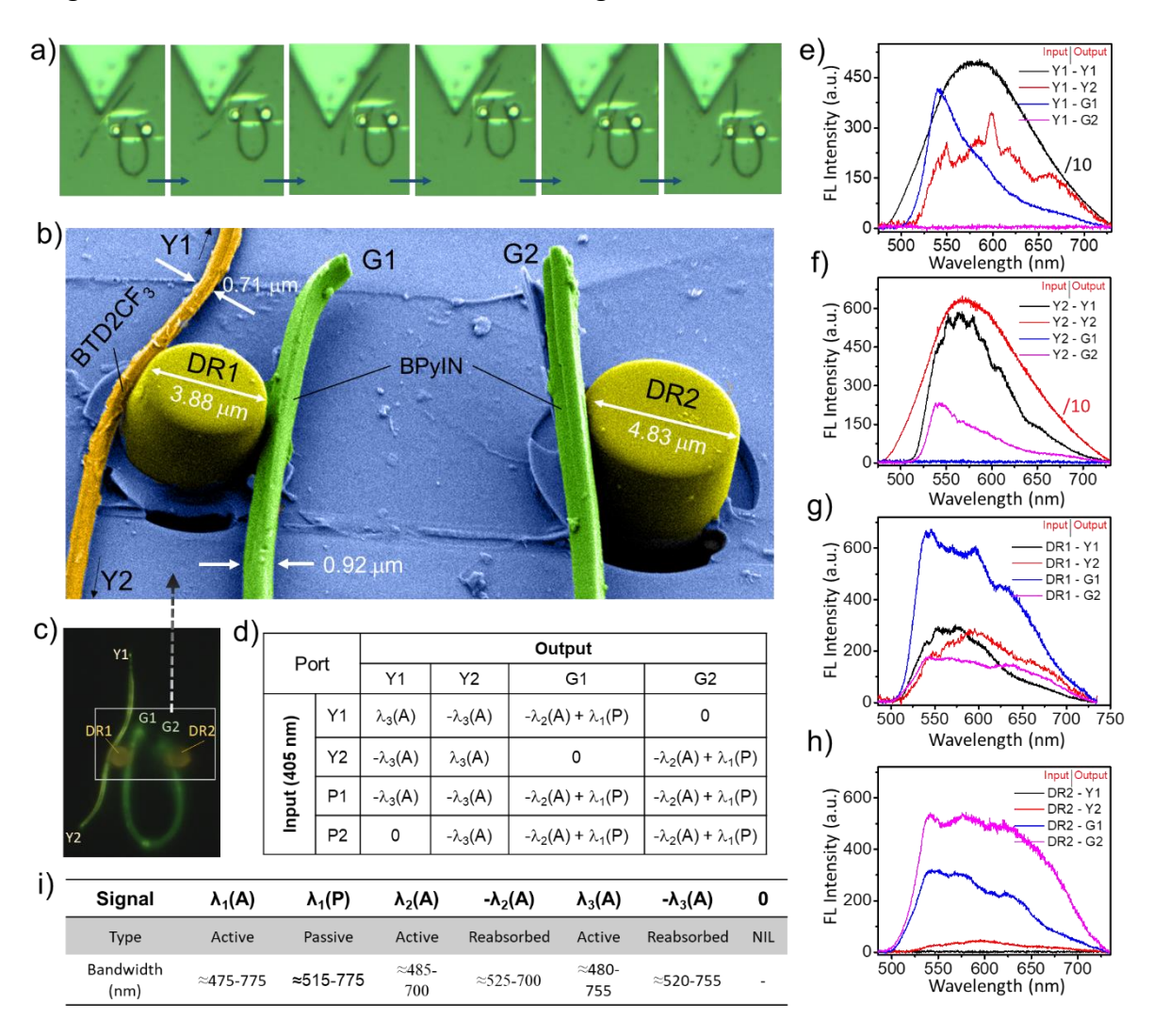


Figure 5.8. Confocal optical microscope images captured while a) transferring and b) positioning of BTD2CF<sub>3</sub> microcrystal at the circuit's site. Scale bar  $10 \mu m$ .

Finally, to fabricate the envisioned hybrid OPIC, i.e., HOADF, BTD2CF<sub>3</sub> microcrystal waveguide was transferred to the circuit site by air-lifting it from another substrate and carefully dropping it near the DRs-coupled waveguide circuit (Figure 5.8a,b). The BTD2CF<sub>3</sub> microcrystal was meticulously brought into evanescent contact with the DR1 via mechanical

micromanipulation to realize HOADF (Figure 5.9a). The color-coded FESEM image shows the physical contact between DR1 and BTD2CF $_3$  waveguide in the fabricated hybrid OPIC (Figure 5.9b). The thickness of BPyIN and BTD2CF $_3$  microcrystals measured from the FESEM image at the depicted places were 0.92 and 0.71  $\mu$ m, respectively. Further, the FESEM image clearly reveals the variation in thickness of the waveguides obtained from the self-assembly process, while the FIB-milled DRs constituted smooth morphology. The corresponding FL image of the constructed HOADF is shown in Figure 5.9c.



**Figure 5.9.** a) Confocal optical microscope images depicting the micromechanical integration of BTD2CF<sub>3</sub> with the DR1. b) The color-coded FESEM image of a portion of hybrid OPIC portraying the contact between DRs and waveguides. c) FL microscope image of the fabricated hybrid OPIC using the FIB milled perylene DRs and BPyIN and BTD2CF<sub>3</sub> microcrystals. d) Input-dependent direction-specific optical outputs obtained in the fabricated hybrid OPIC. e-h) The FL spectra recorded at various outputs for input provided at Y1, Y2, DR1, and DR2, respectively. i) The optical signals, bandwidths, and propagation mechanisms governing the functioning of hybrid OPIC.

The photonic performance of the fabricated HOADF was assessed by exciting one of the termini (with 405 nm) and analyzing the outputs at the rest of the termini. The terminal Y1 (here, Y stands for yellow emission) of BTD2CF3 in HOADF was excited to produce a  $\lambda_3$ (A) (bandwidth  $\approx$ 480-755 nm) signal at Y1. The  $\lambda_3$ (A) signal propagated to the other end of BTD2CF3, and the spectrum revealed a slightly reabsorbed FL  $-\lambda_3$ (A) (bandwidth  $\approx$ 520-755 nm). On its way towards Y2,  $-\lambda_3$ (A) signal evanescently couples to DR1 and excites it via ET to produce  $\lambda_1$ (A) ( $\approx$ 485-775 nm) signal. The generated signal is routed in an anti-clockwise direction by DR1 and guided towards G1 in BPyIN waveguide. Because of the ET from perylene to BPyIN, a  $-\lambda_2$ (A)+ $\lambda_1$ (P) signal was detected at G1 terminal, as observed in the DRs-coupled waveguide. Importantly, due to the controlled light guiding ability of DR1, light is not allowed to travel in the clockwise direction, and therefore no optical signal is observed at G2 (Figure 5.9d,e). Thereby, hybrid OPIC demonstrates the selective light guiding in the circuit and functions as an add-drop filter.

When the laser input position was given to Y2,  $\lambda_3(A)$  signal was observed at the excitation point,  $-\lambda_3(A)$  signal at Y1, and no output was recorded at G1. However, the clockwise rotated signal ( $\lambda_1(A)$ ) in DR-1 is dropped into BPyIN resulting in  $-\lambda_2(A)+\lambda_1(P)$  signal at G2 (Figure 5.9f). Later, excitation at DR1 resulted in bright yellow FL of perylene ( $\lambda_1(A)$ ; ≈485-775 nm), which in turn coupled into both BPyIN and BTD2CF<sub>3</sub> waveguides. Therefore, a signal of  $-\lambda_3(A)$  (bandwidth  $\approx$ 520-755 nm) was observed at Y1 and Y2 due to ET from perylene to BTD2CF<sub>3</sub>. The higher PLQY of BTD2CF<sub>3</sub> enables maximum absorption of perylene FL and no significant contribution from the  $\lambda_1(P)$  signal at Y1 and Y2. Here, the point excitation in DR1 leads to simultaneous scattering in all directions, so the light output at both Y1 and Y2 was observed (Figure 5.9g). However, at G1 and G2 the collected spectra exhibited a broad band corresponding to mixed signals from BPyIN and perylene,  $-\lambda_3(A)$  $+\lambda_1(P)$  due to simultaneous transduction and active and passive signals as seen previously (Figure 5.9g and 5.7f). Similarly, light input at DR2 resulted in FL output at G1, G2, and Y2 but no signal at Y1 due to directional light guiding from DR1 (Figure 5.9h). The resultant signals and their bandwidths at different ports are provided in Figure 5.9d,i. Hence, the design and construction of hybrid OPICs render great significance for the advancement of

the organic photonics field, and the tandem use of different techniques immensely contributes to taking OPICs to the fab processing level.

#### 5.4. Conclusions

In summary, for the first time, crystal photonics foundry and mechanophotonics techniques were utilized to fabricate a hybrid OPIC. The FIB-milled perylene circular DRs (with diameters DR1 =3.88, DR2 =4.83, and DR3 =5.74 µm) display the size-dependent resonator effect. The perylene single crystals were mechanically movable before milling; however, after milling, the fabricated crystal resonators were attached to the substrate firmly due to milling-induced local heat. Hence, to create the envisioned hybrid organic adddrop filter (HOADF), the parental crystal was carefully stripped off the DRs using the AFM cantilever tip. Then, green-emissive U-shaped (E)-1-(((5-bromopyridin-2yl)imino)methyl)naphthalen-2-ol (BPyIN) waveguide was connected to the perylene DRs to DRs-coupled waveguide. yellow realize the Later, а emissive (*Z*)-2-(3,5bis(trifluoromethyl)phenyl)-3-(7-methoxybenzo[c][1,2,5] thiadiazol-4-yl)acrylonitrile (BTD2CF<sub>3</sub>) was transferred near the circuit fabrication place and eventually integrated with DR1 to construct a HOADF. The fabricated HOADF functions as a typical add-drop filter, which dictates directed-light propagation in the circuits. The DRs route optical signals in a clockwise or anti-clockwise direction. The detailed photonics investigations reaffirmed the directional specificity expected from the circuit geometry in HOADF.



# **Conclusions and Future Scope**

#### 6.1. Conclusions

This thesis entitled "Design and Fabrication of Single-Crystal Organic Photonic Circuit Modules Using Focused Ion Beam Lithography" described the fabrication of dimensionally and geometrically precise photonic components like disk resonators (DRs), ring resonators (RRs), waveguides, and directional couplers (DC) by optimizing the ion beam parameters via focused ion beam (FIB) lithography. Further, the first-ever hybrid organic photonic integrated circuit was fabricated by tandem use of both crystal photonics foundry and mechanophotonics processing strategies.

At the beginning of the thesis, *Chapter-1* introduced the various microresonators and the principles governing light confinement in these microresonators. A brief overview of linear and non-linear optical properties was discussed. The bottom-up (self-assembly, sublimation) and top-down (EBL, FIB) approaches involved in nanoscience and nanotechnology for photonics with the help of examples were presented. A significant focus on FIB milling, its fundamentals, and factors affecting the quality of milled microcrystals were briefly discussed. Finally, the crucial *mechanophotonics* approach was addressed for the integration of FIB-processed organic crystalline DRs with different emissive waveguides to achieve all-organic hybrid PICs.

The shape and size of the self-assembled microcrystals are the two most important elements responsible for the optical and mechanical properties of molecular crystals. In Chapter-2, for the first time, both ( $\alpha$ ) square- and ( $\beta$ ) rhombus-shaped polymorphic perylene-based optical microresonators were obtained using the ambient pressure sublimation technique. These crystalline  $\alpha$  and  $\beta$  microresonators demonstrated their ability to work as one- and two-photon pumped nanophotonic WGM resonators. A series of experiments showed the dependence of excitation position and crystal orientation with respect to laser on the FL intensity. Polarized optical microscopic studies further revealed the anisotropic nature of these microresonators. The FDTD numerical simulations revealed the electric field distribution of the trapped light and supported the experimentally observed WGM resonances. Another fascinating feature of these polymorphic optical microresonators is the observation of WGMs in the TPL signal, which is quite rare. These semiconductor-based NLO optical resonators activated by infrared lasers are useful to develop organic nanophotonic devices.

Using the ambient pressure sublimation technique, the size range of the microcrystals and a specific polymorphic form of perylene single-crystals were controlled. However, in nature, the geometrical shape of the microcrystal cannot be precisely controlled externally due to inherent crystal packing tendency and subsequent crystal growth. Hence, in *Chapter-3*, FIB milling has been employed to carve perylene single-crystal resonators into different geometries and sizes. The effects of various substrates, namely, ITO-PET and glass coverslip, and post-processing techniques (removal of the gold layer) were demonstrated. The beam parameters were optimized to 30 kV and 100 pA. The fabrication of circular-, rectangular-, hexagonal-, octagonal-, and ring-shaped photonic resonators is a proof-of-principle experiment that can be applied to other molecular crystals. The following points are pertinent for the successful milling of organic crystals while retaining their optical emission intensities and refractive index homogeneity. i) Milling parameters and crystal thickness need to be appropriate to minimize the amorphization of the exposed crystal surface, ii) thinner crystals take less milling time than thicker ones as the molecular mass to be removed around the crystal is reduced. This minimizes Ga ion exposure to the unmilled crystal area. iii) Further, lowering the beam current reduces beam spot size, providing higher milling focus and minimizing ion exposure to the unmilled area.

iv) Gold coating not only helps as a conductive layer for SEM imaging but also protects the crystal surface from the Ga ion implantation. v) FIB-based secondary-ion imaging of crystals during milling should be avoided to decrease the ion implantation on the crystal surface. The presented technique can be used directly to fabricate circular-, rectangular-, ring-, rod-shaped, and any other possible geometries required to create photonic modules such as resonators, waveguides, interferometers, gratings, couplers, photonic crystals, and circuits.

Further, in *Chapter-4*, FIB milling was performed to obtain organic photonic components, namely, circular and rectangular disk-resonators from single-microcrystals of coumarin 153. The fabricated photonic components reveal optical traits after milling. During chemical treatment, coumarin-153 crystals are reactive. Due to relatively high quantum yield, coumarin-153 crystal resonators show high FL intensity and optical modes, even without gold removal. Hence, the coumarin-153 crystals did not require further post-processing treatment to observe optical resonances. The FDTD numerical calculation revealed light's electric field distribution inside the microresonators. It was localized at the periphery for circular disk resonators, whereas it was primarily situated in the middle of the edges for rectangular disk resonator. These results validate the generality of the FIB milling technique to carve out optical components of desired shape and dimension from organic single-crystals. The field of *crystal photonics foundry*, i.e., FIB milling of organic crystals into photonic modules, has the potential to produce industrial-scale manufacturing of organic photonic circuitry and devices.

Finally, the fields of crystal photonics foundry and mechanophotonics were utilized to attain the first novel hybrid OPIC, i.e., hybrid organic add-drop filter (HOADF). Chapter-5 reveals the fabrication of precise FIB-milled perylene DRs (having diameters DR1=3.88, DR2=4.83, and DR3=5.74 µm) on a single perylene microcrystal. The fabricated DRs displayed the size-dependent resonator effect. Then, the parental crystal was carefully removed from the DRs' site using the AFM cantilever tip to attain isolated DRs. Further, pseudo-plastic subsequent integration with waveguides, namely (Z)-2-(3,5bis(trifluoromethyl)phenyl)-3-(7-methoxybenzo[c][1,2,5] thiadiazol-4-yl)acrylonitrile (BTD2CF<sub>3</sub>) and (E)-1-(((5-bromopyridin-2-yl)imino)methyl)naphthalen-2-ol (BPyIN) resulted in HOADF. For this, a green-emissive U-shaped BPyIN waveguide was connected to the perylene DRs to realize the DRs-coupled waveguide. Later, yellow emissive BTD2CF3 was

transferred near the circuit fabrication place and eventually integrated with DR1 to construct a HOADF. The fabricated HOADF functions as a typical add-drop filter, which dictates directed-light propagation in the circuits. The DRs route optical signals in a clockwise or anti-clockwise direction depending on the input signal. The detailed photonics investigations reaffirmed the directional specificity expected from the circuit geometry in HOADF. This novel work uncovers the hidden potential of organic crystalline materials to thrive as an alternative materials platform to silicon-based materials by demonstrating the fabrication of dimensionally precise optical components. Importantly, it illustrates the ease with which different photonic modules constituting different materials can be integrated on a photonic chip. The amalgamation of micromechanical manipulation technique with crystal milling technology paves the path towards automated bulk-scale manufacturing of OPICs.

#### **6.2.** Future scope of the work

This thesis demonstrated a facile and compatible way to attain control over the size range of perylene microcrystals via the ambient pressure vapor deposition technique. Later, the usage of FIB milling enabled the construction of geometrical and dimensional precise microresonators from chemically, mechanically, and opto-electronically different perylene and coumarin-153 organic molecular single-crystals. Micromanipulation of self-assembled microcrystals using AFM cantilever tip allowed the fabrication of various geometries and facilitated the construction of hybrid photonic circuits. The amalgamation of the FIB milling technique (crystal photonics foundry) and mechanical micromanipulation (mechanophotonics) paved a path to attain hybrid OPIC with precise geometries.

Certain issues need to be addressed and pursued further to commercialize the FIB technique to accomplish industrial standard bulk processing of organic components for photonic device technologies. Therefore, the presented thesis expands the scope of the FIB technique for organic photonics in the following terms:

- Study of various protective layers (conductive materials) while performing FIB
  milling and SEM imaging and their subsequent etchants.
- 2. Fabrication of PIC on a single microcrystal.
- 3. Milling of NLO active microcrystals and subsequent NLO studies.

- 4. Micromechanical transportation of FIB milled microstructures from one substrate to another for the construction of *hybrid* OPICs.
- 5. Finally, automated fabrication of complete functional organic photonic chips for commercial application.

#### References

- M. Wale, Advanced Photonics Congress, Optical Society of America, Colorado Springs, USA 2012, JTu1B, 1.
- D. Thomson, A. Zilkie, J. E. Bowers, T. Komljenovic, G. T. Reed, L. Vivien, D. Marris-Morini, E. Cassan, L. Virot, J. M. F'ed'eli, J. Hartmann, J. Schmid, D. X. Xu, F. Boeuf, P. O'Brien, G. Z. Mashanovich and M. Nedeljkovic, *J. Optics.* 2016, 18, 073003.
- 3. L. Chrostowski and M. Hochberg, Silicon Photonics Design: From Devices to Systems, Cambridge University Press, Cambridge **2015**.
- 4. https://en.wikipedia.org/wiki/Jack\_Kilby.
- 5. https://en.wikipedia.org/wiki/Robert\_Noyce.
- 6. C. Scarcella, J. S. Lee, C. Eason, M. Antier, J. Bourderionnet, C. Larat, E. Lallier, A. Brignon, T. Spuesens, P. Verheyen, P. Absil, R. Baets and P. O'Brien, *Photonics* **2016**, *3*, 1.
- 7. W. Bogaerts, D. Pérez, J. Capmany, D. A. B. Miller, J. Poon, D. Englund, F. Morichetti and A. Melloni, *Nature* **2020**, *586*, 207.
- 8. W. Bogaerts and L. Chrostowski, Laser Photonics Rev. 2018, 12, 1700237.
- 9. X. Chen, M. M. Milosevic, S. Stanković, S. Reynolds, T. D. Bucio, K. Li, D. J. Thomson, F. Gardes and G. T. Reed, *Proc. IEEE* **2018**, *106*, 2101.
- 10. S. Lourdodoss, R. T. Chen and C. Jagadish, Semiconductors and Semimetals Book Series, Academic Press, Cambridge **2018**, *99*, 228.
- 11. P. Dong, Y. K. Chen, G. H. Duan and D. T. Neilson, Nanophotonics 2014, 3, 215.
- 12. R. Chandrasekar, Small 2021, 17, 2100277.
- 13. R. Chandrasekar, *Chem. Commun.* **2022**, *58*, 3415.
- 14. R. Chandrasekar, Adv. Opt. Mater. 2023, 11, 2301124.
- 15. V. V. Pradeep, C. Tardio, I. T. Moya, A. M. Rodriguez, A. V. Kumar, M. Annadhasan, A. de la Hoz, P. Prieto and R. Chandrasekar, *Small* **2021**, *17*, 2006795.
- 16. K. Takazawa, Y. Kitahama, Y. Kimura and G. Kido, Nano Lett. 2005, 5, 1293.
- 17. M. Annadhasan, S. Basak, N. Chandrasekhar and R. Chandrasekar, *Adv. Opt. Mater.* **2020**, *8*, 2000959.
- 18. Y. S. Zhao, Organic Nanophotonics: Fundamentals and Applications, Springer, Berlin **2014**.
- 19. D. Venkatakrishnarao, E. A. Mamonov, T. V. Murzina and R. Chandrasekar, *Adv. Opt. Mater.* **2018**, *6*, 1800343.
- 20. N. Chandrasekhar, S. Basak, M. A. Mohiddon and R. Chandrasekar, *ACS Appl. Mater. Interfaces* **2014**, *6*, 1488.
- 21. V. V. Pradeep, M. Annadhasan and R. Chandrasekar, Chem. Asian J. 2019, 14, 4577.
- Y. Zhang, Q. Liao, X. G. Wang, J. N. A. Yao and H. B. Fu, Angew. Chem. Int. Ed. 2017, 56, 3616.

- 23. M. P. Zhuo, J. J. Wu, X. D. Wang, Y. C. Tao, Y. Yuan and L. S. Liao, *Nat. Commun.* **2019**, *10*, 3839.
- 24. M. Annadhasan, D. P. Karothu, R. Chinnasamy, E. Ahmed, L. Catalano, S. Ghosh, P. Naumov and R. Chandrasekar, *Angew. Chem. Int. Ed.* **2020**, *59*, 13821.
- 25. H. Liu, Z. Lu, Z. Zhang, Y. Wang and H. Zhang, *Angew. Chem. Int. Ed.* **2018**, *57*, 8448.
- 26. Z. Lu, Y. Zhang, H. Liu, K. Ye, W. Liu and H. Zhang, *Angew. Chem. Int. Ed.* **2020**, *59*, 4299.
- 27. S. Hayashi and T. Koizumi, *Angew. Chem. Int. Ed.* **2016**, *55*, 2701.
- 28. L. Catalano, D. P. Karothu, S. Schramm, E. Ahmed, R. Rezgui, T. J. Barber, A. Famulari and P. Naumov, *Angew. Chem. Int. Ed.* **2018**, *57*, 17254.
- 29. J. M. Halabi, E. Ahmed, L. Catalano, D. P. Karothu, R. Rezgui and P. Naumov, *J. Am. Chem. Soc.* **2019**, *141*, 14966.
- 30. R. Chandrasekar, Phys. Chem. Chem. Phys. 2014, 16, 7173.
- 31. N. Chandrasekhar, M. A. Mohiddon and R. Chandrasekar, *Adv. Opt. Mater.* **2013**, *1*, 305.
- 32. P. Hui and R. Chandrasekar, Adv. Mater. 2013, 25, 2963.
- 33. N. Chandrasekhar, R. Reddy, M. D. Prasad and R. Chandrasekar, *Cryst. Eng. Comm.* **2014**, *16*, 4696.
- 34. D. Venkatakrishnarao, M. A. Mohiddon, N. Chandrasekhar and R. Chandrasekar, *Adv. Opt. Mater.* **2015**, *3*, 1035.
- 35. R. Chen, V. D. Ta and H. D. Sun, ACS Photonics **2014**, *1*, 11.
- 36. S. G. Lipson, H. Lipson, and D. S. Tannhauser, Optical Physics (3rd ed.). London: Cambridge U.P. **1995**, 248. ISBN 0-521-06926-2.
- 37. W. Weng, J. D. Anstie, T. M. Stace, G. Campbell, F. N. Baynes and A. N. Luiten, *Phys. Rev. Let.* **2014**, *112*, 160801.
- 38. M. G. Scullion, T. F. Krauss and A. D. Falco, Sensors 2013, 13, 3675.
- 39. F. Vollmer, S. Arnold, and D. Keng, *Proc. Natl. Acad. Sci.* **2008**, *105*, 20701.
- 40. D. V. Strekalov, C. Marquardt, A. B. Matsko, H. G. L. Schwefel and G. Leuchs, *J. Opt.* **2016**, *18*, 123002.
- 41. A. Kiraz, A. Kurt, M. Dündar and A. Demirel, *Appl. Phys. Lett.* **2006**, *89*, 081118.
- 42. F. Albert, T. Braun, T. Heindel, C. Schneider, S. Reitzenstein, S. Höfling, L. Worschech and A. Forchel, *Appl. Phys. Lett.* **2010**, *97*, 101108.
- 43. V. S. Ilchenko and A. B. Matsko, IEEE J. Sel. Top. Quant. Electron. 2006, 12, 15.
- 44. A. Yalcin, K. C. Popat, J. C. Aldridge, T. A. Desai, J. Hryniewicz, N. Chbouki, B. E. Little, O. King, V. Van and S. Chu, *IEEE J. Sel. Top. Quant. Electron.* **2006**, *12*, 148.
- 45. S. T. Chu, B. E. Little, W. Pan, T. Kaneko, S. Sato and Y. Kokubun, *Photon. Technol. Lett.* **1999**, *11*, 691.
- 46. W. Zhang, J. Yao and Y. S. Zhao, *Acc. Chem. Res.* **2016**, *49*, 1691.
- 47. F. Sasaki, S. Kobayashi, S. Haraichi, S.Fujiwara, K. Bando, Y. Masumoto and S. Hotta, *Adv. Mater.* **2007**, *19*, 3653.

- 48. H. Yoshioka, T. Ota, C. Chen, S. Ryu, K. Yasui and Y. Oki, *Sci. Rep.* **2015**, *5*, 10623.
- 49. Y. C. Tao, X. D. Wang, L. S. Liao, J. Mater. Chem. C 2019, 7, 3443.
- 50. K. Tabata, D. Braam, S. Kushida, L. Tong, J. Kuwabara, T. Kanbara, A. Beckel, A. Lorke, Y. Yamamoto, *Sci. Rep.* **2014**, *4*, 5902.
- 51. J. Ravi, D. Venkatakrishnarao, C. Sahoo, S. R. G. Naraharisetty, N. Mitetelo, A. A. Ezhov, E. Mamonov, T. Murzina, R. Chandrasekar, *Chem. Nano. Mat.* **2018**, *4*, 764.
- 52. D. Venkatakrishnarao, C. Sahoo, E. A. Mamonov, I. A. Kolmychek, A. I. Maydykovskiy, N. V. Mitetelo, V. B. Novikov, S. R. G. Naraharisetty, T. V. Murzina and R. Chandrasekar, *J. Mater. Chem. C* **2017**, *5*, 12349.
- 53. C. Fabry and A. Perot, *Ann. Chim. Phys.* **1889**, *16*, 7.
- 54. M. S. Nawrocka, T. Liu, X. Wang and R. R. Panepucci, *Appl. Phys. Lett.* **2006**, *89*, 071110.
- 55. S. Yang, Y. Wang and H. Sun, *Adv. Opt. Mater.* **2015**, *3*, 1136.
- 56. M. L. Gorodetsky, A. A. Savchenkov and V. S. Ilchenko, Opt. Lett. 1996, 21, 453.
- 57. G. C. Righini, Y. Dumeige, P. Féron, M. Ferrari, G. N. Conti, D. Ristic and S. Soria, *Riv. Nuovo Cimento.* **2011**, *34*, 435.
- 58. S. M. Spillane, PhD Thesis, California Institute of Technology, May, **2004**.
- 59. Y.-D. Yang, Y.-Z. Huang and Q. Chen, *Phys. Rev. A* **2007**, *75*, 013817.
- 60. I. Kandas, B. Zhang, C. Daengngam, I. Ashry, C.-Y. Jao, B. Peng, S. K. Ozdemir, H. D. Robinson, J. R. Heflin, L. Yang and Y. Xu, *Opt. Exp.* **2013**, *21*, 18.
- 61. F. Vollmer, S. Arnold and D. Keng, *Proc. Natl. Acad. Sci.* **2008**, *105*, 20701.
- 62. L. Rayleigh, Lond. Edinb. Dubl. Phil. Mag. 1910, 20, 1001.
- 63. L. Rayleigh, *Proc. R. Soc. London A* **1912**, *86*, 207.
- 64. A. Michelson and E. Morley, Am. J. Sci. 1887, 34, 333.
- 65. C. Zhang, C.-L. Zou, Y. Yan, R. Hao, F.-W. Sun, Z.-F. Han, Y. S. Zhao and J. Yao, *J. Am. Chem. Soc.* **2011**, *133*, 7276.
- 66. C. Garrett, W. Kaiser and W. Bond, *Phys. Rev.* **1961**, *124*, 1807.
- 67. C. Y. Chao and L. J. Guo, Appl. Phys. Lett. 2003, 83, 1527.
- 68. A. C. Tamboli, E. D. Haberer, R. Sharma, K. H. Lee, S. Nakamura and E. L. Hu, *Nat. Phot.* **2007**, *1*, 61.
- 69. D. Armani, B. Min, A. Martin and K. J. Vahala, Appl. Phys. Lett. 2004, 85, 5439.
- 70. V. D. Ta, R. Chen, L. Ma, Y. J. Ying and H. D. Sun, Laser Photonics Rev. 2013, 7, 133.
- 71. Y. Yoshida, T. Nishimura, A. Fujii, M. Ozaki and K. Yoshino, *Appl. Phys. Lett.* **2005**, *86*, 141903.
- 72. X. Zhang, L. Liu and L. Xu, *Appl. Phys. Lett.* **2014**, *104*, 033703.
- 73. S. Berneschi, D. Farnesi, F. Cosi, G. N. Conti, S. Pelli, G. Righini and S. Soria, *Opt. Lett.* **2011**, *36*, 3521.
- 74. V. D. Ta, R. Chen and H. D. Sun, *Adv. Mater.* **2012**, *24*, 60.
- 75. J. Haase, S. Shinohara, P. Mundra, G. Risse, V. Lyssenko, H. Fröb, M. Hentschel, A. Eychmüller and K. Leo, *Appl. Phys. Lett.* **2010**, *97*, 211101.

- 76. G. Zhu, J. Li, N. Zhang, X. Li, J. Dai, Q. Cui, Q. Song, C. Xu and Y. Wang, *Sci. Rep.* **2020**, *10*, 253.
- 77. G. Schunk, J. U. Furst, M. Fortsch, D. V. Strekalov, U. Vogl, F. Sedlmeir, H. G. L. Schwefel, G. Leuchs and C. Marquardt, *Opt. Express* **2014**, *22*, 30795.
- 78. A. N. Oraevsky, *Quantum Electron.* **2002**, *32*, 377.
- 79. P. N. Prasad and B. A. Reinhardt, *Chem. Mater.* **1990**, *2*, 660.
- 80. Richard S. Quimby, Photonics and lasers: An introduction, John Wiley & Sons, Inc. **2006**.
- 81. N. Mitetelo, D. Venkatakrishnarao, J. Ravi, M. Popov, E. Mamonov, T. Murzina and R. Chandrasekar, *Adv. Opt. Mater.* **2019**, *7*, 1801775.
- 82. M. Göppert-Mayer, Ann. Phys. 1931, 401, 273.
- 83. G. M. Whitesides, J. P. Mathias and C. T. Seto, *Science* **1991**, *254*, 1312.
- 84. J. V. Barth, Annu. Rev. Phys. Chem. 2007, 58, 375.
- 85. J. W. Steed, Supramolecular chemistry, Wiley, Chichester 2000.
- 86. C. F. J. Faul and M. Antonietti, *Adv. Mater.* **2003**, *15*, 673.
- 87. X. Ye, Y. Liu, Q. Han, C. Ge, S. Cui, L. Zhang, X. Zheng, G. Liu, J. Liu, D. Liu and X. Tao, *Chem. Mater.* **2018**, *30*, 412.
- 88. V. V. Pradeep, N. Mitetelo, M. Annadhasan, M. Popov, E. Mamoniv, T. Murzina and R. Chandrasekar, *Adv. Opt. Mater.* **2020**, *8*, 1901317.
- 89. C. Zhang, C. Zou, Y. Yan, R. Hao, F. Sun, Z. Han, Y. S. Zhao and J. Yao, *J. Am. Chem. Soc.* **2011**, *133*, 7276.
- 90. D. Venkatakrishnarao and R. Chandrasekar, Adv. Opt. Mater. 2015, 4, 112.
- 91. C. Wei, S. Liu, C. Zou, Y. Liu, J. Yao and Y. S. Zhao, *J. Am. Chem. Soc.* **2015**, *137*, 62.
- 92. R. Deng, S. Liu, J. Li, Y. Liao, J. Tao and J. Zhu, Adv. Mater. 2012, 24, 1889.
- 93. T. Adachi, L. Tong, J. Kuwabara, T. Kanbara, A. Saeki, S. Seki and Y. Yamamoto, *J. Am. Chem. Soc.* **2013**, *135*, 870.
- 94. C. Zhang, C. -L. Zou, Y. Yan, C. Wei, J. -M. Cui, F. W. Sun, J. Yao and Y. S. Zhao, *Adv. Opt. Mater.* **2013**, *1*, 357.
- 95. M. Shirayama, M. Kato, T. Miyadera, T. Sugita, T. Fujiseki, S. Hara, H. Kadowaki, D. Murata, M. Chikamatsu and H. Fujiwara, *J. Appl. Phys.* **2016**, *119*, 115501.
- 96. X. Liu, S. Ha, Q. Zhang, M. de la Mata, C. Magen, J. Arbiol, T. C. Sum and Q. Xiong, *ACS Nano* **2015**, *9*, 687.
- 97. M. Jain, A. Singh, P. Basera, M. Kumar and S. Bhattacharya, *J. Mater. Chem. C* **2020**, *8*, 10362.
- 98. X. Li, K. Wang, M. Chen, S. Wang, Y. Fan, T. Liang, Q. Song, G. Xing and Z. Tang, *Adv. Opt. Mater.* **2020**, *8*, 2000030.
- 99. R. Feynman, "There's Plenty of Room at the Bottom", 1959.
- 100. M. D. Austin, H. X. Ge, W. Wu, M. T. Li, Z. N. Yu, D. Wasserman, S. A. Lyon and Y. S. Chou, *Appl. Phys. Lett.* **2004**, *84*, 5299.
- 101. S. Basak, P. Hui and R. Chandrasekar, *Chem. Mater.* **2013**, *25*, 3408.

- 102. C. Martin, G. Rius, X. Borrise and F. P. Murano, Nanotechnology 2005, 16, 1016.
- 103. N. W. Parker, A. D. Brodie and J. H. McCoy, *Proc. SPIE* **2000**, *3997*, 713.
- 104. V. M. Bermudez, J. Vac. Sci. Technol. B Microelectron. Nanom. Struct. Process. Meas. Phenom. 1999, 17, 2512.
- 105. D. R. S. Cumming, S. Thoms, S. P. Beaumont and J. M. R. Weaver, *Appl. Phys. Lett.* **1996**, *68*, 322.
- 106. V. V. Pradeep and R. Chandrasekar, Adv. Opt. Mater, 2022, 10, 2201150.
- 107. J. Ravi and R. Chandrasekar, Adv. Opt. Mater. 2021, 9, 2100550.
- 108. J. Ravi, M. Annadhasan, A. V. Kumar and R. Chandrasekar, *Adv. Funct. Mater.* **2021**, 31, 2100642.
- 109. J. Ravi, A. V. Kumar, D. P. Korathu, M. Annadhasan, P. Naumov and R. Chandrasekar, *Adv. Funct. Mater.* **2021**, *31*, 2105415.
- 110. A. V. Kumar and R. Chandrasekar, Adv. Opt. Mater. 2023, 11, 2201009.
- 111. A. V. Kumar, E. Mamonov, T. Murzina and R. Chandrasekar, *Adv. Opt. Mater.* **2022**, *11*, 2201507.
- 112. K. Takazhawa, J. Inoue and K. Mitsuichi, ACS Appl. Mater. Interfaces 2013, 5, 6182.
- 113. Q. Li, J. Light. Technol. 2008, 26, 3744.
- 114. X. Wang, X. Guan, Q. Huang, J. Zheng, Y. Shi and D. Dai, Opt. Lett. 2013, 38, 5405.
- 115. A. M. Prabhu, A. Tsay, Z. Han and V. Van, IEEE Photon. Technol. Lett. 2009, 21, 651.
- 116. T. Tao, W. Wilkinson and J. Melngailis, J. Vac. Sci. Technol. B 1991, 9, 162.
- 117. L. R. Harriott and M. J. Vasile, J. Vac. Sci. Technol. B: Microelectron. Process. Phenom. 1988, 6, 1035.
- 118. M. T. Abramo and L. L. Hahn, *Microelectron. Reliab.* **1996**, *8*, 361775.
- 119. A. A. Volinsky, L. Rice, W. Qin and N. D. Theodore, Microelectron. Eng. 2004, 75, 11.
- 120. K. Nikawa, J. Vac. Sci. Technol. B 1991, 9, 2566
- 121. J. Mayer, L. A. Giannuzzi, T. Kamino and J. Michael, Mater. Res. Bull. 2007, 32, 400.
- 122. N. I. Kato, *Microscopy* **2004**, *53*, 451.
- 123. R. M. Langford and A. K. Petford-Long, J. Vac. Sci. Technol. A 2001, 19, 2186.
- 124. R. M. Langford, *Microsc. Res. Tech.* **2006**, *69*, 538.
- 125. J. Gierak, P. Mazarov, L. Bruchhaus, R. Jede and L. Bischoff, *J. Vac. Sci. Technol. B* **2018**, *36*, 06J101.
- 126. L. Bischoff, N. Klingner, P. Mazarov, W. Pilz and F. Meyer, *J. Vac. Sci. Technol. B* **2020**, *38*, 042801.
- 127. S. Kellogg, R. Schampers, S. Zhang, A. Graupera, T. Miller, W. D. Laur and A. Dirriwachter, *Microsc. Microanal.* **2010**, 16222.
- 128. T. Hrncir, A. Delobbe, O. Salord, F. Lopour, M. Zadrazil and P. Sudraud, *Proc. 38th Int. Symp. Test. Failure Analys.* **2012**, 26.
- 129. https://periodictable.com/Elements/031/index.html.
- 130. L. A. Giannuzzi and F. A. Stevie, New York: Springer **2005**, *357*, DOI: 10.1007/b101190.

- 131. https://caltech.app.box.com/s/cs0wj4dn89am3fof8ox0vqetaad8ylg8/file/41515547
- 132. S. Reyntjens and R. Puers, J. Micromech. Microeng. 2001, 11, 287.
- 133. C. A. Volkert and A. M. Minor, *Mater. Res. Bull.* **2007**, *32*, 389.
- 134. A. A. Tseng, Small 2005, 1, 924.
- 135. C.-S. Kim, S.-H. Ahn and D.-Y. Jang, *Vacuum* **2012**, *86*,1014.
- 136. F. Watt, A. A. Bettiol, J. A. Vankan, E. J. Teo, and M. B. H. Breese, *Int. J. Nanosci.* **2005**, *4*, 269.
- 137. C. A. Volkert and A. M. Minor, MRS Bull. 2007, 32, 389.
- 138. M. Stepanova and S. Dew, Nanofabrication: techniques and principles, Springer Science & Business Media, GER, **2011.**
- 139. I. Utke, P. Hoffmann and J. Melngailis, *J. Vac. Sci. Technol. B: Microelectron. Nanometer Struct. Process. Meas. Phenom.* **2008**, *26*, 1197.
- 140. D. C. Joy, Helium Ion Microscopy: Principles and Applications, Springer, GER, 2013.
- 141. T. L. Burnett, R. Kelley, B. Winiarski, L. Contreras, M. Daly, A. Gholinia, M. G. Burke and P. J. Withers, *Ultramicroscopy* **2016**, *161*, 119.
- 142. https://lab.kni.caltech.edu/ORION\_NanoFab:\_Helium,\_Neon\_%26\_Gallium\_FIB# Ne-FIB\_Specifications.
- 143. https://assets.thermofisher.com/TFS-Assets%2FMSD%2FDatasheets%2FHelios-Hydra-UX-datasheet.pdf
- 144. S. H. Lee, H. W. Kang, D. W. Cho and W. Moon, *Microsyst. Technol.* **2007**, *13*, 569.
- 145. N. C. Lindquist, P. Nagpal, K. M. McPeak, D. J. Norris, and S. -H. Oh, *Rep. Prog. Phys.* **2012**, *75*, 036501.
- 146. C. K. Malek, F. T. Hartley and J. Neogi, Microsyst. Technol. 2003, 9, 409.
- 147. S. Kim, M. J. Park, N. P. Balsara, G. Liu and A. M. Minor, *Ultramicroscopy* **2011**, *111*, 191.
- 148. R. M. Langford, A. K. Petford-Long, J. Vac. Sci. Technol. A: Vac. Surf. Films 2001, 19, 2186.
- 149. N. Yao, Focused ion beam system a multifunctional tool for nanotechnology. In: Handbook of Microscopy for Nanotechnology, **2005**.
- 150. A. A. Tseng, I. A. Insua, J. S. Park, B. Li and G. P. Vakanas, *J. Vac. Sci. Technol. B* **2004**, *22*, 82.
- 151. H. B. Kim, G. Hobler, A. Lugstein and E. Bertagnolli, *J. Micromech. Microeng.* **2007**, *17*, 1178.
- 152. T. Nenadovic´, B. Perraillon, Z. Bogdanov, Z. Djordjevic´ and M. Milic´, *Nucl. Instrum. Methods Phys. Res. Sect. B* **1990**, *48*, 538.
- 153. S. N. Bhavsar, S. Aravindan and P. V. Rao, Mater. Manuf. Process 2012, 27, 1029.
- 154. J. Benawra, A. Donald and M. Shannon, J. Phys. Conf. Ser. 2008, 126, 2079.
- 155. V. S. Smentkowski, *Prog. Surf. Sci.* **2000**, *64*, 1.

- 156. G. A. Glass, J. F. Dias, A. D. Dymnikov and B. Rout, *Nucl. Instrum. Methods Phys. Res. Sect. B* **2008**, *266*, 3330.
- 157. D. P. Adams, M. J. Vasile, T. M. Mayer and V. C. Hodges, *J. Vac. Sci. Technol. B* **2003**, *21*, 2334.
- 158. Y. Xu and N. Matsumoto, *RSC Adv.* **2015**, *5*, 50638.
- 159. Y. Chen, K. Bi, Q. Wang, M. Zheng, Q. Liu, Y. Han, J. Yang, S. Chang, G. Zhang and H. Duan, *ACS Nano* **2016**, *10*, 11228.
- 160. K. Sloyan, H. Melkonyan and M. S. Dalham, *Int. J. Adv. Manufact. Tech.* **2020**, *107*, 4469.
- 161. S. Basak and R. Chandrasekar, J. Mater. Chem. C 2014, 2, 1404.
- 162. M. Annadhasan, A. R. Agarwal, S. Bhunia, V. V. Pradeep, S. S. Zade, C. M. reddy and R. Chandrasekar, *Angew. Chem. Int. Ed.* **2020**, *59*,13852.
- 163. M. Rohullah, V. V. Pradeep, J. Ravi, A. V. Kumar and R. Chandrasekar, *Angew. Chem. Int. Ed.* **2020**, *61*, e202202114.
- 164. W. Bogaerts, S. K. Selvaraja, P. Dumon, J. Brouckaert, K. De Vos, D. Van Thourhout and R. Baets, *IEEE J. Sel. Top. Quantum Electron.* **2010**, *16*, 33.
- 165. W. Bogaerts, R. Baets, P. Dumon, V. Wiaux, S. Beckx, D. Taillaert, B. Luyssaert, J. Van Campenhout, P. Bienstman and D. Van Thourhout, *J. Light. Technol.* **2005**, *23*, 401.
- 166. J. Ravi, A. V. Kumar, M. Annadhasan and R. Chandrasekar, *Adv. Opt. Mater.* **2022**, *10*, 2102545.
- 167. M. Annadhasan, V. V. Pradeep, A. V. Kumar, J. Ravi and R. Chandrasekar, *Small Struct.* **2022**, *3*, 2100163.
- 168. D. M. Donaldson, J. M. Robertson and J. G. White, *Proc. R Soc. Lon. A Math. Phys. Sci.* 1953, *220*, 311.
- 169. J. Tanaka, Bull. Chem. Soc. Jpn. 1963, 36, 1237.
- 170. P. Ranke, I. Bleyl, J. Simmerer, D. Haarer, A. Bacher and H. W. Schmidt, *Appl. Phys. Lett.* **1997**, *71*, 1332.
- 171. P. R. L. Malenfant, C. D. Dimitrakopoulos, J. D. Gelorme, L. L. Kosbar, T. O. Graham, A. Curioni and W. Andreoni, *Appl. Phys. Lett.* **2002**, *80*, 2517.
- 172. M. Botoshansky, F. H. Herbstein and M. Kapon, Helv. Chim. Acta 2003, 86, 1113.
- 173. K. Takazawa, Chem. Phys. Lett. 2017, 667, 284
- 174. Q. Liao, H. H. Zhang, W. G. Zhu, K. Hu and H. B. Fu, J. Mater. Chem. C 2014, 2, 9695.
- 175. Y. Lei, Q. Liao, H. Fu and J. Yao, J. Phys. Chem. C 2009, 113, 10038.
- 176. A. Pick, M. Klues, A. Rinn, K. Harms, S. Chatterjee and G. Witte, *Cryst. Growth Des.* **2015**, *15*, 5495.
- 177. C. Kloc, P. Simpkins, T. Siegrist and R. Laudise, J. Cryst. Growth 1997, 182, 416.
- 178. X. Zhang, J. Qiu, X. Li, J. Zhao and L. Liu, Appl. Opt. 2020, 59, 2337.
- 179. U. Venkataramudu, M. Annadhasan, H. Maddali and R. Chandrasekar, *J. Mater. Chem. C* **2017**, *5*, 7262.

- 180. J. Feldmann, N. Youngblood, M. Karpov, H. Gehring, X. Li, M. Stappers, M. Le Gallo, X. Fu, A. Lukashchuk, A. S. Raja, J. Liu, C. D. Wright, A. Sebastian, T. J. Kippenberg, W. H. P. Pernice and H. Bhaskaran, *Nature* **2021**, *589*, 52.
- 181. M. Lipson, Nat. Mater. 2022, 21, 974.
- 182. A. V. Kumar, M. Godumala, J. Ravi, and R. Chandrasekar, *Angew. Chem. Int. Ed.* **2022**, *61*, e202212382.

### Appendix-A

#### **Materials**

Perylene Alfa Aesar, 98%

Coumarin-153 Sigma-Aldrich, 98%

2-Hydroxy-1-naphthaldehyde Sigma-Aldrich, 98%

2-amino-5-bromo pyridine TCI, 99%

Sodium methoxide Finar Chemicals Pvt. Ltd. 99.5%

bis(3,5-trifluoromethyl)phenyl acetonitrile Sigma-Aldrich, 97%

7-Bromobenzo[c][1,2,5]thiadiazole-4- Sigma-Aldrich, 98%

carbaldehyde

Potassium iodide Sisco Life Sciences Pvt. Ltd. 99.5%

Iodine Avra, 99%

Sodium cyanide anhydrous Merck, 99%

Tetrahydrofuran Merck, HPLC grade

Ethanol Merck, HPLC grade

Methanol Merck, HPLC grade

Chloroform Merck, HPLC grade

Acetone Merck, HPLC grade

CDCl<sub>3</sub> Sigma-Aldrich, 99.96%

Glass Coverslips Bluestar

ITO coated PET Sigma-Aldrich

#### **Appendix-B**

#### Instrumentation

#### Nuclear magnetic resonance (NMR) spectroscopy

 $^{1}$ H and  $^{13}$ C NMR spectra were recorded on a Bruker DPX 400 and 500 MHz spectrometer with a solvent proton as internal standard (CDCl<sub>3</sub>:  $^{1}$ H: 7.26 ppm,  $^{13}$ C: 77.16 ppm). Commercially available deuterated CDCl<sub>3</sub> was used. Chemical shifts (δ) are given in parts per million (ppm). Spectra were processed using topspin 4. 1. 1. software.

#### Optical absorption spectroscopy

The solution-state and solid-state absorption spectra were collected using Jasco V-750 spectrophotometer in a diffuse reflectance UV-visible (DR-UV-vis) mode. The reflectance spectra were converted to absorbance using the Kubelka-Munk function.

#### Fluorescence spectroscopy

The solid-state emission spectra were recorded using an FP-8500 fluorescence spectrometer. The parameters are as follows; excitation and emission bandwidth are 2.5 nm, sensitivity =medium, data interval =0.5 nm, response =1 sec, and a scan speed of 500 nm/min. The absolute photoluminescence quantum yield is measured using the integrated sphere setup in fluorescence spectroscopy.

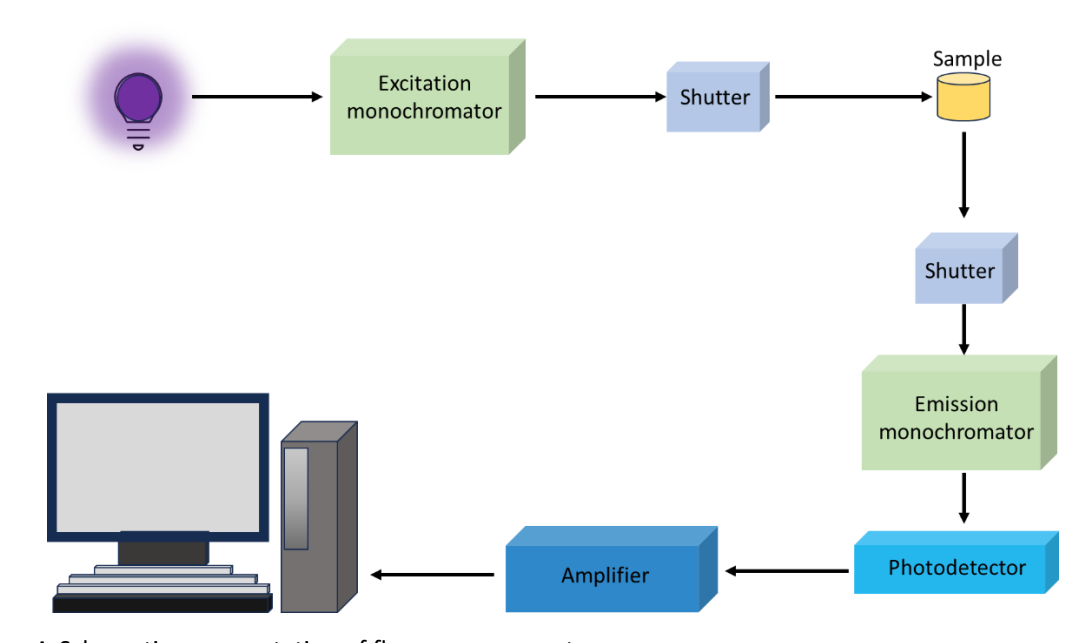


**Figure I.** Schematic representation of fluorescence spectroscopy.

#### Polarized light microscopy

The optical images of microcrystals and the fabricated circuit were captured using a NIKON eclipse LV100N POL polarizing microscope. It was equipped with an epi-illuminator (NIKON 12V 50W), DS-Fi3 camera having a 5.9-megapixel CMOS sensor, which enables superior color reproduction, and NIKON TU plan fluor EPI P series objectives  $(4\times, 10\times, 20\times \text{ and } 50\times)$  for pin-sharp aberration-free images regardless of magnification.

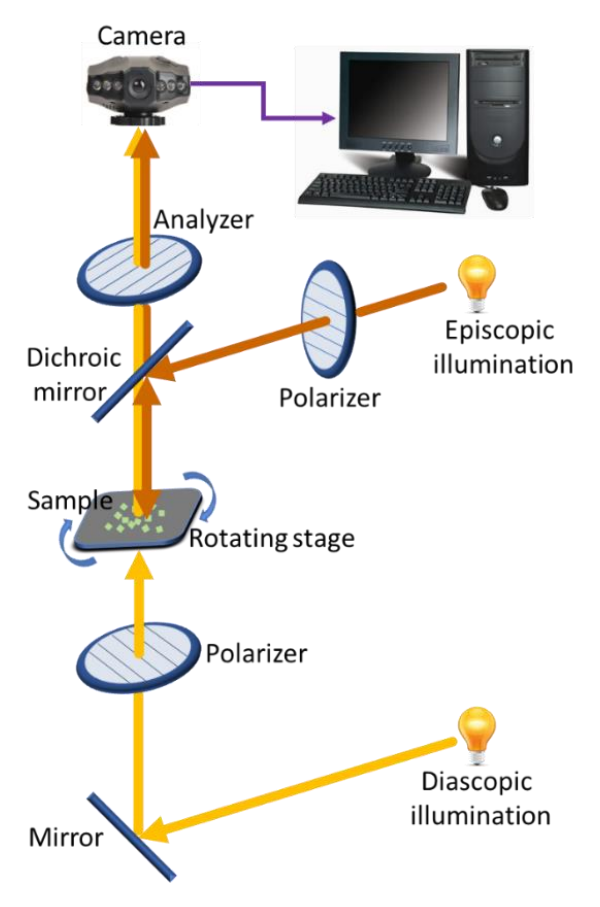


Figure II. Schematic representation of various components and the light path in polarized light microscopy.

#### Atomic force microscopy (AFM)

All the AFM experiments were carried out on an Oxford Asylum Research MFP-3D Origin. The image processing was carried out by using AR 16.25.226 software provided by the manufacturer. The images were recorded in a contact mode topography using a silicon cantilever (NSG 10\_DLC) with a diamond-like carbon tip (NT-MDT). The dimension of the tip is as follows: cantilever length =100±5  $\mu$ m, cantilever width =35±3  $\mu$ m, cantilever thickness =1.7-2.3  $\mu$ m, resonance frequency =190-325 kHz, force constant =5.5-22.5 N/m, and tip height =10-20 nm.

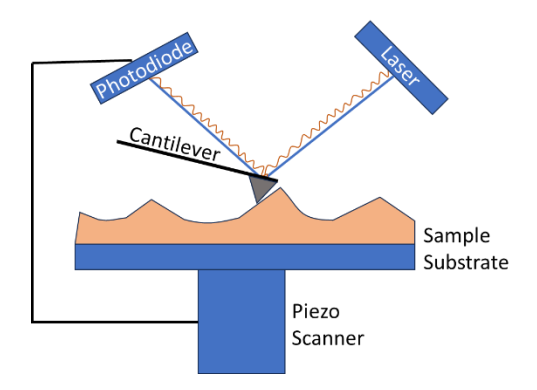


Figure III. Schematic representation of AFM setup to demonstrate the topography study of a material.

#### Field emission scanning electron microscopy (FESEM)

A thin layer of gold was coated on the substrate using a 15  $\mu$ A current for 80 sec. The size and morphology of the microcrystals and the circuit were examined by using a Zeiss FESEM operating at an accelerating voltage of 5 kV.

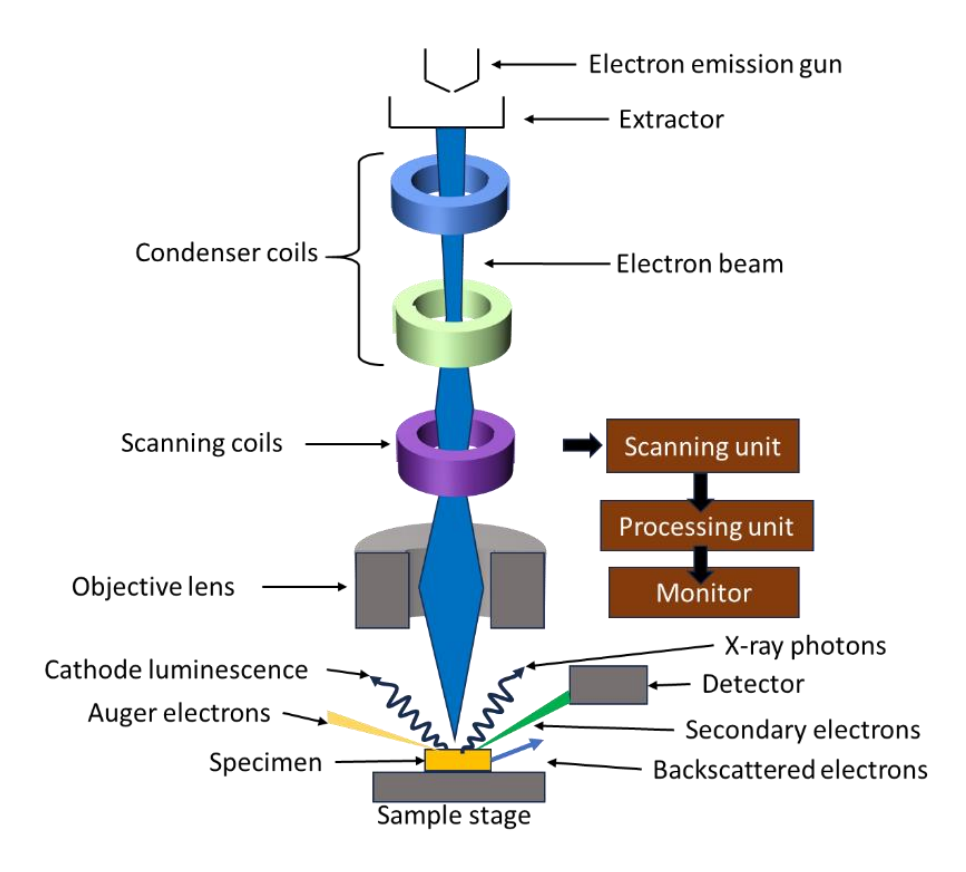


Figure IV. Schematic representation of FESEM setup.

#### Focused ion beam - scanning electron microscopy (FIB-SEM)

For the milling of microcrystals, Thermo Scientific SCIOS 2 Dual Beam or JEOL JIB 4700F FIB-SEM instrument were used. Initially, the microcrystals were imaged in SEM mode with a

0.0° tilt angle, 0.4 nA beam current, and an accelerating beam voltage of 5.00 kV. Later, the sample was tilted 52° to align orthogonal to FIB (Gallium ion source). Using pre-defined shapes in the software (rectangular and circular shapes) or by importing bitmaps, the milling portion was selected. Then, 30 kV accelerating beam voltage and 1.0/0.4/0.1 nA probe current were applied to mill the microcrystals to desired shapes.

### Confocal micro-spectroscopy

Fluorescence spectra of the microcrystals were recorded on a WI-Tec confocal spectrometer equipped with a Peltier-cooled CCD detector. Using 300 grooves/mm grating BLZ =750 nm. All measurements were performed in transmission mode geometry. A solid-state 405 nm laser was used as an excitation source. To collect the output signals from the specific area of microcrystals, 150× objective (N. A.: 0.95) was used. For acquiring a single spectrum before and after FIB milling, the laser power, integration time, and accumulations were given at respective places. To capture the dark field images, higher laser powers were used. The images were processed by using WI-Tec 5.2 software.

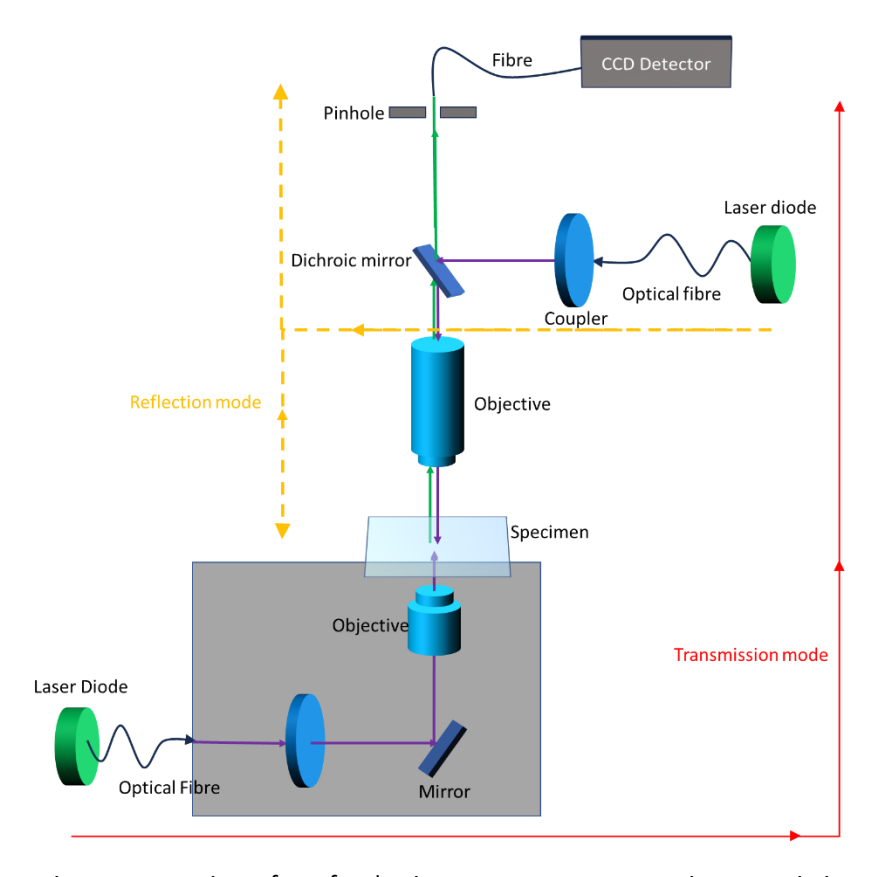


**Figure V.** Schematic representation of confocal micro-spectroscopy setup in transmission and reflection geometry.

### Micromanipulation (Mechanophotonics)

The mechanical micromanipulation approach was inherited to attain desired OPIC. In order to do this, an atomic force microscope (AFM)-equipped WITec alpha-300 confocal optical microscope was used. The holder was loaded with the AFM cantilever (TipsNano: NSG10, Force constant 3.1-37.6 N/m) and is attached to the 20× objective. The typical radius of curvature of the AFM cantilever tip is about 10 nm. The sample holder stage was moved in x-, y-, and the cantilever tip was moved in z-directions for carrying out various micromechanical operations like transferring (lifting and dropping), moving, and aligning/integrating.

### Fluorescence lifetime imaging (FLIM)

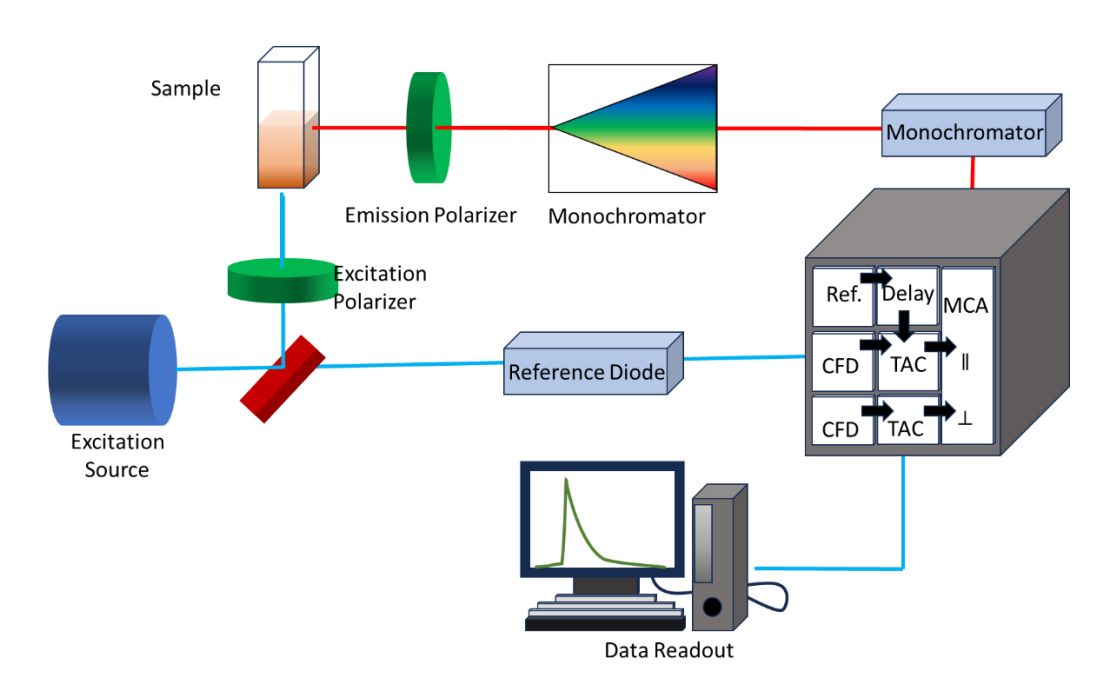


Figure VI. Schematic representation of FLIM setup.

FL decay and FL lifetime images were recorded on a time-resolved (Micro-Time 200, Pico Quant) confocal FLIM setup, which was equipped with an inverted microscope (Olympus IX 71). Measurements were performed at room temperature on microcrystals. The samples were excited by a 405 nm ps diode pulse laser (power  $\approx$ 5  $\mu$ w) with a stable repetition rate of 20 MHz (FWHM: 176 ps) through a water immersion objective (Olympus UPlans Apo: 60×; NA 1.2). The signal from the samples was collected by the same objective and passed through the dichroic mirror, filtered by using a 430 nm long-pass filter to cut off any exciting

light. The signal was then focused onto a 50  $\mu$ m diameter pinhole to remove the out-of-focus signal, recollimated, and directed onto a (50/50) beam splitter prior to entering into two single-photon avalanche photodiodes. The data acquisition was carried out with a SymPhoTime software-controlled PicoHarp 300 time-correlated single-photon counting module in a time-tagged time-resolved mode. The overall resolution of the setup was 4 ps.

### Non-linear optical (NLO) micro-spectroscopy

The experimental setup was based on femtosecond laser: Ti:Sapphire laser (Avesta TiF-60), wavelength 760 nm, pulse frequency 80 MHz, pulse duration 60 fs. During confocal NLO studies fundamental beam was focused on the sample by  $63\times$  objective with NA =0.7, and the focused beam diameter at a wavelength of 760 nm was about 1  $\mu$ m. The nonlinear optical signal (two-photon fluorescence) was collected by the same objective, reflected by the dichroic mirror, and collected by PMT with an appropriate set of filters. Optical images of microcrystals were taken using a CCD camera in the detection channel.

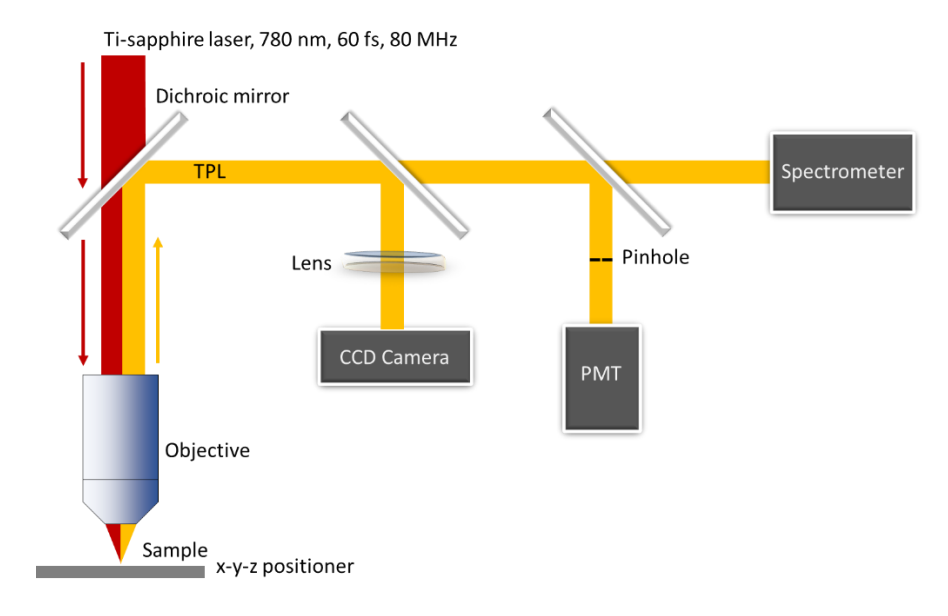


**Figure VII.** Schematic representation of NLO experimental setup.

### **Research Publications from Thesis**

1. V. Vinay Pradeep, N. Mitetelo, M. Annadhasan, M. Popov, E. Mamonov, T. V. Murzina\* and R. Chandrasekar\*

Ambient Pressure Sublimation Technique Provides Polymorph-Selective Perylene Non-Linear Optical Micro Cavities

Adv. Opt. Mater. 2020, 8, 1901317, doi.org/10.1002/adom.201901317.

2. V. Vinay Pradeep and R. Chandrasekar\*

Micromanufacturing of Geometrically- and Dimensionally-Precise Molecular Single-Crystal Photonic Microresonators via Focused Ion Beam Milling arXiv:2203.14218v1 [physics.optics],

Adv. Opt. Mater. 2022, 10, 2201150, doi.org/10.1002/adom.202201150.

- **3. V. Vinay Pradeep**, G. Ummethala, S. R. K. Malladi\* and R. Chandrasekar\* Focused Ga Ion Beam Milling of Perylene Microcrystals into Photonic Modules: Effect of Substrate and the Ion Beam Current Cryst. Growth Des. **2023**, <a href="doi:10.1021/acs.cgd.3c00653">doi:10.1021/acs.cgd.3c00653</a>.
- **4. V. Vinay Pradeep**, M. Chosenyah, E. Mamonov\* and R. Chandrasekar\*

  Crystal Photonics Foundry: Geometrical Shaping of Molecular Single-crystals into Next Generation Optical Resonators

  Nanoscale **2023**, doi.org/10.1039/D3NR02229C.
- 5. V. Vinay Pradeep,† A. V. Kumar† and R. Chandrasekar\*

  A Tandem Approach to Fabricating a Hybrid, Organic-Add-Drop Filter Using Single-Crystal Disk-Resonators and Pseudo-Plastic Crystal Waveguides

  Manuscript submitted. († -Contributed equally)

### **Patents**

V. Vinay Pradeep and R. Chandrasekar

MOLECULAR SINGLE-CRYSTAL PHOTONIC MICRO RESONATORS AND METHOD OF FABRICATING THEREOF

- 1. Indian Patent Application, E-2/1199/2023/CHE (filed)
- 2. Patent Corporation Treaty, IN2023/050278 (filed).

### **Other Research Publications**

- V. Vinay Pradeep, M. Annadhasan and R. Chandrasekar\*
   Vapour-Phase Epitaxial Growth of Dual-Colour-Emitting DCM/Perylene Micro Heterostructure Optical Waveguides
  - Chem. Asian. J. **2019**, 14, 4577, doi.org/10.1002/asia.201901221.
- 2. M. Jyothi, M. Annadhasan, V. Vinay Pradeep and R. Chandrasekar\*

  Direct Microscale Monitoring of Aggregation, its Growth and Diffusion via Aggregation-Induced Emission

  Soft Matter 2020, 16, 2664, doi.org/10.1039/D0SM00108B.
- **3.** M. Annadhasan, A. Agrawal, S. Bhunia, **V. Vinay Pradeep**, S. S. Zade,\* C. M. Reddy\* and R. Chandrasekar\* *Mechanophotonics: Flexible Single-Crystal Organic Waveguides and Circuits Angew. Chem. Int. Ed.* **2020**, *59*, 13852, <a href="doi:org/10.1002/anie.202003820">doi:org/10.1002/anie.202003820</a>.
- **4. V. Vinay Pradeep**, C. Tardío, I. T. -Moya, A. M. Rodrígue, A. V. Kumar, M. Annadhasan, A. de la Hoz, P. Prieto\* and R. Chandrasekar\*

  Mechanical Processing of Naturally Bent Organic Crystalline Microoptical Waveguides and Junctions

  Small **2021**, 17, 2006795, doi.org/10.1002/smll.202006795.
- 5. A. V. Kumar, M. Annadhasan, V. Vinay Pradeep, M. Jyothi, K. V. J. Jose\* and R. Chandrasekar\*
  Spatio-Temporal Growth Anomalies in Photo-Isomerisable Cyanostilbene-Based Crystals Triggered by Light
  J. Phys. Chem. C 2021, 125, 4909, doi.org/10.1021/acs.jpcc.1c00709.
- 6. V. Vinay Pradeep,†\* C. Tardío,† R. Martín, A. M. Rodríguez, A. de la Hoz, R. Jada, M. Annadhasan, P. Prieto\* and R. Chandrasekar\* Polarised Optical Emission from Organic Anisotropic Microoptical Waveguides Grown by Ambient Pressure Vapour-Deposition Chem. Asian J. 2021, 16, 3476, doi.org/10.1002/asia.202100910. (†-Contributed equally)
- 7. M. Annadhasan, V. Vinay Pradeep, A. V. Kumar, J. Ravi and R. Chandrasekar\*

  Integrating Triply- and Singly-Bent Highly Flexible Crystal Optical Waveguides for

  Organic Photonic Circuit with a Long-Pass-Filter Effect

  Small Struct. 2022, 3, 2100163, <a href="mailto:doi.org/10.1002/sstr.202100163">doi.org/10.1002/sstr.202100163</a>.

### Research publications, Patents and Presentations

- 8. V. Vinay Pradeep,† M. Rohullah,† J. Ravi, A. V. Kumar and R. Chandrasekar\*

  Micromechanically-Powered Rolling Locomotion of Twisted-Crystal OpticalWaveguide-Cavity as a Mobile Light Polarization Rotor

  Angew. Chem. Int. Ed. 2022, 61, e202202114, doi.org/10.1002/anie.202202114.

  (†-Contributed equally)
- 9. R. Chinnasamy, J. Ravi, V. Vinay Pradeep, D. Manoharan, F. Emmerling, B. Bhattacharya, S. Ghosh and R. Chandrasekar\*
  Adaptable Optical Microwaveguides from Mechanically Flexible Crystalline Materials
  Chem. Eur. J 2022, 28, e202200905, doi.org/10.1002/chem.202200905.

### **Presentations in Conferences and Symposiums**

**1. V. Vinay Pradeep**, N. Mitetelo, M. Annadhasan, M. Popov, E. Mamonov, T. V. Murzina\* and R. Chandrasekar\*

Ambient Pressure Sublimation Technique Provides Polymorph-Selective Perylene Nonlinear Optical Microcavities

Poster presented at the Chem-fest-2020, School of Chemistry, University of Hyderabad, India.

2. V. Vinay Pradeep, R. Chandrasekar\*

Micromanufacturing of Geometrically- and Dimensionally-Precise Molecular Single-Crystal Photonic Components *via* Focused Ion Beam Milling *Oral and Poster presentation Chem-fest-2022, School of Chemistry, University of Hyderabad, India.* 

(BEST ORAL PRESENTATION)

**3. V. Vinay Pradeep,** R. Chandrasekar\*

Micromanufacturing of Geometrically- and Dimensionally-Precise Molecular Single-Crystal Photonic Components *via* Focused Ion Beam Milling

Poster presented at the 12th India-Japan Science & Technology Conference: (ICFAST-2022), University of Hyderabad, India. (International Conference).

4. V. Vinay Pradeep, R. Chandrasekar\*

Micromanufacturing of Geometrically- and Dimensionally-Precise Molecular Single-Crystal Photonic Components *via* Focused Ion Beam Milling

Poster presentation at the Indo-Sweden, DST-VR conference, 2022, IIT Roorkee, Uttarakhand, India. (International Conference).

### Curriculum vitae

### **Personal Details:**

Name Vuppu Vinay Pradeep

Father's name Satyanarayana

Nationality Indian

Date of Birth 15-06-1995

Permanent Address 33-69/1, 6<sup>th</sup> Lane, Anand Nagar Colony, Payakaraopeta,

Visakhapatnam, Andhra Pradesh, India-531126.

### **Education Details:**

2017-2023 Ph.D. in Organic Nanophotonics under the supervision of Prof. R.

Chandrasekar, School of Chemistry, University of Hyderabad, India. **Thesis Title:** "Design and Fabrication of Single-Crystal Organic Photonic

Circuit Modules Using Focused Ion Beam Lithography".

**2012-2017** | **I.M.Sc in Chemical Sciences** (First Class) at the University of Hyderabad,

Hyderabad, Telangana, India.

2011-2012 Intermediate in Mathematics, Physics, Chemistry, and Computer

**Science** (1<sup>st</sup> Rank holder) at Jawahar Navodaya Vidyalaya,

Visakhapatnam, Andhra Pradesh, India.

2009-2010 | S.S.C. (First Class) at Jawahar Navodaya Vidyalaya, Visakhapatnam,

Andhra Pradesh, India.

### **Awards and Recognitions:**

- April 2022 Winner of "Best Oral Presentation" in in-house Chem-fest, School of Chemistry, University of Hyderabad, India.
- 2019-2022 Awarded as a Senior Research Fellow by CSIR, India.
- **2017-2019** Awarded as a **Junior Research Fellow** by CSIR, India.
- December 2016 Qualified All India Level CSIR-JRF conducted by New Delhi, India.
- 2011 Qualified for the National-level Mathematics Olympiad.
- Number of Publications: 13.
- Number of Patents: 02.
- *h*-index: **6**.

# Design and Fabrication of Single-Crystal Organic Photonic Circuit Modules Using Focused Ion Beam Lithography

by Vuppu Vinay Pradeep

Librarian

Indira Gandhi Memorial Library UNIVERSITY OF HYDERABAD

Central University P.O. HYDERABAD-500 046.

Submission date: 14-Jul-2023 03:20PM (UTC+0530)

**Submission ID:** 2130990456

File name: VUPPU VINAY PRADEEP.pdf (8.91M)

Word count: 31295

Character count: 170862

## Design and Fabrication of Single-Crystal Organic Photonic Circuit Modules Using Focused Ion Beam Lithography

**ORIGINALITY REPORT** 

**77**%

SIMILARITY INDEX

INTERNET SOURCES

**PUBLICATIONS** 

STUDENT PAPERS

6%

**PRIMARY SOURCES** 

Vuppu Vinay Pradeep, Govind Ummethala, Sai Rama Krishna Malladi, Rajadurai Chandrasekar. "Focused Ion Beam Milling of Perylene Microcrystals into Photonic Modules: Effect of Substrate and the Ion Beam Current", Crystal Growth & Design, 2023 University of Hyderobad

Hyderabad-500046, India Vinay Pradeep Vuppu, Melchi Chosenyah, Evgeniy Mamonov, Rajadurai Chandrasekar. "Crystal Photonics Foundry: Geometrical Shaping of Molecular Single Crystals into Next Generation Optical Cavities", Nanoscale, 2023

Publication

Publication

Vuppu Vinay Pradeep, Rajadurai Chandrasekar. "Micromanufacturing of Geometrically and Dimensionally Precise Molecular Single - Crystal Photonic Microresonators via Focused Ion Beam Milling", Advanced Optical Materials, 2022

Publication

versity of Hyderchad

Hemistry

University of Hyderobad Welapad-500046, India



Publication

2019

Rajadurai Chandrasekar. "Mechanophotonics
—Mechanical Micromanipulation of Single Crystals toward Organic Photonic Integrated
Circuits", Small, 2021
Publication

<1%

- 11
- Ping Li, Siyu Chen, Houfu Dai, Zhengmei Yang, Zhiquan Chen, Yasi Wang, Yiqin Chen, Wubin Shan, Wenqiang Peng, Huigao Duan. "Recent Advances in Focused Ion Beam Nanofabrication for Nanostructures and Devices: Fundamentals and Applications", Nanoscale, 2020

Publication

- Fatin Syazana Jamaludin, Mohd Faizul Mohd Sabri, Suhana Mohd Said. "Controlling parameters of focused ion beam (FIB) on high aspect ratio micro holes milling", Microsystem Technologies, 2013

<1%

- Publication
- 13

docksci.com

Internet Source

<1%

14 Co

Chuang Zhang, Chang-Ling Zou, Yongli Yan, Cong Wei, Jin-Ming Cui, Fang-Wen Sun, Jiannian Yao, Yong Sheng Zhao. "Self-Assembled Organic Crystalline Microrings as Active Whispering-Gallery-Mode Optical Resonators", Advanced Optical Materials, 2013

**2013** Publication

<1%

onlinelibrary.wiley.com

15

<1%

Wenbo Wu, Kui Chen, Ting Wang, Na Wang, Xin Huang, Lina Zhou, Zhao Wang, Hongxun Hao. "Stimuli-Responsive Flexible Organic Crystals", Journal of Materials Chemistry C, 2023

Publication

Jada Ravi, Mari Annadhasan, Avulu Vinod Kumar, Rajadurai Chandrasekar. "Mechanically Reconfigurable Organic Photonic Integrated Circuits Made from Two Electronically Different Flexible Microcrystals", Advanced Functional Materials, 2021

<1%

Publication

Xiaojun Li, Kaiyang Wang, Mingming Chen, Sisi Wang, Yubin Fan, Tao Liang, Qinghai Song, Guichuan Xing, Zikang Tang. "Stable Whispering Gallery Mode Lasing from Solution - Processed Formamidinium Lead Bromide Perovskite Microdisks", Advanced Optical Materials, 2020

<1%

Publication

pure-oai.bham.ac.uk

<1%

Wei Zhang, Jiannian Yao, Yong Sheng Zhao.
"Organic Micro/Nanoscale Lasers", Accounts

<1%

Joseph E. Thomaz, Patrick L. Kramer,
Sebastian M. Fica-Contreras, David J.
Hoffman, Michael D. Fayer. "Reorientationinduced Stokes shifts caused by directional
interactions in electronic spectroscopy: Fast
dynamics of poly(methyl methacrylate)", The
Journal of Chemical Physics, 2019
Publication

<1%

Meltem Sezen. "Chapter 6 Focused Ion Beams (FIB) — Novel Methodologies and Recent Applications for Multidisciplinary Sciences", IntechOpen, 2016

<1%

Publication

Zinfeng Liu, Son Tung Ha, Qing Zhang, Maria de la Mata, César Magen, Jordi Arbiol, Tze Chien Sum, Qihua Xiong. "Whispering Gallery Mode Lasing from Hexagonal Shaped Layered Lead Iodide Crystals", ACS Nano, 2015
Publication

<1%

Avulu Vinod Kumar, Rajadurai Chandrasekar.
"Mechanophotonics: fabrication of a 2 × 2
hybrid directional coupler from flexible
organic crystals", Journal of Materials

<1%

Publication

Chemistry C, 2023

Dasari Venkatakrishnarao, Evgeniy A.
Mamonov, Tatiana V. Murzina, Rajadurai
Chandrasekar. "Advanced Organic and
Polymer Whispering-Gallery-Mode
Microresonators for Enhanced Nonlinear
Optical Light", Advanced Optical Materials,
2018

<1%

Publication

Ping Li, Siyu Chen, Houfu Dai, Zhengmei Yang, Zhiquan Chen, Yasi Wang, Yiqin Chen, Wenqiang Peng, Wubin Shan, Huigao Duan. "Recent advances in focused ion beam nanofabrication for nanostructures and devices: fundamentals and applications", Nanoscale, 2021

<1%

Publication

Xu, Yan, and Nobuhiro Matsumoto. "Flexible and in situ fabrication of nanochannels with high aspect ratios and nanopillar arrays in fused silica substrates utilizing focused ion beam", RSC Advances, 2015.

Publication

<1%

Dasari Venkatakrishnarao, Rajadurai Chandrasekar. "Engineering the Self -Assembly of DCM Dyes into Whispering -Gallery - Mode μ - Hemispheres and Fabry-Pèrot - Type μ - Rods for Visible-NIR (600–875)

<1%

# nm) Range Optical Microcavities", Advanced Optical Materials, 2015

Publication

- Mari Annadhasan, Abhijeet R. Agrawal, Surojit
  Bhunia, Vuppu Vinay Pradeep et al.
  "Mechanophotonics: Flexible Single Crystal
  Organic Waveguides and Circuits",
  Angewandte Chemie, 2020
  Publication
- omu.repo.nii.ac.jp
  Internet Source

  <1 %
- Rajadurai Chandrasekar. "Mechanophotonics
   A guide to integrating microcrystals toward
  monolithic and hybrid all-organic photonic
  circuits", Chemical Communications, 2022
  Publication
- Xiaokun Wang, Xiaowei Guan, Qiangsheng Huang, Jiajiu Zheng, Yaocheng Shi, Daoxin Dai. "Suspended ultra-small disk resonator on silicon for optical sensing", Optics Letters, 2013

  Publication

<1%

Gerhard Schunk, Josef U. Fürst, Michael Förtsch, Dmitry V. Strekalov et al. "Identifying modes of large whispering-gallery mode resonators from the spectrum and emission pattern", Optics Express, 2014
Publication

34	Jada Ravi, Dasari Venkatakrishnarao,
	Chakradhar Sahoo, Sri Ram Gopal
	Naraharisetty et al. "A Two-Photon Pumped
	Supramolecular Upconversion
	Microresonator", ChemNanoMat, 2018

<1%

Rajadurai Chandrasekar, Carlos Tardío, Vuppu Vinay Pradeep, Raúl Martín et al. "Polarized optical emission from organic anisotropic microoptical waveguides grown by ambient pressure vapour - deposition", Chemistry – An Asian Journal, 2021

<1%

Publication

Publication

Nikolai Mitetelo, Dasari Venkatakrishnarao, Jada Ravi, Mikhail Popov et al. "Chirality -Controlled Multiphoton Luminescence and Second - Harmonic Generation from Enantiomeric Organic Micro - Optical Waveguides", Advanced Optical Materials, 2019

<1%

Publication

Liu, Tongliang, Chao Yang, Jinfeng Li, Lingyu Bu, Meng Zheng, Wei Liu, and Wenjun Yang. "Synthesis and two-photon absorption properties of a red-emitting poly(2,6-anthracenevinylene) derivative with donor-acceptor-donor motif", Journal of

<1%

**Publication** 

Luminescence, 2013.

38	Karen Sloyan, Henrik Melkonyan, Harry Apostoleris, Marcus Dahlem, Matteo Chiesa, Amal Al Ghaferi. "A review of focused ion beam applications in optical fibers", Nanotechnology, 2021	<1%
39	Toshinori Matsushima, Chuanjiang Qin, Kenichi Goushi, Fatima Bencheikh et al. "Enhanced Electroluminescence from Organic Light - Emitting Diodes with an Organic- Inorganic Perovskite Host Layer", Advanced Materials, 2018 Publication	<1%
40	Mari Annadhasan, Durga Prasad Karothu, Ragaverthini Chinnasamy, Luca Catalano et al. "Micromanipulation of Mechanically Compliant Organic Single - Crystal Optical Microwaveguides", Angewandte Chemie International Edition, 2020 Publication	<1%
41	ufdcimages.uflib.ufl.edu Internet Source	<1%
42	Cong Wei, Si-Yun Liu, Chang-Ling Zou, Yingying Liu, Jiannian Yao, Yong Sheng Zhao. "Controlled Self-Assembly of Organic Composite Microdisks for Efficient Output Coupling of Whispering-Gallery-Mode Lasers",	<1%

# Journal of the American Chemical Society, 2015

Publication

43

Hajime Asahi, Yoshiji Horikoshi. "Molecular Beam Epitaxy", Wiley, 2019

<1%

Publication

44

Song Chen, Ming-Peng Zhuo, Xue-Dong Wang, Guo-Qing Wei, Liang-Sheng Liao. "Optical waveguides based on one-dimensional organic crystals", PhotoniX, 2021

<1%

Publication

45

Vuppu Vinay Pradeep, Mari Annadhasan, Rajadurai Chandrasekar. "Vapour - Phase Epitaxial Growth of Dual - Colour - Emitting DCM - Perylene Micro - Heterostructure Optical Waveguides", Chemistry – An Asian Journal, 2019

<1%

Publication

46

Mari Annadhasan, Vuppu Vinay Pradeep, Avulu Vinod Kumar, Jada Ravi, Rajadurai Chandrasekar. "Integrating Triply - and Singly - Bent Highly Flexible Crystal Optical Waveguides for Organic Photonic Circuit with a Long - Pass - Filter Effect", Small Structures, 2021

<1%

Publication

# Submitted to Thapar University, Patiala Student Paper

<1%

Exclude quotes On Exclude bibliography On

Exclude matches

< 14 words